SPACECRAFT ELECTRIC POWER SYSTEM SIZING AND ANALYSIS COMPUTATIONS

FINAL REPORT

by

Herbert Riess • Ralph L. Robinson

Hampden O. Banks Jr. • Paul Bauer

William G. Binckley

STL 8584-6001-RU000

15 MARCH 1964

Prepared for

JET PROPULSION LABORATORY

CALIFORNIA INSTITUTE OF TECHNOLOGY

Purchase Order No. BK3-211739

This work was performed for the Jet Propulsion Laboratory, California Institute of Technology, sponsored by the National Aeronautics and Space Administration under Contract NAS7-100.

TRW SPACE TECHNOLOGY LABORATORIES

THOMPSON RAMO WOOLDRIDGE INC.

Prepared for
JET PROPULSION LABORATORY
CALIFORNIA INSTITUTE OF TECHNOLOGY
Under Purchase Order BK3-211739

Prepared H. Riess
H. Riess, Project Engineer

Approved A. Krausz
A. Krausz, Manager
Electric Power Department

Approved P. F. Glaser
P. F. Glaser, Director
Space Power and Support System Lab.

TRW Space Technology Laboratories
Thompson Ramo Wooldridge Inc.
One Space Park · Redondo Beach, California

FOREWORD

This report was prepared by TRW Space Technology Laboratories for the Jet Propulsion Laboratory under Purchase Order No. BK3-211739. The work covered by the report was conducted from July 1963 through February 1964 by Members of the Technical Staff in the Electric Power Department of STL. The Jet Propulsion Laboratory technical representative for this program was Mr. E. Lee Levanthal of JPL.

N65-15711

ABSTRACT

15711

This report presents a method of empirically designing electrical power systems that utilize solar energy, based upon present-day technology. It includes computation procedures suitable for computer programming. Power ratings of the systems investigated are within the 100 to 1000 watt range. Covered are the following:

- Power Source. Photovoltaic, flat-plate thermo-electric, thermionic and dynamic.
- Energy Storage. Silver-zinc and silver-cadmium batteries.
- Power Conditioning. Inverters.

A summary of current developments on system components includes the source of the information, an estimate of its validity and an identification of gaps in the technology concerned. Typical data, obtained either from the manufacturers or from user agencies, is presented in parametric form. For each major system component, a computation procedure in the form of a flow diagram is presented. These diagrams contain:

- Design constraints factored into the mathematical treatment
- Iterative processes, where necessary
- Results, expressed as size and electrical characteristics

Sample calculations are provided in appendices to illustrate the use of the computation procedure and the appropriate parametric data.

Author

CONTENTS

	Page
FOREWORD	iii
ABSTRACT	iv
LIST OF TERMS	xvi
I. INTRODUCTION	1-1
II. SYSTEM CONSIDERATIONS	2-1
A. Power System Definition	2-1
B. Power System Requirements	2-2
III. SOLAR POWER PLANTS	3-1
A. Solar Photovoltaic Plants	3-1
1. State of Development	3-2
2. Development of Computation Process	3-2
B. Flat-Plate Solar Thermoelectric Generator	3-46
1. Assumptions for Study	3-46
2. Development of Design Computation Process	3-49
C. Solar Thermionic Sources	3-58
1. State of Development	3-59
2. Systems Application	3-80
3. Assumptions for Design Study	3-81
4. Development of Design Computation Process	3-83
5. Parametric Data Generation	3-89
6. Problem Areas	3-92
7. Conclusions	3-96
D. Solar Dynamic Power Plants	3-98
1. State of Development	3-98
2. Development of Design Computation Process	3-101
E. Power Source Control and Conditioning	3-111
1. Power Source Control	3-111
2. Boost-Regulator	3-117
Bibliography and Reference List	3-122
IV. ELECTROMECHANICAL SOURCES	4-1
A. Primary Silver-Zinc Batteries	4-1
B. Secondary Silver-Zinc Batteries	4-11
C. Secondary Silver-Cadmium Batteries	4-19

CONTENTS (Continued)

Page

V. POWER CONDITIONING (INVERTER) 5-1

A. State of Development 5-1

B. Assumptions for Design Study 5-2

C. Development of Design Computation Process 5-2

VI. CONCLUSIONS AND RECOMMENDATIONS 6-1

APPENDICES

A1 Solar Photovoltaic Parametric Data

A2 Solar Thermoelectric Parametric Data

A3 Solar Thermionic Parametric Data

A4 Solar Power Source Controls Parametric Data

A5 Solar Dynamic Power Plant Parametric Data

A6 Primary Silver-Zinc Battery Parametric Data

A7 Secondary Silver-Zinc Battery Parametric Data

A8 Secondary Silver-Cadmium Battery Parametric Data

A9 Power Conditioning (Inverters) Parametric Data

B1 Sample Calculations for Solar Photovoltaic Sources

B2 Sample Calculations for Thermoelectric Sources

B3 Sample Calculations for Solar Thermionic Sources

B4 Sample Calculations for Solar Dynamic Sources

B5 Sample Calculations for Inverters

C Current-Voltage Relationships Anticipated for a Solar Flat-Plate Thermoelectric Module

D A Study of the Electro-Thermal Behavior of a Thermionic Converter

ILLUSTRATIONS

		Page
2-1	Photovoltaic Power System Block Diagram	2-3
2-2	Flat-Plate Thermoelectric Power System Block Diagram	2-4
2-3	Solar Dynamic Power System Block Diagram	2-5
2-4	Solar Dynamic Power System Block Diagram	2-6
2-5	Power System Voltages and Currents	2-7
2-6	Power System Requirements Computation Flow Diagram	2-9
3-1	Photovoltaic Design Computation Flow Diagram	3-4
3-2	Solar Array Reliability Calculation Flow Diagram	3-16
3-3	Solar Cell Current-Voltage Characteristics	3-28
3-4	Electron Integral Energy Spectrum	3-30
3-5	Proton Integral Energy Spectrum	3-31
3-6	Electron Energy Spectrum	3-32
3-7	Relative Damage Effectiveness of Electrons as a Function of Electron Energy	3-33
3-8	Equivalent 1-Mev Electron Energy Spectrum Incident on Solar Cells	3-34
3-9	Example Solar Array Configuration for Maximum Cell Density	3-41
3-10	General Flat-Plate Solar Thermoelectric Module	3-47
3-11	Flat-Plate Solar Thermoelectric Design Computation Flow Diagram — Couple Electrical-Thermal Characteristics	3-50
3-12	Flat-Plate Solar Thermoelectric Design Computation Flow Diagram — Heat Balance and Panel Design	3-53
3-13	Flat-Plate Solar Thermoelectric Design Computation Flow Diagram — Mission Influence on Panel Oversizing	3-55

ILLUSTRATIONS (Continued)

		Page
3-14	Typical CCG Performance at 2000°K Emitter Temperature, 3.08 Cm^2 Emitter Area, and 2 Mils Spacing (References 3-23 and 3-25)	3-60
3-15	Maximum Obtainable Efficiency with State-of-the-Art CCG Converters (Reference 3-25)	3-61
3-16	Solar Test Data, Five-Converter CCG (One Passive Converter), Optimized Generation Output Versus Solar Intensity (Reference 3-23)	3-63
3-17	CCG Test Data, Average Converter Load Current Versus Emitter Temperature (Figure 16 of Reference 3-25)	3-63
3-18	CCG Test Data, Average Converter Power Versus Emitter Temperature (Figure 16 of Reference 3-25)	3-64
3-19	Generator Performance Versus Emitter Temperature (Five Converters, 3 Volts)	3-64
3-20	Solar Test Data for General Electric, Three-Converter Cavity Vapor Generator (Run No. 15 of Reference 3-19)	3-67
3-21	Type A Set Converter Performance for an Emitter Temperature of 1700°C and Optimized Cesium Temperature (Reference 3-30)	3-70
3-22	Type B Set Converter Performance for a Corrected Emitter Temperature of 1700°C and Optimized Cesium Temperature (Reference 3-30)	3-71
3-23	Type D Set Converter Performance Steady State Data for an Observed Emitter Temperature of 1677°C and Optimized Cesium Temperature (Reference 3-30)	3-74
3-24	Solar Thermionic Design Computation Flow Diagram	3-85
3-25	Temperature-Entropy Diagram—Biphenyl Rankine Cycle	3-99
3-26	Solar Dynamic Design Computation Flow Diagram	3-102
3-27	Basic Configuration—Mercury Rankine Cycle Solar Dynamic Power Supply	3-103
3-28	Required Number of Petals as a Function of the Ratio of Outside to Inside Concentration Diameter	3-107

ILLUSTRATIONS (Continued)

		Page
3-29	Operating Modes of the Full-Shunt and Partial-Shunt Regulators	3-113
3-30	Power Control	3-115
3-31	Boost Regulator Design Computation Flow Diagram	3-119
4-1	Primary Battery and Regulator Design Computation Flow Diagram	4-3
4-2	Secondary Silver-Zinc Battery Flow Diagram	4-13
4-3	Silver-Cadmium Secondary Battery Design Computation Flow Diagram	4-22
5-1	Regulated, Single-Phase Converter	5-3
5-2	Regulated, Three-Phase Converters (Type 2A, 4A)	5-4
5-3	Unregulated, Single-Phase Converters (Type 1B, 3B)	5-4
5-4	Inverter Design Computation Flow Diagram	5-5
A1-1	Solar Cell Current—Voltage Characteristics (Block A)	A1-2
A1-2	Solar Cell Short Circuit Current as a Function of Electron Dose (Block B)	A1-3
A1-3	Solar Cell Open Circuit Voltage as a Function of Electron Dose (Block C)	A1-4
A1-4	Solar Cell Cover Glass Transmission as a Function of Electron Dose (Block D)	A1-5
A1-5	Solar Cell Adhesive Transmission as a Function of Electron Dose (Block E)	A1-6
A1-6	Short Circuit Current as a Function of Angle of Incidence (Block F)	A1-7
A1-7	Current Temperature Coefficient as a Function of Electron Dose (Block N)	A1-8
A1-8	Voltage Temperature Coefficient as a Function of Insolation (Block Q)	A1-9
A1-9	Solar Array Structure Weight (Block JJ)	A1-10

ILLUSTRATIONS (Continued)

		Page
A2-1	Seebeck Voltage, P-Type Elements (Block A)	A2-2
A2-2	Seebeck Voltage, N-Type Elements (Block B)	A2-3
A2-3	Electrical Resistivity, P-Type Elements (Block C) . . .	A2-4
A2-4	Electrical Resistivity, N-Type Elements (Block D) . . .	A2-4
A2-5	Thermal Conductivity, P-Type Elements (Block E) . . .	A2-5
A2-6	Thermal Conductivity, N-Type Elements (Block F) . . .	A2-5
A2-7	Steady State Degradation (Block G)	A2-6
A2-8	Thermal Recycling Degradation After Less Than 10^3 Hours at Steady State (Block H)	A2-7
A2-9	Thermal Recycling Degradation After Less Than 10^3 Hours at Steady State (Block I)	A2-8
A2-10	Pointing Accuracy (Block J)	A2-9
A3-1	Reflectivity Versus Time, Solar Thermionic Function (Block A)	A3-2
A3-2	Ratio of Average Converter Efficiency to Initial Converter Efficiency Versus Time, Solar Thermionic Function (Block B)	A3-3
A3-3	Initial Converter Efficiency Versus Emitter Temperature, Solar Thermionic Function (Block C)	A3-4
A3-4	Concentrator-Absorber Efficiency as a Function of Emitter Temperature and Relative Orientation Error, Solar Thermionic Function (Block D)	A3-5
A3-5	Weight of Absorber Cavity as a Function of Initial Power Capability and Emitter Temperature, Solar Thermionic Function (Block E)	A3-6
A3-6	Weight of Solar Concentrator as a Function of Projected Active Area, Solar Thermionic Function (Block F)	A3-7
A3-7	Stowage Volume of Concentrator as a Function of Projected Active Area, Solar Thermionic Function (Block G)	A3-8

ILLUSTRATIONS (Continued)

		Page
A3-8	Weight of Supporting Structure and Mechanisms as a Function of Total Concentrator-Absorber Weight, Solar Thermionic Function (Block H)	A3-9
A3-9	Stowage Volume of Supporting Structure and Mechanisms as a Function of Total Stowage Volume of Concentrators, Solar Thermionic Function (Block I)	A3-10
A4-1	Power Control Volume as a Function of Shunt Current (Block A)	A4-2
A4-2	Power Control Weight as a Function of Shunt Current (Block W)	A4-3
A4-3	Assumed Thermionic Power Source Output Voltage as a Function of Output Power (Block B)	A4-4
A4-4	Boost Regulator Efficiency as a Function of Output Power and Input Voltage (Block C)	A4-5
A4-5	Boost Regulator Weight as a Function of Output Power and Input Voltage (Block D)	A4-6
A4-6	Boost Regulator Volume as a Function of Output Power and Input Voltage (Block E)	A4-7
A5-1	Estimated Power Required to Control Parasitic Load as a Function of Maximum Parasitic Load Power Dissipation (Block B)	A5-2
A5-2	Accessories Shaft Power as a Function of Rated Output for Mercury Rankine Power Supply (Block E)	A5-2
A5-3	Fluid Subcooling Required as a Function of Rated Output for Mercury Rankine Power Supply (Block G)	A5-3
A5-4	Collector Performance Characteristics as a Function of Concentrator Accuracy and Cavity Aperture Diameter (Block L)	A5-4
A5-5	Estimated Concentrator Diameter Normalized to AU as a Function of Rated Output for Mercury Rankine Power Supply (Block J)	A5-5
A5-6	Estimated Absorber Weight Excluding Heat Storage Unit vs Boiler Heat Input Rate (Block KK)	A5-5

ILLUSTRATIONS (Continued)

		Page
A5-7	Total Heat Storage Weight as a Function of Energy Storage Material Weight (Block LL)	A5-6
A5-8	Weight of Rotating Unit (Generator, Turbine, and Pump) as a Function of Electrical Output (Block II)	A5-6
A5-9	Estimated Weight of Control Equipment as a Function of Rated Output — Weight Includes Speed Control and Startup System — (Block OO)	A5-7
A5-10	Fluid Inventory Weight for Mercury Rankine Power Supply as a Function of Generated Power (Block NN)	A5-7
A5-11	Support Structure Weight for Silar Dynamic Power Supply vs Total Weight of Components (Block PP)	A5-9
A6-1	Temperature Exponent of Activated Storage Versus Temperature (Block P)	A6-2
A6-2	Temperature Exponent of Unactivated Storage Versus Temperature (Block K)	A6-3
A6-3	Cell Plateau Voltage as a Function of Discharge Rate and Temperature (Block S)	A6-4
A6-4	Converter Efficiency Factor, α, Versus Rated Design Voltage (Block I)	A6-5
A6-5	Converter Efficiency Factor, λ, as a Function of Rated Load (Block L)	A6-6
A6-6	Converter Weight and Volume Versus Rated Power (Blocks BB and CC)	A6-7
A6-7	Capacity Weight Relationship of Manually Activated Primary Silver-Zinc Batteries (Block DD)	A6-8
A6-8	Battery Packaging Factor as a Function of Watt-Hour Capacity (Block EE)	A6-9
A6-9	Capacity Volume Relationship of Manually Activated Primary and Sealed Solar Discs (Block GG)	A6-10
A6-10	Volume Capacity Relationship of Automatically Activated Primary Silver-Zinc Batteries (Block GG)	A6-11

ILLUSTRATIONS (Continued)

		Page
A6-11	Capacity Weight Relationship of Packaged Automatically Activated Silver-Zinc Batteries (Block GG)	A6-12
A7-1	Temperature Exponent of Activated Storage Versus Temperature (Block N)	A7-2
A7-2	Temperature Exponent of an Activated Storage Versus Temperature (Block O)	A7-3
A7-3	Capacity Weight Relationship of Sealed Secondary Silver-Zinc Batteries (Block U)	A7-4
A7-4	Capacity Volume Relationship of Manually Activated Primary and Sealed Solar Discs (Block W)	A7-5
A7-5	Battery Package Factor as a Function of Watt-Hour Capacity (Block V)	A7-6
A8-1	Depth of Discharge—Cycle Life Relationship of Silver-Cadmium Secondary Cells	A8-2
A8-2	Maximum Achievable State of Charge Versus Temperature, Charge Rate, a Parameter (Blocks G and II)	A8-3
A8-3	Secondary Silver-Cadmium Cells, Change in Lower Plateau Voltage with Discharge Current and Density (Block I)	A8-4
A8-4	Change in Upper Plateau Voltage with Discharge Current Density (Block I)	A8-4
A8-5	50°F Silver-Cadmium Cell Voltage Versus State of Charge (Block I)	A8-5
A8-6	60°F Silver-Cadmium Cell Voltage Versus State of Charge (Block I)	A8-6
A8-7	70°F Silver-Cadmium Cell Voltage Versus State of Charge (Block I)	A8-7
A8-8	80°F Silver-Cadmium Cell Voltage Versus State of Charge (Block I)	A8-8
A8-9	90°F Silver-Cadmium Cell Voltage Versus State of Charge (Block I)	A8-9

ILLUSTRATIONS (Continued)

		Page
A8-10	100°F Silver-Cadmium Cell Voltage Versus State of Charge (Block I)	A8-10
A8-11	110°F Silver-Cadmium Cell Voltage Versus State of Charge (Block I)	A8-11
A8-12	Silver-Cadmium Battery Volume as a Function of Capacity (Block EE)	A8-12
A8-13	Silver-Cadmium Unpackaged Battery Weight as a Function of Capacity (Block FF)	A8-13
A8-14	Battery Packaging Factor as a Function of Watt-Hour Capacity (Block GG)	A8-14
A9-1	Power Per Unit Weight as a Function of Power Rating (Block A)	A9-2
A9-2	Density as a Function of Power (Block B)	A9-3
A9-3	Load Ratio Factor as a Function of Load Ratio (Block D)	A9-4
B1-1	Solar Cell Current-Voltage Characteristics of Sample Calculations	B1-3
B4-1	Preliminary Configuration Analysis, 1 Kilowatt Solar Mercury Rankine Power Supply	B4-9
C-1	I-V Curve, Flat-Plate Solar Thermoelectrics for Earth Orbit	C-6
D-1	Energy Flow Diagram	D-2
D-2	Emitter Temperature Versus Thermal Input as a Function of Electron Cooling	D-8
D-3	I-V Curve for a Thermionic Diode at a Constant Temperature of 2000°K	D-9
D-4	Calculated I-V Curves as a Function of Emitter Temperature and Thermal Input	D-12
D-5	Plot of Electron Cooling Versus Voltage as a Function of Emitter Temperature and Thermal Input	D-13

TABLES

		Page
3-1	Specific Weights of Solar Array	3-42
3-2	Steady State Temperatures in Sun	3-44
3-3	Orbit Parameters	3-45
3-4	Transient Eclipse Temperatures	3-45
3-5	Solar Thermionic Converter Performance Summary (Individual Converters)	3-76
3-6	Solar Thermionic Generator Laboratory Test Summary (Electrical Heating)	3-77
3-7	Solar Thermionic Generator Solar Test Summary (5-Foot Diameter Mirrors)	3-78
3-8	State of Development of Elements of Solar Thermionic Energy Conversion Systems (Excluding Converters and Generators)	3-79
3-9	Structure of Thermionic Diode Power Sources	3-118
3-10	Booster Regulator Power Losses	3-120

LIST OF TERMS

Systems Requirements

$E_{b\,(max)}$	Maximum specified bus voltage (volt)
$E_{b'}$	Bus voltage during time t_1 (battery charging) (volt)
E_{b2}	Bus voltage during time t_2 (battery discharge) (volt)
E_d	Battery cell average discharge voltage (volt)
E_{di}	Isolating diode voltage drop (volt)
E_{ec}	Battery cell end of charge voltage (volt)
E_s	Source voltage (volt)
E_{sa}	Solar array voltage (volt)
I_{b1}	Current from bus during time t_1 (amp)
I_{b2}	Current from bus during time t_2 (amp)
I_c	Average battery charge current (amp)
I_d	Average battery discharge current (amp)
I_{i1}	Inverter current during time t_1 (amp)
I_{i2}	Inverter current during time t_2 (amp)
I_{pc2}	Power control current during time t_2 (amp)
I_{pi}	Power control current during time t_1 (amp)
I_{sa}	Solar array current (amp)
I_1	Direct bus load current during time t_1 (amp)
I_2	Direct bus load current during time t_2 (amp)
$I_{\ell 1}$	Total bus load current during time t_1 (amp)
$I_{\ell 2}$	Total bus load current during time t_2 (amp)
N_s	Number of power source energy converters connected in series
P_{b1}	Bus power during time t_1 (watt)
P_{b2}	Bus power during time t_2 (watt)

Systems Requirements (Continued)

P_{i1}	Inverter average power required during time t_1 (watt)
P_{i2}	Inverter average power required during time t_2 (watt)
P_{pc}	Power control power requirements (watt)
P_r	Inverter power rating (watt)
$P'_{s\ (max)}$	Maximum source power (watt)
P_1	Direct bus connected load average power required during time t_1 (watt)
P_2	Direct bus connected load average power required during time t_2 (watt)
t_1	Battery charging period (sunlight) (hours)
t_2	Battery discharge period (eclipse, peak load, etc.) (hours)
t_d	Mission time at design point (hours)

Photovoltaic Sources

A_c	Solar cell area (cm^2)
A_{c-a}	Solar cell active area (cm^2)
A_p	Solar cell panel area (ft^2)
$A_{p(max)}$	Maximum solar panel area (ft^2)
A_{sa}	Solar array area (ft^2)
AU	Astronomical unit
d_{cg}	Solar cell cover glass thickness (mil)
d_{cb}	Solar cell connection and insulation board (mil)
E	Solar cell voltage under design conditions (volt)
E_{di}	Isolation diode voltage drop (volt)
$E(P_m)$	Solar cell voltage at maximum power under design conditions (volt)
E_s	Solar plant voltage output (volt)
E_{sa}	Solar array output voltage (volt)
E_o	Solar cell voltage under standard conditions (volt)
$E_o(P_m)$	Solar cell voltage at maximum power under standard conditions (volt)
$E_o\|I_o = 0$	Solar cell open circuit voltage under standard conditions (volt)
F_a	Adhesive transmission factor (per unit)
F_{cg}	Cover glass transmission factor (per unit)
F_i	Installation factor (per unit)
F_p	Panel packing factor (per unit)
I	Solar cell current under design conditions (ma)

Photovoltaic Sources (Continued)

$I(P_m)$	Solar cell current at maximum power under design conditions (ma)
$I = f(E)$	Solar array installed solar cell current-voltage characteristics at time t
I_{sa}	Solar array output current (amp)
I'_{sa}	Solar array output current without failures (amp)
I''_{sa}	Solar array output current with failures (amp)
$I_{sc} - \Phi$	Solar cell short current after Φ particle radiation under standard conditions (ma)
I_o	Solar cell current under standard conditions (ma)
$I_o(P_m)$	Solar cell current at maximum power under standard conditions (ma)
$I_o = f(E_o)$	Solar cell current-voltage characteristics at standard conditions
$I_o \vert E_o = 0$	Solar cell short circuit current under standard conditions (ma)
K_1	Constant
K_2	Constant
N_p	Number of parallel solar cell strings in solar array
n_p	Number of panels in solar array
N_s	Number of series connected solar cells per string in solar array
N_{sa}	Total number of solar cells in solar array
P_m	Maximum solar cell power output (watt)
P_s	Solar plant power output (watt)
P'_s	Solar array power output with no cell failures (watt)
P''_s	Solar array power output with cell failures (watt)

Photovoltaic Sources (Continued)

r_s	Solar cell series resistance (ohms)
R_{sa}	Reliability of solar array (per unit)
R_{sc}	Solar cell short circuit current ratio $\left[I_{sc}(\theta)/I_{sc}(0^{\circ})\right]$ (per unit)
S	Insolation on solar array (mw/cm^2)
s	Relative insolation with respect to $1\Delta U$ (per unit)
s'	Effective relative insolation on solar cell (per unit)
t	Time (hours)
t_d	Mission time at design point (hours)
T_{sa}	Solar cell temperature ($^{\circ}C$)
T_o	Standard solar cell temperature ($^{\circ}C$)
w_c	Weight of solar cell (gram)
w_c/A	Solar cell weight per unit area ($gram/cm^2$)
w_c'	Weight of solar cell, cover glass, adhesive, connections, insulation, etc. per cell (gram)
w_{eb}	Weight of connection and insulation board (gram)
w_{cg}	Weight of cell cover glass (gram)
w_h	Weight of cell connection, adhesive, terminals, etc. per cell (gram)
w_n/A	Weight of cell connection, adhesive, terminals, etc. per cell unit area ($gram/cm^2$)
W_{sa}	Weight of solar array (lb)
W_s/A	Weight of structure per unit Area (lb/ft^2)
β_I	Solar cell current temperature coefficient ($amp/^{\circ}C$)

Photovoltaic Sources (Continued)

β_I/I_{sc}	Relative solar cell current temperature coefficient (per unit/^{o}C)
β_E	Solar cell voltage temperature coefficient (volt)/^{o}C)
ΔE_i	Change in cell voltage due to panel assembly (ma)
ΔE_s	Change in cell voltage due to change in insulation from standard (volt)
ΔE_T	Change in cell voltage due to difference in temperature from standard (volt)
ΔE_Φ	Change in cell voltage due to particle radiation (volt)
ΔI_i	Change in cell current due to panel assembly (volt)
ΔI_s	Change in cell current due to change in insolation from standard (ma)
ΔI_T	Change in cell current due to difference in temperature from standard (ma)
ΔI_Φ	Change in cell current due to particle radiation (ma)
ΔT	Difference in temperature from standard (^{o}C)
Γ	Solar array sun angle (deg)
λ_c	Cell failure rate (failures/10^6 hours)
λ_d	Diode failure rate (failures/10^6 hours)
λ_i	Interconnection failure rate (failures/10^6 hours)
ρ_{cb}	Circuit board density (gram/cm^3)
ρ_{cg}	Cover glass density (gram/cm^3)
Φ'_a	Equivalent 1 MEV electron dose on adhesive (electrons/cm^2)
Φ'_c	Equivalent 1 MEV electron dose on solar cell (electrons/cm^2)
Φ'_{cg}	Equivalent 1 MEV electron dose on cover glass (electrons/cm^2)

Thermoelectric Sources

A	Area of absorber/radiator, per couple (cm^2)
A_a	Array area (cm^2)
AU	Maximum mission distance from sun (astronomical units)
AU_x	Any distance during mission less than maximum (astronomical units)
d_n	Density of negative element material ($gram/cm^3$)
d_p	Density of positive element material ($gram/cm^3$)
D_r	Degradation factor due to thrusting
$D_{r\ell 1}$	Degradation factor after less than 1000 hours steady state
D_{rm2}	Degradation factor after more than 1000 hours steady state
D_{ss}	Degradation factor due to steady state operation
I_c	Current per couple (amp)
K_a	Nonproductive array support area factor
K_{ca}	Corrected array area (cm^2)
K_N	Thermal conductivity, negative element ($mw\text{-}cm/cm^2\text{-}^oC$)
$K_{\bar{N}}$	Mean thermal conductivity, negative element ($mw\text{-}cm/cm^2\text{-}^oC$)
K_p	Thermal conductivity, positive element ($mw\text{-}cm^2/cm^2\text{-}^oC$)
$K_{\bar{p}}$	Mean thermal conductivity, positive element ($mw\text{-}cm/cm^2\text{-}^oC$)
K_r	Radiator density ($gram/cm^2$)
K_1	Length to cross section are (constant)
K_2	Temperature rise from hot junction to absorber (^oK)
K_3	Temperature drop from cold shoe to radiator (^oK)
K_4	Absorber density per cm^2 ($gram/cm^2$)
K_5	Internal structure density ($gram/cm^2$)

K_6	Modular support weight factor
K_7	Thrusting loss factor
K_8	Number of orbits after 10^3 hours steady state
K_9	Number of orbits after 10^3 hours steady state
L	Length of thermoelectric elements (cm)
L_N	Length of negative thermoelectric element (cm)
L_p	Length of positive thermoelectric element (cm)
M_o	Matching factor
N_1	Modular enlargement factor
N_2	Array enlargement factor for mission factor
P_d	Design power requirement (electrical watt)
P_{el}	Power available at earth launch (electrical watt)
P_{tc}	Theoretical power/couple (electrical watt)
P_{lc}	Load power output per couple (electrical watt)
Q_a	Heat input per module (thermal watt)
Q_{ch}	Conducted heat per couple (thermal watt)
Q_j	Joule heating per couple (thermal watt)
Q_{ptc}	Peltier-Thompson effect at cold junction/couple (thermal watt)
Q_{pth}	Peltier-Thompson effect at hot junction/couple (thermal watt)
Q_{rr}	Heat reradiated at the outer surface absorber panel (thermal watt)
Q_1	Heat input per couple (thermal watt)
Q_2	Heat output per couple (thermal watt)
r	Ratio of thermal to electrical conductivities factor
R_{ci}	Internal resistance per couple (ohms)

R_{lc}	Load resistance per couple (ohms)
S_d	Solar constant at maximum design mission distance (watts per cm^2)
S_e	Solar constant at 1 AU (watt per cm^2)
S_m	Mean Seebeck voltage/couple ($\mu v/^{o}C$)
S_N	Seebeck voltage, negative thermoelectric element ($\mu v/^{o}C$)
$S_{\overline{N}}$	Mean Seebeck voltage, negative element ($\mu v/^{o}C$)
S_p	Seebeck voltage, positive thermoelectric element ($\mu v/^{o}C$)
$S_{\overline{p}}$	Mean Seebeck voltage, positive element ($\mu v/^{o}C$)
T_a	Heat absorber temperature (^{o}K)
T_c	Thermoelectric cold junction temperature (^{o}K)
T_h	Thermoelectric hot junction temperature (^{o}K)
T_r	Heat radiator temperature (^{o}K)
T_l	Cumulative time at steady state (hours)
V_c	Voltage per couple (volt)
W_a	Array weight (gram)
W_{ac}	Absorber weight per couple (gram)
W_{ca}	Corrected array weight (gram)
W_m	Modular weight (gram)
W_{mc}	Modular weight per couple (gram)
W_{ms}	Modular support weight (gram)
W_N	Weight per negative thermoelectric element (gram)
W_p	Weight per positive thermoelectric element (gram)
W_{rc}	Radiator weight per couple (gram)
W_{sc}	Internal structure weight, per couple (gram)

Thermoelectric Sources (Continued)

Γ	Angular error in pointing accuracy (deg)
ϵ_a	Emissivity coefficient of the outer surface absorber panel
ϵ_{ai}	Emissivity coefficient of inside surface of absorber panel
ϵ_n	Net internal emissivity coefficient
ϵ_r	Emissivity coefficient of the outer surface radiator panel
ϵ_{ri}	Emissivity coefficient of inside surface of radiator panel
η_{th}	Thermal efficiency per module (percent)
θ	Figure of merit (factor)
ρ_N	Electrical resistivity, negative thermoelectric element (milliohms/cm)
$\rho_{\overline{N}}$	Mean electrical resistivity, negative element (milliohms/cm)
ρ_p	Electrical resistivity, positive thermoelectric element (milliohms/cm)
$\rho_{\overline{p}}$	Mean electrical resistivity, positive element (milliohms/cm)
σ_N	Cross section area, negative element (cm^2)
σ_p	Cross section area, positive element (cm^2)
σ_{sb}	Stefan-Boltzmann constant (5.67×10^{-12} watt/cm^2-^oK-sec)
ν_a	Absorptivity coefficient of absorber outer surface
φ	Array correction angle to maintain design power (deg)

Solar Thermionic Source

A_c	Actual projected active area of individual solar concentrator as calculated (ft^2)
A_{cm}	Maximum allowable projected active area of any single concentrator (ft^2)
A_t	Total projected active area required for the solar thermionic source (ft^2)
N_c	Actual minimum number of concentrators with area $\leq A_{cm}$ which are required to produce power
n_d	Per unit average converter efficiency after life
n_{do}	Initial average per unit converter efficiency before life
n_{ca}	Per unit concentrator-absorber efficiency including losses in cavity where energy absorbed bypasses the converters
n_s	Per unit fraction of active area not shadowed by generator and supporting structure
P_{c1}	The initial power capability required for each generator unit (watt)
P_l	The average load power requirements at the design point including all power requirements of the source (watt)
P_{si}	The initial total power capability required for the source (watt)
R	The surface reflectivity of the solar concentrator or mirror
S_d	The solar intensity at the design point (watt/ft^2)
t_d	The period of time from the beginning of the mission to the point under consideration
T_c	The average thermionic converter emitter temperature in degrees Kelvin
V_c	The stowage volume for each concentrator-generator unit (ft^3)
V_s	The stowage volume for the support structures and deployment mechanisms, etc. (ft^3)
V_t	The total stowage volume for the solar thermionic source (ft^3)

W_a The weight of the absorber cavity-generator unit including flux controls, converters, etc. (lb)

W_c The weight of the concentrator or mirror (lb)

W_t The total weight of the solar thermionic source (lb)

ϕ Maximum relative orientation error allowed at design point which is calculated as the ratio of absolute error to the solar image half angle at that point.

Power Control Computation

E_s	Value of regulated source voltage (volt)
E_s^k	Maximum value of source voltage at $I_{bl(min)}$ (volt) (A virtual value occurs when no regulation is assumed)
$E_{u(max)}$	Maximum value of the unshunted portion of the source voltage ($E_a = 0$ in a thermionic system) (volt)
E_s^{ij}	Series of values of source voltage for various i (see I_b^i) and various j (see $g^j\left[I_b(min)\right] = E_s^j$) (volt)
E_{sh}^{ij}	Series of values of shunted portion of the source voltage for various i, j (volt)
$g^j\left[I_{b(min)}\right] = E_s^j$	Inverted functional relation of $I_s = f^j\left[E_s\right]$ evaluated at $I_{bl(min)}$ for all time-mission events, j (function)
E_u^{ij}	Series of values of unshunted portion of the source voltage for various i, j (volt)
I_b^i	Series of values of bus current from minimum to maximum (i = 1, 2 . . . , 10) (amp)
$I_{b(max)}$	Maximum value of shunt current (amp)
$I_{bl(min)}$	Minimum value of the bus current (amp)
I^{ij}	Series of values of available source current corresponding to E_{sh}^{ij} (amp)
$I_{s(max)}$	Maximum source current available (amp)
$I_s = f^j\left[E_s\right]$	I-V characteristic of source (I as a function of E) at any time-mission event j (function)
I_{sh}^{ij}	Series of values of shunt element current corresponding to E_{sh}^{ij} (amp)
k	Event (j = k) which yields a maximum value for E_s^j, E_s^k
m	Shunted fraction of source series energy converters
n	Unshunted fraction of source series energy converters
N_s	Total number of series energy converters in the source
N_{sh}	Number of shunted series energy converters ($N_{sh} = mN_s$)

Power Control Computation (Continued)

N_u	Number of unshunted series energy converters ($N_u = nN_s$)
$P_{bl(max)}$	Maximum required bus power (watt)
$P_{bl(min)}$	Minimum required bus power (watt)
P_{br}	Rated output power of the booster regulator (watt)
P_c	Constant value of power dissipation in the control and monitor circuits (watt)
P_{pc}^{ij}	Total power dissipation in the power control unit for various i, j (watt)
P_s	Same as $P_{bl(max)}$ (watt)
$P'_{s(max)}$	Maximum available source power (watt)
$P_{sh(max)}$	Maximum value of P_{sh}^{ij} (watt)
P_{sh}^{ij}	Series of values of shunt element power dissipation for various i, j (watt)
Q_{pc}	Power dissipated in the shunt regulator (watt)
Q_{br}	Power dissipated in the booster regulator (watt)
V_{br}	Volume of the booster regulator (cubic inch)
V_{pc}	Volume of the power control unit (cubic inch)
W_{br}	Weight of the booster regulator (lb)
W_{pc}	Weight of the power control unit (lb)
N_{br}	Calculated value of booster regulator efficiency (percent)
N_o	Assumed booster regulator efficiency (percent)

Dynamic Power Plants

Mission Requirements

AU_{max}	Maximum distance from Sun at which power supply must operate in AU (where 1 AU = semimajor axis of Earth orbit about Sun = 92,959,670 miles)
C_s	Solar constant at maximum AU (kw/ft^2)
$P_{l(max)}$	Maximum load power used as rated power supply output (kw)
$P_{l(min)}$	Minimum load power (kw)
t_s	Sunlight time per orbit (hours)
t_e	Eclipse time per orbit (hours)
ϕ_s	Angle subtended by solar disc at maximum AU (minutes

Manufacturers' Design Data

K_{wm}	Concentrator weight per unit frontal area (lb/ft^2)
R_m	Total concentrator surface reflectivity integrated over solar spectrum = reflected energy/incident energy (per unit)
β	Equivalent angular surface deviation of concentrator from paraboloidal geometry (minutes)
η_g	Generator efficiency = electrical output/shaft input (per unit)
η_t	Turbine efficiency = shaft output/heat input (per unit)
θ_r	Concentrator rim angle = angle between geometrical concentrator axis and rim with vertex at the focal point (deg)

Parameters Determined by Cycle Analysis and Material Selection

C_p	Specific heat of energy storage material in operating temperature range ($kw\text{-}hr/lb^oF$)
F_c	Ratio of ideal cycle efficiency (100 percent turbine efficiency) to equivalent Carnot efficiency (per unit)
H_{fes}	Heat of fustion of energy storage material (kw-hr/lb)

K_{es}	Thermal conductivity of energy storage material (kw-hr/ft^2-^{o}F/ft)
T_{ac}	Equivalent absorber cavity temperature during eclipse = average external surface temperature of solidifying energy storage material (^{o}R)
T_c	Condensing temperature (^{o}R)
T_h	Boiling (or superheat) temperature (^{o}R)
T_{sc}	Effective subcooler radiation temperature (^{o}R)
ρ_{es}	Density of energy storage material (lb/ft^3)

Assumptions and Constants

A	Mirror inside diameter factor = ratio of inside diameter to absorber diameter
K_{wr}	Radiator weight per unit area (of one side) (lb/ft^2)
W_{hd}	Weight of energy storage material required to make up diffusion losses (lb)
ΔT_{es}	Temperature drop between absorbing surface and boiler surface of energy storage material (^{o}F)
$\Delta T_{es(ls)}$	Temperature change of energy storage material during sunlight (^{o}F)
ϵ_c	Effective emissivity of cavity aperture
ϵ_r	Emissivity of radiator surface at end of mission
η_r	Radiator efficiency = ratio of actual heat rejection per unit area to heat rejection per unit area from isothermal flat plate with same front surface emissivity and perfectly insulated back surface (per unit)
Ω	Orientation error = angular displacement between concentrator axis and solar vector (minutes)
σ	Stefan-Boltzmann constant = 0.507×10^{-12} kw/ft^2-^{o}R^4

Computation Parameters

A_{es}	Surface area of energy storage material absorbing thermal energy (ft^2)
$^*A_{rc}$	Area of condenser radiating surface (ft^2)
$^*A_{rsc}$	Area of subcooler radiating surface (ft^2)
$^*D_a$	Approximate overall absorber diameter based on spherical configuration (ft)
D_c	Diameter of absorber aperture (ft)
D_{m1}	Mirror outside diameter used in computations (ft)
$^*D_{mc}$	Calculated outside mirror diameter (ft)
D_{me}	Estimated mirror outside diameter (ft)
D_s	Diameter of theoretical solar image (circular) in focal plane (ft)
$^*f$	Focal length of concentrator (ft)
$^*H_{in}$	Depth of concentrator parallel to concentrator axis (ft)
n	Number of sequential iterative calculations
$(P/A)_{rc}$	Condenser heat rejection rate per unit surface area (area of one side) (kw/ft^2)
$(P/A)_{rsc}$	Subcooler heat rejection rate per unit area (area of one side) (kw/ft^2)
P_{acc}	Accessories shaft power (includes pump, bearings and seals (kw)
P_b	Heat input rate to boiler (kw)
P_c	Sensing and control power requirement (kw)
P_e	Generator output power (kw)
P_{es}	Thermal power input to energy storage material during sunlight (kw)

---

*Denotes computational outputs

η_{th}	Actual cycle thermal efficiency = available turbine input/boiler input (per unit)
$\sum W_u$	Total weight of system components excluding support structure (lb)

P_{fsc}	Working fluid subcooling heat rejection rate (kw)
P_g	Generator input shaft power (kw)
P_{re}	Thermal power loss due to radiation from cavity during eclipse (kw)
P_{rc}	Required heat rejection rate of condenser radiator (kw)
P_{rsc}	Required heat rejection rate of subcooler radiator (kw)
P_s	Required total solar power incident on concentrator (kw)
P_t	Turbine output shaft power (kw)
W_{ab}	Weight of absorber and boiler exclusive of heat storage unit weight (lb)
W_{acs}	Weight of heat storage unit portion of absorber = weight of energy storage material and container (lb)
W_{ahs}	Total weight of absorber-heat storage unit (lb)
W_c	Weight of controls and startup auxiliaries (lb)
W_{es}	Weight of energy storage material (lb)
W_f	Weight of working fluid inventory (lb)
W_m	Weight of concentrator (lb)
$^*W_{ps}$	Total power supply weight
W_{rc}	Weight of condenser (lb)
W_{rsc}	Weight of subcooler (lb)
W_{ru}	Weight of rotating unit (turbine, generator, pump) (lb)
W_{ss}	Weight of support structure (lb)
ΔH_{tes}	Enthalpy change of energy storage material due to temperature change (kw-hr/lb)
ΔP_l	Load power variation (kw)
η_{ca}	Collection efficiency = power absorbed/power incident on concentration (per unit)

*Denotes computational outputs.

Primary and Secondary Silver-Zinc Batteries

C_b	Battery capacity installed (amp-hr)
$C_{b\ (req)}$	Battery capacity required (amp-hr)
C_p	Preliminary estimate of capacity (amp-hr)
D	Depth of discharge
E_b	Battery voltage (volt)
E_c	Battery cell voltage (volt)
$E_{b\ (Avg)}$	Average battery voltage (volt)
E_l	Load voltage requirements (volt)
F_a	Fraction of capacity remaining after activated storage
F_c	Fraction of capacity remaining after cycling
F_p	Packaging factor
F_u	Fraction of capacity remaining after unactivated storage
$f_1(T)$	Temperature exponent of battery storage time (activated)
$f_2(T)$	Temperature exponent of battery storage time
I_i	Current (amp)
K_c	Exponent of cycle life relationship
N	Number of cells
P_{max}	Maximum load power (watt)
P_{min}	Minimum load power (watt)
P_i	Power (watt)
Q	State of charge (relative)
Q_o	Full charge

Primary and Secondary Silver-Zinc Batteries (Continued)

T_a	Battery temperature (activated) ($^{\circ}F$)
t_a	Activated storage time (hours)
t_b	Battery temperature ($^{\circ}F$)
T_{Pl}	Time of activated stand during prelaunch
T_u	Battery storage temperature (unactivated) ($^{\circ}F$)
t_u	Time of unactivated storage (hours)
V_a	Volume of automatically activated battery (in^3)
V_m	Volume of manually activated battery (in^3)
V_r	Volume of regulator (in^3)
W_a	Weight of packaged automatically activated battery (lb)
W_b	Weight of unpackaged battery (manually activated) (lb)
W_p	Weight of packaged battery (manually activated) (lb)
W_r	Weight of regulator (lb)
Δt_i	Time interval (hours)
η	Regulator efficiency
ΔE	Voltage range (volt)
α	Converter efficiency factor $[F(E_b)]$
β	Converter efficiency factor $[F(\alpha)]$
λ	Converter efficiency factor $[F(P_i)]$
ϵ	Energy (watt-hr)
Σ	Sum of all successive ϵ of the same sign (watt-hr)

Secondary Silver-Cadmium Batteries

C_b	Battery capacity (amp-hr)
C_p	Battery specific heat (watt/lb/hr/$^{\circ}$K)
DD	Depth of discharge
E_b	Battery voltage (volt)
E_o	Reversible potential (volt/cell)
F_p	Package weight factor
I	Current (amp)
I_c	Charge current (amp)
I_d	Discharge current (amp)
K	Battery heat capacity (watt/hr/$^{\circ}$K)
n	Number of iterations in the time cycle
P_l	Load power (watt)
Q	State of charge (instantaneous)
q	Heat quantity (generated in battery) (watt/cell)
q'	Heat quantity (lost from battery) (watt/cell)
Q_{ec}	State of charge at the end of charge
R_c	Charge rate (hours)
R_d	Discharge rate (hours)
T	Temperature (instantaneous) ($^{\circ}$K)
T_a	Average temperature ($^{\circ}$K)
$t_1 = t_c$	Time of charge (hours)
$t_2 = t_d$	Time of discharge (hours)
T_{ep}	Temperature at the end of the available charge period ($^{\circ}$K)

T_{ec}	Temperature at the moment of termination of charge (^{o}K)
T_m	Maximum temperature (^{o}K)
T_p	Total orbit or cycle period (hours)
V_b	Battery volume (packaged) (in^3)
W_b	Battery weight (unpackaged) (lb)
W_p	Battery weight (packaged) (lb)
ΔC_b	Capacity increment (amp-hr)
ΔQ	Charge increment
Δt	Time increment (hours)

Inverter

E_i	Inverter input voltage
F_{LR}	Load ratio factor
F_w	Weight factor
$I(P)$	Inverter input current
$I(P_r)$	Inverter input current at rated load
P	Output volt (amp)
P_r	Rated output volt (amp)
Q_i	Heat dissipation
V_i	Volume
W_i	Weight
W_i'	Modified weight
η_o	Efficiency at rated load and minimum rated voltage

1 INTRODUCTION

The design of a spacecraft electric power system normally requires the evaluation and comparison of several alternate concepts to define an optimum system configuration. This selection must be based on valid tradeoffs involving not only the basic energy conversion equipment, but also the energy storage, power control, power conditioning, and distribution equipment that are part of the complete system. To accomplish this tradeoff process, a considerably detailed system design, based on valid equipment characteristics and performance data and on specific mission and spacecraft requirements, is necessary for each concept considered. Significant problems frequently arise, however, because of the unavailability of current useful parametric data and because of the tedious design computations necessary. Even though large quantities of data have been published, much of it has been devoted to theoretical system and component analysis and predicted performance capabilities that are seldom achieved in system usage. Moreover these data are often presented in a form that is not suitable for direct application to the system design calculations. To obtain design optimization, these calculations normally require iterative processes to resolve the many interrelated variables involved.

This study effort has been directed toward development of design computation procedures that constitute a suitable basis for computer programming. This objective has been translated into the following specific tasks:

- Prepare design computation procedures in the form of flow diagrams on major system components
- Evaluate available performance and characteristics data and assess its validity
- Convert this data into parametric curves required by the computation procedures

In accomplishing these tasks, the study effort was confined to representative system configurations and components within the following scope:

- Solar powered systems and electrochemical energy storage
- Range of nominal power system ratings of 100 to 1000 watts
- One-year spacecraft mission duration
- DC-AC power conditioning equipment (inverters)

This report presents the procedures and supporting data for the above study tasks and also provides a basis for the development of similar procedures for alternate systems or equipment.

II. SYSTEM CONSIDERATIONS

A. POWER SYSTEM DEFINITION

The spacecraft electrical power system defined in this report includes all functions and components necessary to provide the quantity and quality of power required at the spacecraft loads. Major power system elements are defined as follows:

1) Power Source. The device that collects solar energy and converts it to electrical energy. The power generated by the source has the required electrical characteristics only at the design point.

2) Power Source Control. The device that controls the power source to assure that the power output has the required electrical characteristics throughout the mission. The power control also includes power source protection and monitoring circuits.

3) Power Plant. The combination of the power source and its associated controls.

4) Energy Storage. The device that provides the power for peak load operations and, except for power sources having thermal storage, the power during the operating time when insufficient solar energy is available to the source (i.e., eclipse).

5) Power Supply. The combination of the power plant and the energy storage. The power supply supplies required power whether solar energy is available or not.

6) Power Distribution. The components which distribute the power to the spacecraft loads. It includes circuit protection, switching, and monitoring.

7) Power Conditioning. The devices which convert supply power into power having other than the generated electrical characteristics.

8) Power System. The combination of the power supply, power distribution, and power conditioning.

The simplified block diagrams for the four solar power systems studied:

Figure 2-1. Photovoltaic Power System

Figure 2-2. Flat-Plate Solar Thermoelectric Power System

Figure 2-3. Solar Thermionic Power System

Figure 2-4. Solar Dynamic Power System

B. POWER SYSTEM REQUIREMENTS

Electrical requirements of individual major components of the power system are determined from mission and spacecraft constraints, power utilizing equipment requirements, and interactions between power system components. Power capacity of a system is defined as the power supplied from the main bus. When connected in accordance with the configuration shown in Figures 2-1 through 2-4, the power requirement of a power system component (except for thermionic sources) is the amount it either provides to the bus or removes from the bus. For the thermionic power source, the power required is that which must be supplied to the boost regulator. Figure 2-5 shows the various voltages and currents in the power system. The power system requirements computation provides the electrical input functions to the computation for the power source design, power control design, and battery design.

The inputs needed for the requirements computation are:

P versus t	Power profile and its characteristics (voltages, frequencies, regulation, number of phases, harmonics, etc.) for each power consuming equipment in the spacecraft.
$E_{b(max)}$	Maximum permissible power system bus voltage.
E_{ec}	Battery single-cell end of charge (maximum) voltage
E_d	Battery single-cell average discharge voltage.

In addition to the above factors, the following inputs are required:

t_d	<u>Design Point Mission Time.</u> Mission requirements are studied to determine the point in the mission where the greatest demands are made on the capability of each power system component to be designed. For each major component in the power system, the mission time at the design point may be different and a separate requirements computation is needed for each. In most applications, the design point mission time can be determined readily.

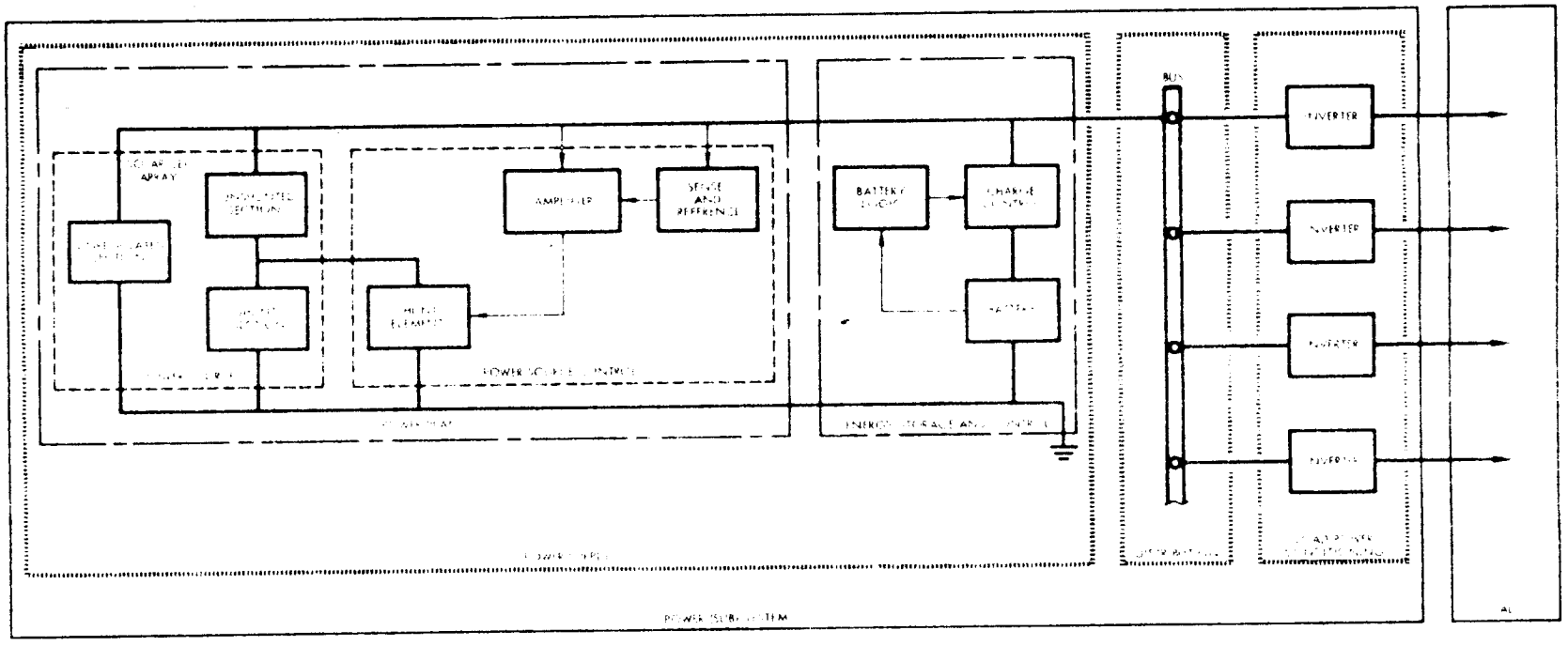

Figure 2-1. Photovoltaic Power System Block Diagram

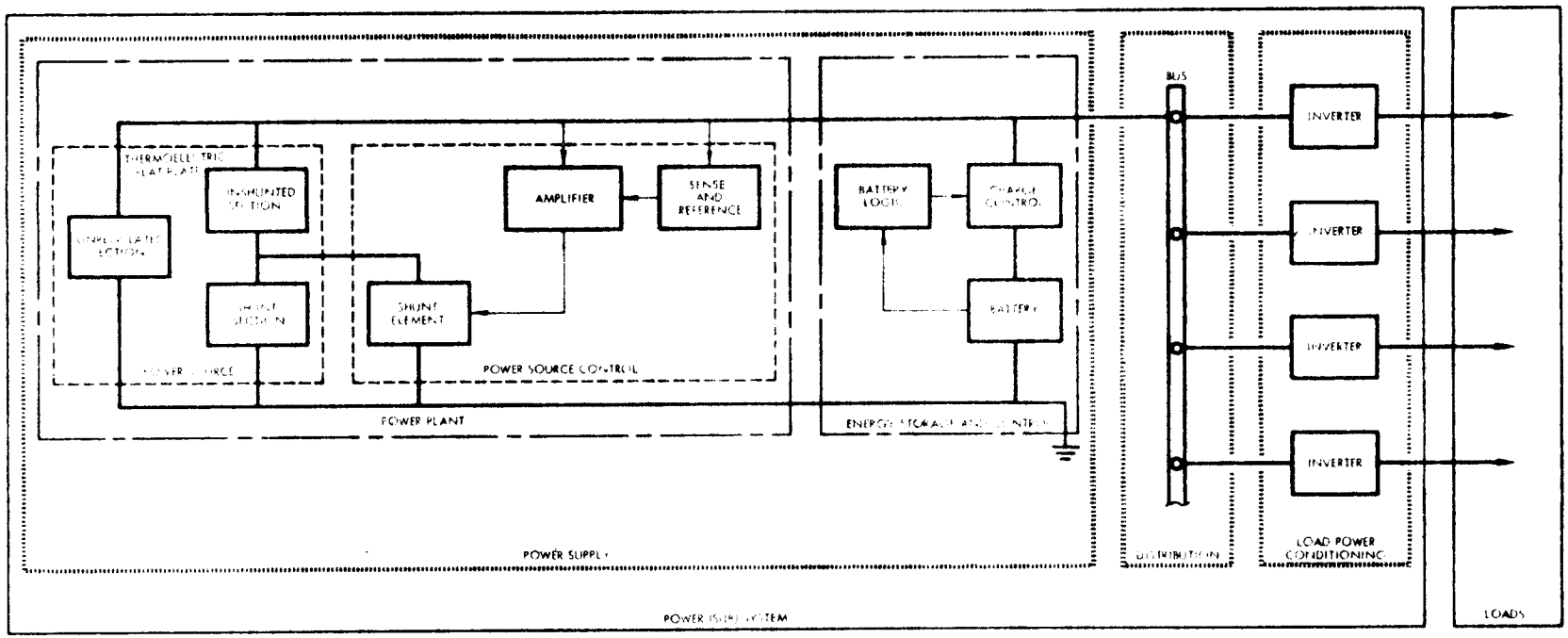

Figure 2-2. Flat-Plate Solar Thermoelectric Power System Block Diagram

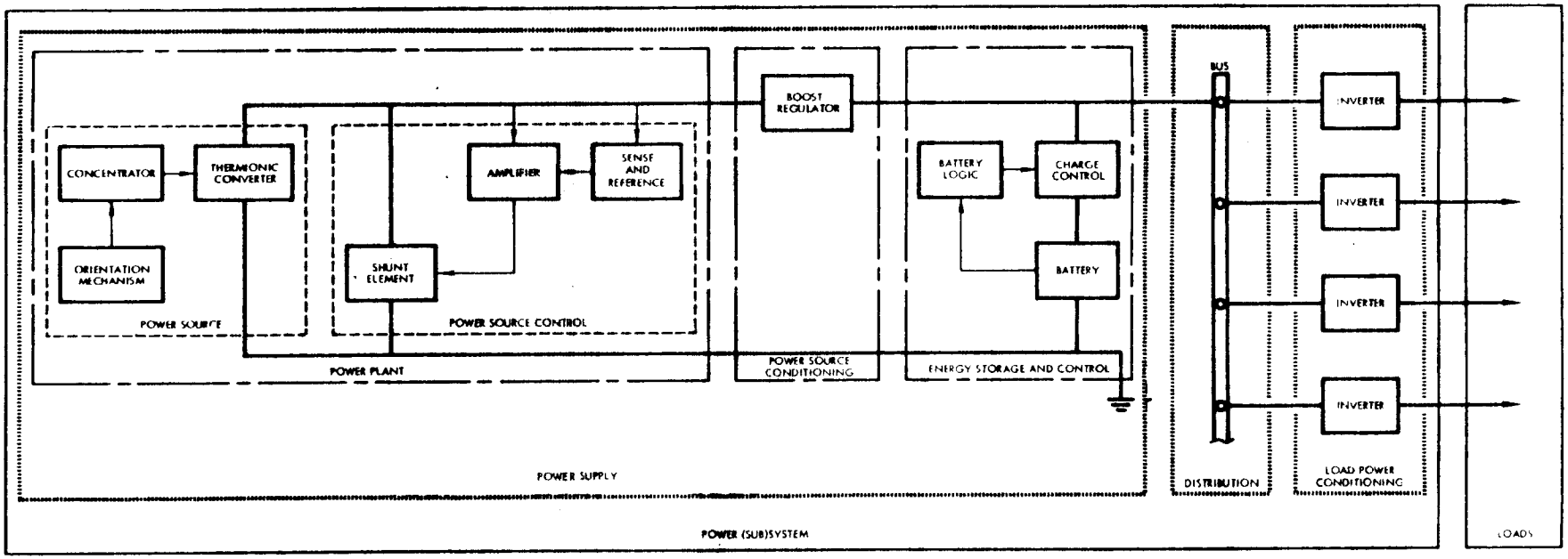

Figure 2-3. Solar Thermionic Power System Block Diagram

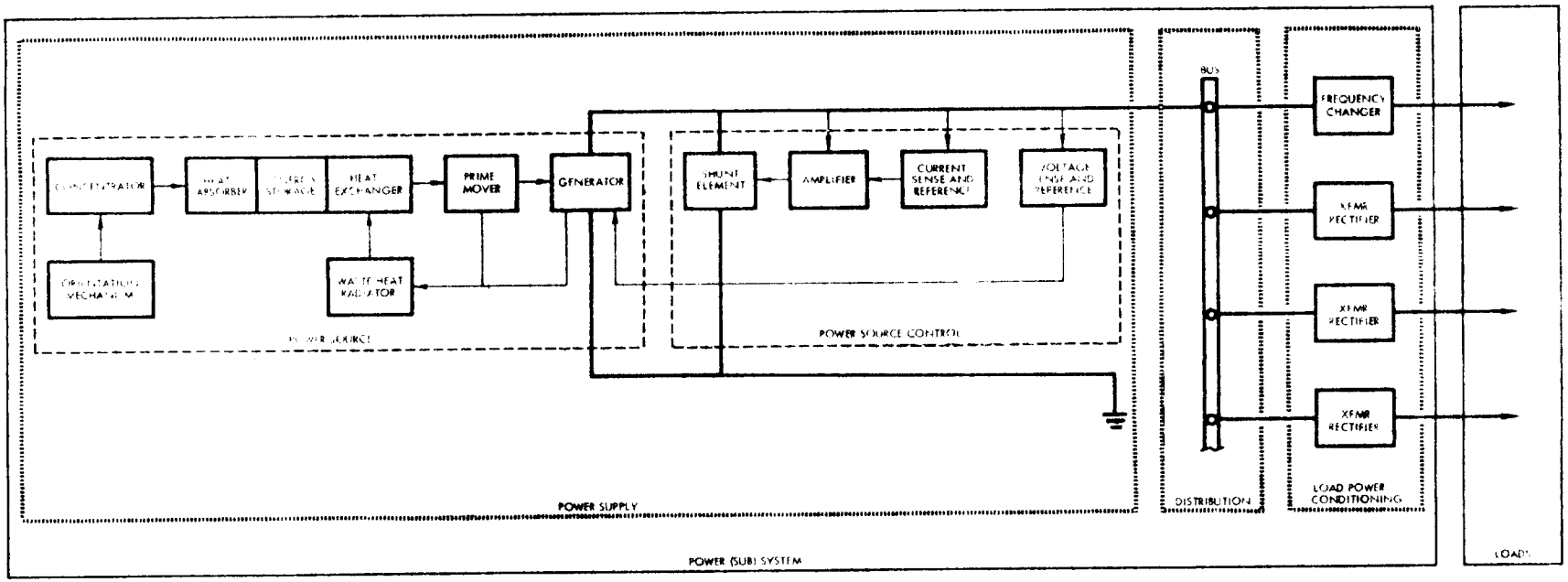

Figure 2-4. Solar Dynamic Power System Block Diagram

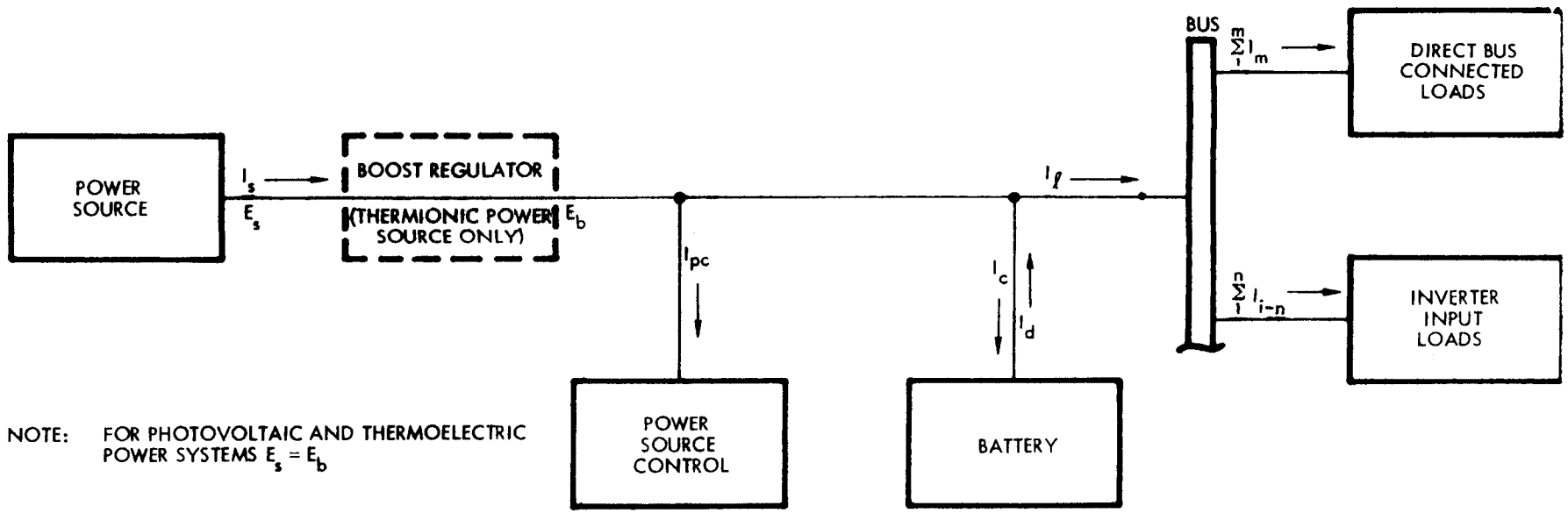

NOTE: FOR PHOTOVOLTAIC AND THERMOELECTRIC POWER SYSTEMS $E_s = E_b$

Figure 2-5. Power System Voltages and Currents

In Earth and Mars orbiting operations, for example, the design point for the power source and for the battery usually occurs at the end of spacecraft life. If the solar illumination on the spacecraft and the power loads are constant throughout the mission, the greatest demand on power source capability occurs after maximum degradation and the greatest demand on the battery occurs after the maximum number of cyclings. In cases where the design point is not readily assessible, a design point time is assumed. The requirements and component design computations are performed for the assumed time and the results compared parametrically with results at other assumed mission times until the true design point for each power system component can be determined.

t_1 and t_2 — Battery Charging and Discharge Periods. The operation of the spacecraft is analyzed at the design point mission time to determine the requirement for cyclic battery operation and resulting battery charge-discharge time (t_1 and t_2).

The computation is performed according to the following sequence (Figure 2-6):

1) System Bus Voltage. The system bus is clamped by the battery (see Figure 2-5). Therefore, the bus voltage (E_b) is determined by the battery. Maximum bus voltage is then the maximum charging voltage of the selected battery, and minimum bus voltage is the minimum battery discharge voltage.

Block A, number of battery cells (N_b).

Input, $E_{b(max)}$ (maximum permissible bus voltage from input data)

E_{ec} (battery single-cell end of charge voltage from input data)

Computation:*

$$N_b = \frac{E_{b(max)}}{E_c}$$

*Adjust to next lower integer.

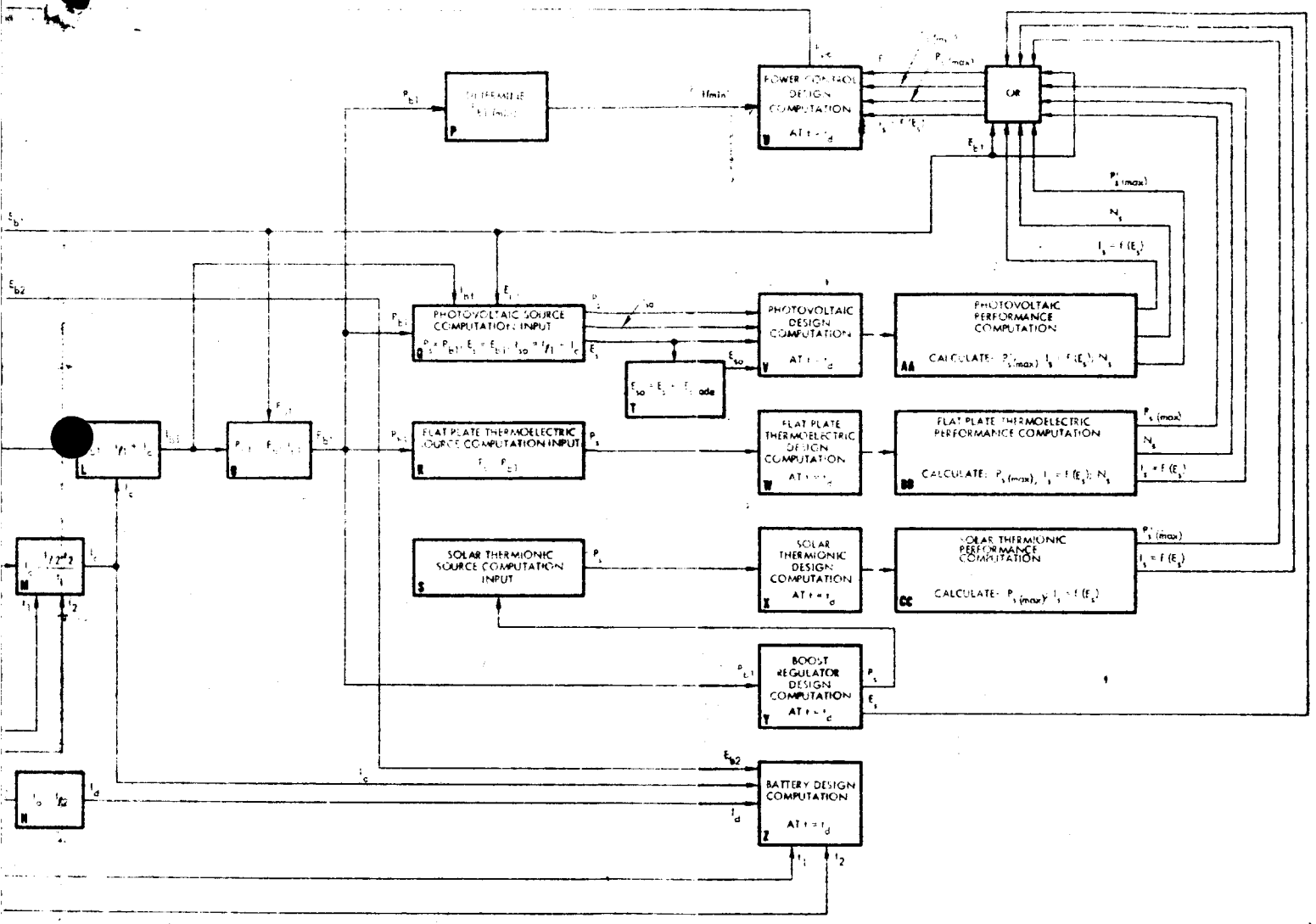

Figure 2-6. Power System Requirements Computation Flow Diagram

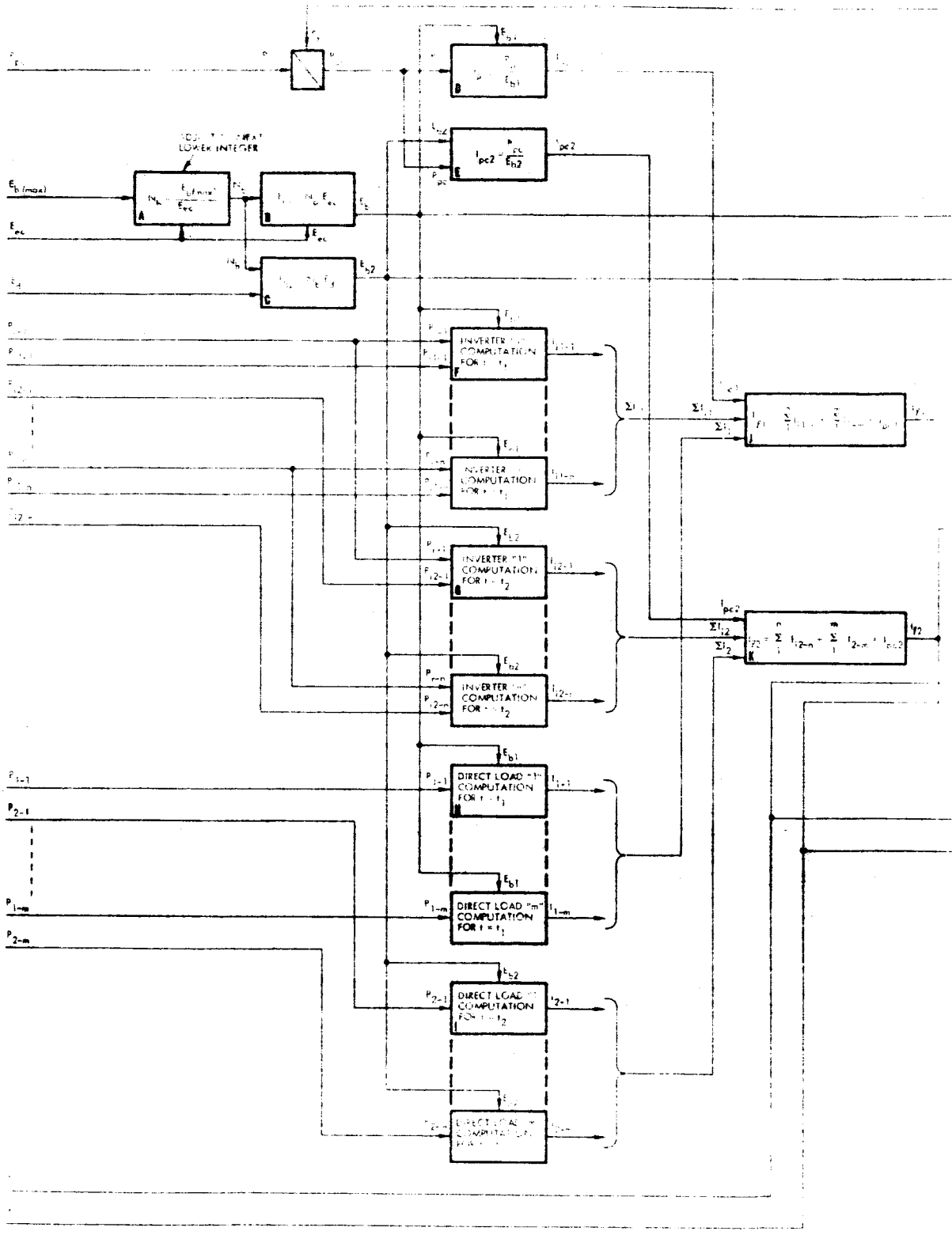
LOWER INTEGER
A
B
C
D
E
F
G
H
I
J
K
INVERTER COMPUTATION
DIRECT LOAD COMPUTATION

Block B, bus voltage during battery charge t_1 (E_{b1}).

Input, N_b (from Block A)

E_{ec} (input data)

Computation:

$$E_{b1} = N_b E_{ec}$$

Block C, average bus voltage during battery discharge t_2 (E_{b2}).

Input, N_b (from Block A)

E_d (battery single-cell average discharge voltage from input data)

Computation:

$$E_{b2} = N_b E_d$$

2) Power Control Input Current (I_{pc}). The exact power used by the power source controls can only be calculated after the power source computation has been performed and its performance characteristic is determined. For this requirements computation, therefore, a power control power load is estimated.

Block D, power control input current at t_1.

Input, P'_{pc} (estimated power)

E_{b1} (from block B)

Computation:

$$I_{pc1} = \frac{P'_{pc}}{E_{b1}}$$

Block E, power control input current at t_2.

Input, P'_{pc} (estimate)

E_{b2} (from Block C)

Computation:

$$I_{pc2} = \frac{P'_{pc}}{E_{b2}}$$

3) Inverter Input Current (I_i) (See Figure 5-1). The input currents to the inverters are determined with the individual inverter design computations described in Section V.

Block F, inverter "1" input current at t_1.

Input, P_{r-1} (maximum mission steady-state output power on inverter "1" from load power profile)

P_{i1-1} (output power on inverter "1" at t_1 from power profile)

E_{b1} (from Block B)

Output, I_{i1-1} (input current)

Repeat above computations for inverters 2, 3 · · · n.

The total inverter input currents, therefore, are,

$$\sum I_{i1} = I_{i1-1} + I_{i1-2} + I_{i1-3} + \cdots + I_{i1-n}$$

Block G, inverter "1" input current at t_2.

Input, P_{r-1} (maximum mission steady-state output power on inverter "1" from load power profile)

P_{i2-1} (output power on inverter "1" at t_2 from power profile)

E_{b2} (from Block C)

Output, I_{i2-1} (Input current)

Repeat above computations for inverters 2, 3, · · · n.

The total inverter input currents therefore, are,

$$\sum I_{i2} = I_{i2-1} + I_{i2-2} + I_{i2-3} + \cdots + I_{i2-n}$$

4) Direct Bus-Connected Load Current (I)

Block H, bus-connected load "1" current at t_1.

Input, P_{l-1} (load "1" power at t_1)

E_{b1} (from Block B)

Computation:

$$I_{1-1} = \frac{P_{1-1}}{E_{b1}}$$

Repeat above computation for bus loads 2, 3, · · · m.

The total direct bus-connected load current, therefore, is

$$\sum I_1 = I_{1-1} + I_{1-2} + I_{1-3} + \cdot \cdot \cdot + I_{1-m}$$

Block I, bus-connected load "1" current at t_2.

Input, P_{2-1} (load "1" power at t_2)

E_{b2} (from Block C)

Computation:

$$I_{2-1} = \frac{P_{2-1}}{E_{b2}}$$

Repeat above computation for bus loads 2, 3, · · · m.
The total direct bus-connected load current, therefore, is,

$$\sum I_2 = I_{2-1} + I_{2-2} + I_{2-3} + \cdot \cdot \cdot + I_{2-m}$$

5) <u>Total Bus Load Current</u> (I_ℓ)

Block J, total bus load current at t_1.

Input, $\sum I_{i1}$ (from Block F)

$\sum I_1$ (from Block H)

I_{pc1} (from Block D)

Output, $I_{\ell 1} = \sum I_{i1} + \sum I_1 + I_{pc1}$

Block K, total bus load current at t_2

Input, $\sum I_{i2}$ (from Block G)

$\sum I_2$ (from Block I)

I_{pc2} (from Block E)

Output, $I_{\ell 2} = \sum I_{i2} + \sum I_2 + I_{pc2}$

6) <u>Battery Currents</u> (I_c, I_d)

Battery discharge current is equal to the total bus load current at t_2, or

Block N, $I_d = I_{\ell 2}$ (battery discharge current) <u>Input to battery design computation</u>

Block M,

Input, $I\ell_1$ (from Block J)

$I_{\ell 2} = I_d$ (from Block K or N)

t_1 (input data)

t_2 (input data)

Computation:

$$I_c = \frac{I_{\ell 2} t_2}{t_1}$$ (Average battery charging current assuming 100 percent ampere-hour efficiency) <u>Input to battery design computation</u>

7) <u>Bus Power and Current</u> (P_b, I_b)

Block L, bus current at t_1

Input, $I_{\ell 1}$ (from Block J)

I_c (from Block M)

Computation:

$I_{b1} = I_{\ell 1} + I_c$ <u>Input to photovoltaic design computation</u> ($I_{sa} = I_{b1}$)

Block O, bus power at t_1.

Input, I_{b1} (from Block L)

E_{b1} (from Block B)

Computation:

$P_{b1} = E_{b1} I_{b1}$ Input to photovoltaic or thermoelectric design computations ($P_s = P_{b1}$). Input to thermionic boost regulator design computation.

8) Computation Outputs. The outputs of the computation process are as follows:

a) Bus voltage during battery charge (E_{b1}). This is the bus voltage during power source operation. For Photovoltaic and Thermoelectric Power Sources, $E_s = E_{b1}$.

b) Bus voltage during battery discharge (E_{b2}).

c) Average battery charge current (I_c).

d) Battery discharge current (I_d).

e) Bus power (P_{b1}). This is the power supplied by the source.

f) Bus current (I_{b1}).

The inputs derived from the preceding sequence at the applicable design point mission time will permit the design computation for each major power system component (Blocks V, W, X, Y, Z). For the resulting design of the power source and, if applicable, the boost regulator, the performance of this component (Block AA or BB or CC) can be computed at other than the applicable design point mission time. These performance characteristics can then form the basis for the power control design computation (Block U and Section IIIE) and a refinement of the original requirements computation.

III. SOLAR POWER PLANTS

A. SOLAR PHOTOVOLTAIC SOURCES

Solar arrays consisting of silicon solar cells have been widely used as spacecraft power plants because of their successful operational performance. Factors that influence and limit performance of solar cells have been investigated in various photovoltaic research, design, and development efforts and most of these factors are well understood. Because of this background of experience and information, a solar array design and its performance in a specific space environment can be computed readily from the physical, electrical, optical, and thermal characteristics of the single bare solar cell.

For most applications, the design computations are straightforward, but tedious. Simplifying assumptions are usually made to facilitate the computation for a preliminary design. The resulting analysis often is not sufficiently detailed to permit determination of the effects of variations in all significant parameters and thus cannot be used for accurate optimization of the design. To permit more detailed design calculations early in a spacecraft power system development program, a computer program is needed.

This section of the report describes a procedure for calculating the size and performance of photovoltaic solar arrays for given power and reliability requirements and mission parameters. Included are computation flow diagrams which can be translated readily into a computer program. The required design computation parametric data for a typical 10 ohm-cm, 10 percent efficient, silicon N-on-P solar cell and one type of structural concept is presented in Appendix A1, and a sample calculation using this procedure and parametric data is given in Appendix B1.

The solar array design calculation procedure presented is applicable to any type of photovoltaic device now under development if the necessary parametric data (e.g., current-voltage characteristic, temperature coefficient resistance, etc.) are available. The computation procedure is also flexible with regard to the structural configuration of the array, for only the necessary structural parametric data information is required. The design computation flow diagram has been tailored to oriented solar arrays

possessing uniform temperature distribution, like panels, and uniform illumination. Modification of the existing flow diagram by adding a sub-computation will permit designs of multifaceted, random, non-oriented solar arrays.

1. State of Development

The usual method of generating power for space applications makes use of the photovoltaic effect, and the most frequently used photovoltaic device is the silicon solar cell. This cell is a single-crystal semiconductor junction device, similar to a silicon rectifying diode. Two types of silicon solar cells are presently available: P-on-N and N-on-P, with the P-on-N consisting of a positive layer on top of a negative layer, and the N-on-P having opposite arrangement.

At present, the P-on-N cells are somewhat more efficient than the N-on-P. The P-on-N efficiencies run as high as 12 to 13 percent at present and the N-on-P efficiencies around 10 to 11 percent. The N-on-P, however, is much more resistant to particle radiation than the P-on-N. Although the output of each type deteriorates with exposure to radiation, both as a function of energy and dosage for each type of radiation, the output of N-on-P cells deteriorates much less rapidly (by as much as several orders of magnitude) than that of P-on-N cells. It has been found that 1 ohm-cm N-on-P silicon solar cells can tolerate 6 to 50 times more electron radiation than P-on-N cells for the same degradation, and that 10 ohm-cm N-on-P cells are 3 to 4 times more radiation-resistant than the 1 ohm-cm N-on-P cells. This property of N-on-P cells makes them much more suitable than P-on-N cells for space missions that are exposed to radiation to any appreciable extent.

Other photovoltaic semiconductor junction devices are under study at present, chief among them being the gallium arsenide cell. Past work on a gallium arsenide single-crystal device has failed to produce a device comparable to the silicon solar cell in efficiency and cost, but high temperature properties and radiation resistance superior to those of silicon solar cells have been observed. Presently under investigation is a thin-film gallium arsenide device. Attempts are being made to attain the expected 10 percent efficiency level. Like the single-crystal device, this is a semiconductor junction device, with the gallium arsenide and impurities deposited on a substrate as films.

Other materials presently under investigation include cadmium sulfide and cadmium telluride, gallium phosphide and indium phosphide, but none of these materials have proven to be competitive with the silicon solar cells as yet. Interest also exists in large-area devices, especially large-area thin-film devices. Because of their reduced weight, these devices could prove to be competitive with silicon solar cells for applications with large power requirements, such as 1 kilowatt or more, in spite of a lower unit efficiency than the silicon solar cell. An example of such a device is the cadmium sulfide large-area thin-film device.

One limitation to silicon solar cells as presently used in space power applications is their high cost. This is due in part to the waste involved in fabricating the rectangular waters now being used from the cylindrical crystals that are grown. A possible means of circumventing this waste and reducing the cost of solar cells is to fabricate the cells as long single-crystal strips (dendrites). Such a configuration under certain circumstances, could increase the reliability of an array, since it would reduce the number of individual cells required and hence the number of connections. Both P-on-N and N-on-P strips have been fabricated, and efficiencies as high as 12 percent have been attained with strips 30 centimeters in length. The strips differ only in geometric configuration from the rectangular wafer cells presently being used.

2. Development of Computation Process

The design of the photovoltaic source is determined from the electrical characteristics taking of a single solar cell at the design point, modifying this characteristic to account for average losses in a cell when installed in a solar array, then determining the number of parallel and series-connected cells needed in the array when supplying required load and battery demands, and finally determining the physical configuration of the array. Once the physical characteristics of the solar array are known, its performance at any time in the mission can be determined, providing the influence of factors such as insolation, radiation, failure rates, and temperature are also known.

Figure 3-1 shows the computation flow diagram that has been developed to obtain a design for the power source and to determine the characteristics of the design at any point in time. The computation begins with

standard condition current-voltage (I-V) characteristics of the solar cell selected for the design. This I-V curve is then translated along the current and the voltage axis according to factors determined by the difference from standard conditioning that exists at the chosen design point. The following computation inputs based on mission factors are required:

T_{sa}	Solar cell temperature.
Γ	Maximum orientation error of solar array.
AU	Distance of spacecraft from sun in astronomical units.
t_d	The time during mission at the design point.
E_s	Photovoltaic source voltage. The voltage at the terminals of the source is the same as the bus and the battery charging voltage for the selected power system configuration.
E_{sa}	Solar array voltage. The voltage generated by the array is equal to the source voltage plus the isolation diode voltage drop.
I_{sa}	Solar array current. The sum of the currents required by the bus-connected loads, inverters, converters, power control, and battery charging.
Φ_c'	Particle radiation dose (proton, electron, etc.) on solar cell, converted into equivalent 1-Mev electron dose for the particular solar cell, adhesive, cover glass, and filter selected.
Φ_a'	Particle radiation dose on adhesive, converted into equivalent 1-Mev electron dose for the particular adhesive, cover glass, and filter selected.
Φ_{cg}'	Particle radiation dose on cover glass, converted into equivalent 1-Mev electron dose for the particular cover glass selected.

The following characteristic functions for the selected solar cell, cover glass, adhesive, and solar array structural concept are required for the computation:

Function A	Solar cell current-voltage characteristics (I versus E) at standard conditions of air mass zero solar spectrum, 140 mw/cm^2 illumination, 28°C temperature, nonirradiated, and no cover glass.
Function B	Solar cell short circuit current (I_{sc}) as a function of equivalent 1-Mev electron dose (Φ_c').
Function C	Solar cell open circuit voltage (E_{oc}) as a function of equivalent 1-Mev electron dose on solar cell (Φ_c').
Function D	Solar cell adhesive relative transmissability (F_a) as a function of equivalent 1-Mev electron dose on adhesive (Φ_a').
Function E	Solar cell cover glass relative transmissability (F_{eg}) as a function of equivalent 1-Mev electron dose on cover glass (Φ_g').
Function F	Solar cell relative short circuit current (R_{sc}) as a function of solar array orientation error (Γ) and equivalent 1-Mev electron dose on cover glass (Φ_{cg}').
Function N	Solar cell relative short circuit current temperature coefficient (β_I/I_{sc}) as a function of equivalent 1-Mev electron dose on solar cell (Φ_c').
Function Q	Solar cell voltage temperature coefficient (β_E) as a function of equivalent 1-Mev electron dose on solar cell (Φ_c').
Function JJ	Solar panel weight per unit area (W_s/A) as a function of panel area (A_p).

In addition to the mission factors and functional relationships previously described, the following specific design inputs are required:

A_c	Solar cell area.
A_{c-a}	Solar cell active area.
A_{p-max}	Maximum single-panel area permitted by vehicle launch configuration, orbit configuration, maximum deflection, etc.
F_p	Solar array packing factor. The ratio of total solar cell area to total panel area.

F_i Solar cell installation factor. The average ratio of solar cell maximum power output after array panel installation and connection to the maximum power output before array panel installation.

r_s Solar cell series resistance.

w_c Solar cell weight.

w_h Array panel miscellaneous hardware (terminals, adhesive, interconnecting wiring, etc.) weight per solar cell.

ρ_{cg} Solar cell cover glass density.

ρ_{cb} Solar cell connection and insulation circuit board density.

d_{cg} Solar cell cover glass thickness.

d_{cb} Solar cell circuit board thickness.

R_{sa} Required solar array reliability at time, t.

λ_c Failure rate of solar cells.

λ_i Failure rate of interconnecting wiring.

λ_d Failure rate of isolating diodes.

Photovoltaic Design Computation Sequence. The computation is performed according to the following sequence (see Figure 3-1):

1) Solar Cell Characteristics

Block A.* Select desired solar cell type. Use either the standard condition (bare, nondegraded, 140 mw/cm^2, 28°C) solar cell current-voltage characteristics or derive the equivalent functional relationship $I_o = f(E_o)$.

Block I. Derive equivalent I-V function $\left[I_o = f(E_o)\right]$.

Block J. $$I_o = I_o\Big|_{E_o=0}\left\{1 - K_2\left[\exp\left(\frac{F_o}{K_1 E_o\Big|_{I_o=0}}\right) - 1\right]\right\}$$

*The blocks discussed in Subsection III. A are shown in Figures 3-1 and 3-2.

where

$$K_1 = \frac{\dfrac{E_o(P_m)}{E_o\big|_{I_o=0}} - 1}{\ln\left[1 - \dfrac{I_o(P_m)}{I_o\big|_{E_o=0}}\right]}$$

$$K_2 = \left[1 - \frac{I_o(P_m)}{I_o\big|_{E_o=0}}\right]\left\{\exp\left[\frac{-E_o(P_m)}{K_1 E_o\big|_{I_o=0}}\right]\right\}$$

2) Degradation Due to Particle Radiation. Particle radiation directly reduces the cell output current and voltage. Additional, indirect reductions after radiation occurs in cell output are due to decreases in cover glass transmittance, adhesive transmittance, and change in spectral response. The direct reduction in cell output is computed as follows:

Block K. Change in current (ΔI_Φ)

Input, $I_{sc-\Phi}$ (short circuit current after dose Φ_c from Block B)

$I_o\big|_{E_o=0}$ (short circuit current of new cell from Block A)

Computation,

$$\Delta I_\Phi = I_{sc-\Phi} - I_o\big|_{E_o=0}$$

Block L. Cell output considering only reduction in current $\left[I_1 = f(E_o)\right]$

Input, $I_o = f(E_o)$ (cell characteristics from Block A or J)

ΔI_Φ (Block K)

Translate the curve in Block A along current axis by ΔI_Φ

Output, $I_1 = f(E_o)$ (cell characteristics)

$E_o\big|_{I_1=0}$ (open circuit voltage)

Block M. Change in voltage (ΔE_Φ)

Input, $E_{oc-\Phi}$ (open circuit voltage after dose Φ_c' from Block C)

$E_o|_{I_1=0}$ (from Block L)

Computation,

$$\Delta E_\Phi = E_{oc-\Phi} - E_o|_{I_1=0}$$

Block R. Cell output after radiation damage $\left[I_1 = f(E_1)\right]$

Input, $I_1 = f(E_o)$ (from Block L)

ΔE_Φ (from Block M)

Translate $I_1 = f(E_o)$ along voltage axis by ΔE_Φ

Output, $I_1 = f(E_1)$ (cell characteristics)

$I_1|_{E_1=0}$ (short circuit current)

3) Effective Solar Cell Insolation. The amount of solar irradiation reaching the cell is a direct function of the sun distance from the spacecraft, the transmission losses in the cover glass and adhesive, and the angle of incidence. In addition, changes in the cover glass and adhesive spectral transmittance and the spectral response of the solar cell due to particle radiation and angle of incidence reduces the effective insolation.

Block P. Relative effective solar cell insolation

Input, s (relative insolation from Block G)

F_{cg} (cover glass transmission factor after dose Φ_{cg}' from Block E)

F_a (adhesive transmission factor after dose Φ_a' from Block D)

R_{sc} (relative short circuit current at angle of incidence Γ and after dose Φ_{cg}' from Block F)

Computation,

$$s' = sR_{sc}F_{cg}F_a$$

4) Output Change Due to Operating Temperature. The deviation of the operating temperature from the standard condition of the curve in Block A changes the cell output current and voltage. An increase in temperature from the standard results in a decrease in voltage and a relatively small increase in current. The percent of current change due to temperature also depends on particle radiation dose. The amount of voltage change due to temperature depends also on effective solar cell insolation.

Block O. Temperature deviation from standard (ΔT)

Input, T_{sa} (array installed solar cell temperature)

T_o (standard solar cell temperature)

Computation,

$$\Delta T = T_{sa} - T_o$$

Block S. Change in current (ΔI_T)

Input, $\beta_I\big|_{I_{sc}}$ (relative current temperature coefficient after dose Φ_c' from Block N)

$I_1\big|_{E_1=0}$ (from Block R)

ΔT (from Block O)

Computation,

$$\Delta I_T = \left(I_1\big|_{E_1=0}\right)\left(\frac{\beta_I}{I_{sc}}\right)\Delta T$$

Block U. Change in voltage (ΔE_T)

Input, β_E (voltage temperature coefficient at insolation s' from Block Q, s' from Block P)

ΔT (from Block O)

Computation,

$$\Delta E_T = \beta_E \Delta T$$

Block T. Cell output at operating temperature $\left[I_2 = f(E_2)\right]$

Input, $I_1 = f(E_1)$ (from Block R)

ΔI_T (from Block S)

ΔE_T (from Block U)

Translate curve $I_1 = f(E_1)$ along current axis by ΔI_T and along voltage axis by ΔE_T.

Output, $I_2 = f(E_2)$ (cell characteristics)

$I_2\big|_{E_2=0}$ (short circuit current)

5) Output Change Due to Solar Cell Insolation. The short circuit current of the cell is directly proportional to the cell insolation. Change in current of the cell is equal to the change in short circuit current. Output voltage change of the cell is effected indirectly by insolation change. The voltage will change due to an increase or decrease in cell series resistance drop.

Block V. Change in current (ΔI_s)

Input, s' (relative effective insolation from Block P)

$I_2\big|_{E_2=0}$ (from Block T)

Computation,

$$\Delta I_s = (s' - 1) I_2\big|_{E_2=0}$$

Block X. Change in voltage (ΔE_s)

Input, r_s (solar cell series resistance from cell data)

ΔI_s (from Block V)

Computation,

$$\Delta E_s = -r_s \Delta I_s$$

Block W. Cell output at solar cell insolation $\left[I_3 = f(E_3)\right]$

Input, $I_2 = f(E_2)$ (from Block T)

ΔI_s (from Block V)

ΔE_s (from Block W)

Translate curve $I_2 = f(E_2)$ along current axis by ΔI_s and along voltage axis by ΔE_T.

Output, $I_3 = f(E_3)$ (cell characteristics)

6) Array-Installed Solar Cell Output. The wiring and connection losses in the solar array are entered into the computation process by considering it a proportionate decrease in cell output power at or near the operating point.

Block Y. Cell current and voltage at maximum power point $\left[I_e(P_{max});\ E_3(P_{max})\right]$

Input, $I_3 = f(E_3)$ (from Block W)

Find maximum power point of curve $I_3 = f(E_3)$

Output, $I_e(P_{max})$

$E_3(P_{max})$

Block Z. Current and voltage change $(\Delta I_i;\ \Delta E_i)$

Input, $I_3(P_{max})$, $E_3(P_{max})$ (from Block Y)

Computation,

$$\Delta I_i = I_3(P_m)\left(1 - \sqrt{F_i}\right)$$

$$\Delta E_i = E_3(P_m)\left(1 - \sqrt{F_i}\right)$$

Block AA. Cell output $\left[I = f(E)\right]$

Input, ΔI_i, ΔE_i (from Block Z)

$I_3 = f(E_3)$ (from Block W)

Translate curve $I_3 = f(E_3)$ along current axis by ΔI_1 and along voltage axis by ΔE_1

Output, $I = f(E)$ (cell characteristics)

7) Array-Installed Solar Cell Operating Current and Voltage. In order to realize the maximum output of the array at the design point, each cell should be operated at the maximum power point. However, practical cell series and parallel connections and interconnections and array oversizing to gain desired reliability must be considered. As a result, the cell operation at the design point will deviate from the maximum power point.

Block BB. Cell maximum power point (P_{max})

Input, $I = f(E)$ (cell characteristics from Block AA)

Find maximum power point of the curve $I = f(E)$

Output, $I(P_{max})$

$E(P_{max})$

Block CC. Number of series and parallel cells in array (N_s, N_p)

Input, I_{sa} (required solar array current from systems requirement computation, Figure 2-6)

E_{sa} (required solar array voltage from systems requirement computation, Figure 2-6)

$I(P_m)$ (from Block BB)

$E(P_m)$ (from Block BB)

Computation,*

$$N_p = \frac{I_{sa}}{I(P_m)}$$ (first estimate of number of cells in parallel)

$$N_s = \frac{E_{sa}}{E(P_m)}$$ (number of cells in series)

*N_p and N_s must be integers.

Block DD. Cell operating voltage (E_{op})

Input, E_{sa} (required solar array voltage)

N_s (from Block CC)

Computation,

$$E_{op} = \frac{E_{sa}}{N_s}$$

Block EE. Cell operating current (I_{op})

Input, $I = f(E)$ (cell characteristics from Block AA)

E_{op} (from Block DD)

Determine I_{op}; the current on $I = f(E)$ at E_{op}

Block MM. Array output current at required reliability (I''_{sa})

(Refer to Step 8 for detail of reliability computation)

Input, $I = f(E)$ (from Block AA)

I_{op} (from Block EE)

E_{op} (from Block DD)

N_s (from Block CC)

N_p

t_d (mission time at design point)

R_{sa} (required solar array reliability)

λ_c (random cell failure rate from input data)

λ_i (interconnection failure rate from input data)

λ_d (block diode failure rate from input data)

Output, I''_{sa} (array output current with computed design and required reliability)

Blocks NN and OO. Comparison of calculated and required array output currents.

Input, I_{sa} (required solar array current)

I''_{sa} (from Block MM)

Compare I''_{sa} with I_{sa}. If $I''_{sa} < I_{sa}$, increase N_p by 1 in Block OO and change this input to Block MM. Repeat reliability computation and find resulting I''_{sa}. Again compare the new I''_{sa} with I_{sa}.

Repeat above procedure until $I''_{sa} \geq I_{sa}$.

8) Solar Array Reliability (Reference 3-7). The calculation of the array output current at a specified reliability (Figure 3-2) considers the effects of redundant interconnections within the module array. Open circuits due to mechanical breaks in the circuit are considered to be the predominant failure mode. Output current at a given reliability cannot be determined from parts counts since it is impossible to define that a given number of failed cells fails the array while one fewer failed cell does not fail the array.

The effect of various combinations of open-circuited cells, isolation diodes, and interconnections on current output at the fixed voltage (E_{op}) from a series-parallel interconnected array is determined, using the solar cell I-V characteristics generated in Block EE.

The probability of specific types of failures in the array is calculated together with their associated fractional output current. These probabilities are then arranged in order of decreasing value. An incremented reliability of the solar array is then calculated for each of the types of failures. These increments are summed in the order of decreasing probability values, starting with the highest probability of occurrence, until the total reliability is equal to or greater than the required reliability. The fractional output current associated with the last incremented reliability used in the summation is then the fraction of the solar array current with respect to the required source current.

The reliability computation is performed according to the following sequence (see Figure 3-2):

Block a. Solar array modulator configuration (m; s)

Input. N_p (from Block CC or OO)

Output. Choose least integer among $N_p/3$, $N_p/4$, ..., $N_p/10$

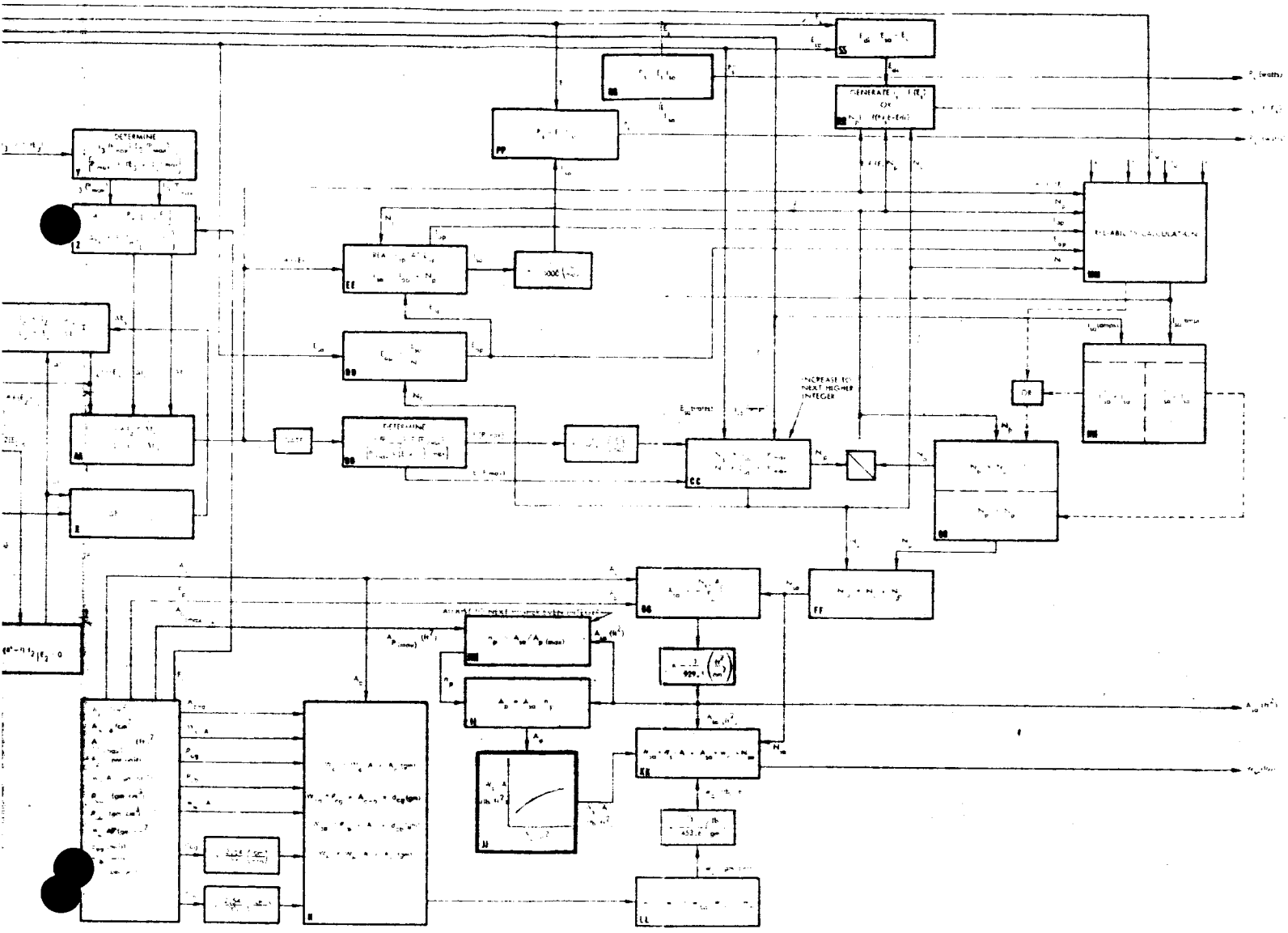

Figure 3-1. Photovoltaic Design Computation Flow Diagram

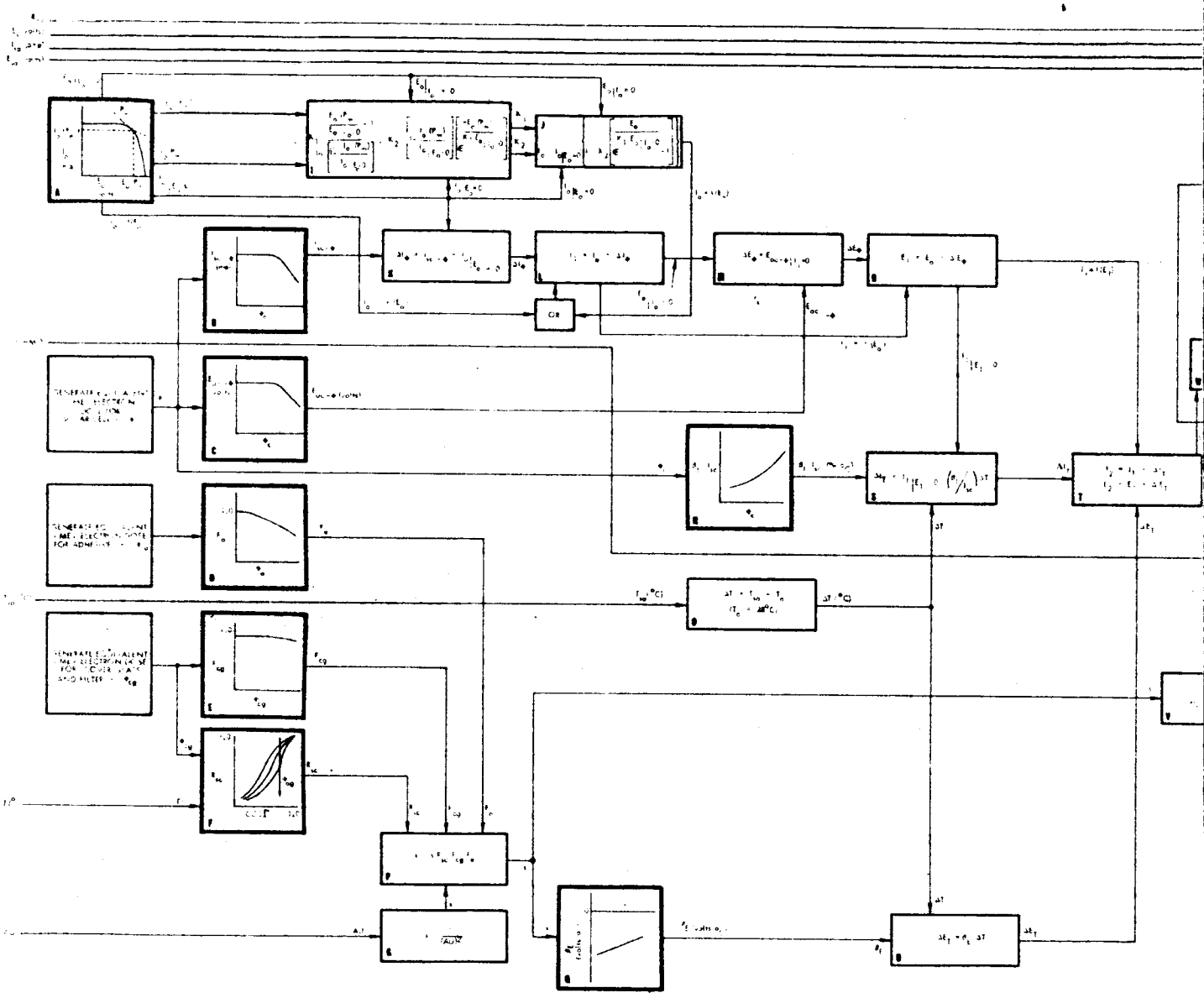

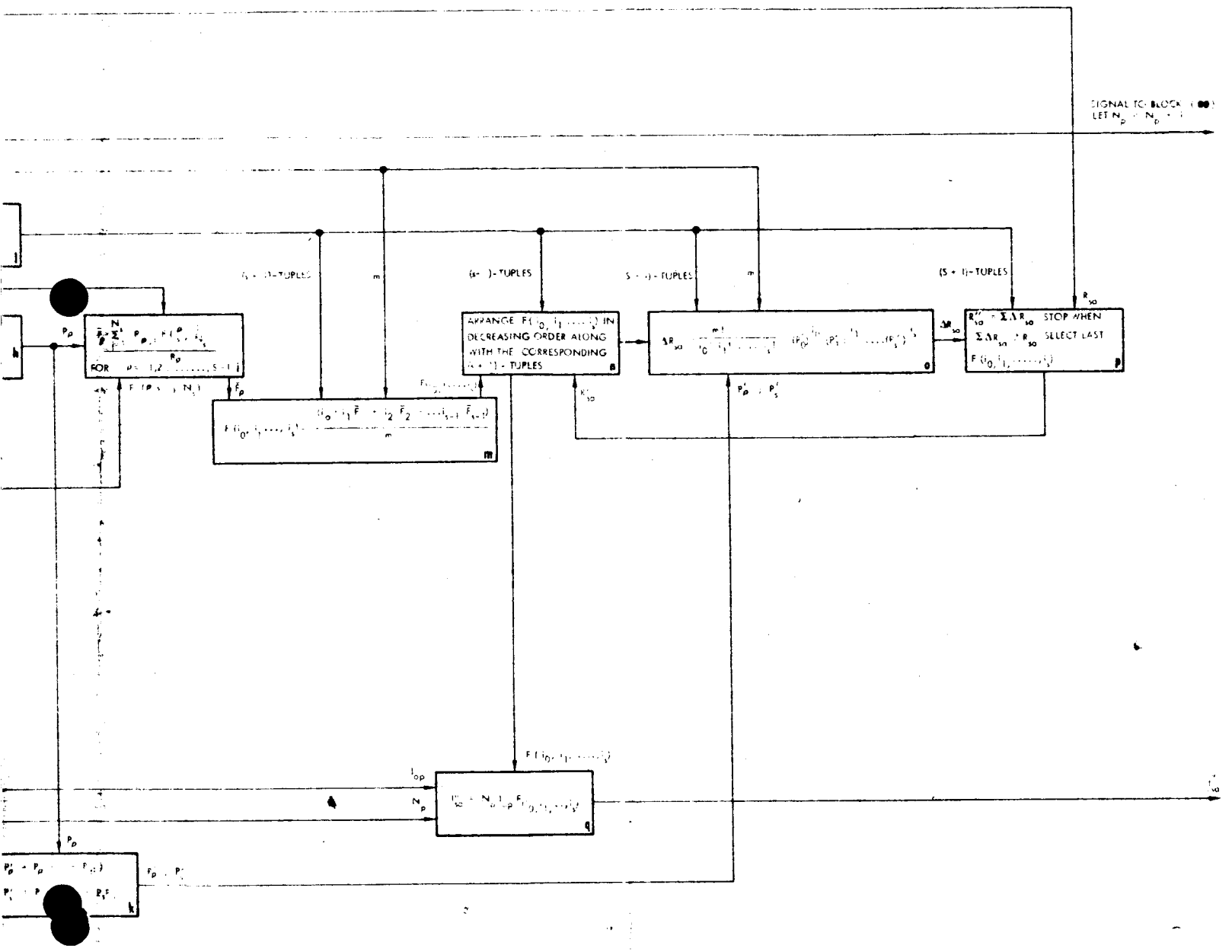

Figure 3-2. Solar Array Reliability Calculation Flow Diagram

70

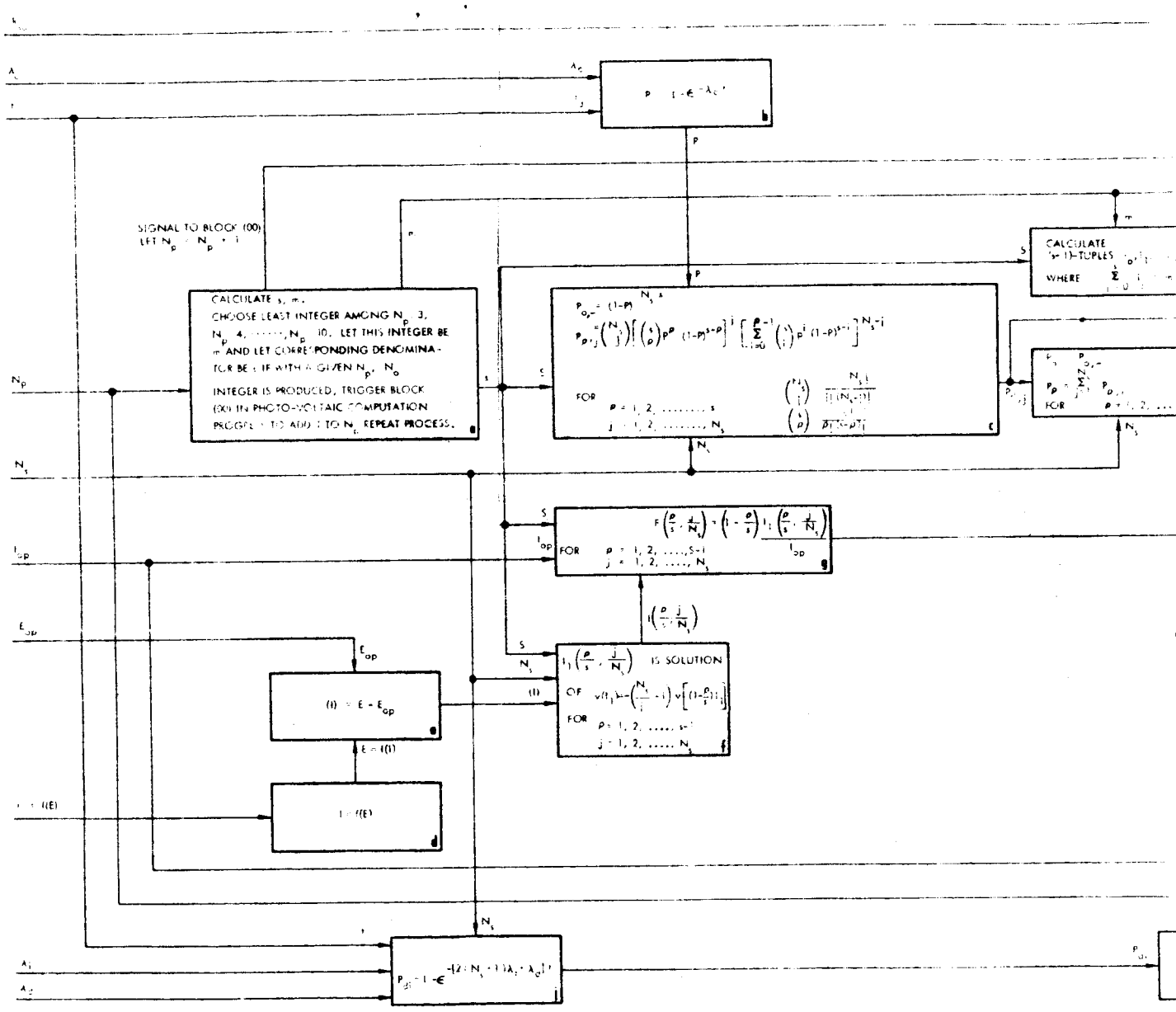

SIGNAL TO BLOCK (00)
LET $N_p = N_p + 1$
CALCULATE s, m.
CHOOSE LEAST INTEGER AMONG N_p 3, N_p 4, ..., N_p 10. LET THIS INTEGER BE m AND LET CORRESPONDING DENOMINATOR BE s IF WITH A GIVEN N_p, N_o INTEGER IS PRODUCED, TRIGGER BLOCK (00) IN PHOTO-VOLTAIC COMPUTATION PROGRAM TO ADD 1 TO N_p REPEAT PROCESS.
CALCULATE (s-1)-TUPLES
WHERE
FOR
IS SOLUTION
OF
FOR
$(I) = E - E_{op}$
$E = f(I)$
$I = f(E)$

This integer is "m" (number of parallel modules) and the corresponding denominator is "s" (number of parallel cells per module). If none of the above ratios produce an integer, trigger Block OO so that $N_p = N_p + 1$.

Block b. Probability of individual cell failure (P)

Input, λ_c (single cell failure rate from input data)

t (time from mission data)

Computation,

$$P = 1 - \epsilon^{-\lambda_c t}$$

Block c. Probability of failures in a module ($P_{\rho, j}$)

Input, P (from Block b)

s (from Block a)

N_s (from Block DD)

Computation,

$$P_{o,} = (1 - P)^{N_s s}$$

$$P_{\rho, j} = \binom{N_s}{j}\left[\binom{s}{\rho} P_\rho (1 - P)^{s-\rho}\right]^j \left[\sum_{i=0}^{\rho-1} \binom{s}{i} P^i (1 - P)^{s-i}\right]^{N_s - j}$$

where

$$\rho = 1, 2, \cdots, s$$

$$j = 1, 2, \cdots, N_s$$

$$\binom{N_s}{j} = \frac{N_s!}{j!(N_s - j)!}$$

$$\binom{s}{\rho} = \frac{s!}{\rho!(s - \rho)!}$$

Block d. Inversion of cell characteristics $\left[E = f(I)\right]$

Input, $I = f(E)$ (from Block AA)

E_{op} (from Block DD)

Invert $I = f(E)$ such that $E = f(I)$

Block e. Translation of cell characteristics curve $\left[v = f(I)\right]$

Input, $E = f(I)$ (from Block d)

Computation,

$$v = E - E_{op}$$

Output, $v = f(I)$

Block f. Current in a single solar cell $\left[I_c\left(\frac{\rho}{s}, \frac{j}{N_s}\right)\right]$

Input, $v = f(I)$ (from Block e)

N_s (from Block CC)

s (from Block a)

Solve

$$v(I_1) = -\left(\frac{N_s}{j}\right) v\left[\left(1 - \frac{\rho}{s}\right) I_c\right]$$

for

$$I_c\left(\frac{\rho}{s}, \frac{j}{N_s}\right)^*$$

for

$$\rho = 1, 2, \cdots, s - 1$$

$$j = 1, 2, \cdots, N_s$$

Block g. Fractional output current of module

Input, $I_c\left(\frac{\rho}{s}, \frac{j}{N_s}\right)$ (from Block f)

s (from Block a)

I_{op} (from Block EE)

---

*Compute I_c and F to not more than three significant figures.

73

Computation

$$F\left(\frac{\rho}{s}, \frac{j}{N_s}\right) = \left(1 - \frac{\rho}{s}\right) \frac{I_c\left(\frac{\rho}{s}, \frac{j}{N_s}\right)^*}{I_{op}}$$

for

$$\rho = 1, 2, \cdots, s - 1$$

$$j = 1, 2, \cdots, N_s$$

Block h. Probability of failures in module rows (P_ρ)

Input, P_o (from Block c)

$P_{\rho, j}$ (from Block c)

Computation,

$$P_o = P_{o,-}$$

$$P_\rho = \sum_{j=1}^{N_s} P_{\rho, j} \quad \rho = 1, 2, \cdots, s$$

Block i. Fractional output current

Input, $P_{\rho, j}$ (from Block c)

P_ρ (from Block h)

$F\left(\frac{\rho}{s}, \frac{j}{N_s}\right)$ (from Block g)

Computation,

$$\bar{F}_\rho = \frac{\sum_{j=1}^{N_s} P_{\rho, j} F\left(\frac{\rho}{s}, \frac{j}{N_s}\right)}{P_\rho}$$

$$\rho = 1, 2, \cdots, s - 1$$

*Compute I_c and F to not more than three significant figures.

Block j. Probability of diode and interconnection failures (P_{di})

Input, N_s (from Block CC)

λ_i (input data)

λ_d (input data)

Computation,

$$P_{di} = 1 - \epsilon^{-2(N_s+1)\lambda_i+\lambda_d t}$$

(Assuming nonredundant series interconnections and one isolating diode for each module)

Block k. Input, P_ρ (from Block h)

P_s (from Block h)

P_{di} (from Block j)

Computation,

$$P_\rho' = P_\rho(1 - P_{di}) \qquad \rho = 0, 1, 2, \cdots, s - 1$$

$$P_s' = P_s + P_{di} - P_s P_{di}$$

Block l. Define the (s + 1)-tuples (i_o, i_1, $\cdots$, i_s) where each i_j is a positive integer and where

$$\sum_{j=0}^{s} i_j = m$$

Block m. Fractional output current

Input, (s + 1)-tuples (from Block l)

$\overline{F}_\rho$ (from Block i)

Computation,

$$F(i_o, i_1, \cdots, i_s) = \frac{i_o + i_1, \overline{F}_1 + i_2\overline{F}_2 + \cdots i_{s-1}\overline{F}_{s-1}}{m}.$$

Block n. Arrange $F(i_o, i_1, \cdots, i_s)$ in decreasing order and arrange the corresponding (s + 1)-tuples in the same order.

Block o. Incremented reliability of solar array (ΔR_{sa})

Input, m (from Block a)

$i_o, i_1, \cdots, i_s$ for each (s + 1)-tuple (from Blocks l and n)

$P_o', P_1', \cdots, P_s'$ (from Block k)

Computation,

$$\Delta R_{sa} = \frac{m!}{(i_o!)(i_1!)\cdots(i_s!)} \left(P_o'\right)^{i_o}\left(P_1'\right)^{i_1} \cdots \left(P_s'\right)^{i_s}$$

for each (s + 1)-tuple in Block l.

Block p. Sum of incremental reliabilities (R''_{sa})

Input, ΔR_{sa} (from Block O)

Computation,

$$R''_{sa} = \sum \Delta R_{sa}$$

Starting from first (s + 1)-tuple in order determined in Block n until

$$R''_{sa} \geq R_{sa}$$

Output, The $F(i_o, i_1, \cdots, i_s)$ corresponding to the (s + 1)-tuple which resulted in $R'_{sa} \geq R_{sa}$

Block q. Solar array current output with cell failures (I''_{sa})

Input, $F(i_o, i_1, \cdots, i_s)$ (from Block n)

corresponding to (s + 1)-tuple determined in Block p

I_{op} (from Block EE)

N_p (from Block OO)

Computation,

$$I''_{sa} = FN_p I_{op}$$

9) Solar Array Area

Block FF. Total number of cell in array (N_{sa})

Input, N_s (from Block CC)

N_p (last output from Block OO)

Computation,

$$N_{sa} = N_s N_p$$

Block GG. Array area (A_{sa})

Input, N_{sa} (from Block FF)

A_c (solar cell area from cell data)

F_p (area packing factor from input data)

Computation,

$$A_{sa} = \frac{N_{sa} A_c}{F_p}$$

10) Solar Array Weight

Block LL. Weight of cell, cover glass, adhesive, wire, connectors and insulation per unit cell (w_c')

Input, w_c (cell weight from input and cell data)

w_{cg} (cover glass weight from input data and selected thickness)

w_{cb} (circuit board weight from input data)

w_h (miscellaneous hardware weight from input data)

Computation,

$$w_c' = w_c + w_{cg} + w_{cb} + w_h$$

Block HH. Number of solar panels in array (n_p)

Input, $A_{p(max)}$ (area limit of solar panel from input data)

A_{sa} (from Block GG)

Computation,

$$n_p = \frac{A_{sa}}{A_{p(max)}}$$

Adjust to next higher even integer if solar panels are to be paired. Otherwise adjust to next higher integer. (Assumes all panels are identical.)

Block II. Area of each solar panel (A_p)

Input, A_{sa} (from Block GG)

n_p (from Block HH)

Computation,

$$A_p = \frac{A_{sa}}{n_p}$$

Block JJ. Weight of array structure (W_s/A)

Input, A_p (from Block II)

Type structure (input data)

Output, W_s/A (structure weight per area)

Block KK. Area weight (W_{sa})

Input, w_c' (from Block LL)

W_s/A (from Block JJ)

A_{sa} (from Block GG)

N_{sa} (from Block FF)

Computation,

$$W_{sa} = (W_s/A)A_{sa} + w_c'N_{sa}$$

11) <u>Solar Array Output with No Cell Failures</u>

Block EE. Array current with no cell failures (I'_{sa})

Input, I_{op} (last output from Block EE)

N_p (last output from Block OO)

Computation,

$$I'_{sa} = I_{op} N_p$$

Block PP. Array output power with no cell failures (P_s')

Input I'_{sa} (from Block EE)

E_s (source voltage from systems requirements computation Figure 2-6)

Computation,

$$P_s' = E_s I'_{sa}$$

12) Solar Array Performance at Other Than Design Point. The performance of the solar array at other than the design point can be computed by keeping N_p in Block OO and N_s in Block CC fixed and changing the mission dependent input functions of T_{sa}, Γ, AU, Φ_c', Φ_a', Φ_{cg}', t, and possibly E_{sa} and R_{sa}. Repeat Steps 1 through 6.

Block AA'. Output, $I = f(E)$ (cell characteristics)

Block EE'. Cell operating current (I_{op})

Input, $I = f(E)$ (from above procedure and Block AA)

E_{op} (from Block DD)

Determine I_{op} on $I = f(E)$ at E_{op}

Block MM'. Array output current at required reliability (I''_{sa})

Input, $I = f(E)$ (from Block AA')

I_{op} (from Block EE')

t (new input data)

N_s, N_p, R_{sa}, λ_c, λ_i, and λ_d. Same as used in design computation.

Output, I''_{sa} (array output current with computed design and required reliability)

Block EE'. Array current with no cell failures (I'_{sa})

Input, I_{op} (from Block MM')

N_p (last output from Block OO)

79

Computation,

$$I'_{sa} = I_{op} N_p$$

Block PP'. Array output power with no cell failures (P_s')

Input, I'_{sa} (from Block EE')

E_s (input data)

Computation,

$$P_s' = E_s I'_{sa}$$

Block QQ. Array output power with cell failures (P''_s)

Input, I''_s (from Block MM')

E_s (input data)

Computation,

$$P''_s = E_s I''_{sa}$$

13) Computation Outputs. The output of the computation process are as follows:

(a) Solar array area (A_{sa})

(b) Solar array weight (W_{sa})

(c) Power output with no cell failures (P_s')

(d) Power output with cell failures at other than design point calculations (P''_s)

(e) Solar array output characteristics $\left[I_{sa} = f(E_s)\right]$

A sample calculation is performed in Appendix B1 to illustrate the computation process. Parametric data for the functions required is given in Appendix A1.

3. Parametric Data Generation

a. Bare Solar Cell Characteristics - $I_o = f(E_o)$ (See Figure A1-1)

The solar array design computation is based on the use of a bare cell current-voltage characteristic under standard conditions of 140 mw/cm^2

normal solar irradiation at air mass zero* (AMO) and 28°C. Data which permits direct utilization can be obtained from electrical measurements made under illumination closely approximating the spectrum of solar irradiation in outer space and at the intensity of the solar constant (Reference 3-6). Sufficient number of cells of the desired type for design should be tested so that a minimum I-V curve can be evolved. Use of a minimum I-V curve for the selected cell eliminates the need for considering matching losses in the solar array design. The current-voltage characteristics in Appendix A1 represent the results of solar simulation tests on numerous silicon N-on-P solar cells having 10 ohm-cm resistivity material and 10 percent AMO conversion efficiency. These cells were manufactured by several companies.

A solar cell current-voltage characteristic can also be presented in an equivalent functional form. The equation for the current-voltage relationship is

$$I = I_L - I_o\left[\epsilon^{\frac{q}{AKT}(E-IR_s)} - 1\right] - \frac{E}{R_{sh}}$$

where

I = solar cell current

I_L = light-generated current

I_o = diode saturation current

E = solar cell voltage

A = dimensionless constant

q = electronic charge

k = Boltzman constant

T = temperature

R_s = series resistance

R_{sh} = shunt resistance

*The illumination spectrum and intensity of the mean earth distance from the sun is referred to as "air mass zero" condition, abbreviated AMO.

An approximate but simpler function based on the diode equation usually provides sufficient accuracy for a solar array design computation. This function is

$$I = I_{sc}(1 - K_2)\left(\epsilon^{\frac{E}{K_1 E_{oc}}} - 1\right)$$

where

I_{sc} = short circuit current

E_{oc} = open circuit voltage

K_1 = constant (see Step 1 of Subsection III. A. 2)

K_2 = constant (see Step 1 of Subsection III. A. 2)

Figure 3-3 shows the comparison between the test data obtained current-voltage characteristic curve of a 10 percent, 10 ohm-cm, N-on-P cell and the approximate functional form.

b. Particle Radiation Environment and Equivalent 1-Mev Electron Dose (Φ_c, Φ_a, Φ_{cg})

To facilitate evaluation and interpretation of environmental radiation damage to a given type of solar cell and comparison with experimental data, the energy-dosage spectra of environmental electron and proton radiation and of solar flare radiation are adjusted to 1-Mev electron energy and all cell damage phenomena are considered as a function of equivalent 1-Mev electron dosage. The experimental data on radiation damage is obtained by means of a 1-Mev Van de Graaf generator, and the limitation imposed by this energy requires adjustment of all cell damage data to 1-Mev electron energy and equivalent dosages.

If the solar cell is covered with cover glass and adhesive, the degradation of these with exposure to radiation must also be considered. The radiation spectra incident on the cover material are adjusted to 1-Mev electron energy and damage to the cover material is considered as a function of equivalent dosage.

To adjust the energy-dosage spectrum of environmental electron radiation to 1-Mev energy for the solar cell itself, the integral spectrum is differentiated with regard to energy to obtain the dosage as a function of

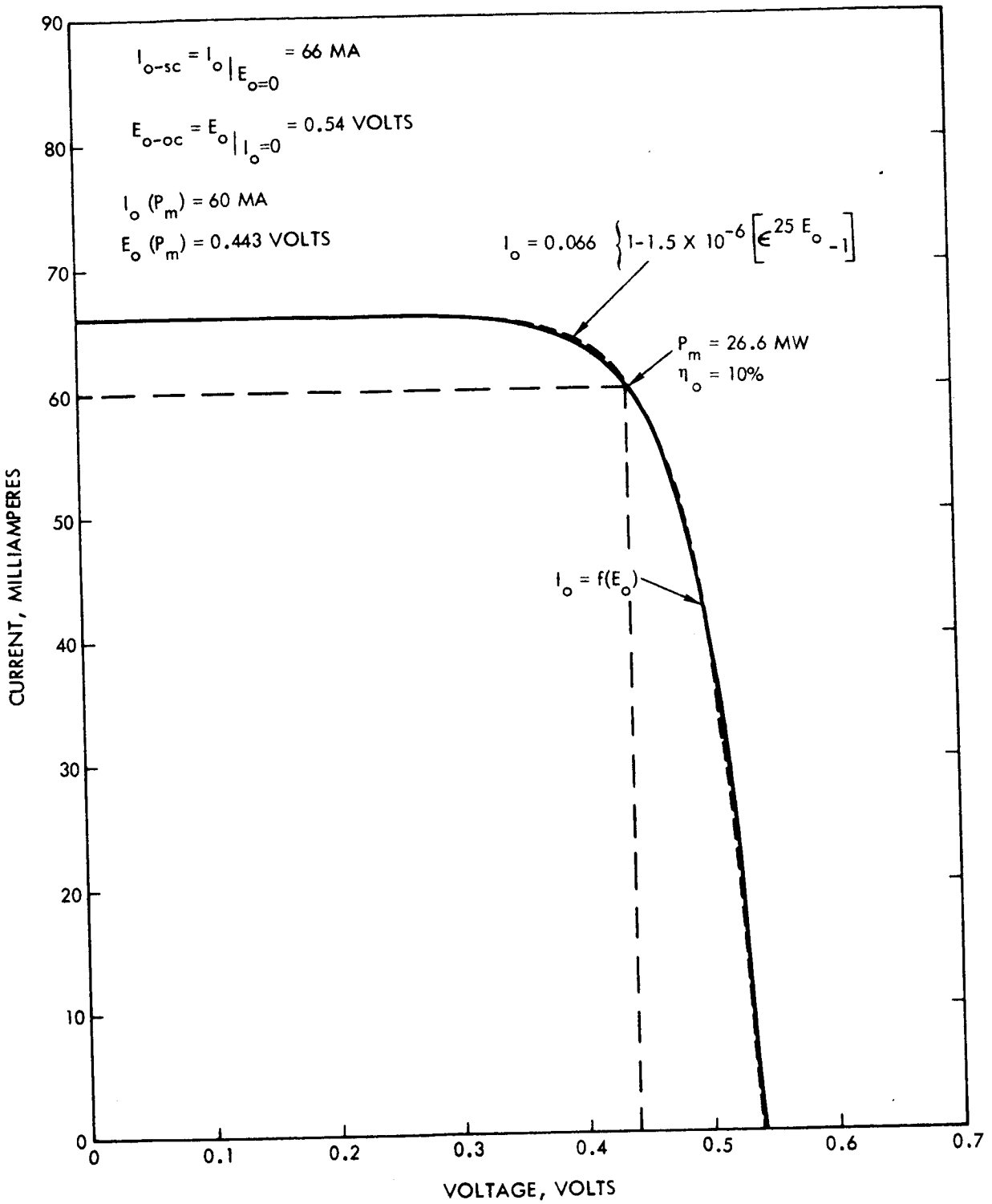

Figure 3-3. Solar Cell Current-Voltage Characteristics

energy. The omnidirectional flux per unit energy internal is then adjusted for geometry of particle incidence and cover material thickness to yield the energy-dosage spectrum actually striking the cell surface (Reference 3-2). This adjustment is independent of the type of solar cell but varies for different cover materials and thickness. The threshold energy for the cover material, below which electrons will not penetrate, is slightly different for different cover materials (such as quarts or microsheet). For a given cover material, the threshold is a function of thickness. Because the magnitude of the threshold influences the energy-dosage spectrum incident on the cell surface, both the particular cover material and the thickness being used must be considered in calculating the energy-dosage spectrum incident on the solar cell surface.

For both proton and electron radiation, the energy-dosage spectra vary with the anticipated environment and thus from one mission to another. A typical example of the procedure discussed here is shown for a 10 ohm-cm N-on-P solar cell. The integrated electron energy-dosage spectrum for a given orbit is shown in Figure 3-4 and the integrated proton energy-dosage spectrum in Figure 3-5. The differentiated electron spectrum, i.e., the dosage as a function of energy, is shown in Figure 3-6. The differentiated proton spectrum is similar.

The relative damage effectiveness of electrons with respect to 1-Mev electron energy and that of protons with respect to 10-Mev proton energy have been determined experimentally by STL (References 3-4 and 3-5). For 10 ohm-cm N-on-P cells, the relative effectiveness of electrons relative to 1-Mev electron radiation is shown in Figure 3-7. The relative damage effectiveness of electron or proton radiation gives the equivalent dosage of radiation at a reference energy level (e.g., 1 Mev for electrons, 10 Mev for protons) and is independent of any particular radiation environment but varies for different types of solar cells.

The damage effectiveness for protons relative to 10-Mev proton energy is converted to effectiveness relative to 1-Mev electron energy by means of comparing experimentally observed proton and electron damage to the given type of solar cells. The product of differentiated electron or proton spectrum results in the respective equivalent 1-Mev electron spectrum. Figure 3-8 shows this product for the example cell and electron

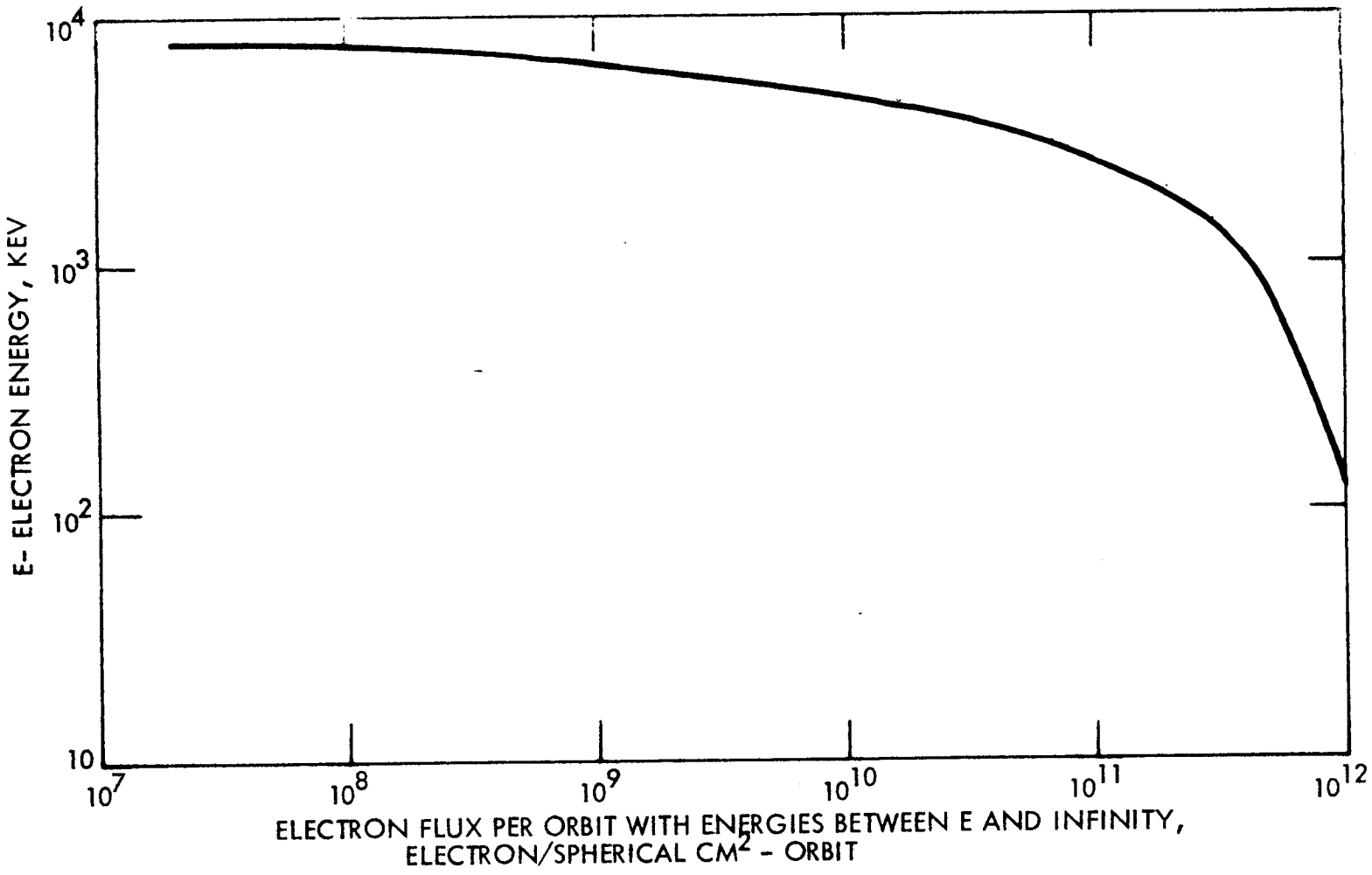

Figure 3-4. Electron Integral Energy Spectrum

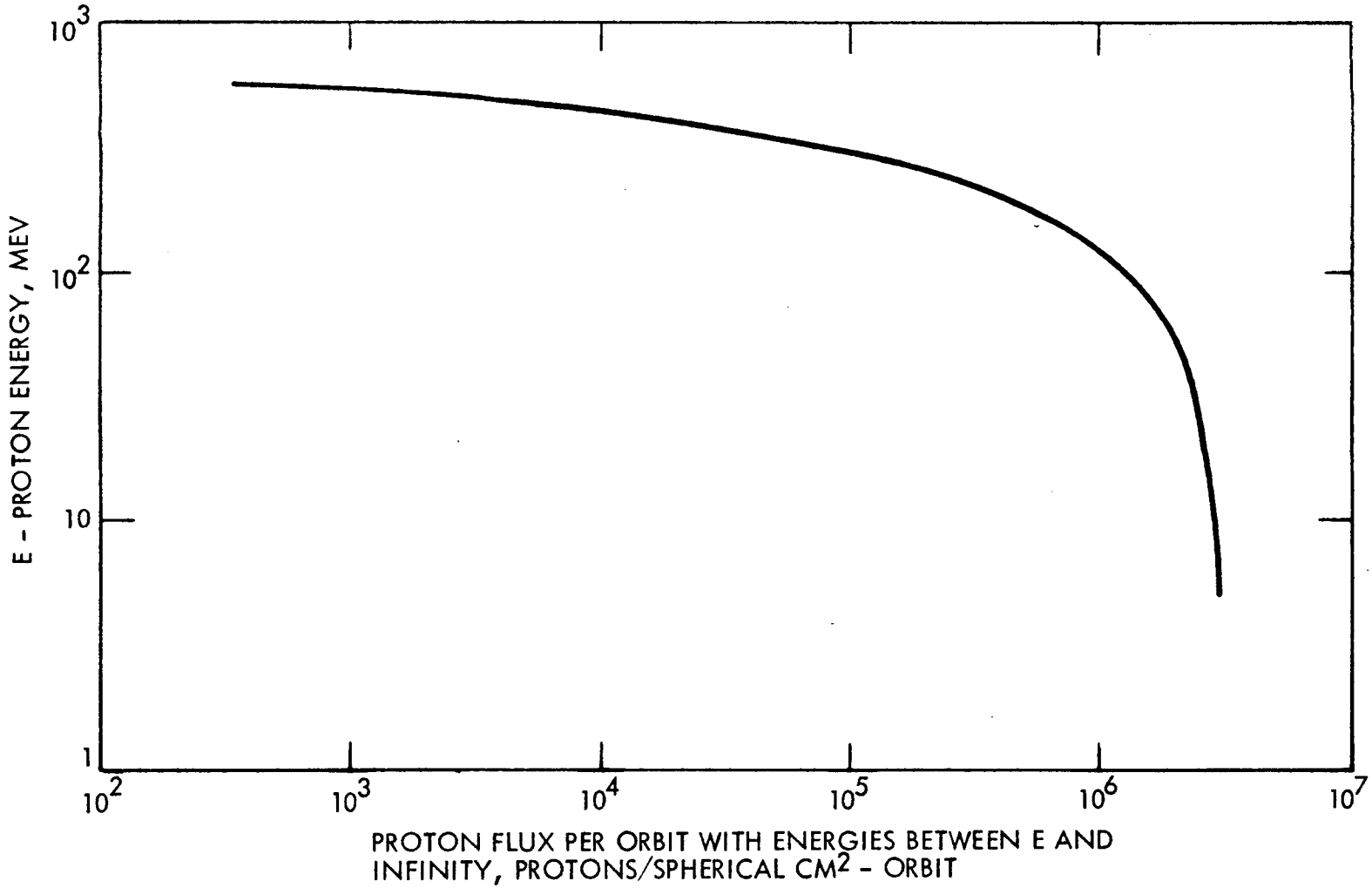

Figure 3-5. Proton Integral Energy Spectrum

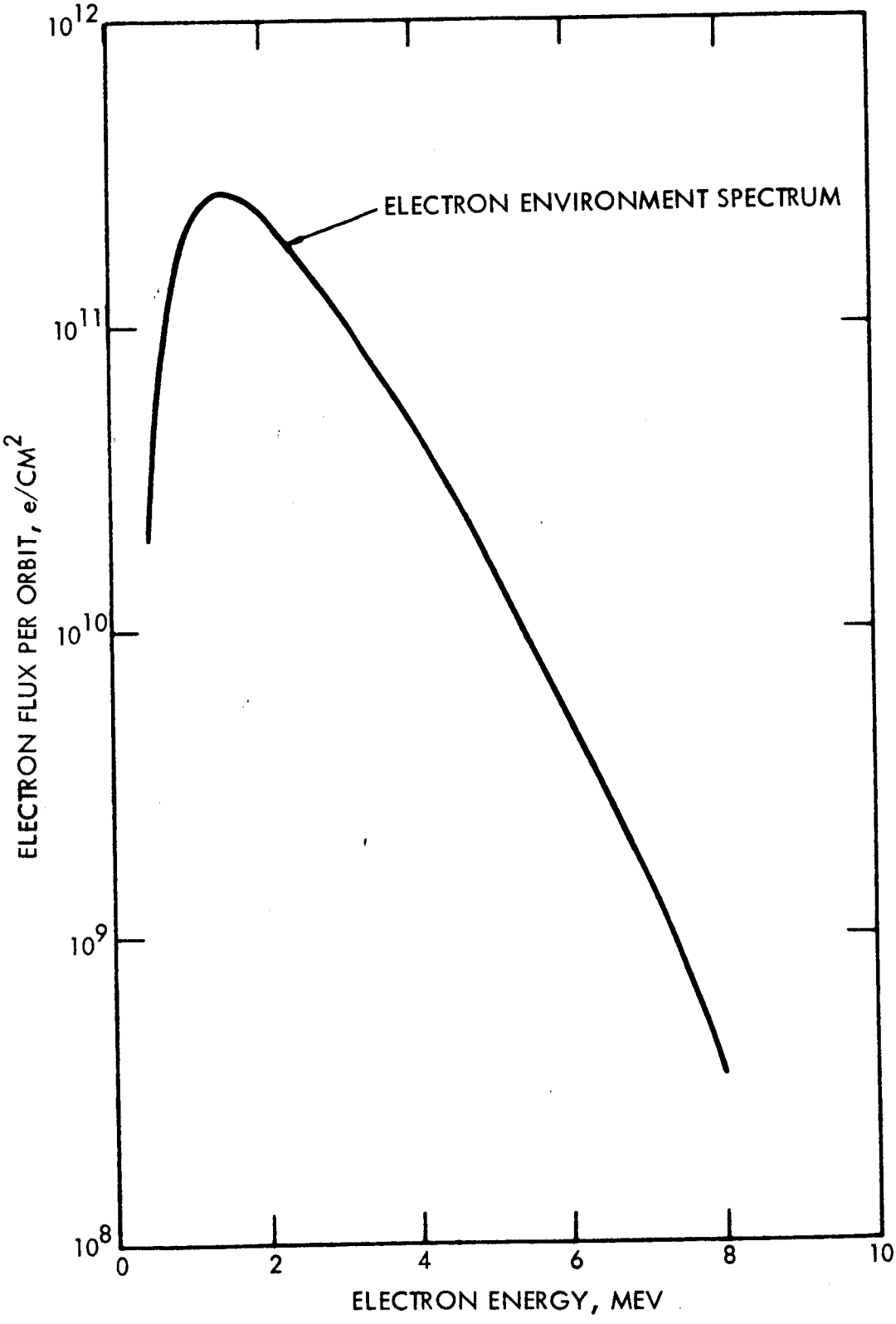

Figure 3-6. Electron Energy Spectrum

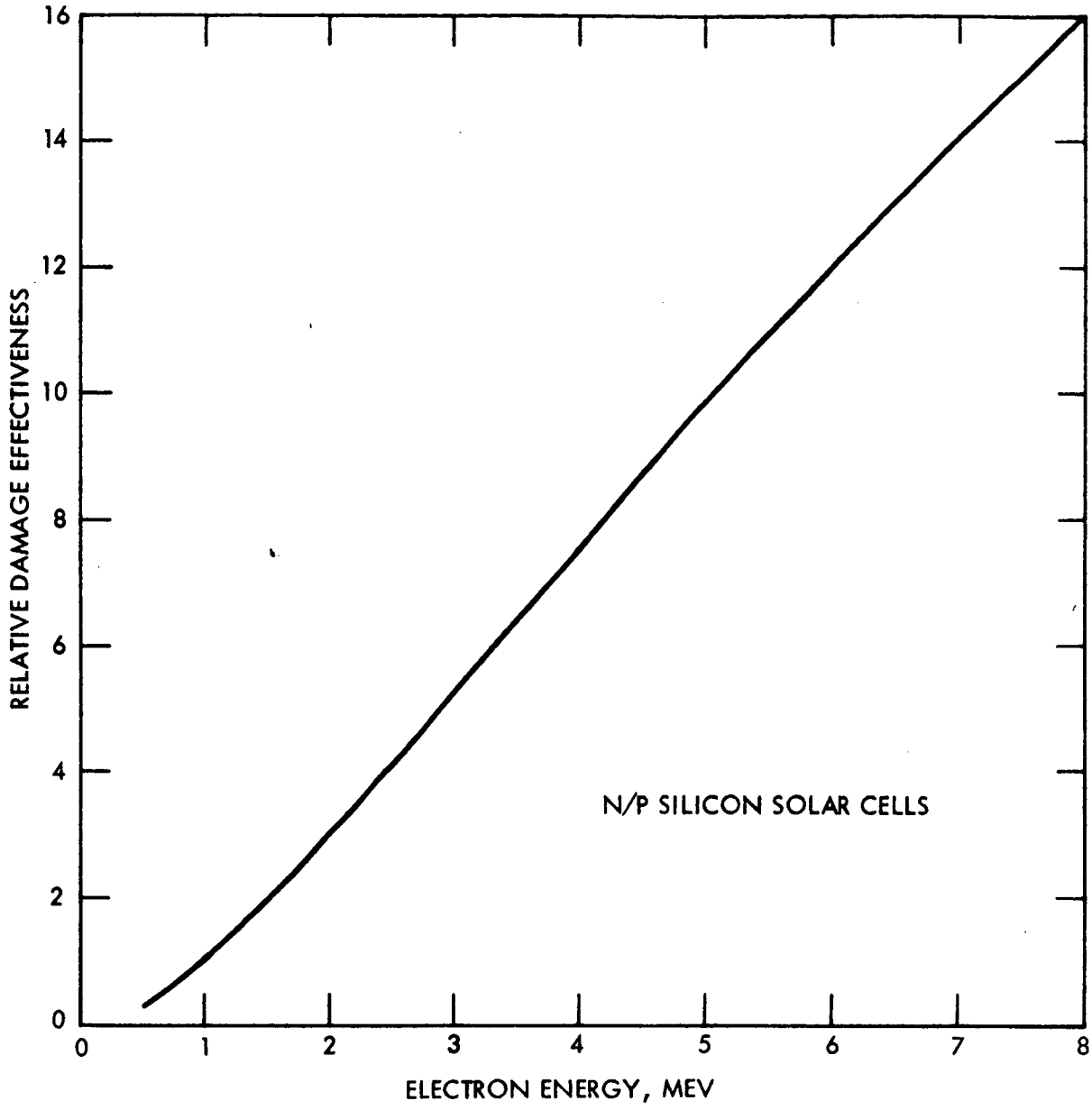

Figure 3-7. Relative Damage Effectiveness of Electrons as a Function of Electron Energy

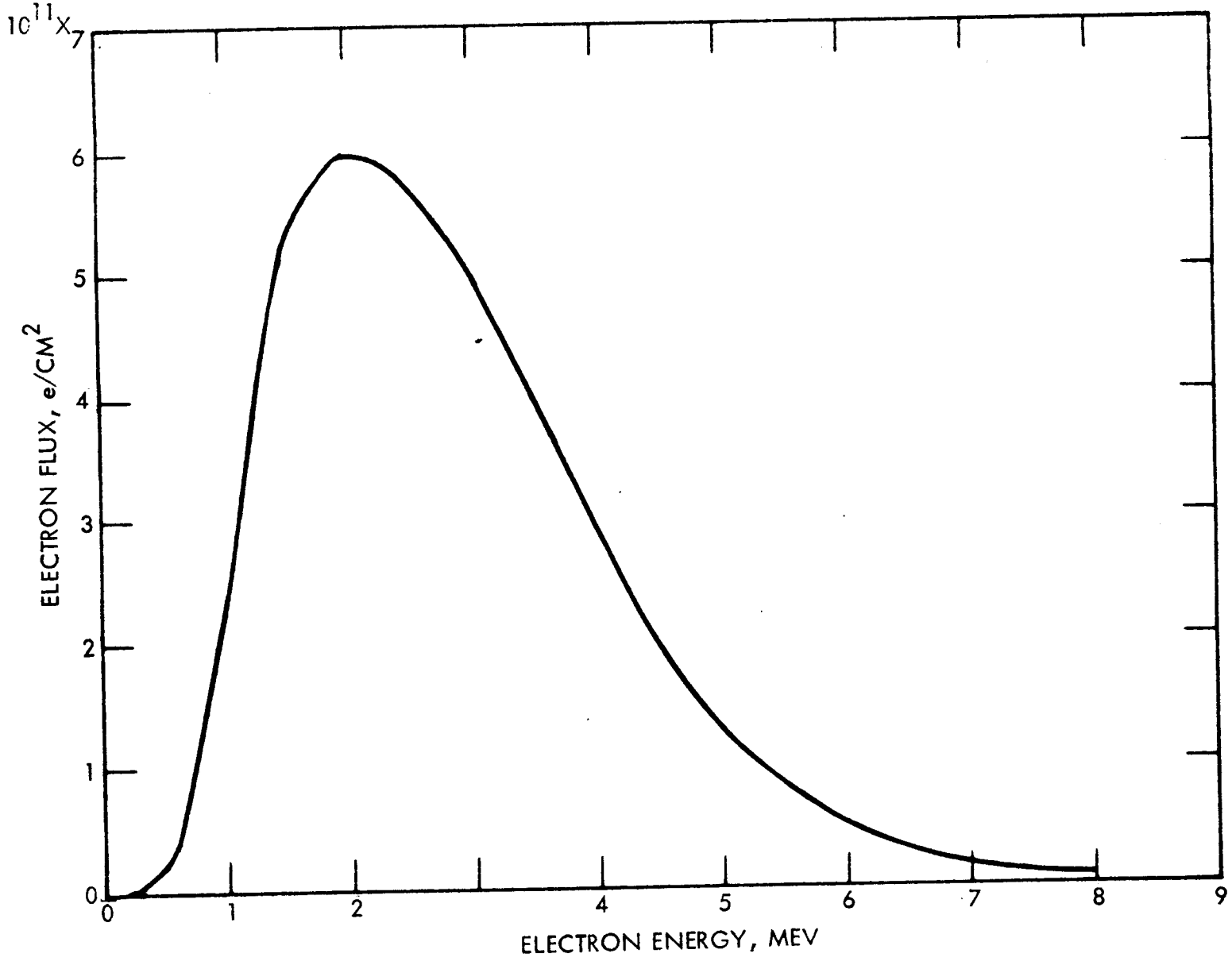

Figure 3-8. Equivalent 1-Mev Electron Energy Spectrum Incident on Solar Cells

dosage. The integral of these spectra yields the dosage for both protons and electrons for the anticipated environment in terms of 1-Mev electron dosage. The same procedure may be employed for solar flare radiation, which consists primarily of high energy protons.

For covered cells, in addition to degradation of cell output with exposure to radiation, the shielding capability and degradation of the cover material must also be considered in calculating the effect of radiation on a solar array. The cover materials presently used are glasses (e.g., quartz) in the form of thin sheets which are bonded to the solar cell by a transparent adhesive.

The same procedure used for evaluating radiation damage to solar cells is used for the cover material. The dosage-energy spectra of the environmental electrons and protons (and also the spectrum of solar flare radiation) are transferred into equivalent dosages of 1-Mev electron radiation. The relative damage effectiveness of electrons relative to 1-Mev electron radiation and that of protons relative to 10-Mev proton radiation are calculated as for the solar cell itself. The relative damage effectiveness for protons relative to 10-Mev protons is then converted to the relative damage effectiveness for electrons relative to 1-Mev electrons, as is done for the solar cells. Dosage-degradation relationships are then calculated for the cover material in terms of 1-Mev electron radiation. Since different cover materials deteriorate at different rates when exposed to radiation, these degradation-dosage relationships will vary with different cover materials. In addition, these degradation-dosage relationships will depend on the thickness of the cover material.

The adhesive does not appreciably affect the energy-dosage radiation spectra incident on the solar cell. The spectra incident on the cell is considered the same as emerges from the cover material. The adhesive itself, however, becomes increasingly opaque with radiation. Radiation damage to the adhesive may be treated the same way as for the cover material.

As mentioned above, the energy-dosage spectra of the radiation incident on the surface of a covered cell must be adjusted for the presence of the cover material and the effect of radiation on the cover material. Since one of these effects may be a change in the optical properties of the cover

material, the illumination of the solar cell is also affected. Hence, the illumination of the covered solar cell and the radiation incident on the cell must be considered as a function of the radiation incident on the cover material and its effect on the cover material in dealing with any particular combination of solar cell and cover material. Mathematically, the resulting relationship would tend to be complicated, and necessary approximations may have to be used.

c. Short Circuit Degradation

The short circuit current as a function of integrated electron flux is based on data reported in References 3-1 and 3-3. Measurements were performed on 1 x 2 cm, 10 ohm-cm, N-on-P silicon solar cells produced by different manufacturers, using simulated solar illumination at an intensity of 140 mw/cm^2. Figure A1-2 represents the average of the test results.

d. Open Circuit Degradation

Open circuit voltage also exhibits a degradation with electron dose. This degradation is in addition to that which would be expected by the decrease in short circuit current alone. The component of the decrease in open circuit voltage that is due only to the decrease in short circuit current is defined and described in Reference 3-11. The change in open circuit voltage from that of a nonirradiated cell is, therefore, the sum of voltage degradation due to electron dose and due to the decrease in short circuit current caused by the electron dose. The open circuit voltage a function of integrated electron flux is also based on data reported in References 3-1 and 3-3. Corresponding open circuit voltage is shown in Figure A1-3.

e. Cover Glass and Adhesive Degradation

Solar cells are covered with cover slides of fused silica or microsheet glass in order to:

- Screen-out low energy protons
- Reduce the electron and proton flux experienced by the solar cells themselves

- Provide protection from micrometeoroid erosion of the solar cell surface
- Enhance the spectral emittance of the surface.

The cover slides are provided with interference filters of two kinds. One filter, placed on one side of the cover slides, is an anti-reflective coating of MgF_2, the function of which is to reduce the reflectance loss. The other filter, placed on the other side of the cover slides, is an ultraviolet reflective filter whose function is to protect the cover slide adhesive from ultraviolet radiation, which otherwise would cause a loss of transparency of the cement used to secure the covers to the cells. The use of the filter also reduces the cell temperature slightly because of the reduced solar absorptance. This tends to increase the power output from the cells. However, an overall decrease in power output results, since part of the solar spectrum is prevented from reaching the solar cell and being converted to electrical energy. This decrease is a function of the cutoff wavelength of the ultraviolet filter.

Cover slides, plus the adhesive, reduce the initial effective insolation on solar cells. Both fused silicon and microsheet glass, when bonded to the cell, have an effective transmittance in the solar cell response spectrum of approximately 94 to 98 percent depending on the solar cell surface treatment. The adhesive is assumed to cause no reduction in transmittance within the cell response spectrum. However, particle radiation induces a transmittance change in adhesive and cover material, and, as a result, reduces the cell current further, in addition to that caused directly by radiation. At high electron dosages, the transmittance for the bare cover material decreases only slightly, whereas for cover glass with adhesive, a greater degradation results. The resulting reduction in cell short circuit current is partially caused by the change in transmittance of the cover materials and partially by delamination occurring between adhesive and cover material and between adhesive and cell surface. Figure A1-4 (adhesive transmission factor as a function of electron dose) and Figure A1-5 (cover glass transmission factor as a function of electron dose) are based on results of radiation tests on bare N-on-P silicon solar cells and on solar cells with various cover materials, performed with 1-Mev energy electrons for integrated fluxes up to 10^{16} e/cm^2. The data

presented in Appendix A1 is for 10 ohm-cm, 10 percent, N-on-P solar cells. Experiments to date have been conducted in air at 1 Mev. It is not known what effect actual charged particle environment in space will have upon the adhesive. According to data obtained in the TRS-1 flight program (Reference 3-3), adhesive damage may be less than indicated by laboratory test results.

f. Temperature Coefficients

The temperature coefficient of the electrical output of a solar cell is a function of temperature, electron flux, and illumination intensity. For a given condition of electron flux and illumination, the temperature coefficient for short circuit current and open circuit voltage are nearly constant in the temperature range of 10°C to 80°C. At lower temperatures, the absolute values of temperature coefficient decrease.

Based on measurements reported in References 3-8 and 3-9, the short circuit current temperature coefficient increases both in actual and normalized values after electron irradiation. Actual temperature coefficient for short circuit current has a positive correlation to light intensity. The normalized temperature coefficient for short circuit currents, however, remains nearly constant with light intensity. This applies both to nonirradiated and electron irradiated solar cells. Therefore, the normalized short circuit current temperature coefficient is a function only of particle radiation and is shown as the curve in Figure A1-7 for a 10 ohm-cm, 10 percent, N-on-P solar cell in the temperature range of 10°C to 80°C.

Temperature coefficient for the open circuit voltage is negative and remains nearly constant in actual values with increasing electron dosage. The normalized values, however, show an increase in magnitude. Both the actual and normalized values of the temperature coefficient for the open circuit voltage show a decrease in magnitude with increased light intensity. Therefore, the actual open circuit voltage temperature coefficient is a function only of insolation and is shown in Figure A1-8 for a 10 ohm-cm, 10 percent, N-on-P solar cell in the temperature range of 10°C to 80°C.

g. Effects of Angle of Incidence

The short circuit current output from silicon solar cells under constant collimated illumination is a function of the angle of incidence. This function is dependent upon the optical absorption coefficient of silicon and, when covers are used, upon the cover material and interference filters. Electron irradiation affects the reflectance of the interference filters and, consequently, the short circuit output current.

The ratio of short circuit current of a covered solar cell with interference filter at any angle to the short circuit current at normal incidence ($I_\Gamma/I_o = R_{sc}$) as a function of the cosine of the angle of incidence (cos Γ), as described in Reference 3-8, is shown in Figure A1-6. It is seen that the ratio R_{sc} is greater than the value of cos Γ between 1.0 (cos 0 degrees) and approximately 0.5 (cos 60 degrees). The cause for values of R_{sc} above cos Γ for the covered cells is a decrease in the reflectance of the interference filters at short wavelengths and approximately constant reflectance at longer wavelengths with increasing angle of incidence up to about 60 degrees. This decrease in reflectance in the region of 0.32 to 0.43 micron is a property of the reflective interference filters. At angles of incidence above 50 degrees, the reflectance of the cover above 0.43 micron starts to increase at an accelerated rate, which results in a rapid decrease below cos Γ in the function R_{sc}.

Electron irradiation changes the spectral reflectance in such a manner that the spectral reflectance below 0.45 micron decreases at all angles of incidence, whereas it increases slightly at longer wavelengths. As a result, R_{sc} decreases more below cos Γ at all angles of incidence with increasing electron dosage. The rate of change is higher for larger angles of incidence than for smaller angles.

h. Series Resistance (r_s)

Variation of series resistance with 1-Mev electron dosage at 28°C have been investigated. The series resistance was determined in accordance with the method described in Reference 3-11 from the I-V characteristics of solar cells at various light intensities after various levels of electron irradiation. The results showed no definite trend of the series resistance with electron dosage. As a result, it is assumed that the

series resistance remains constant up to 1-Mev electron dosages of 10^{15} e/cm^2. The values obtained experimentally per Reference 3-10 are approximately 0.38 ohms for P-on-N cells and 0.73 ohms for N-on-P cells.

i. Solar Array Structure

Studies were conducted on a series of rectangular solar panels varying in area from 10 to 100 square feet. As an aid in establishing array specific weights and area utilization factors, the following conditions were assumed:

- o Module containing 20 standard 1 x 2 cm cells each 20 mils thick.
- o Panel width of approximately 60 inches, such that maximum area utilization can be obtained using above modules.
- o Panel area increase by means of panel length increase.
- o Panel of sufficient strength to support itself horizontally in a 1-g field with a nominal deflection. This condition was established for purposes of selecting material gauges in the absence of other load criteria.
- o Minimum weight materials and latest fabrication techniques.

Figure A1-9 shows the structure specific weight (W_s/A) versus panel area (A_p) for primary panels (deployed-fixed single fold) and secondary panels (deployed-fixed double fold). For comparison, Table 3-1 gives the specific weights for a number of existing solar array configurations, including oriented arrays, body-mounted spinning arrays, and oriented spacecraft arrays. A possible maximum cell density array configuration for a large oriented spacecraft is shown in Figure 3-9. The maximum possible cell density was based on a packing factor of 0.96.

j. Solar Array Temperature (T_{sa})

Temperature of the cells in a solar array is calculated from a separate computation. Under steady state conditions, the equation for temperature is

$$A_t \bar{\epsilon} \sigma T^4 = AH_s \bar{\alpha}_{s1}(1 - \eta)F_s + AH_{pr}\bar{\alpha}_{s2}F_{pr} + AHp\epsilon_{s2}F_p \qquad (1)$$

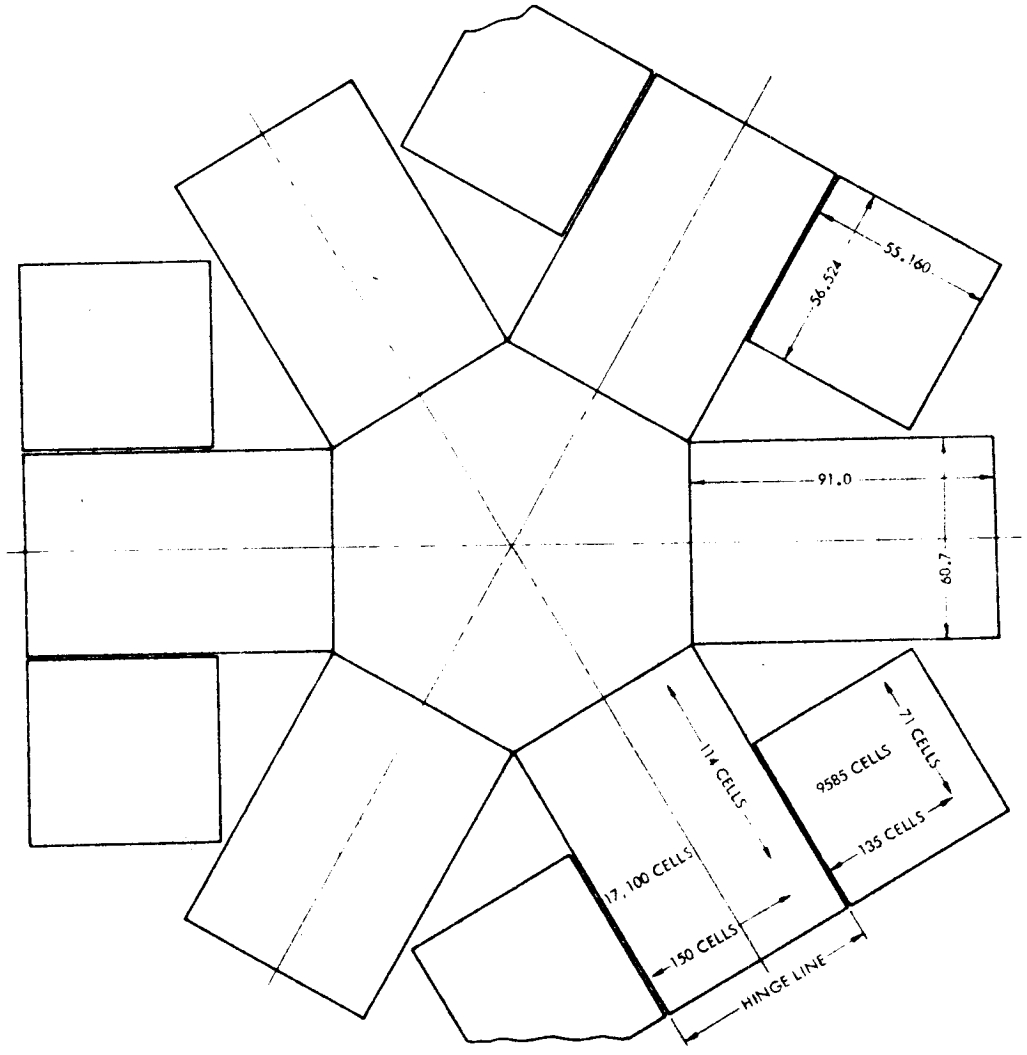

TOTAL ARRAY - AREA		360.07 FT^2
NO. OF CELLS		159,720
CELLS/FT^2		443.67
SIX PRIMARY RECTANGULAR PANELS-AREA (38.36 FT^2 EACH)		230.16 FT
NO. OF CELLS		102,600
CELLS/FT^2		445.77
SIX AUXILLIARY RECTANGULAR PANELS-AREA (21.652 FT^2 EACH)		129.91 FT^2
NO. OF CELLS		57,510
CELLS/FT^2		442.73
TOTAL ARRAY - WEIGHT		376.35 LB
SPECIFIC WEIGHTS	CELLS	0.576 LB/FT^2
	STRUCTURE	0.468 LB/FT^2
	TOTAL	1.05 LB/FT^2

PRIMARY PANELS-WEIGHT

230.16 X 0.579 = 133.263 LB - CELLS
230.16 X 0.551 = 126.818 LB - STRUCTURE

SPECIFIC WEIGHTS	CELLS	0.579 LB/FT^2
	STRUCTURE	0.551 LB/FT^2
	TOTAL	1.130 LB/FT^2

AUXILLIARY PANELS-WEIGHT

129.91 X 0.575 = 74.698 LB - CELLS
129.91 X 0.320 = 41.571 LB - STRUCTURE

SPECIFIC WEIGHTS	CELLS	0.575 LB/FT^2
	STRUCTURE	0.320 LB/FT^2
	TOTAL	0.895 LB/FT^2

Figure 3-9. Example Solar Array Configuration for Maximum Cell Density

Table 3-1. Specific Weights of Solar Arrays

	Total Array Area (ft^2)	Number of Cells	Cells Per ft^2	Method	Spars Structure Substrates (lb/ft^2)	Cells Wiring Adhesive (lb/ft^2)	Drive Mechanism (lb/ft^2)	Total (lb/ft^2)	Packing Factor Cell A / Total A
1. Oriented Array									
OGO (2 paddle assembly) each	39.7	16,128	406.3	Flat	0.387	0.868	0.314	1.599	0.87
Center rectangular panel	20.2	8,056	399.4		0.485	0.852		1.337	0.86
Auxiliary rectangular panels	19.5	8,056	413.5		0.312	0.883		1.195	0.90
2. Body Mounted-Spinning Array									
Relay (8 panels)	18.3	1,055	461.7	Shingled	0.240	1.505		1.745	0.92
Rectangular panels } 2.3 ft^2 panel	1.2	600	476.2		0.240	1.552		1.792	0.95
Trapezoidal panel } 2.3 ft^2 panel	1.0	455	443.9		0.240	1.447		1.687	0.89
Nuclear Test Detection Satellite									
Trapezoidal panel	2.15	765	355.4	Flat	0.376	0.534		0.910	0.77
Mil-COMSAT (preliminary design)									
Rectangular panel (8 panels)	0.86	390	451.4	Flat				1.172	0.92
Trapezoidal panel (16 panels)	1.03	430	418.7					0.970	0.85
Pioneer (Interplanetary Probe)									
Rectangular (25 panels)	21.0	10,000	476.8	Shingled				0.764	0.95
3. Oriented Spacecraft and Array									
Mariner 2	12.5	4,896	391.7	Flat				1.92	0.85
Mariner C	17.5	7,056	403.2	Flat	0.485	0.515		1.00	0.87

where

A = projected area to radiation (m^2)

A_t = total emitting area (m^2)

H_s = solar irradiation at array (watts/m^2)

H_p = planet emission (watts/m^2)

H_{pr} = planet reflected solar radiation (watts/m^2)

T = array temperature (^oK)

$\bar{\alpha}_{s1}$ = average solar absorptivity, sun facing side

$\bar{\alpha}_{s2}$ = average solar absorptivity, rear surface

$\bar{\epsilon}$ = average emissivity at temperature T

ϵ_{s2} = emissivity at temperature T, rear surface

η = solar cell conversion efficiency

σ = Stefan Bolzman's constant $\left[5.67 \times 10^{-8} \frac{\text{watts}}{m^2(^oK^4)}\right]$

F_s = shape factor to solar irradiation

F_p = shape factor to planet emission

F_{pr} = shape factor to planet reflected solar radiation

Spacecraft operating in orbital trajectories are exposed to alternate high and low thermal inputs. The highest and lowest temperatures of the cells depend on the orbital period of intensity of the incident radiation and on the thermal capacity of the solar array. Usually, the thermal response rate of solar arrays is rapid enough so that reasonable approximations of temperature can be obtained from the use of both the steady state and a transient analysis. The two equations to be used describe the heating as a function of time from the array entering sunlight from an eclipse, Equation (1), and the cooling of the array during eclipse. The cooling relation (assuming no planet input) is

$$T = \frac{1}{\left(T_o^{-3} + \frac{3A_t\bar{\epsilon}\,t}{W_c}\right)^{1/3}} \qquad (2)$$

where

T_o = temperature at start of eclipse

t = time after entering eclipse

W = array weight per unit area

c = specific heat of array

The temperature calculated from steady state conditions Equation (1) at start of eclipse is used as starting temperature T_o in Equation (2). Temperature-versus-time relation is then solved semi-graphically from generalized curves of the fundamental parameters in Equation (1).

Steady-state temperatures and end of eclipse temperatures for various Mars orbits and one Venus orbit have been analyzed and are presented in Table 3-2. The orbits are described in Table 3-3. Table 3-4 shows the predicted end of eclipse temperatures for the various orbits.

Table 3-2. Steady State Temperatures in Sun

Orbit	Position	Temperature (°F) AU 1.386	AU 1.540	AU 1.667	Estimated Error* (°F)	Planet
1A	Subsolar Terminator	67 35	50 12	39 0	±10	Mars
1B	Subsolar Terminator	67 35	50 12	39 0	±10	Mars
2A	Subsolar Terminator	60 30	40 8	28 -10	±10	Mars
2B	Subsolar Terminator	60 30	40 8	28 -10	±10	Mars
X	Subsolar Terminator		280** 225**		+10, -20 ±10	Venus

*Due to variation in surface finishes, proximity of vehicle to array, etc.

**AU = 0.72.

Table 3-3. Orbit Parameters

Orbit*	Period (min)	Altitude (km) Perigee	Apogee	Inclination (deg)	Eclipse
1A	456	1800	10,700	70	Full sun first 140 days
1B	456	1800	10,700	33	85 min. eclipse
2A	219	2300 circular polar		Polar	Full sun first 50 days
2B	219	2300 circular polar		33	45 min
3A	190	1800 circular		33	45 min
X*	138	2300 circular		0	37 min

*All orbits are around Mars except X (Venus).

Table 3-4. Transient Eclipse Temperatures

Orbit	Maximum Eclipse Time (hr)	Temperature Entering Eclipse (°F)	Temperature end of Eclipse (°F)
1A	1.42	0	-200
1B	1.42	0	-200
2A	0.75	-10	-160
2B	0.75	-10	-160
X	0.61	+225	-120

B. FLAT-PLATE SOLAR THERMOELECTRIC GENERATOR

The flat-plate solar thermoelectric generator has been developed to provide a low cost, high reliability power supply that would be directly applicable to space uses. The thermoelectric elements comprising the solar array are relatively insensitive to Van Allen radiation and, at contemplated operating temperatures, would exhibit a longevity equal to or better than photovoltaic cells. Since unconcentrated solar heat creates the temperature differential across the elements, an array must consist of many small elements within a large surface area in order to provide power at a realistic load voltage.

The development of such a system (Figure 3-10) has been pursued by the General Atomics Division, General Dynamics Corp., first as company-sponsored research and later under contract to the U.S. Air Force. Results of this work provide the only obtainable data relating to many phases of flat-plate thermoelectrics, including flight acceptance testing and orbital test data. This portion of the study, therefore, relates solely to the General Atomics (GA) flat-plate development effort. While it is understood that at least one other similar effort is in progress, insufficient information has been made available to permit its assessment or to consider the effort as competitive with the present state-of-the-art.

The parametric data relating thermoelectric characteristics to degradation, as found in Appendix A2, were derived from two principal sources. Where experimental values could be obtained from GA, these data are provided. Where information necessary to the development of this study was lacking, estimates based on the composite results of numerous thermoelectric generator programs were made. As future flight test data is generated and becomes available, revised values may be inserted into the flow diagram and computations updated accordingly.

1. Assumptions for Study

The data provided by this study and the conclusions drawn from it presuppose a competitive state of development between flat-plate solar thermoelectrics and other space power supplies. Furthermore, a continuing capability by GA to supply panels is assumed. Important considerations which have been ignored, including cost, fabrication time, and launch

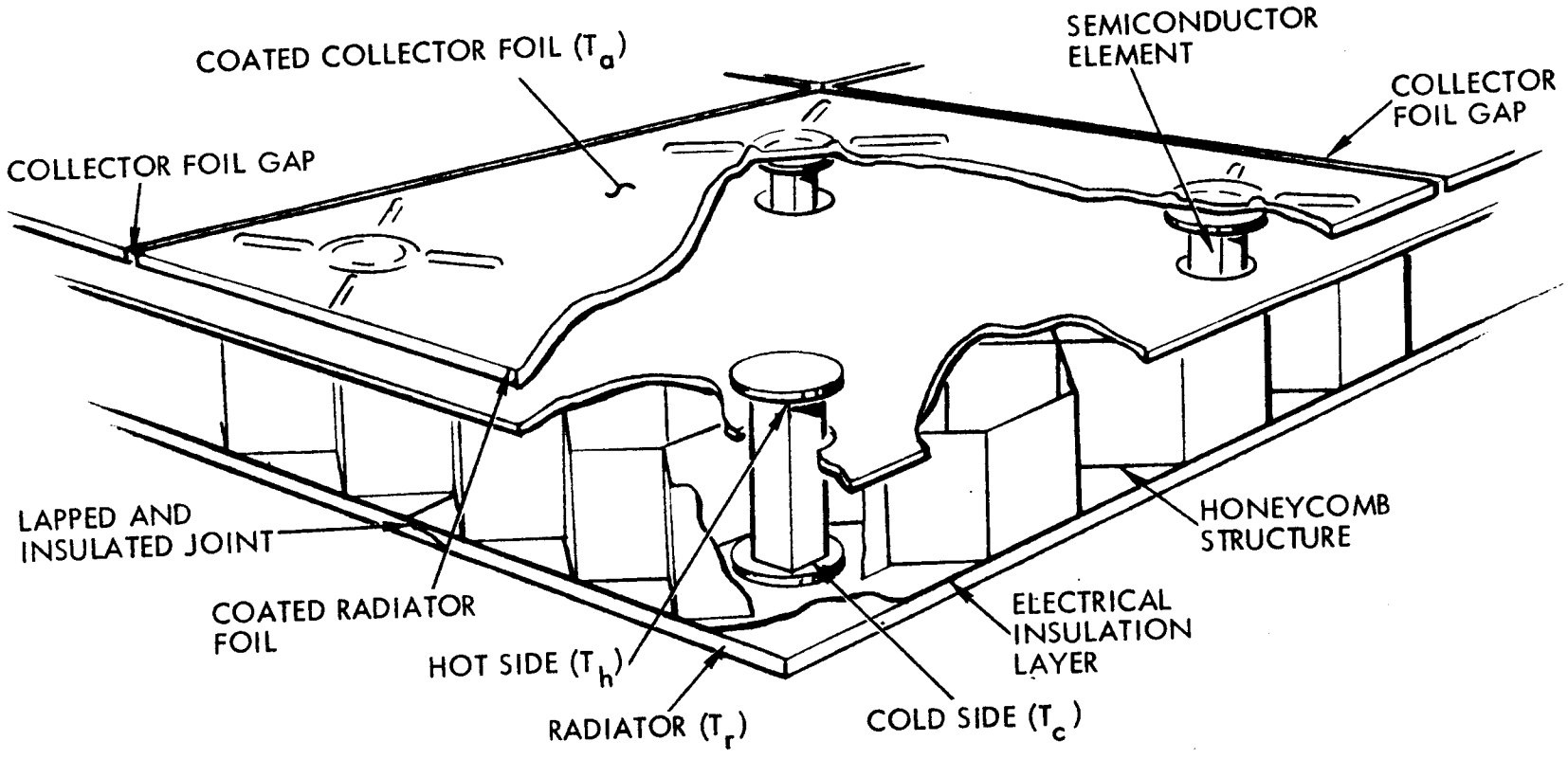

Figure 3-10. General Atomic Flat-Plate Solar Thermoelectric Module

vehicle compatibility, are also assumed competitive. Thus, this study is limited to a consideration of the thermodynamic and electrical characteristics to be expected from an array composed of GA-type thermoelectrics.

The sample calculations (Appendix B2) used to illustrate the usefulness of the flow diagram are predicated upon a hypothetical mission with the following general characteristics. A spacecraft will travel between Earth and Mars while maintaining a constant power level for housekeeping and transmission. On reaching the vicinity of Mars, the vehicle will orbit that planet, still maintaining a constant power output level for the designed life of the mission.

A flat-plate thermoelectric efficiency depends on solar intensity for energy conversion. Consequently, the distance from the sun as well as the array angle to the sun are determining factors in array performance. It has been assumed for this study that design power shall be deliverable to the end of mission life; therefore, excess power is potentially available from two sources. First, solar collector surface has been increased to compensate for the low solar intensity at Mars orbit. Secondly, the thermoelectric panel has been increased to compensate for degradations that will probably occur during mission life. Since these compensatory factors would tend to overpower the vehicle at any time before end of life, the following means has been assumed feasible to regulate on-board power. At any position closer than Mars orbit, solar intensity may be reduced at the collector by introducing a tilt error in the array as it faces the sun. In this way, heat input can be maintained at a Mars solar intensity of 0.050 watt/cm^2. At any time before end of life, if more than the design power is produced because of an excess of thermoelectric couples still operable, a variable resistive load may be employed to automatically maintain design power at the bus.

While the above regulatory techniques might not be attractive to either the contracting agency or the manufacturer, they have been introduced into this study to reconcile power conversion with a hypothetical mission. As such, they provide the means of overcoming degradation and insuring the delivery of design power throughout mission life.

2. Development of Design Computation Process

The process for flat-plate solar thermoelectric design computation has been prepared in three separate but related steps. The first step, Electrical-Thermal Characteristics per Couple, defines the power output in terms of voltage, current, and load resistance is a function of recommended temperature. The second step, Heat Balance and Panel Design, reconciles the heat flow through the module with thermocouple power output, permitting the collector-radiator surface area to be calculated. Modular weight per couple and, in turn, sizing of an array that would deliver the designed power, may then be determined. In the third step, Mission Influence on Panel Oversizing, various factors that contribute to power degradation with time and/or distance are factored into panel oversizing to yield design power at end of mission.

a. Electrical-Thermal Characteristics per Couple (Figure 3-11)

Performance data relating to element thermal conductivity, electrical resistivity, and Seebeck voltage vary as a function of temperature. Separate parametric data curves are supplied by the manufacturer for "n" and "p" elements of the matrix material selected for the thermoelements. Different dopants in the same matrix material require separate performance curves, and even varying percents of the same dopant will exhibit individual characteristics. Temperatures anticipated during the mission usually define the "n" and "p" elements to be employed. From these data, the electrical properties which may be exhibited by the flat-plate couple are calculable. The equations given will provide figure of merit, matching factor, voltage, current, and internal resistance at the temperature selected or recommended. These equations are based upon maximum power generation rather than matched impedance between source and load, since, with thermoelectricity, current is not independent of voltage. In turn, theoretical power (watts) per couple is determined. An independent check may be made by calculating theoretical power as a function of heat economy through the couple. The Peltier-Thompson effect, conducted heat, and Joule heating are used to calculate heat in and heat out of a couple. The difference between the two is that portion of heat converted to electricity. However, theoretical power is unrealistic and does not take into consideration the resistance encountered as current passes through

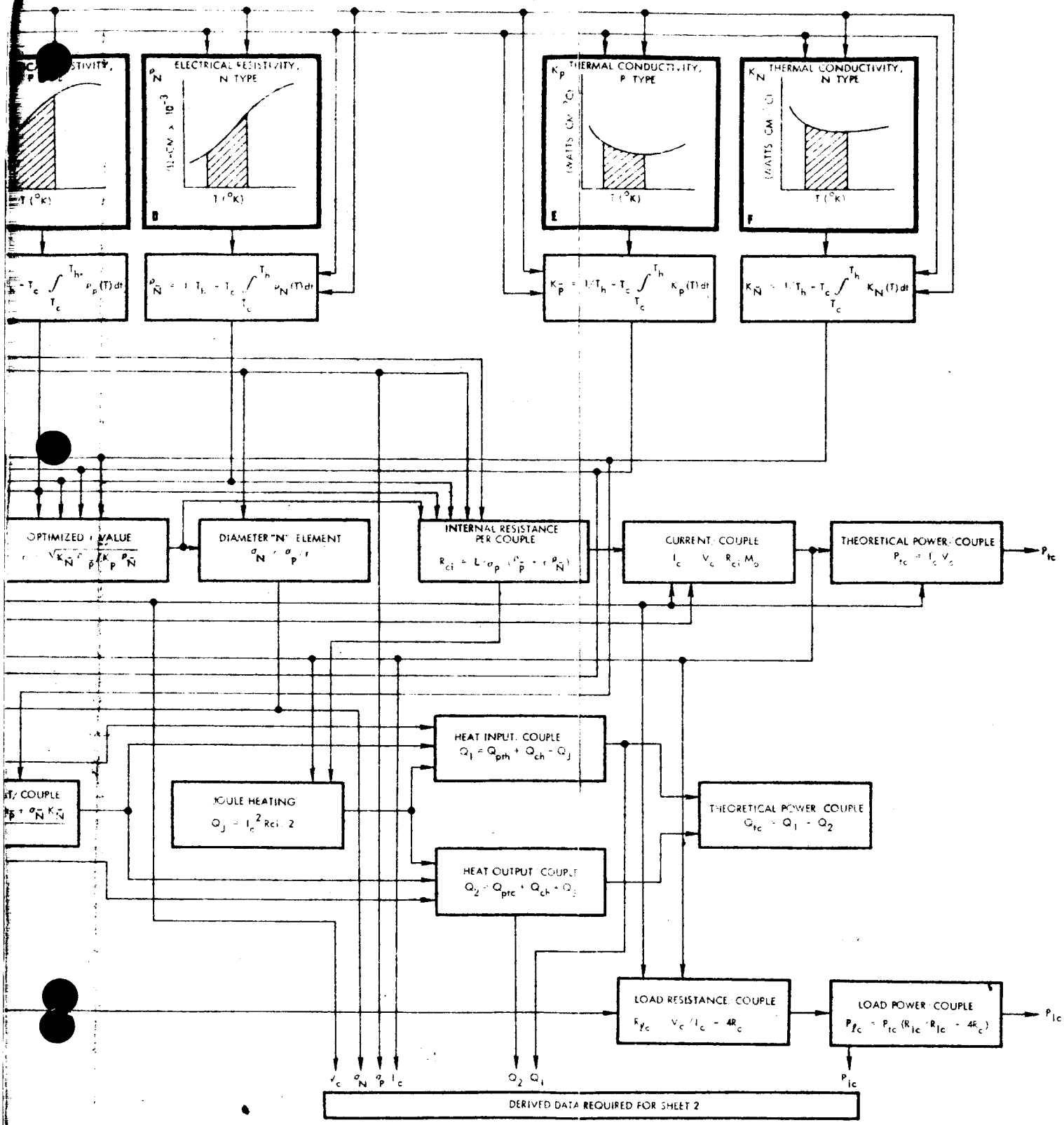

Figure 3-11. Flat-Plate Solar Thermoelectric Design Computation Flow Diagram — Couple Electrical-Thermal Characteristics

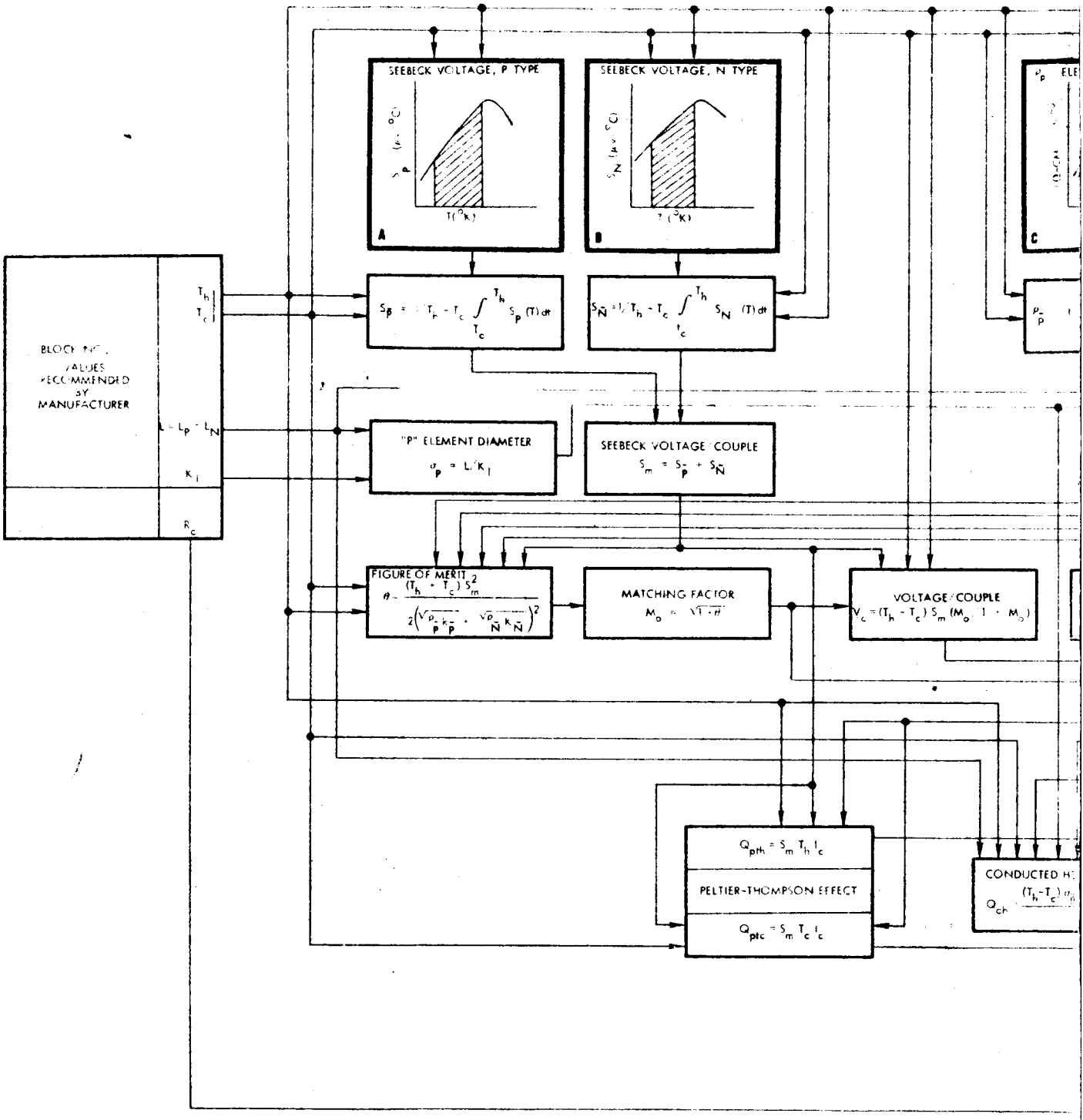
SEEBECK VOLTAGE, P TYPE
A
SEEBECK VOLTAGE, N TYPE
B
C
BLOCK NO. 1
VALUES RECOMMENDED BY MANUFACTURER
T_h
T_c
$L = L_p = L_N$
K_1
R_c
$S_{\bar{p}} = 1/(T_h - T_c) \int_{T_c}^{T_h} S_p(T)\,dT$
$S_{\bar{N}} = 1/(T_h - T_c) \int_{T_c}^{T_h} S_N(T)\,dT$
"P" ELEMENT DIAMETER
$\sigma_p = L/K_1$
SEEBECK VOLTAGE/COUPLE
$S_m = S_{\bar{p}} + S_{\bar{N}}$
FIGURE OF MERIT
$\theta = \frac{(T_h + T_c) S_m^2}{2\left(\sqrt{\rho_{\bar{p}} k_{\bar{p}}} + \sqrt{\rho_{\bar{N}} k_{\bar{N}}}\right)^2}$
MATCHING FACTOR
$M_o = \sqrt{1 + \theta}$
VOLTAGE/COUPLE
$V_c = (T_h - T_c) S_m (M_o - 1 + M_o)$
$Q_{pth} = S_m T_h I_c$
PELTIER-THOMPSON EFFECT
$Q_{ptc} = S_m T_c I_c$
CONDUCTED H

the elements and bonded shoes. To reconcile this power loss, the load resistance (per couple) must be calculated, and from this, load power. The sometimes gross difference between theoretical and load power has been a major obstacle in overall thermoelectric development in the United States. While thermoelectric element resistance is a fixed and intrinsic property of the material and dopant employed in element fabrication, this resistance can be only a small part of total couple resistance. The chief contributor is usually the contact resistance, usually initiating at the fused, brazed, soldered, etc., junction between the element and "shoe." Each element employs shoes at its hot and cold ends to provide the means of connecting elements to a common bus and thereby forming thermoelectric couples. Dissimilar expansion and contraction of element and shoe cause cracks that can increase the contact resistance from several milliohms to a complete open circuit, depending on the extent of damage. It is usually the p-type element bonds which exhibit the higher resistance, because these elements are more brittle.

In calculating the theoretical power of a couple by means of heat flow (Appendix B2), the following phenomena must be considered. At the heat absorber, a part of the solar energy spectrum is reflected back to space. That which is absorbed on the surface is further reduced by reradiation to space. The remainder flows through the flat-plate cross section, but not necessarily through the elements. However, this calculation is concerned solely with the portion of heat that does flow through the elements. At both the hot and cold ends, the Peltier-Thompson effect manifests itself. This tends to cool the hot junction and warm the cold junction, reducing the temperature differential and, consequently, the voltage. In addition, Joule heating, a somewhat less detrimental effect, is the result of reconversion of electricity back into heat. While this effect occurs uniformly throughout the length of the element and does not affect the Seebeck voltage, it does constitute a waste of converted electrical energy. The preponderance of heat flows through the elements, contributing nothing to power production. The quantity of heat conducted through is greatest at lower temperatures, where the thermal conductivity is the highest. This is why thermoelectric efficiency increases with operating temperatures, through a constant differential.

Having calculated the foregoing losses, the heat into and the heat out of a couple may be determined, with the difference being equal to the theoretical power of the couple. In determining load power from load resistance, the manufacturer usually provides a resistance per couple, or else per contact. A typical input is employed in the sample calculation, where the contact resistance per shoe is taken to be 5 percent of internal resistance per couple. This represents a best value that may later be increased by array operation. Since there are four such contact joints per couple, the unit contact resistance must be increased fourfold for calculation purposes.

b. Heat Balance and Panel Design (Figure 3-12)

Thermoelectric characteristics leading to load power determination per couple were predicated upon recommended working temperatures across the "n" and "p" elements. Calculations are aimed at a verification of the realism of selected operating temperatures and, based upon them, determining an absorber/radiator area compatible with the solar input. To accomplish this, one must examine the factors governing the thermodynamic balance existing through the cross section of a couple module. Such a module consists of (1) the heat absorber, (2) a thermocouple, (3) the internal structural support honeycomb, and (4) the heat radiator. The absorptivities, emissivities and thermal conductivities of these components regulate heat flow and, hence, temperature. A collector area is then determined, based upon assumed hot and cold operating temperatures. From this area, the "Q" through the components is determined. Validity of the assumed temperature is verified by a recalculation of radiator temperature, based upon the recently calculated modular area. If both the assumed and calculated radiator temperatures agree (within 1 degree), then the module (as defined) is both realistic and feasible. However, if a discrepancy is found to exist between T_R and T'_R, then iterative recalculation becomes necessary. The latter value of radiator temperature is taken to be the more correct, and, retaining the assumed collector temperature, a new T_c value is introduced into the first step (Electrical-Thermal Characteristics per Couple) of the calculation process and the entire calculation remade. Obviously, each recalculation may change the electrical properties of the couple as well as the required modular collector area.

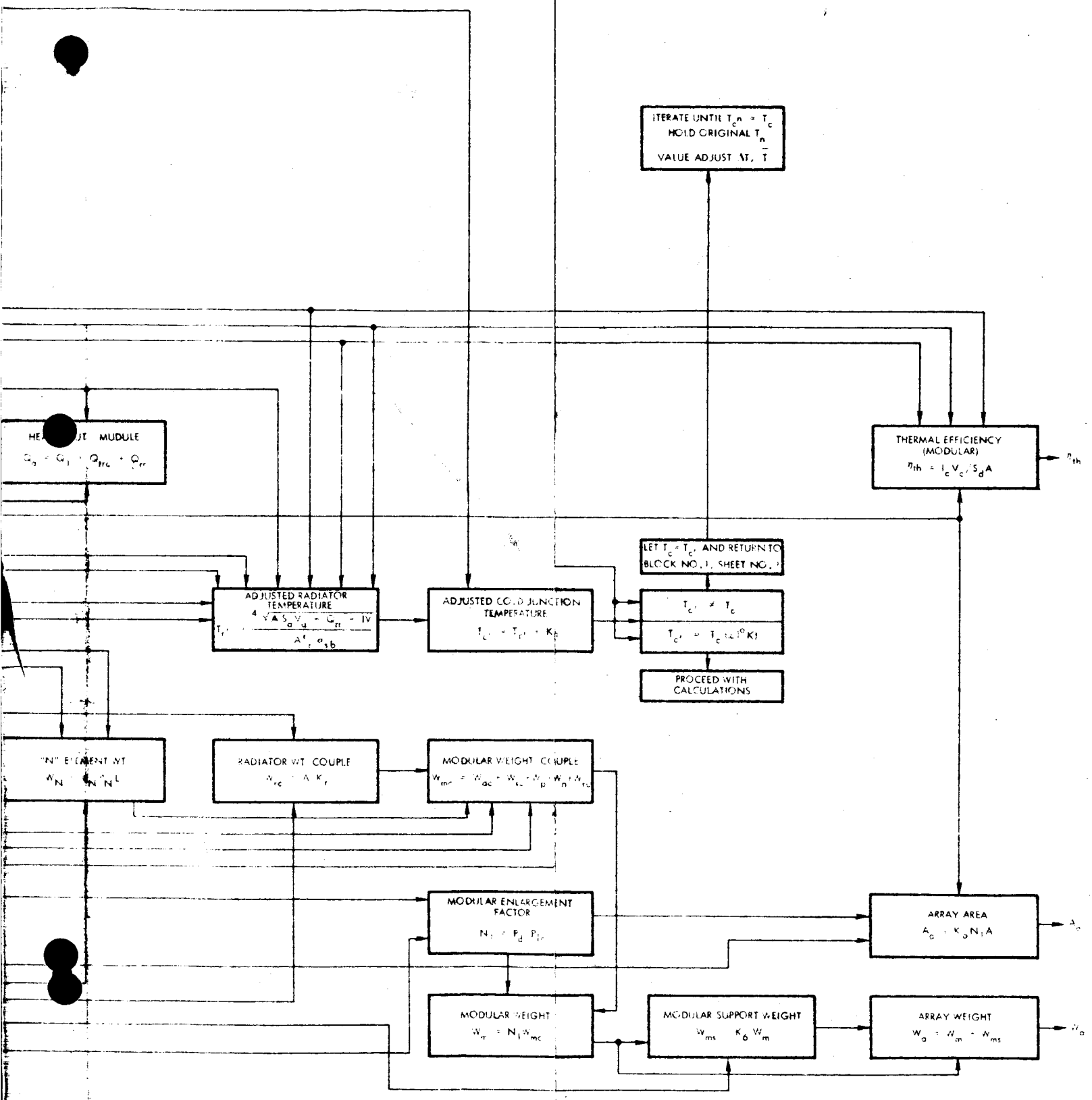

Figure 3-12. Flat-Plate Solar Thermoelectric Design Computation Flow Diagram — Heat Balance and Panel Design

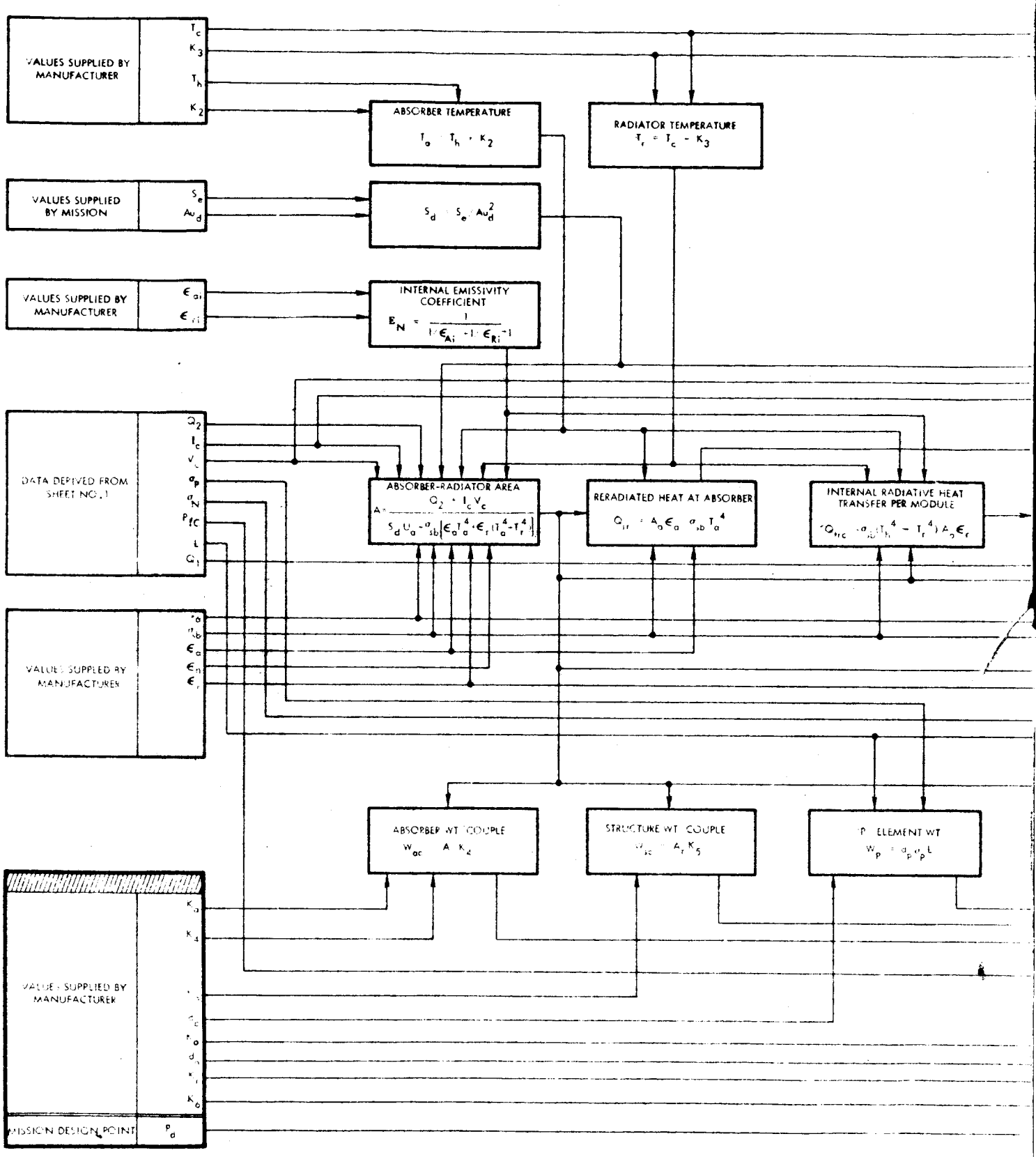
VALUES SUPPLIED BY MANUFACTURER
T_c
K_3
T_h
K_2
ABSORBER TEMPERATURE
$T_a = T_h + K_2$
RADIATOR TEMPERATURE
$T_r = T_c - K_3$
VALUES SUPPLIED BY MISSION
S_e
Au_d
$S_d = S_e / Au_d^2$
VALUES SUPPLIED BY MANUFACTURER
ϵ_{ai}
ϵ_{ri}
INTERNAL EMISSIVITY COEFFICIENT
$\epsilon_N = \frac{1}{1/\epsilon_{Ai} - 1 + 1/\epsilon_{Ri} - 1}$
DATA DERIVED FROM SHEET NO. 1
Q_2
I_c
V_c
σ_p
σ_N
P_{fc}
L
Q_1
ABSORBER-RADIATOR AREA
$A = \frac{Q_2 + I_c V_c}{S_d U_a - \sigma_{sb}[\epsilon_a T_a^4 + \epsilon_r (T_a^4 - T_r^4)]}$
RERADIATED HEAT AT ABSORBER
$Q_{ir} = A_a \epsilon_a \sigma_{sb} T_a^4$
INTERNAL RADIATIVE HEAT TRANSFER PER MODULE
$Q_{irc} = \sigma_{sb}(T_h^4 - T_r^4) A_a \epsilon_r$
VALUES SUPPLIED BY MANUFACTURER
σ_a
σ_b
ϵ_a
ϵ_n
ϵ_r
ABSORBER WT COUPLE
$W_{ac} = A K_4$
STRUCTURE WT COUPLE
$W_{sc} = A_r K_5$
P ELEMENT WT
$W_p = \sigma_p \sigma_p L$
VALUES SUPPLIED BY MANUFACTURER
K_a
K_4
σ_c
K_6
MISSION DESIGN POINT
P_d

When agreement is reached on the radiator temperature, the modular thermal conversion efficiency may be calculated. This value expresses electricity generated as a function of all heat seen by the module, including that portion which was reflected and reradiated at the absorber. This method of expression is preferred over one limited to heat passed into a couple, as it permits a judgement of the flyable system rather than a laboratory-measured thermocouple.

Having defined the area of a one-couple module, its weight is next determined. To do this, individual component weights are determined, based upon manufacturer supplied values. These are then added to obtain a modular weight, per couple. The modular enlargement factor or number of such couples required to provide the designed power is calculated from load power per couple and designed power value. If one then multiplies the module weight and area in turn by this enlargement factor, panel characteristics are obtained. However, to fly such a panel, structural support and an unfolding mechanism are required. They do not contribute to array sizing but do increase array weight. This weight increase will be provided by the manufacturer and has been represented by a percent of increase in panel weight.

c. Mission Influence on Panel Oversizing (Figure 3-13)

The flat-plate thermoelectric array designed in the preceding step could supply the designed power if no degradation occurred during the mission life. The design also neglects such factors as pointing angle error and meteorite damage. The present state of development of this power supply has not included an assessment of many modes of degradation; the state-of-the-art understanding may not have defined all kinds of degradation. However, based upon data made available from the GA study as well as other thermoelectric generator programs, the following effects have been included in oversizing:

1) Degradation Due to Thrusting. The shock and vibration which accompany lift-off and continue throughout powered flight may exert a detrimental effect upon the thermoelectric bonds. This will manifest itself as an increase in load resistance and could reduce voltage if "opens" occurred in element bonded joints. While lead telluride-type thermoelectric elements exhibit high (10^4 psi) compressive load strengths, they are quite sensitive to shear forces. The "p" materials are usually several times

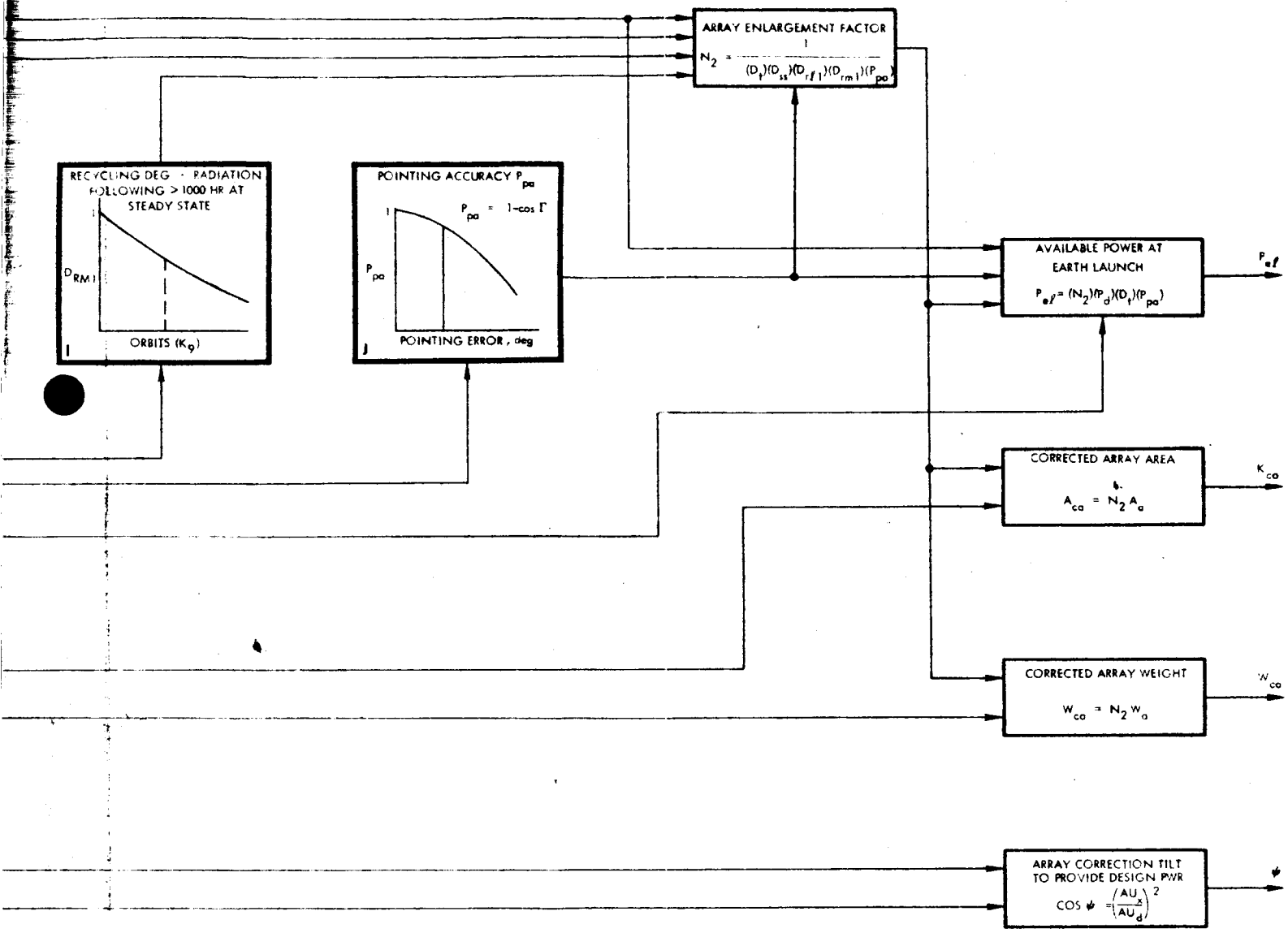

Figure 3-13. Flat-Plate Solar Thermoelectric Design Computation Flow Diagram — Mission Influence on Panel Oversiging

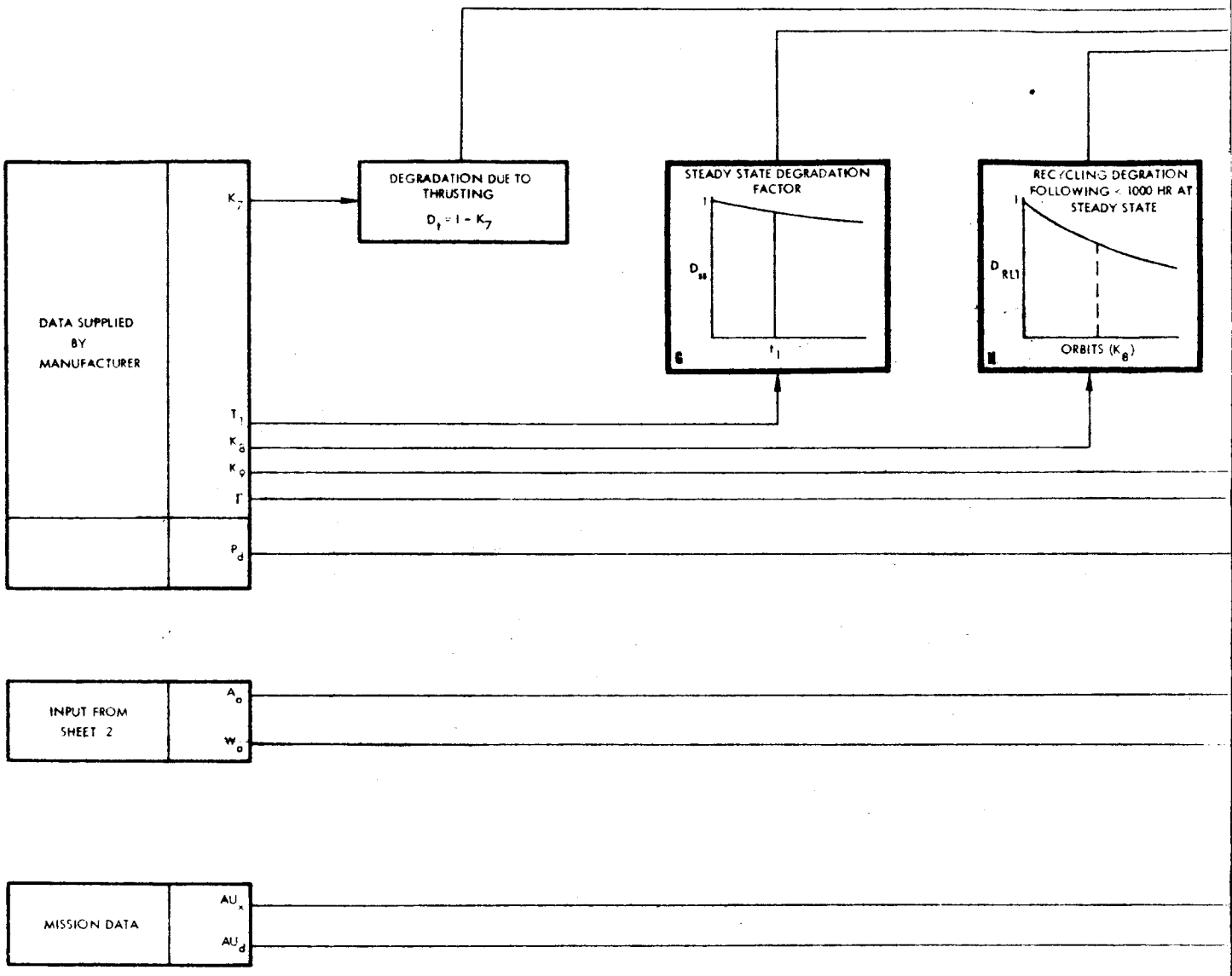
DATA SUPPLIED BY MANUFACTURER
K_7
T_1
K_8
K_9
Γ
P_d
DEGRADATION DUE TO THRUSTING
$D_t = 1 - K_7$
STEADY STATE DEGRADATION FACTOR
1
D_{ss}
t_1
G
RECYCLING DEGRATION FOLLOWING < 1000 HR AT STEADY STATE
1
D_{RL1}
ORBITS (K_8)
H
INPUT FROM SHEET 2
A_a
W_a
MISSION DATA
AU_x
AU_d

more fragile than the "n" materials. For this reason, folded panel position would be most critical aboard a launch vehicle. Preflight acceptance tests by the manufacturer have provided combined effect data on shock and vibration in various planes which has been interpreted as a constant for this mission.

2) Steady-State Degradation. It has been demonstrated by every extensive testing program that thermoelectric materials have a finite life expectancy even under the most controlled operating conditions. This gradual reduction in power per couple may be attributed to (a) dopant migration within an element, (b) dopant volatilization out of an element, (c) grain growth, (d) poisoning and perhaps several phenomena not yet observed. It is imprudent to estimate life by extrapolating a short-term test period or by testing under other than true environmental conditions. Valid conclusions can only be drawn from tests which approximate the anticipated mission time and approximate mission environment. Lacking such data for this study, the effect of steady-state operation can only be approximated as 2 percent per 1000 hours of operation. A graphic representation of this effect is shown in Figure A2-7.

3) Thermal Cycling (after $< 10^3$ hours steady-state operation). Because cast-formed thermoelectric elements fracture more easily, lead telluride-type elements are usually made by pressing and sintering. This more finely grained and randomly oriented crystal structure better resists cracking from mechanical or thermal stresses. It has been reported that if thermocouples are recycled continually, the effect of cycling is a negligible one, provided low hot junction temperatures are maintained. If recycling is performed after less than 1000 hours of steady-state operation, the effect on degradation is still small, although measurable. Apparently, insufficient time would have elapsed for grain growth to become critical; then, with the initiation of thermal cycling, further growth is arrested. Here again, 1000 hours is considered a safe interval, provided operating temperatures of the thermocouples have been kept below 300°C. Crystal growth is a function of time and temperature. For a hypothetical Mars mission, this situation is not indicative, since journey time between Earth and Mars would be in excess of 200 days. However, a degradation plot is shown in Figure A2-8 for future consideration.

4) Thermal Cycling (after $> 10^3$ hours steady-state operation). The crystal growth described above will, if allowed to progress beyond 1000 hours, constitute a real detriment to reliability. Although insufficient information has been made available to accurately assess this effect for the purpose of this study, it has been assumed to be double that discussed in the preceding paragraph. Based upon this assumption, a graphic degradation, with time at recycling temperature, is shown in Figure A2-9.

It is this curve that is employed for the Mars mission calculation in Appendix B2. The assumed degradation here is 4 percent per 100 thermal cycles (Mars orbits).

5) Sun Pointing Accuracy. The flat-plate thermoelectric panel area, as calculated in the second step (Heat Balance and Panel Design), is predicated upon the panel being normal to the sun. Therefore, the total array size and weight also depend upon perfect sun alignment. However, it is not within present state-of-the-art capability to guarantee such accuracy. For this reason, a diminution in solar input must be understood to be present. If we assume an accuracy comparable to that designed into the Orbiting Geophysical Observatory satellite, then an error of only ±3 degrees will exist. From the graphic interpretation seen in the appendix, it follows that such error would reduce solar intensity to 0.9985 that expected. Since such an error is actually less than the error in the solar constant, it loses significance from panel sizing calculations. However, malfunction of attitude control resulting in a 14-degree error would depress solar intensity by 3 percent. A graphic representation of this effect is shown in Figure A2-10.

If each of the above described degradations is expressed in decimal form (subtracted form unity), then multiplied together and divided into unity, the mission enlargement factor may be calculated. This new constant, when multiplied by array weight and area, will yield the flat-plate thermoelectric generator required for a Mars mission. It follows that, with the built-in array enlargement to provide design power at end of mission, there will be an excess of power generated at any time, t, earlier than end of mission. During the Earth-to-Mars flight, excess power may be reduced by introducing a tilt in the designed declination angle. Then, as the panel is gradually brought to the perpendicular at Mars orbit, a constant wattage is delivered. This same procedure may be followed should flight conditions result in a less-than-expected degradation of power with time. Alternatively, a variable resistive load can be used to dissipate other than design power. It must be remembered that any panel declination which causes a change in collector temperature will initiate a totally different and not necessarily desirable change in thermoelectric efficiency and/or longevity of the generator.

C. SOLAR THERMIONIC SOURCES

Solar thermionic energy conversion systems have been under study and development for almost a decade, with the achievement of an efficient, radiation-resistant, high density source as the goal. Although this method of energy conversion is not competitive with the photovoltaic process at the present time, it remains a promising approach. Life tests on solar thermionic converters are now extending into the thousands of hours. It is expected that their feasibility for long duration missions will be demonstrated soon.

Many features required for a solar thermionic energy conversion system have yet to be developed. These include such items as deployment mechanisms for multi-collector systems, orientation controls, and solar heat flux or cavity temperature controls. The converters themselves have not been produced with the efficiencies predicted in the laboratory. The concentrators or mirrors required have not been made with specific weights low enough to keep system weights competitive with other sources. Because of this incomplete state of development, any study attempting to provide system design data must be based on numerous arbitrary assumptions. The assumptions made during this study are summarized later in this report.

At the beginning of this study, the following goals were established:

1) Collect state-of-the-art information concerning the system and its elements.

2) Devise a logical method for using state-of-the-art information to perform preliminary design of solar thermionic energy conversion systems for various missions.

3) Demonstrate the use of the data and design methods developed with typical mission requirements.

4) Point out areas where problems exist or where more data is required.

Included in this report are a summary of the state-of-the-art information obtained, a description of the solar thermionic conversion technique, a summary of the assumptions made to facilitate the design study, a detailed description of the design computation process developed,

a. TRW/EMD Program

Applied research work on cesium thermionic converters and cavity-type solar generators is being performed at the Electromechanical Division of Thompson Ramo Wooldridge Inc. under USAF sponsorship. The current program has three phases:

Phase I,	Continued solar testing of the cubical cavity generator (CCG)
Phase II,	Sustained performance testing of advanced converters
Phase III,	Advanced generator design

Phase I has been completed with solar tests of the CCG at the JPL test site at Table Mountain, California. Under Phase II, the Series 2B converter design has been modified and the new design designated as Series 300. These modified converters are intended to operate for 2000 hours on both a continuous and cyclic basis. The Series 2B converters had all failed in less than 600 hours because of cracks that developed in the nickel tubulation connecting the collector to the cesium reservoir.

The performance characteristics of two typical converters tested are shown in Figure 3-14. The solid curves are for a Series 2B life test unit and the broken curves are for a Series 300 prototype unit. These converters were manufactured by Thermo Electron Engineering Corporation under subcontract to TRW/EMD. The data was taken from References 3-23 and 3-25. At the design point emitter temperature of 2000°K, the maximum power output of Converter 301 was 28 watts at 0.5 volts, or 9.1 watts/cm^2. No data on efficiencies is available for these converter tests. Figure 3-15, however, shows a curve of the maximum efficiency obtainable with state-of-the-art converters of this type, as a function of emitter temperature as given in Reference 3-25.

The latest solar tests of the CCG were conducted at Table Mountain in 1963. Solar flux levels between 80 and 100 watts/ft^2 were available at the time of the test. The generator was mounted within a vacuum chamber and heated by a 5-foot diameter parabolic concentrator. Three types of tests were performed: (1) optimization runs at various flux levels, (2) misorientation tests, and (3) cyclic and transient response tests.

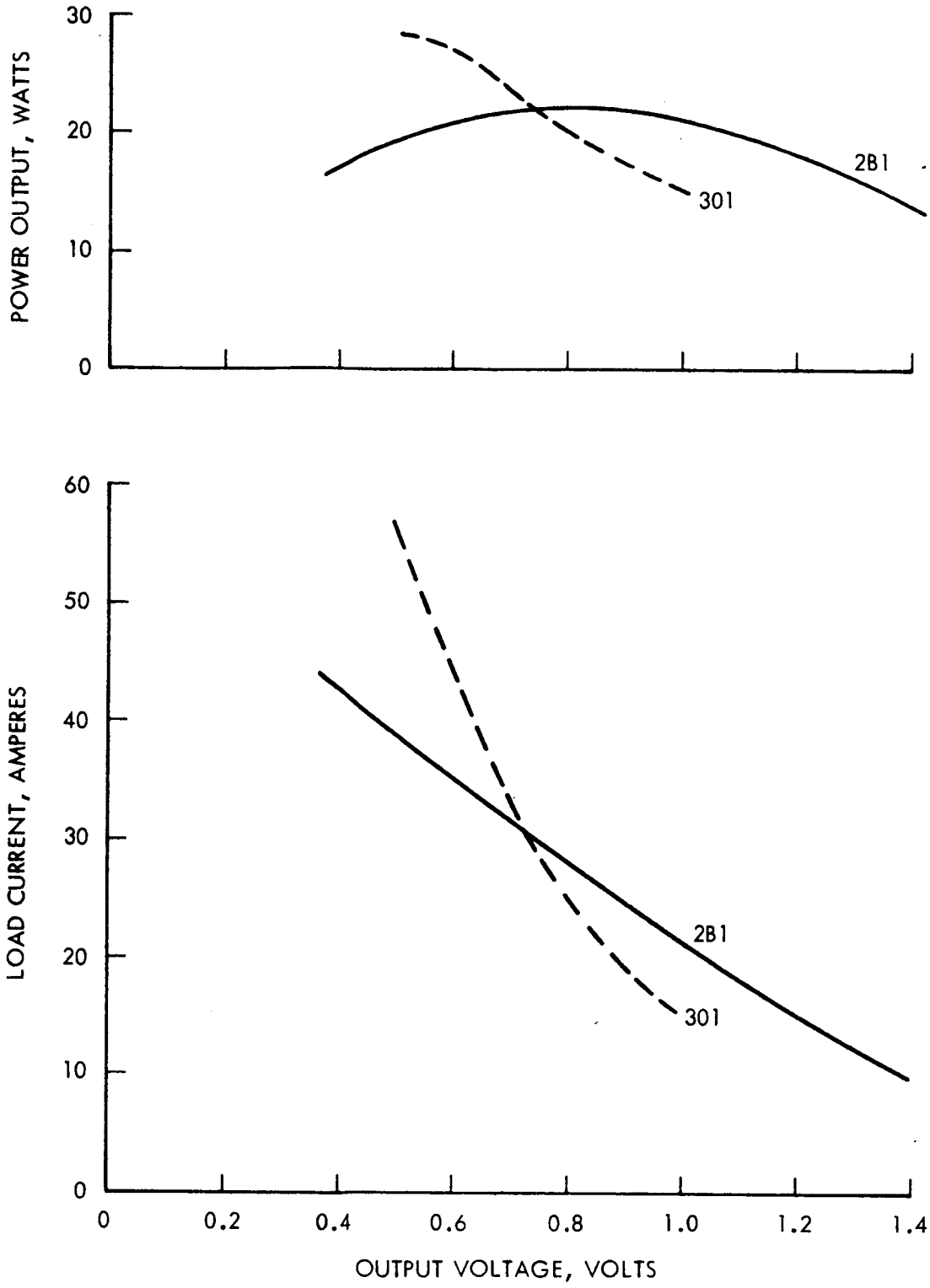

Figure 3-14. Typical CCG Converter Performance at 2000°K Emitter Temperature, 3.08 Cm^2 Emitter Area, and 2 Mils Spacing (References 3-23 and 3-25)

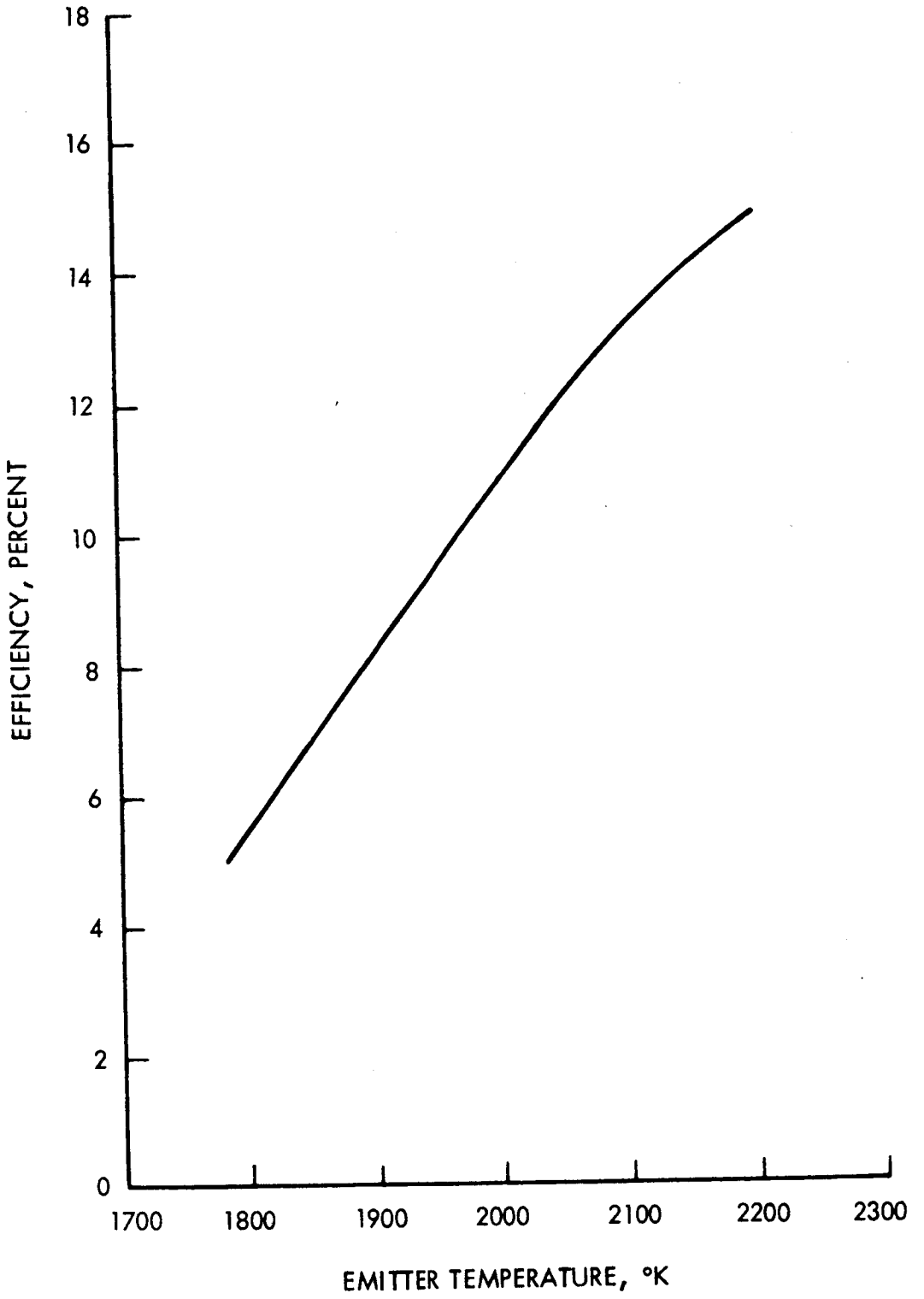

Figure 3-15. Maximum Obtainable Efficiency With State-of-the-Art CCG Converters (Reference 3-25)

The data obtained during the optimization runs were for steady-state operation with constant solar power inputs. As in other programs, the flux distribution within the cavity was not uniform with the converter opposite the aperture contributing little or no output. The five-converter configuration may not be workable and may have to be modified for future designs.

The variation in maximum generator output with incident solar flux is shown in Figure 3-16. At the highest flux level of 97 watts/ft^2, the maximum power of 35 watts was obtained at 2 volts. Emitter temperature was estimated to be between 1800 and 1850°K at this condition.

The results of the misorientation tests showed that orientation errors of 5 to 7 minutes led to a degradation in generator output of approximately 10 percent and errors of 15 minutes led to a degradation of over 50 percent. These results are for a particular aperture size in earth sunlight and general conclusions cannot be drawn from them except to indicate the precision of the orientation required for high temperature solar thermionic systems.

Thermal response tests performed indicated that without auxiliary cesium reservoir heating or other means of temperature control warm-up times of 25 minutes are required to reach 90 percent of steady state power output. TRW/EMD claims this period can be reduced to 2 to 3 minutes if cesium reservoir temperatures are maintained by electrical heating. This improvement has not been demonstrated yet.

The average performance characteristics of converters of the CCG type are shown as a function of emitter temperature in Figures 3-17 and 3-18. These curves are based on the data of Reference 3-25 and represent the average converter performance deduced from generator tests. Figure 3-19 shows the performance of a five-converter generator as a function of emitter temperature, with the converters connected in series to a total output voltage of 3 volts. The maximum generator efficiency of 7.5 percent represents the current state-of-the-art in multiconverter solar thermionic generators.

TRW/EMD has developed concentrators along with this program. Orientation controls have been developed to some degree and concepts for electrical and thermal control, structures, and deployment mechanisms have been formulated.

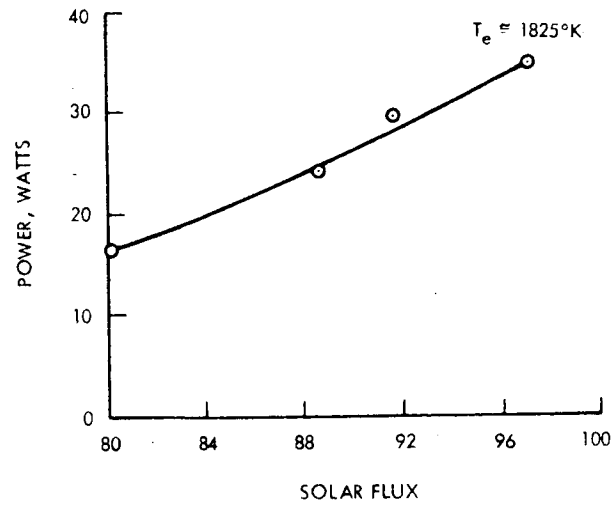

Figure 3-16. Solar Test Data, Five-Converter CCG (One Passive Converter), Optimized Generator Output Versus Solar Intensity (Reference 3-23)

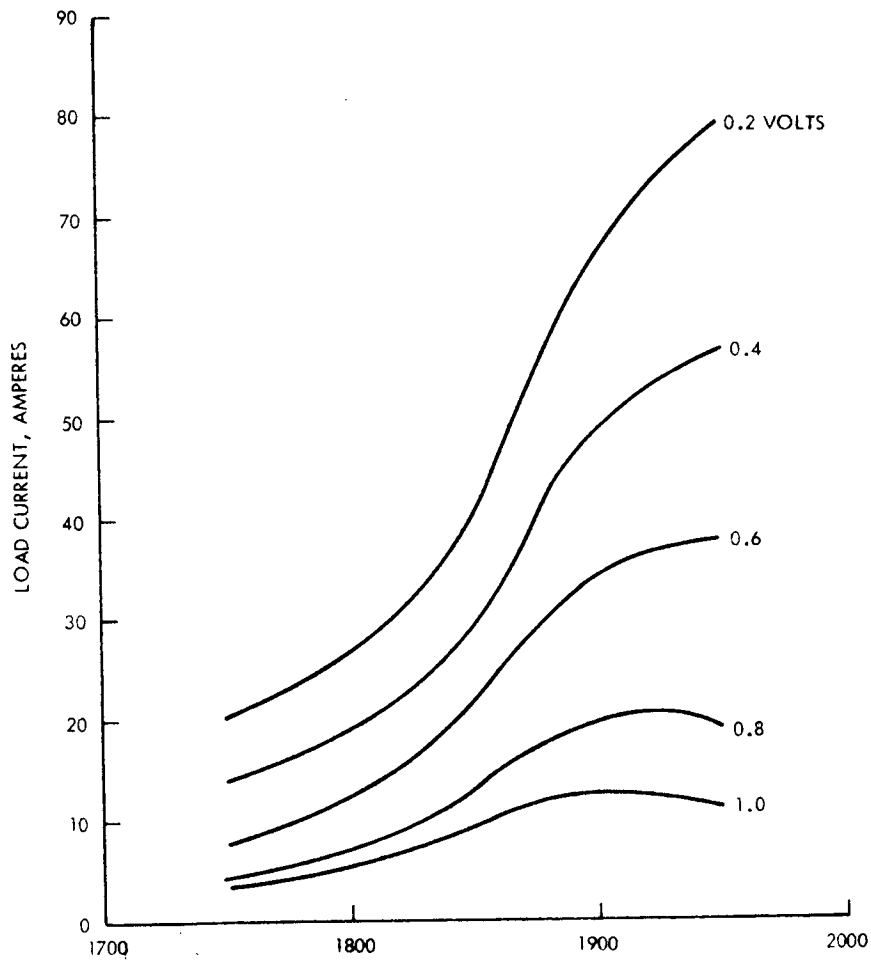

Figure 3-17. CCG Test Data, Average Converter Load Current Versus Emitter Temperature (Figure 16 of Reference 3-25)

One-piece parabolic concentrators up to 5 feet in diameter with a 60-degree rim angle have been fabricated with an electroformed nickel process (Reference 3-32). These concentrators have been used for solar testing. Surface reflectivities of up to 0.90 have been achieved and overall concentrator efficiencies (gross heat available to cavity) from 84 percent to 95 percent have been measured. The electroformed nickel concentrators of this size have a specific weight of approximately 1.0 lb/ft^2, including a torus rim for stiffening. TRW/EMD also has done some work on similar concentrators constructed of stretch-formed aluminum which promise a specific weight of approximately 0.5 lb/ft^2 in similar sizes.

TRW/EMD has done some work on a bimetallic, heliotropic mount for the concentrator which can be used for fine positioning (less than 5-degrees)(Reference 3-19). The pointing accuracy of the device was tested sufficiently to demonstrate its feasibility for thermionic systems, but the device has not been demonstrated as part of a working system. An orientation system designed for ground testing has been built with pointing accuracy between 2 and 6 minutes of arc.

Thermal control as proposed by TRW/EMD would not include thermal storage and would allow thermal cycling of the converters (Reference 3-20 and 3-23). Electrical heating is proposed to maintain cesium reservoir temperatures at operating levels so that warm-up time is minimized (2 to 3 minutes). A parasitic load is proposed for electrical control of the source. The load would be used to limit generator voltage to values that would not allow emitter temperatures to go above design levels. An input or solar flux control that works like an iris between the concentrator and the absorber has been considered by TRW/EMD in Reference 3-36.

TRW/EMD has performed a preliminary design, as described in Reference 3-20. This design is for a 1500-watt solar thermionic power system using 18 five-foot diameter concentrators. Some consideration was given to structures and deployment mechanisms. Similar concepts are also given in Reference 3-37. The concentrator-generator units are stacked in clusters and deployed in rows supported by expandable arms, with the rows of units supported by a tower-like structure attached to the spacecraft.

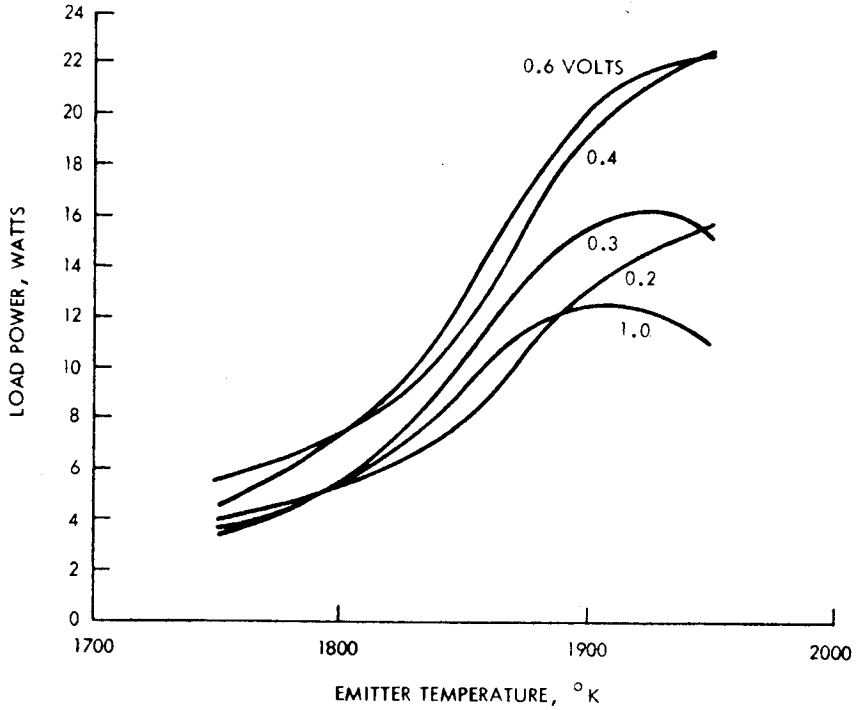

Figure 3-18. CCG Test Data, Average Converter Power Versus Emitter Temperature (Figure 16 of Reference 3-25)

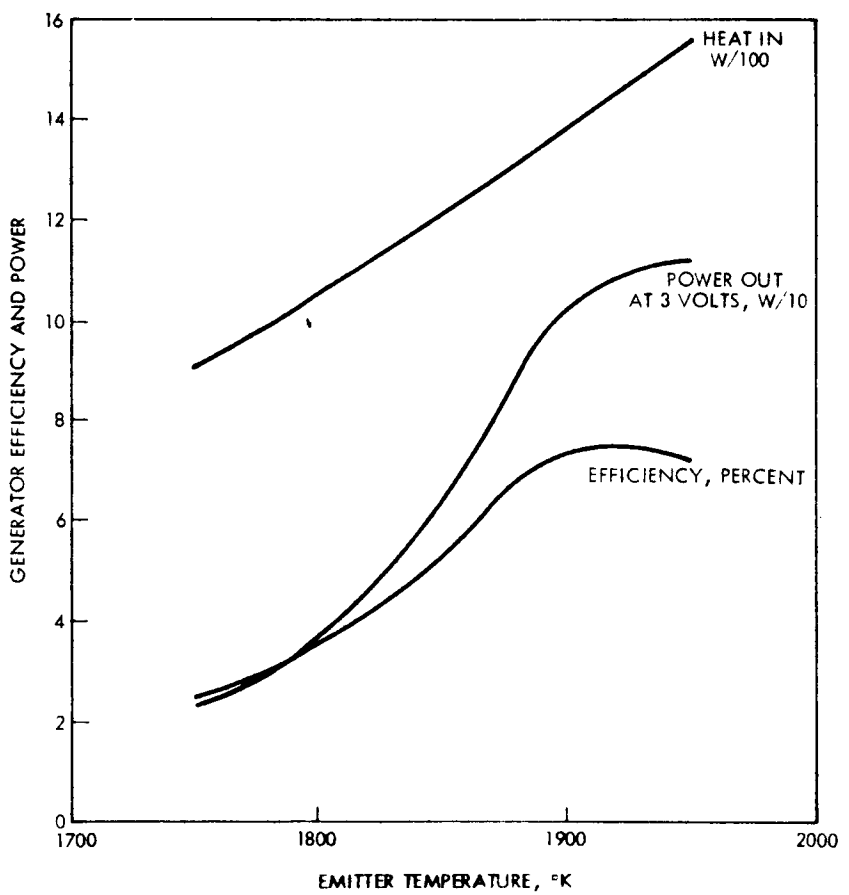

Figure 3-19. Generator Performance Versus Emitter Temperature (Five Converters, 3 Volts)

b. GE/MSD Program

The General Electric Company Missile and Space Division performed work on solar thermionic systems during the original Solar Thermionic Electric Power System (STEPS) Program, which was based on a vacuum diode converter. The performance of these converters was so poor that they were abandoned and the program redirected to cesium vapor type converters. The average conversion efficiency of a generator equipped with vacuum converters was found to be around 2.5 percent.

The Gavity Vapor Generator (CVG) Program was initiated to demonstrate the feasibility of operating three vapor type converters connected in series, with solar heating. The objectives for the converters were: 14 percent converter efficiency in the emitter temperature range from 1400 to 1850°K. The results of solar testing of the CVG system are reported in References 3-19 and 3-22, giving data obtained in December 1962. Reference 3-22 also presents the plans for the STEPS III system and the expected performance with improved vapor converters.

The CVG consists of three cesium vapor converters with planar geometry and molybdenum electrodes positioned radially around the cavity axis. Tantalum cathode shoes are welded to the emitters. Each emitter has an area of 3 cm^2. The interelectrode spacing is in the vicinity of 9 mils (Reference 3-22).

At the design point (emitter temperatures of 1380°C or 1653°K, performance tests on a typical engineering model converter, No. 45, showed a maximum power output of 6.2 watts at 27 amps and 0.23 volts (Reference 3-23). An efficiency of 6.5 percent is quoted in Reference 3-28 for this temperature.

The performance of the three-converter CVG with solar heat input is shown in Figure 3-20 for two levels of emitter temperature, 1673°K and 1773°K. These are steady-state operation data obtained with optimized cesium reservoir temperatures. The generator efficiencies (ratio of electrical power to thermal power entering the cavity) quoted in Reference 3-19 for these two temperatures are 1.68 percent and 1.44 percent, respectively. The highest output reported (as of December 1962) is 25.5 watts at 1.55

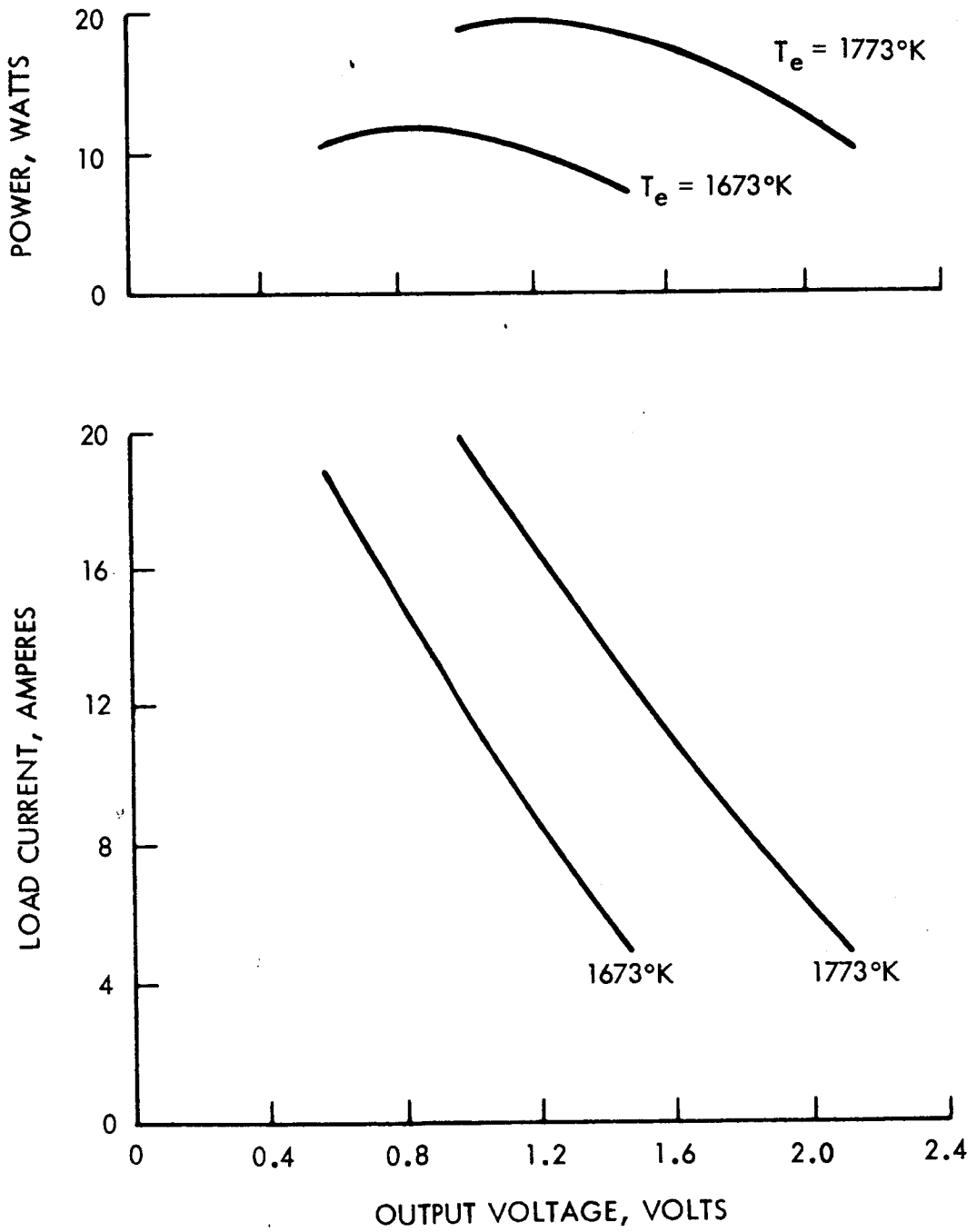

Figure 3-20. Solar Test Data for General Electric, Three-Converter Cavity Vapor Generator (Run No. 15 of Reference 3-19)

volts and 1900°K average emitter temperature. A 5-foot diameter concentrator was used for these tests. The solar flux intensity at the Phoenix, Arizona, test site varied between 80 and 90 watts per square foot.

The improved converters for the STEPS III system are expected to result in higher power output and conversion efficiency compared to the CVG converters. The spacing between electrodes will be reduced to between 2 and 5 mils. Converter efficiency is expected to approach 9 percent at 1850°K emitter temperature, with an output of about 50 watts from a three-converter generator.

The original STEPS Program resulted in the development of a large segmented collector which was designed to develop temperatures in the 1000°K range for vacuum converters. For the CVG program, a 5-foot diameter searchlight mirror with a 60-degree rim angle was coated with a high reflectivity coating (Reference 3-21). A reflectivity approaching 0.92 was measured. Surface accuracy was found to be within 0.125 degrees for 90 percent of the minor surface, which was good enough to obtain the desired temperatures. A great deal of solar testing was performed with this collector. The resulting data provides the most complete source of information published on concentrator absorber efficiencies and the effects of misorientation, etc.

During the STEPS Program, a sun-pointing system of orientation control was developed for solar testing (Reference 3-35). The equipment demonstrated accuracy sufficient for this type of device, with zero measureable error maintained for significant periods. The equipment was not made up of flight type hardware but the sensors and scheme of operation could be used in flight. A louver-type arrangement outside the concentrator (Reference 3-22) was used to control solar flux input to the cavity. No description of flight type flux or temperature controls is available. No work has been reported on flight type supporting structure, deployment mechanisms, and other accessories associated with a system of this type. An attempt was made to develop thermal storage techniques but it was unsuccessful (Reference 3-22).

c. JPL/EOS Program

The Solar Energy Thermionic Conversion Program (SET) was undertaken by the Caltech Jet Propulsion Laboratory for the National Aeronautics and Space Administration, with Electro-Optical Systems Inc. as the prime contractor for JPL. The program included tests and work on flight type hardware.

Converters of the planar electrode configuration were fabricated by several manufacturers to meet the specific requirements of the SET Program. The SET IB configuration incorporates a 5-foot diameter solar concentrator and a five-converter generator mounted at the focus. SET II, an advanced configuration, will use a 9.5-foot diameter mirror and will be designed to provide approximately 500 watts output in the vicinity of Mars. The data described was supplied by JPL in Reference 3-30. The data was obtained under steady-state conditions with electrical heating. Most of the data is for the design point emitter temperature of 1973°K, with the cesium pressure optimized at each operating point.

The performance characteristics of several converters of Type A (TEECO) are shown in Figure 3-21. Most of these converters used tantalum electrodes with a 2-mil spacing. The observed efficiency was 8.5 to 9 percent at a corrected emitter temperature of 1973°K. Variations in the interelectrode spacing are believed to be the cause for the spread in power outputs, which range from 3 to 8 watts/cm^2 at 1.0 volt and 11 to 18 watts/cm^2 at 0.6 volts.

The performance of converters of Type B (EOS) is shown in Figure 3-22, also at a corrected emitter temperature of 1973°K. Tantalum emitters and molybdenum collectors were used. Positive spacing was employed in the design of some of these converters. Short circuit failures occured in two converters with positive spacing. The best converter without positive spacing showed a power output of about 9 watts/cm^2 and an efficiency of 7.4 percent. Maximum power occured between 0.5 and 0.7 volts. Tests with a three-converter generator resulted in 50 watts output at 1.8 volts, with a 4.5 percent efficiency.

Initial failures with converters of Type D (RCA) were corrected by improved fabrication techniques, and later units exhibited the performance

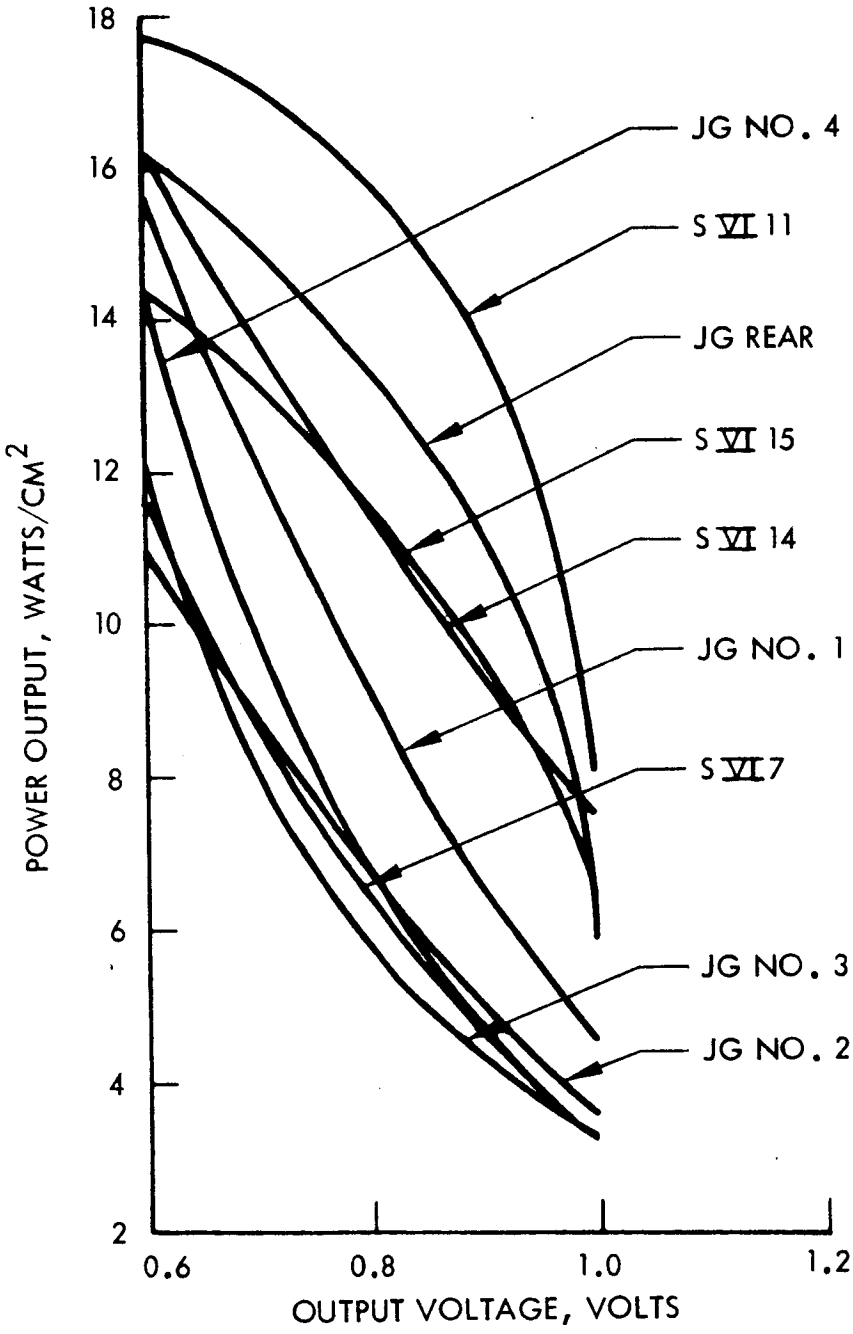

Figure 3-21. Type A Set Converter Performance for an Emitter Temperature of 1700°C and Optimized Cesium Temperature (Reference 3-30)

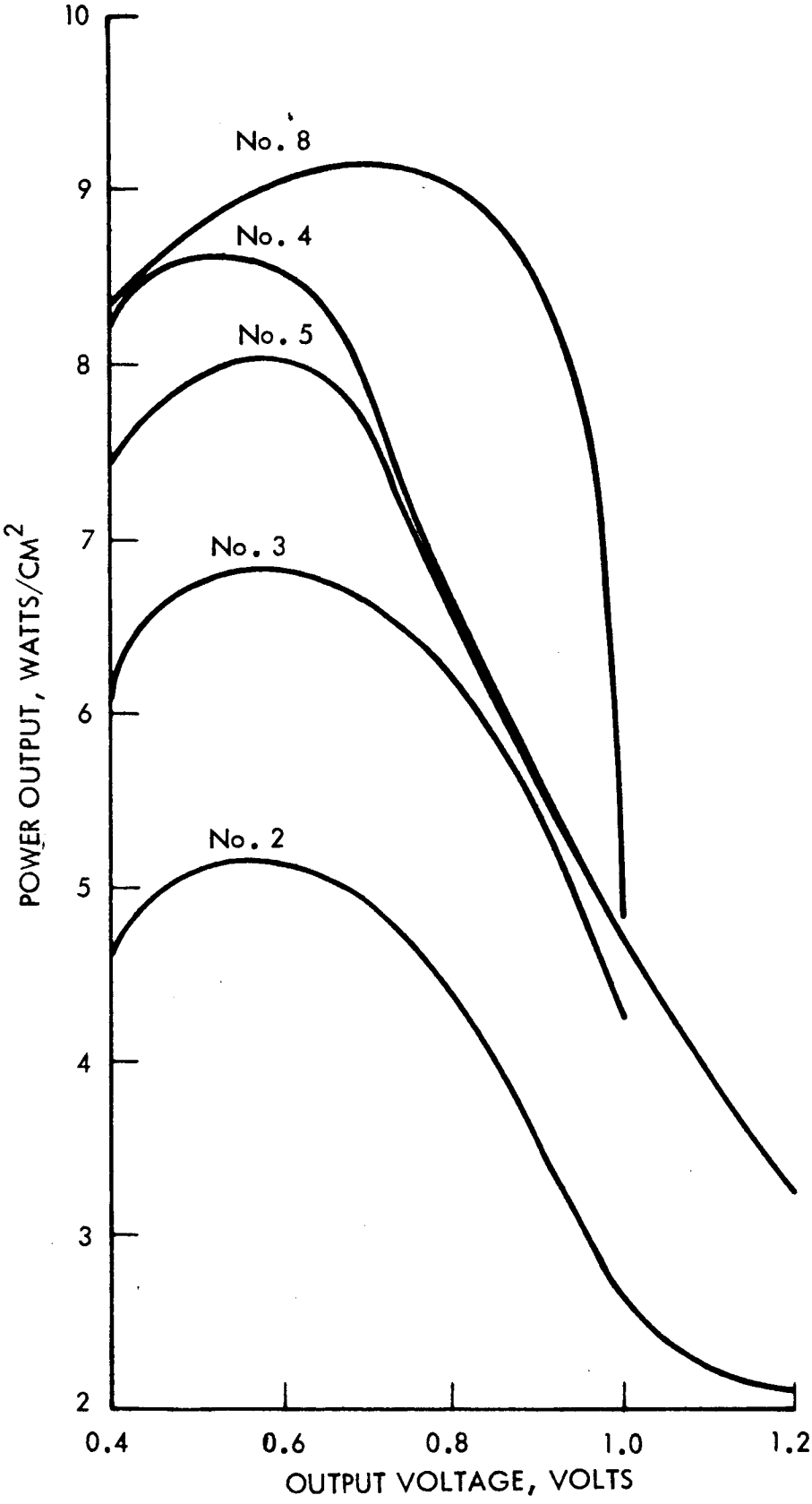

Figure 3-22. Type B Set Converter Performance for a Corrected Emitter Temperature of 1700°C and Optimized Cesium Temperature (Reference 3-30)

shown in Figure 3-23 at an observed emitter temperature of 1677°C. The emitter and collector were tantalum and molybdenum, respectively. Maximum power (approximately 11 watts/cm^2) occurred between 0.4 and 0.6 volts.

Thermionic generator JG-2 consists of five converters mounted in a cubical support, with the five emitter faces forming the cavity walls. The rear converter never reached the proper emitter temperature during generator tests. The generator tests were performed at constant power inputs from 800 to 1100 watts (electric heating). A maximum power of 82.4 watts was obtained at an efficiency of 7.5 percent. During solar tests on generator JG-1, an efficiency of 3.8 percent was obtained with 1080 watts input.

No statistically significant mean-time-to-failure data are available for the SET type converters tested by JPL. A life test underway on five converters indicates that a converter life of 2000 hours or more can be obtained. Failures have been caused by cesium attack on the thin emitter support sleeve, by poor metal-to-ceramic seals, and by corrosion of electrodes due to impurities trapped in the system during processing.

EOS fabricated several 5.5-foot diameter concentrators having a 62-degree rim angle (Reference 3-34). The mirrors were constructed using an electroformed nickel process. The specular reflectivity was measured to be between 0.87 and 0.90. The concentrator efficiency approached 100 percent for a 0.5-inch diameter aperture. The specific weight of the concentrator, including the torus rim, is approximately 1.0 lb/ft^2 for a mirror of this size. The 9.5-foot diameter mirror for the SET II Program is being fabricated by General Electric Company using electroformed nickel. GE has also developed a process for fabricating the masters required to produce these mirrors. Some progress has also been reported on aluminum concentrators having a specific weight of approximately 0.5 lb/ft^2.

EOS has proposed the use of bimetallic devices for solar flux control, emitter and collector temperature control, and cesium temperature control (Reference 3-33). The input solar flux would be controlled by a segmented flap driven by bimetallic elements so as to intercept part of the

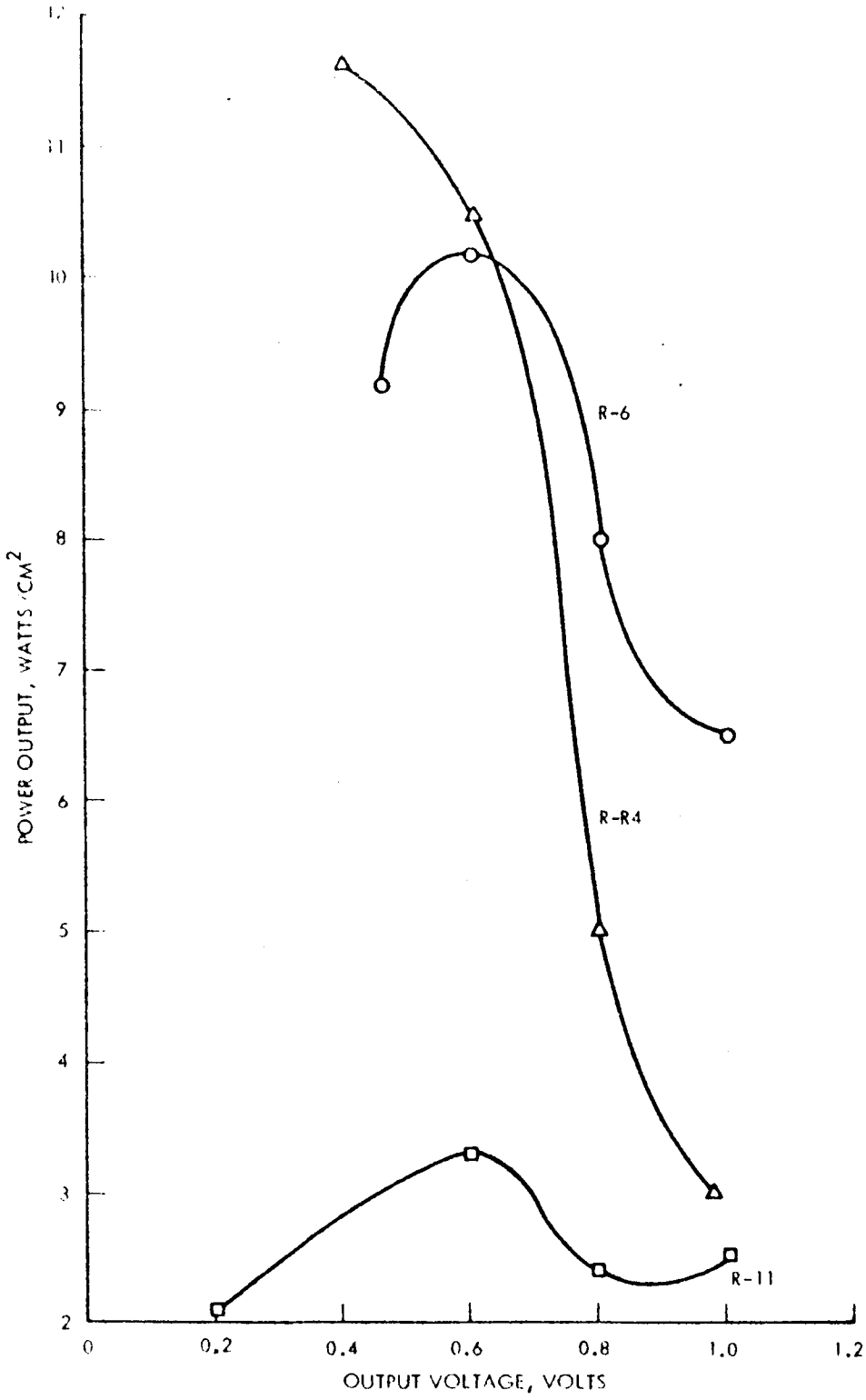

Figure 3-23. Type D Set Converter Performance Steady State Data for an Observed Emitter Temperature of 1677°C and Optimized Cesium Temperature (Reference 3-30)

solar flux concentrated on the aperture. The concept has not been reduced to hardware. No effort is reported on orientation or electrical controls for flight use.

EOS has fabricated a telescoping, retractable three-arm arrangement (Reference 3-34) for supporting the generator on the concentrator. The generator is stowed in the concave portion of the mirror and is restrained in that position by a support arm which protrudes through the center area of the concentrator. This area is normally shadowed by the generator and is not utilized. Methods for incorporating mounting brackets in the torus ring have been developed. No work is reported on structures and deployment schemes for multi-unit power systems.

d. Summary of State of Development

The characteristics and status of the converters and generators, concentrators, controls, structures, and mechanisms discussed above are summarized in Tables 3-5 through 3-8.

e. Conclusions

The following conclusions may be drawn regarding the current state-of-the-art in solar thermionic converters:

1) All converters under development for solar heating are of the cesium vapor type, with planar electrode geometry.

2) Converters with 2 to 3 cm^2 emitter area are capable of producing output power varying from 5 watts at 1650^oK to 36 watts at 1973^oK emitter temperature, with conversion efficiencies between 6 percent and 9 percent.

3) Statistically significant mean-time-to-failure data is not available, although some converters have survived life tests of approximately 2000 hours.

The following conclusions can be made regarding multi-converter solar thermionic generators:

1) Generators consisting of three to five converters arranged around a common cavity have been built and tested.

2) A major design problem with cavity generators appears to be the unequal heating of the individual emitters. The bottom converter in a cubical cavity design is particularly sensitive in this regard.

Table 3-5. Solar Thermionic Converter Performance Summary (Individual Converters)

Reference	Type	Weight (GM)	Emitter Area (cm^2)	Emitter Temperature (^oK)	Maximum Power (watt)	Voltage at Maximum Power (volt)	Efficiency (percent)	Manufacturer
3-25	2 B	*	3.08	2000	19 - 23	0.5 - 0.8	*	TEECO
3-24	301	*	3.08	2000	28	0.5	*	TEECO
3-30	SET (A)	170	2	1973	22 - 36	0.4 - 0.6	8.5 - 9	TEECO
3-30	SET (B)	260	2	1973	18.6	0.4 - 0.8	7.4	EOS
3-30	SET (C)	960	2	1973	17	0.6	*	AI
3-30	SET (D)	550	2	1950	20 - 24	0.4 - 0.6	*	RCA
3-26, 3-28	CVG	*	3	1650	5 - 6	0.2 - 0.4	6.5	GE

*Not reported.

Table 3-6. Solar Thermionic Generator Laboratory Test Summary (Electrical Heating)

Reference	No. of Converters	Type of Converters	Power In (watt)	Power Out (watt)	Voltage (volt)	Emitter Temperature (^{o}K)	General Efficiency (percent)	Tested By
3-25	5	CCG	1070	52	3.3	1794	4.9	TRW/ EMD
			1368	88	3.2	1900	6.4	
			1488	107	3.2	1953	7.2	
			1605	122	3.7	2000	7.6	
3-30	3	SET (B)	1100	50	1.8	*	4.5	JPL
3-30, 3-31	5 (1 passive)	SET 1B (JG-2)	800	31.5	2.75	*	3.9	JPL
			900	52.6	2.8	*	5.8	
			1100	82.4	2.9	1973	7.5	

*Not reported.

Table 3-7. Solar Thermionic Generator Solar Test Summary (5-Foot Diameter Mirrors)

Reference	No. of Converters	Type of Converters	Estimated Power Into Cavity (watt)	Maximum Power (watt)	Voltage At Maximum Power (volt)	Average Emitter Temperature (^{o}K)	Solar Flux Level (watt/ft^2)	Tested By
3-19	3	CVG	*	25.5	1.55	1900	90 (estimated)	GE (12/62)
3-23	5 (1 passive)	CCG	1400	35	2.0	1800 - 1850 (estimated)	97	TRW/ EMD (7/63)
3-31	5	SET IA (JG-1)	1080	41	2.4	1700 - 1800 (estimated)	72 (estimated)	JPL (9/62)

*Not reported.

Table 3-8. State of Development of Elements of Solar Thermionic Energy Conversion Systems (Excluding Converters and Generators)

Item	Program					
	TRW/EMD	Ref	GE/MDS	Ref	JPL/EOS	Ref
Concentrators (one-piece parabolic)						
Initial Reflectivity	*0.80 to 0.89	3-24, 3-32	0.83 - 0.92	3-23, 3-26, 3-29	0.87 - 0.90	3-27, 3-34
Concentrator Efficiency	*84 to 95 percent	3-24, 3-32	82.5 to 96 percent	3-33	85 to 100 percent	3-27, 3-34
Construction						
Sizes	5-ft dia, 60 deg	3-24	5-ft dia, 60 deg	3-33	5.5-ft dia, 62 deg	3-34
Material	Electroformed nickel Stretch-formed Aluminum	3-24	Modified search-light mirror	3-33	Electroformed nickel	3-34
Surface Accuracy	0.10 deg required	3-32	0.125 deg for 90 percent of surface	3-21	Not given	3-34
Specific Weight	1.0 lb/ft^2 nickel 0.5 lb/ft^2 aluminum	3-24 3-24	Not applicable Not applicable		1.0 lb/ft^2 for nickel	3-34
Orientation Controls	Bimetallic-heliotropic mount; fine control Ground type system; good to 2-6 min	3-20	Ground type system with high accuracy; -0 deg error	3-22, 3-35	Ground type system; good to 0.33 min error	3-34
Thermal Controls	Proposed flux control; responds to insolation Cesium reservior heating	3-36 3-23	Louver type system for ground only	3-22	Proposed bimetallic driven-control; responds to insolation, emitter and radiator temperature	3-33
Electrical Controls	Proposed parasitic load	3-20	None		None	
Structures and Deployment Mechanisms	Paper study of multi-unit source	3-20, 3-37	None		Support structures for single-generator system	3-34

*This range of values includes data on five-foot glass search-light mirror in Reference 3-24.

The following conclusions can be made regarding solar concentrators of the type required for solar thermionic energy conversion:

1) Only one-piece, parabolic mirrors with rim angles of 60 to 62 degrees are being used as solar concentrators for solar thermionic energy conversion systems employing cesium vapor type converters.

2) At this time, only electroformed nickel concentrators with specific weights of approximately 1.0 lb/ft^2 for 5-foot diameter mirrors are developed to the point where they can be used for solar thermionic energy conversion.

3) Aluminum concentrators fabricated with stretch-forming techniques or electroforming techniques are promising and offer specific weights on the order of 0.5 lb/ft^2 for 5-foot diameter mirrors. Aluminum has another advantage over nickel in that it is nonmagnetic.

The following conclusions can be made regarding electrical, altitude, and thermal controls; structures; and deployment mechanisms for solar thermionic power systems:

1) Orientation control concepts have not been completely developed for solar concentrators, but ground tests have demonstrated feasibility.

2) Thermal control techniques have not been developed to the hardware stage, but a number of concepts have been formulated.

3) Thermal energy storage has not been developed to the point where it can used for solar thermionic conversion systems.

4) Electrical controls on the solar thermionic source will probably consist of a parasitic load regulated to limit maximum converter voltage.

5) Very little work has been done on the structures and deployment mechanisms required for a multi-generator thermionic energy conversion system.

2. Systems Application

A general block diagram for a solar thermionic energy conversion system or power supply is shown in Figure 2-3. This diagram includes elements common to all such systems. The specific arrangement or nature of the elements may change from system to system depending on the mission and other constraints.

The thermionic power source consists of the concentrator-generator unit required to produce the energy consumed by the electrical loads, including that required to recharge the secondary batteries and that required to control and regulate the source. The thermionic converters are usually connected in series in each cavity or generator, which may contain one to five converters. Depending on the number of generators required to supply loads and the choice of source voltage, the generators may be connected in any desired series-parallel arrangement. At maximum efficiency, the output of the generator consisting of five series-connected converters will generally be between 3 and 4 volts. Trade-offs are required for specific mission requirements to determine the best choice of source voltage and the resulting series-parallel generator arrangement.

The entire source is provided with a shunt element for control purposes. This control will probably be a parasitic load designed to dissipate the energy not required by the loads. The parasitic load will be controlled so that source voltage is limited to values that would prevent overheating of the converter emitter. A brief study of the characteristics of the converters, as given in Appendix D, indicates that precise control of source voltage is not required (within 10 percent) to prevent overheating.

Secondary batteries are charged directly from the load bus. Since the source voltage level will probably be below that required for the load bus, a boost regulator is included to raise the source voltage to an acceptable load bus and battery level. Separate computations for the shunt control element and the boost regulator are covered in another section of this report. The equipment from the source up to the load bus is defined as the power supply.

The special orientation controls and thermal controls which are required for proper system performance are considered as a part of the source itself, along with the concentrator and cavity generator.

3. Assumptions for Design Study

To develop a system design procedure and obtain useful data requires a number of assumptions at the outset, so that gaps in the state-of-the-art

can be overcome and so the scope of the design can be kept within workable limits. Assumptions made to facilitate the design procedure described in this report are as follows:

1) The concentrators used for the study will be one-piece, parabolic reflectors with a 60-degree rim angle. The concentrators may be made from nickel or, for future programs, aluminum.

2) Each cavity generator is assumed to consist of five series-connected converters. The temperature distribution is assumed to be uniform if the orientation error is within limits.

3) No thermal storage material as such is used to minimize or prevent thermal cycling of any portion of the converter or generator. It is assumed that all elements of the system are able to withstand thermal cycling.

4) Orientation controls will be divided into coarse and fine controls. The coarse controls will be those normally associated with the spacecraft and will not be considered an added burden. Fine controls will be considered as a part of the source and, for want of alternative means, the TRW/EMD heliotropic mount will be used.

5) Cesium reservoir temperatures will be maintained by electric heating to minimize warm-up period and maximum efficiency. It is assumed 1 watt is required for each converter. It is also assumed that it takes 10 minutes for a cold generator to produce 90 percent of its capability after solar flux has been obtained. Therefore, this period of 10 minutes must be subtracted from the daylight period available when computing the power requirements for the source.

6) The conversion system will be designed for the worst case, which will be assumed to be the furthest point from the sun at which the system must operate. It is assumed that the design is optimized for this condition so that concentrator-generator efficiency is maximized at the particular emitter temperature and orientation error limits chosen.

7) The absorber-cavity or generator will be assumed to operate with a constant power flux input at steady state except for variations resulting from a variable pointing accuracy or degraded specular reflectivity of the mirror. In other words, the solar flux will be maintained constant by an iris or louver arrangement which controls the flux

into the aperture in response to the variable solar intensity. Assuming a simple fourth power relationship between input flux and emitter temperature, a $\pm 50^{\circ}K$ temperature variation at $2000^{\circ}K$ would require a ± 10 percent input flux variation. It seems reasonable, therefore, not to attempt to regulate input flux as a function of emitter temperature. The brief electro-thermal study performed in Appendix D strengthens this conclusion and indicates that the flux can vary over even wider limits with the same temperature limits.

8) Since one-piece rigid concentrators are used, it is assumed that clusters of concentrator-generator units will be used where power requirements dictate. The maximum diameter of the concentrator and the resulting area per concentrator will be limited by the stowage area and volume limitation associated with the launch vehicle.

9) It is assumed that all generators contain five series-connected converters that will be operated at a voltage between 0.6 and 0.8 volts with a resulting generator voltage between 3 and 4 volts. Collector temperature and cesium temperature will be assumed optimized for the chosen emitter temperature and for operation within these voltage limits.

4. Development of Design Computation Process

Because the type of information required to produce parametric data for design of solar thermionic energy conversion systems does not exist, a generally applicable design procedure cannot be formulated. In the present study, therefore, the problem was attacked in as simple a manner as possible. Only the very critical factors, such as emitter temperature, orientation errors, allowable individual concentrator area, and so on, were considered. This simplified approach, together with the simplifying assumptions discussed previously, cannot yield a design that fits any specific design problem, but it can demonstrate what is required of a design procedure for this type of equipment and may prove useful as a starting point for a more complicated, general approach as more information becomes available.

The design approach chosen is to evaluate the efficiency of the various major elements of the thermionic conversion system as a function of environment and life, operating temperature, and sun pointing accuracy.

The watts converted per square foot of concentrator projected active area are used to determine the total area required for a particular power output. Concentrator size limitations are used to determine the minimum number of concentrator-generator units required. System weight and volume computations are based on the area and number of concentrators and the generator power rating. The computation flow diagram developed is shown in Figure 3-24. In setting up the computation, the following characteristic functions are required. They are described in order, according to the letters indicated in the blocks in Figure 3-24. Terms are defined in the List of Terms.

- Function A: Mirror surface reflectivity (R) as a function of time (t) during the mission.

- Function B: The ratio of average converter efficiency (η_d) to maximum initial converter efficiency (η_{do}) as a function of time (t) and emitter temperature (T_e). This ratio is 1 at t = 0, and thereafter indicates the degradation in efficiency at the operating voltage and temperature as a function of time.

- Function C: Maximum initial converter efficiency (η_{do}) in per unit as a function of emitter temperature (T_e). This data assumes that the converter design is optimized for operation at this temperature and that the converters are operated at the best combination of voltage, cesium temperature, and collector temperature.

- Function D: Concentrator-absorber efficiency (η_{ca}) in per unit as a function of maximum relative orientation error (ϕ_e) and emitter temperature (T_e). Relative orientation error is defined as the ratio of absolute error allowed in pointing accuracy expressed in minutes, to the solar image half angle at the distance from the sun for which the conversion system is being designed. The efficiency figure can be used for any design point distance from the sun that is desired when pointing error is expressed in relative terms like this. For example, a system designed for a 6 minute of arc absolute error near earth (relative error of 6 minutes of arc/16.125 = 0.372) would have the same concentrator-absorber efficiency at the same temperature as a system designed for a 3.5 minute of arc error near Mars, providing the mirror surface accuracy and the diameter of the aperture have the same relative values for each system.

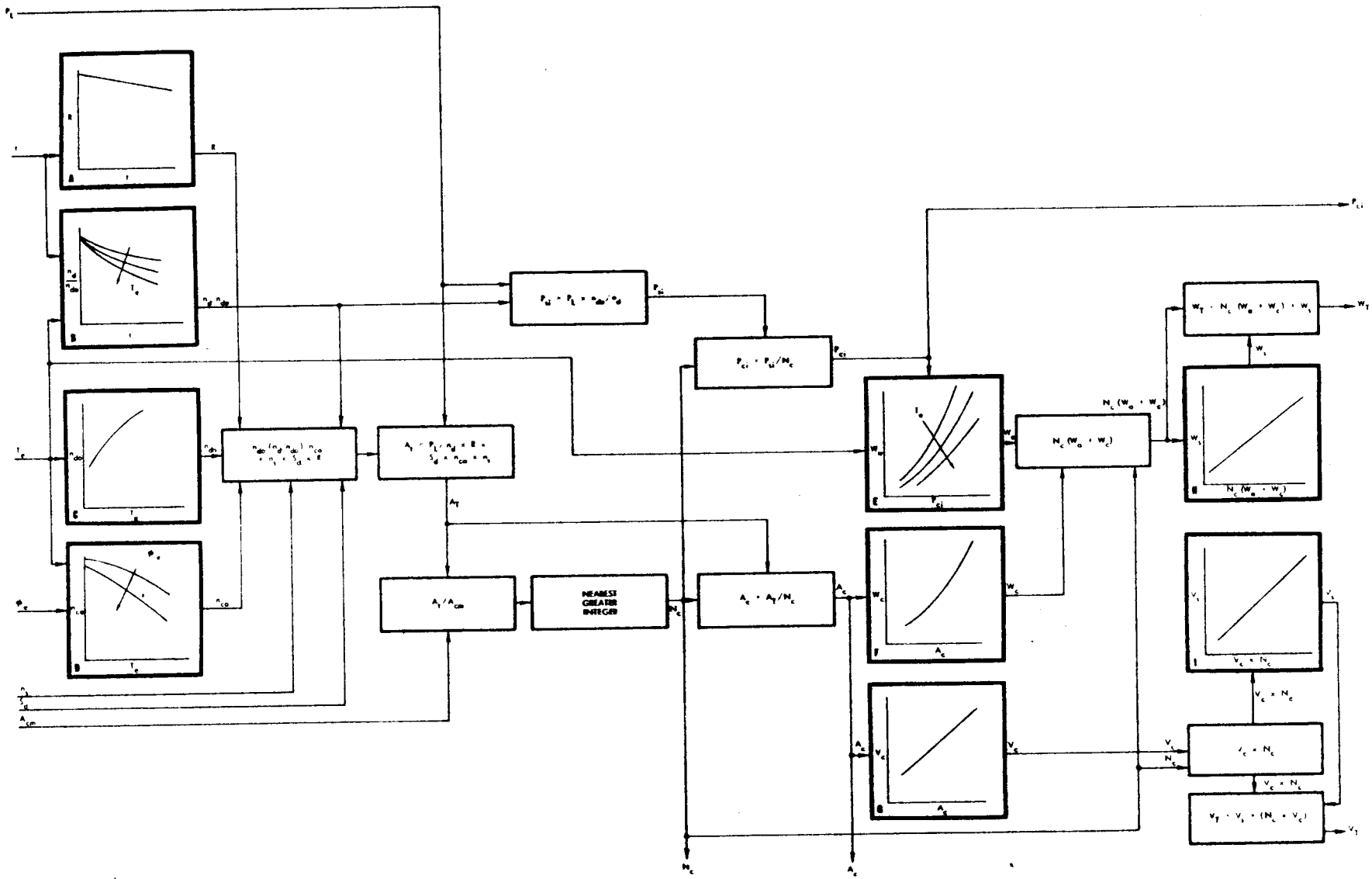

Figure 3-24. Solar Thermionic Design Computation Flow Diagram

- Function E: The weight of the absorber-cavity or generator (W_a) including diodes, collector radiator, heliotropic mount, and input flux control, as a function of initial power output per generator (P_{ci}) and emitter temperature (T_e). The support arms for the generator assembly are not included.

- Function F: The weight of the solar concentrator or mirror (W_c), including the torus support rim and fittings, as a function of concentrator projected active area (A_c). Supporting structure for generator or mirror is not included.

- Function G: The stowage volume of each concentrator-generator assembly (V_c) as a function of concentrator area (A_c). This figure is the product of the total projected area and the depth of the mirror. It is assumed the JPL/EOS scheme of stowing the generator in the concave portion of the mirror is used.

- Function H: The weight of supporting structure, deployment mechanisms, generator supports, and related hardware (W_s) as a function of the total weight of concentrator generator units $\left[N_c(W_a + W_c)\right]$.

- Function I: The stowage volume of the supporting structure and deployment mechanisms, and so on (V_s), as a function of the total volume of the concentrator-generator units ($N_c \times V_c$).

The computation flow shown in Figure 3-24 is described in detail in the following paragraphs.

a. Inputs

Besides the functional relationships previously described, the following specific inputs are required:

1) The average load power requirements (P_L), including battery recharge requirements and power required to control the source, to heat the cesium reservoirs, and to raise the voltage level to that required for the bus. The latter power requirements may have to be estimated initially before the number of generator units is determined.

2) The time during the mission at which minimum insolation (solar intensity) occurs (t).

3) The emitter temperature chosen for the design (T_e).

4) The maximum relative orientation error at the design point (ϕ_e).

5) The percent of active concentrator area which is not shadowed by generator and supporting structure (η_s).

6) The solar intensity or insolation that occurs at the design point, in watts/ft^2 (S_d).

7) The maximum allowable projected active area of the concentrators used for a particular design (A_{cm}).

b. Computation Sequence

The computation is performed according to the following sequence:

1) At the design point, functions A, B, C, and D are used to determine the reflectivity (R), the degradation in converter efficiency (η_d/η_{do}), the initial converter efficiency (η_{do}), and the concentrator-absorber efficiency (η_{ca}).

2) The product of initial converter efficiency, degradation in converter efficiency, concentrator absorber efficiency, shadowing effect, design point solar intensity, and mirror reflectivity ($\eta_{do} \times \eta_d/\eta_{do} \times \eta_{ca} \times \eta_s \times S_d \times R$) is taken to yield the number of watts per square foot of projected active area that can be converted to electrical energy.

3) Dividing the average load power requirements by the product obtained in Step 2) yields the total projected active area of concentrators required for the source (A_T).

4) The average load power requirements (P_L) divided by the ratio of converter efficiency at the design point to initial converter efficiency (η_d/η_{do}) yields the initial source power capability (P_{si}).

5) The total concentrator area required (A_T) as obtained in Step 3) divided by the maximum allowable individual concentrator area (A_{cm}) yields a number approximately equal to the number of concentrator-generator units required.

6) The number of concentrator-generator units obtained in Step 5) may not be an integer. When it is not, the nearest greater integer is determined and this becomes the actual number of concentrator-generator units (N_c) which can be used. This is the minimum number required. If this number is not satisfactory for some reason, it can be increased to a greater integer. For instance, if the number obtained cannot be divided by another number to yield an integer, only one series connection of generators

can be made, with no parallel strings of generators, unless all generators are paralleled. This may be unsatisfactory from a reliability standpoint or from a source voltage standpoint. In this case, another greater integer can be chosen for N_c so that parallel strings, each with more than one generator in series, can be obtained.

7) The total concentrator area (A_T) divided by the number of concentrator-generator units (N_c) yields the actual projected active area per concentrator (A_c).

8) The total initial source capability (P_{si}) divided by the number of concentrator-generator units (N_c) yields the initial power capability of each generator (P_{ci}).

9) Function E with inputs of emitter temperature (T_e) and initial unit power rating (P_{ci}) yield the weight of each absorber or generator unit (W_a).

10) Functions F and G with the input of concentrator area (A_c) yield the concentrator weight (W_c) and stowage volume (V_c), respectively.

11) The product of the sum of the absorber weight and concentrator weight ($W_a + W_c$) with the number of concentrator-generator units (N_c) yields the total concentrator-generator weight minus supporting structures, etc.

12) The product of the stowage volume of a concentrator-generator unit (V_c) and the number of units (N_c) yields the total concentrator stowage volume minus that required for supporting structures, etc.

13) Function H with the input of the total concentrator-generator weight obtained in Step 11 yields the weight of supporting structure and deployment apparatus, etc., (W_s).

14) Function I with the input of the total stowage volume of the concentrator-generator units obtained in Step 12) yields the total stowage volume of supporting structures and deployment apparatus, etc., (V_s).

15) The sum of the weights obtained in Steps 11) and 13) yields the total source weight (W_T).

16) The sum of the stowage volumes obtained in Steps 12) and 14) yield the total source stowage volume (V_T).

c. Outputs

The outputs of the computation process described are as follows:

1) Number of concentrator-generator units required (N_c).
2) Projected active area for each concentrator (A_c).
3) Initial power capability of each generator unit (P_{ci}).
4) Total source weight (W_T).
5) Total source stowage volume (V_T).

A sample calculation is performed in Appendix B3 to illustrate the use of the process just described. Parametric data for the functions required is given in Appendix A3. The generation of these functions is described in the following section. This computation process can be used as desired to generate design tradeoff information using combinations of inputs as independent variables. For instance, source weight and volume can be determined as a function of emitter temperature with the other inputs held constant.

5. Parametric Data Generation

The parametric data required for Functions A through I must be obtained from data made available from the three major programs previously described in the state of development discussion. In many cases, the data required for each function is not available from all three sources and the data that is available is not complete. Therefore, the data and the results of a computation based on this data can be considered only as a first-order approximation. Any one of the functions described will have to be revised for individual cases. Sources of the data are listed in the Reference List, and the applicable reference numbers are given in the following discussion of functions and in the summary tables in the state-of-the-art discussion. The function curves themselves are shown in Appendix A3.

a. Function A

Initial reflectivities have been measured in each of the major programs and are given in Table 3-8. Since no data is available on degradation of reflectivity, an arbitrary allowance of 10 percent is used. This allowance is consistent with the allowable change in design temperature ($50^{\circ}K$) as input solar flux changes and is a figure that must be met to obtain a useful concentrator.

b. Function B

No data is available which gives the degradation of converter efficiency versus emitter temperature and time. Life tests on a few converters have exceeded several thousand hours but have not been uniformly controlled, so that few conclusions can be drawn. Since no data is available, an arbitrary allowance of 10 percent degradation in efficiency is assumed for a converter operating at 1700°K. This degradation is assumed to occur in the first few hours of operation, after which no further degradation occurs until complete failure. Since increased temperature is assumed to result in increased degradation, another arbitrary assumption is made that the degradation increases by 1 percent for each 100°K above 1700°K.

c. Function C

Maximum converter efficiency as a function of emitter temperature is a function of many factors including the type of converter configuration, the spacing, and so on. Therefore, it is hard to generalize in this area. The best data available for the purposes of performing this computation is obtained from TRW/EMD in Reference 3-25. This data is given in Figure A3-3.

d. Function D

Data applicable to this function is available from each major program. For this report, data published by GE/MSD in Reference 3-29 was chosen to generate the basic relationship since the data is the most complete. The GE/MSD data gives only the concentrator-absorber efficiency, i.e., the ratio of the energy absorbed by the cavity to that which is available in the focal plane of the concentrator. Not all of the energy absorbed by the cavity is available to the thermionic converters. There are losses due to the radiation and conduction associated with the cavity support block and insulators, etc. An estimate of this effect is obtained from TRW/EMD in Reference 3-36, which indicates only 75 percent of the heat retained by the cavity is available to the converters. Therefore, the GE/MSD data converted to relative angular error is multiplied by 0.75 to obtain Function D. This data is more conservative than that presented from the other data programs which indicate that up to 90 percent of the absorbed energy is available to the converters.

e. Function E

The weight of the absorber-cavity or generator unit is a function of the design temperatures, the accessories required, and the power output required. The weight must include converters, insulators, cavity structure, terminals, radiators, and any temperature or flux controls. The design approach used in the three major programs are not really compatible, but enough data does exist from TRW/EMD and JPL/EOS to generate several points of the desired function. The TRW/EMD calculation given in Reference 3-20 is for a generator unit rated at 172 watts at 2000°K, and weighing 6.06 pounds, including all details except a flux control. The JPL/EOS unit described in Reference 3-34 weighs 3.36 pounds when rated at 135 watts at 2000°K. This figure does not include flux or temperature controls. The TRW/EMD figure was chosen because it is more conservative. The weight of a suitable flux control and heliotropic mount must be estimated, since no figures are available. A 3-pound allowance is arbitrarily assigned to this equipment and it is assumed to be proportional to the weight of the remainder of the generator. At 172 watts, 2000°K, therefore, the unit weighs 9 pounds.

The function curves are generated from this one point. A family of constant temperature curves are required. Since maximum power density (watts/cm^2) is a function of temperature, emitter area must be varied to keep power level at a constant temperature. At constant temperature therefore, linear dimensions for the device must change as the square root of the power, and volume and weight (if density is constant) will change as the 3/2 power of the power rating. Each constant temperature curve is then a 3/2 power curve. To obtain curves at different temperatures, the data point at 2000°K and 172 watts is shifted up or down proportional to the change in efficiency with emitter temperature as given in Function C. The sample calculation in Appendix B3 should be checked to clarify this point.

f. Function F

Weight information is available from TRW/EMD and JPL/EOS on electroformed nickel mirrors. The data from JPL/EOS gives the weight of a concentrator having an active area of 20.5 feet^2 as 19.7 pounds, including the torus with built-in brackets. Examination of the equations

for the material volume of a concentrator of this sort, including the torus, indicates that if the relative geometry is maintained constant, the weight of the concentrator will vary as the 1-1/6 power of the active area. Information on aluminum mirrors indicates that specific weights of one-half that of nickel can be obtained in future programs.

g. Function G

The stowage volume of each concentrator-generator unit is the product of the overall projected area and the depth of the concentrator. The stowage volume is found to vary as the 1-1/2 power of the projected active area. Using the concentrator dimensions obtained for 5-foot diameter concentrators, the curve relating stowage volume to active projected area can be generated as shown in Figure A3-7.

h. Function H

This relationship is based on weight information from JPL/EOS (Reference 3-34) for the three generator support arms, which extend between the concentrator rim and the generator, and on information from TRW/EMD concerning the weights for supporting structure and deployment mechanisms (Reference 3-20). It is arbitrarily assumed that the weight of this equipment varies directly with the total weight of the concentrators and generators. The equation obtained describing the relationship between structure and total concentrator-generator weight is

$$W_s = N_c (W_a + W_c) \times 0.51 + 7$$

i. Function I

The only information available relating concentrator stowage volume to structure and deployment mechanism volume is from TRW/EMD in Reference 3-20. The relationship is assumed to be a direct proportionality and the equation is $V_s \pm 0.5 \times N_c \times V_c$ ft^3.

6. Problem Areas

The problem areas associated with solar thermionic energy conversion systems for space application fall into two categories. One category consists of those areas where insufficient design effort has been expended and where the hardware required to perform necessary functions has not been fabricated or tested. The other category consists of those

areas where hardware feasibility has been demonstrated but where data sufficient for system design and analysis has not been generated. In both of these categories, the system aspects are considered as the prime criteria with which to evaluate the status of various problem areas. The following discussion attempts to summarize the problem areas in this field. It is assumed for the purpose of this discussion that converter feasibility has been demonstrated and that no major design problems remain with the converter itself. This is no doubt an optimistic assumption.

a. Design Problem Areas

The following problem areas exist because insufficient design and development effort has been spent in developing devices required to complete a solar thermionic system.

Cavity Heat Flux Controls or Temperature Controls. At this time, no hardware has been developed and tested that can be used to provide thermal control for a cavity generator. This control will be required if the system is expected to operate over a range of solar intensities or with degradation in elements of the system, such as the reflector. EOS has proposed (Reference 3-33) an adjustable flap type control between the concentrator and the focal point that is controlled by several bimetalic elements responding to solar intensity levels, cavity temperature, and radiator temperature. A number of problems could exist with a control of this type, including sensor drift and insulation problems. The problems cannot be evaluated and solved unless hardware is built and tested.

TRW/EMD has proposed (Reference 3-36) a similar device that responds only to solar intensity variations and uses gas pressure to drive an iris type device mounted just outside the aperture. Similar problems would seem to be associated with this device as with the EOS device. None of the programs has mechanized other thermal controls that may be required, such as cesium reservoir heaters, so that they may be used with flight hardware.

Cavity Thermal Design. Solar concentrator testing on five-converter cubical cavity generators has demonstrated that the temperature distribution is not uniform and that, in fact, the converter forming the rear wall of the cavity opposite the aperture will often be passive. Generators made up

of three converters have also been tested, with somewhat more uniform temperature distributions but with a reduction in power capability. More design and testing is required to maximize cavity generator efficiency by obtaining a more uniform temperature distribution.

Orientation Systems. Orientation systems suitable for solar thermionic energy conversion systems have not been developed to the flight stage. Accuracy sufficient for earth orbit has been demonstrated with ground type equipment. The concept of using one highly accurate attitude control system for the entire spacecraft and the concentrators seems to be an unlikely solution for systems requiring more than one concentrator. It will probably be necessary to provide each concentrator with a separate fine orientation control such as the TRW/EMD heliotropic mount. At this point, neither approach has been perfected for flight use.

Structures and Deployment Mechanisms. Some hardware, such as the telescoping generator support arms developed for the JPL/EOS program, has been fabricated for support and deployment of solar thermionic concentrator-generator units. TRW/EMD has made some paper studies on concepts for multi-unit sources. At this time, however, no evidence exists that anyone has developed the hardware necessary for stowing, deploying, and supporting a multi-unit source through the environment associated with space vehicles. Problem areas, such as thermal stress due to temperature extremes, electrical interconnection, vibration, and dynamic loading during in-flight maneuvers, must be evaluated and the hardware feasibility demonstrated by environmental testing.

Systems Integration. No work has been reported on the many problems that will no doubt arise in combining the multi-element solar thermionic source (or even the single-element source) with other elements of a complete spacecraft system. Some of the problem areas that must be studied are: the effect of the concentrators and structures on the spacecraft temperature distribution; the effect of the converters, concentrators, and structures on the communication equipment, including electromagnetic noise, disturbance of antenna patterns, etc.; the effect of magnetic materials and large current loops associated with these sources on the magnetic moments and fields associated with the spacecraft; and the effect of the

mass distribution of the source on the dynamic characteristics of the vehicle, including possible excess fuel requirements for the attitude control system, etc. Other similar problems must be explored before a vehicle utilizing solar thermionic energy conversion can be developed.

b. Test Data Problem Areas

In considering a device that has not yet demonstrated sufficient life or performance to perform the job required of it, it is premature to point out the lack of sufficient data for system design work. It is reasonable, however, to comment on data deficiencies from a system design view, since, in the end, much of the data generated must be tailored to meet system design requirements. Certainly, data acquisition and reduction for a device such as a thermionic converter is a problem, just as it is for any nonlinear device whose performance is dependent on many variables. A good example of another device of this type would be a sealed secondary battery designed for space vehicle operation. Much of the early data taken on such batteries was not useful to the power system designer and had to be redone so that spacecraft power system design could be improved. The following comments concern the present data problem areas and the areas where more information is required if solar thermionic power system design is to be performed in a competent manner.

Converter and Generator Characteristics. More complete families of I-V characteristics for thermionic converter and cavity generators are required. Families of converter characteristics for constant emitter temperature and constant heat input when operated in space environment are needed. The characteristics should be for converters optimized for operation at a range of voltages and emitter temperatures. Complete I-V curves, and not just sections, are needed so that the effects of thermal and electrical perturbations can be explored. With this sort of data, the system designer can choose the best design for his purposes and optimize the design of controls and related system hardware.

Converter-Generator Life Tests. Life tests must be performed that will allow the system designer to be able to predict the performance characteristics described in the preceding paragraph for converters or generators after a particular period of time in a space environment for a

specific mission. The effects of emitter temperature and other variables on converters optimized for particular conditions must be evaluated. Life tests must be performed under carefully controlled conditions that simulate flight operation, including thermal cycling. Presently, life test data corresponding with this requirement has not been obtained. The life test data published at this point extends only to a few thousand hours for one or two converters. The data was not taken under carefully controlled conditions, and the conditions did not simulate flight conditions. It is hoped that with improved converters, the life testing performed will be controlled so that true operating feasibility is demonstrated and the effects of important variables can be understood.

System Test Data. Since many of the elements of a solar thermionic system have not been perfected, no true system tests have been performed. When equipment is available, however, system operation must be simulated to gain a more complete picture of the performance of such a complex energy conversion device. The behavior of generators as the sun is focused on them after an eclipse, their behavior upon entering eclipse, etc., must be understood. It is recognized that much of the information of this type will not be general but pertinent to only one program.

Effects of Space Environment on Mirrors. Nothing has been published that allows the designer to predict what the reflectivity of the concentrator surface will be after a certain time in the space environment, although the EROS program is investigating this area. This information is quite important in evaluating the life and performance of a system.

7. Conclusions

Because of the lack of data and design work in specific areas, the computational method formulated for preliminary design of solar thermionic energy conversion systems has been over-simplified. The design information is probably conservative in regard to performance, weight, and volume. The power outputs computed, however, will correspond to the solar test results obtained to date. This method of energy conversion should continue to be treated conservatively in comparison with more fully developed systems, both because a working system has not yet been developed and because the solar test data available on converters and

associated equipment is not as favorable as the predicted values. As more information becomes available, the program will have to be expanded and revised.

Much has been accomplished in the development of solar energy conversion and it appears likely that a workable system will be developed, but probably not in the next year or two. It is more reasonable to expect that it will be around 1970 before a competitive solar thermionic power system meeting the requirements of a Mars or Venus orbiting vehicle will be ready for flight operation.

D. SOLAR DYNAMIC POWER PLANTS

Solar dynamic power plants may be categorized in one of three thermodynamic cycles: Rankine, Brayton (or Joule), and Stirling. Each of these defines a basic concept by which thermal energy is converted to mechanical energy to drive a rotating electric generator. In combination with the energy conversion equipment, the typical solar dynamic power plant includes a solar collector, an energy storage unit, and power plant controls. A major portion of the published literature covering these types of systems has been devoted to comparisons of basic cycles for space applications. As a result, this material is not repeated here except to point out salient features of specific designs that appear to offer improvements in power plant weight or reliability.

This study effort has been directed toward the determination of a method for using parametric data from current hardware development programs to calculate preliminary power plant design data for any space application within a power range of 1 to 10 kw. Specifically, the resultant design data consists of power plant weight and principal dimensions. Mission requirements are defined by specified power output, orbital sunlight-eclipse periods, and maximum operating distance from the sun.

1. State of Development

The NASA-sponsored Sunflower development by TRW appears to be further advanced than any other solar dynamic power plant. The 3-kw Sunflower design consists of a petal-type paraboloidal concentrator, a cavity absorber-heat storage unit using the heat of fusion of lithium hydride for energy storage, and a mercury-Rankine cycle energy conversion system operated at super heat and condensing temperatures of approximately 1250°F and 600°F, respectively. Prototypes of the power plant components have been fabricated and tested, including the concentrator, absorber-heat storage unit, rotating unit, radiator and speed control. Detailed description of the system and development testing is contained in References 3-38, 3-49, 3-50, and 3-51.

A second Rankine cycle development program of significant interest in the lower power range is the 1.5-kw biphenyl system designed by Sundstrand. The thermodynamic cycle is illustrated in Figure 3-25.

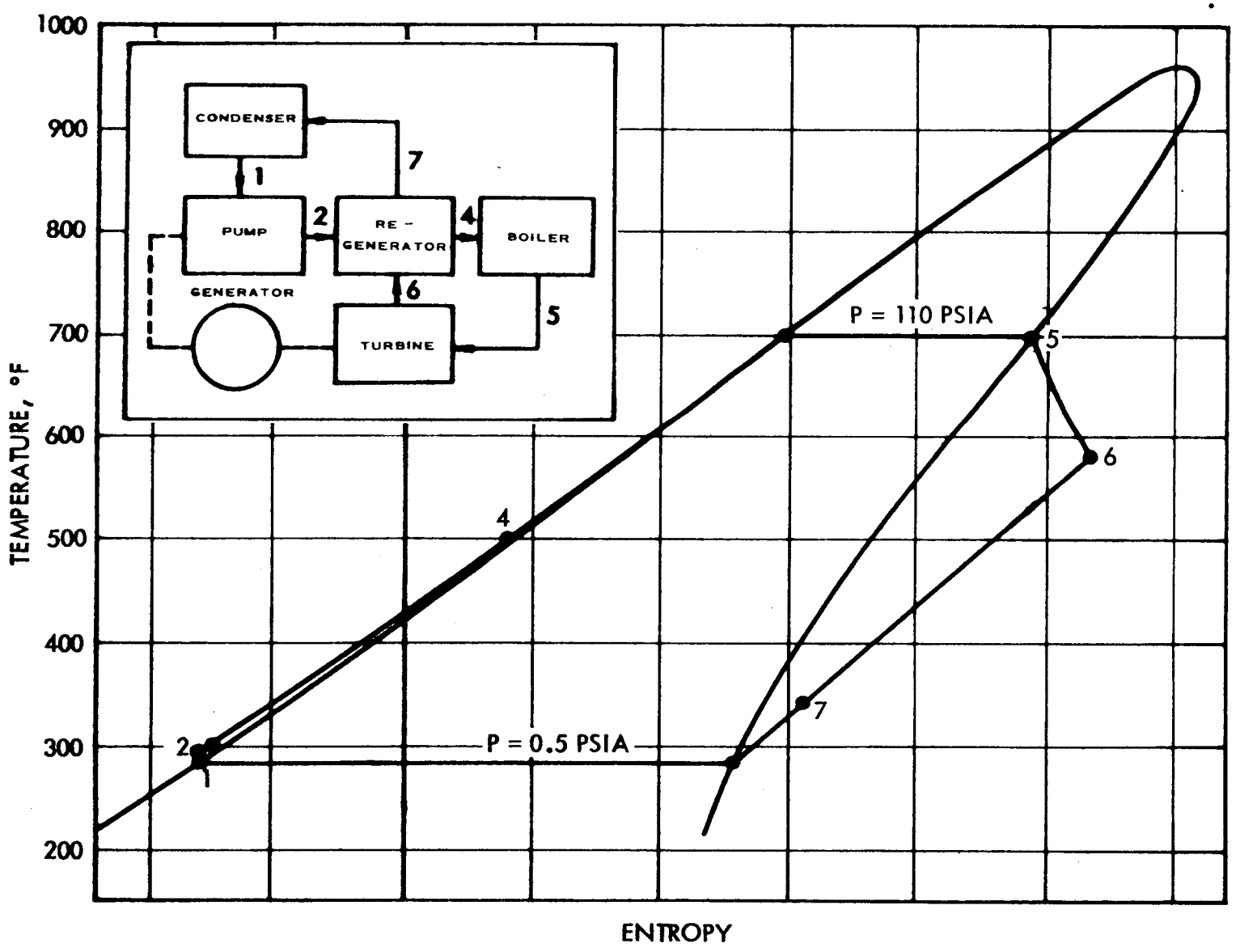

Figure 3-25. Temperature-Entropy Diagram-Biphenyl Rankine Cycle

A noteworthy characteristic of this working fluid is the shape of the vapor dome, which causes the turbine exhaust to fall in the superheat region, thus precluding the partial condensation and accompanying performance penalties during expansion that are typical of mercury systems. Cooling of the exhaust vapor to the condensing temperature is accomplished by regeneration of the condensate before it enters the boiler. An interesting design feature of this system is the presently planned use of lithium fluoride rather than lithium hydride for thermal energy storage in order to eliminate the hydrogen containment problems encountered in programs employing lithium hydride. The system appears to offer a significant weight reduction over an equivalent mercury-Rankine system. However, prototype hardware fabrication and testing has not yet been completed.

The Allison Division of General Motors has developed the 3-kw Stirling reciprocating engine to a relatively advanced stage. System description and prototype engine-generator test results are contained in Reference 3-43. This system also offers an apparent weight saving in comparison to the mercury-Rankine cycle, but at the expense of increased complexity. An advantage of the Stirling vapor cycle, as with the Brayton vapor cycle, is the elimination of zero-g boiling and condensing requirements. Associated with the Stirling engine-generator development effort is a Fresnel concentrator development program by Allison. Due to its flat configuration, this concentrator offers an advantage in minimizing stowed volume. Available data, however, indicates a reduced concentrator efficiency in comparison to the paraboloidal configuration. Available data for both the biphenyl and Stirling cycles are, in general, limited to the specific power level for which the systems are designed.

There is renewed interest in the Brayton cycle, which was previously considered less favorable than the Rankine cycle for space applications because of its nonisothermal radiator and large compressor power requirement. If presently predicted turbine and compressor efficiencies can be achieved, however, this type of system appears competitive for solar dynamic system applications because of its inherent simplicity.

Because of its relatively advanced development, the Sunflower mercury-Rankine cycle program has produced the majority of the available detailed parametric data for solar dynamic systems in the 1 to 10-kw range.

2. Development of Design Computation Process

The calculations necessary to define size and weight of a solar dynamic power supply for a given mission are shown in the computation flow diagram (Figure 3-26). The diagram is based on a mercury-Rankine cycle turbogenerator system similar to the Sunflower design. The assumed simplified system configuration is shown in Figure 3-27.

Inputs to the computation for a specific mission are defined by:

1) Spacecraft location (maximum AU)
2) Orbital conditions (eclipse/sunlight periods)
3) Power requirements (min/max loads)

Outputs of the computation are:

1) Power plant weight
2) Principal power plant dimensions

To accommodate varying load power requirements with a system of this type, a simple parasitic load control appears most suitable. The power supply is designed to operate at the maximum load continuously. Reductions in load are compensated for by adding parasitic load to maintain the constant design point electrical output. Although frequency (speed) variations resulting from load changes may be sensed to control the dissipative load, improved response is achieved by sensing load current directly. Analysis of the load power profile is necessary to establish maximum levels for power supply design. Methods of supplying short duration peaks without oversizing the complete power system are based on provision of additional energy storage either in the absorber or as supplementary electro-chemical power sources.

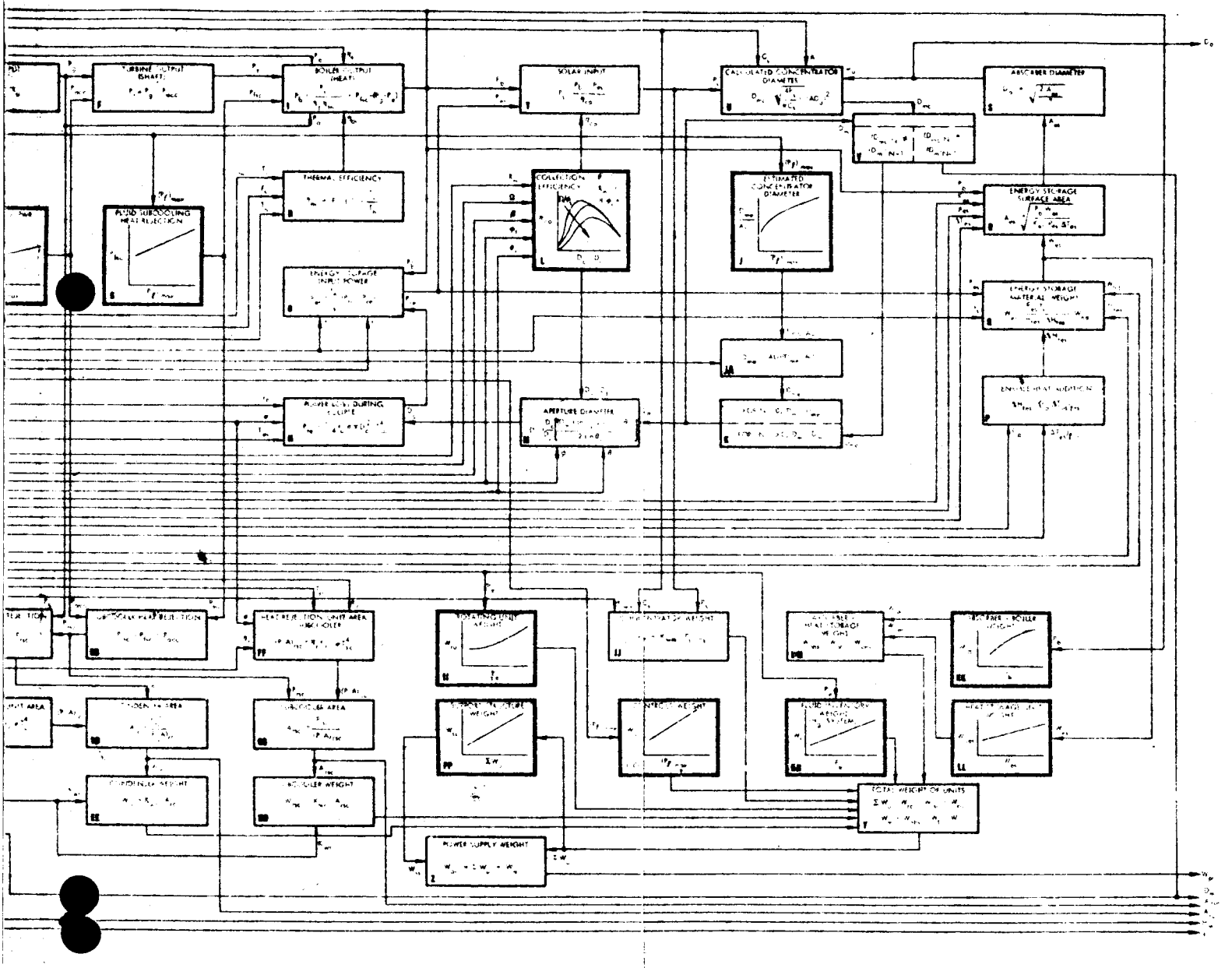

Figure 3-26. Solar Dynamic Design Computation Flow Diagram

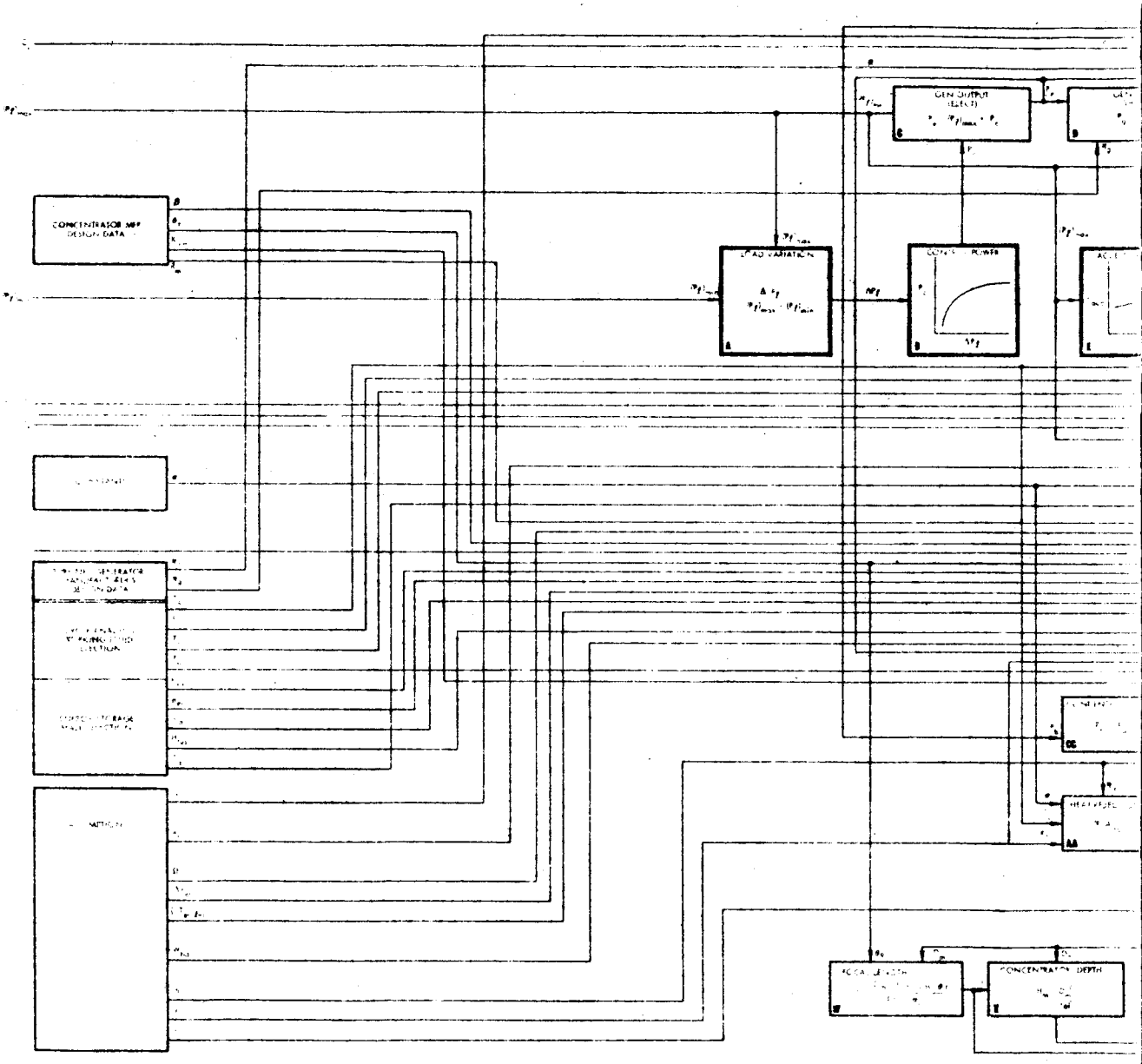
CONCENTRATOR MPP DESIGN DATA
LOAD VARIATION
GEN OUTPUT (ELEC)
CONCENTRATOR DEPTH

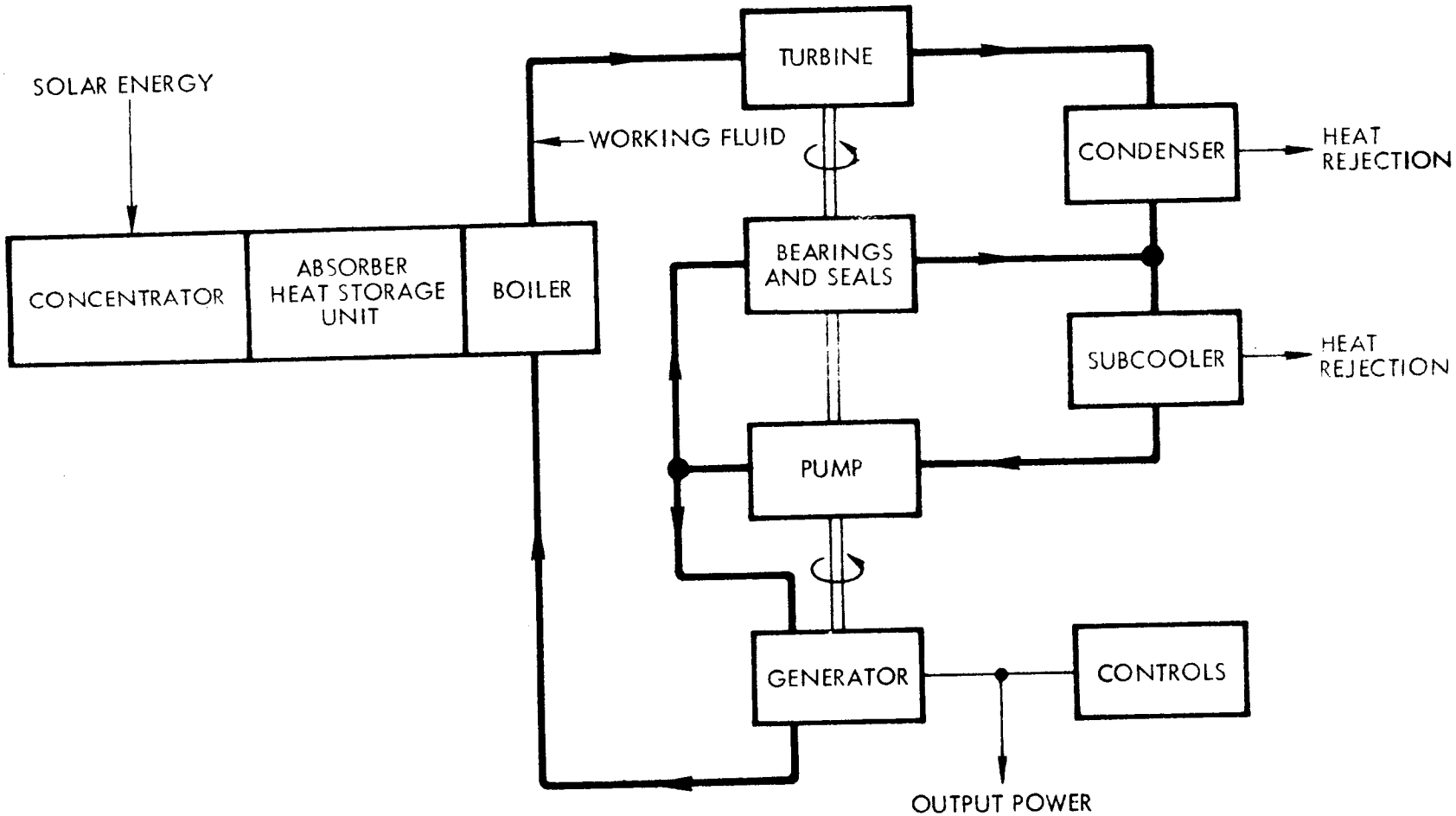

Figure 3-27. Basic Configuration-Mercury Rankine Cycle Solar Dynamic Power Supply

Blocks A, B, and C of the flow diagram define the total power required as the sum of the constant load power (equipment load + dissipative load) and the sensing/control power required for the dissipative load control (assumed constant). Parametric control power data (Figure A5-1) is based on state-of-art solid-state shunt regulation techniques utilizing silicon-controlled rectifiers in a gating mode.

Block D defines generator input shaft power as a simple function of generator efficiency. State-of-art three-phase ac brushless machines achieve full load efficiencies approaching 90 percent. As an example, the measured efficiency of the Sunflower 40,000 rpm, 2000-cps, generator is 87 percent.

Block E, shown in the flow diagram and in Figure A5-2, provides additional shaft power requirements for typical mercury-Rankine systems as a function of electrical power output. These shaft loads include the condensate pump power, bearing losses, and shaft seal losses. Turbine output (Block F) is therefore the sum of the above shaft power requirements.

Condensate subcooling is provided in the pump inlet line to prevent cavitation (see Figure 3-27). Heat rejection rate as a function of rated load is given in Block G (See Figure A5-3). The subcooler also provides for rejection of the pump, bearing, and seal heat losses by the circulating bearing lubrication loop. Generator heat losses are returned to the condensate in the boiler input line. The required heat addition to the working fluid in the boiler, therefore, may be determined as indicated in Block I. The shaft work is divided by the basic cycle efficiency, exclusive of fluid subcooling, to determine the principal heat input requirement. To this is added the fluid subcooling heat requirement minus the generator losses. The basic cycle efficiency is defined as the product of turbine efficiency (shaft power/available thermal power) and the thermal efficiency from Block H.

Determination of turbine efficiency requires detailed unit design computations beyond the scope of this study. Estimated efficiencies for

Sunflower type units vary from approximately 50 percent at 3 kw to 65 percent at 10 kw electrical output. The factors entering into computation of the thermal efficiency (T_c, T_h, and F_c) are determined from analysis of the selected thermodynamic cycle. Specific state points are functions of the working fluid, turbine characteristics, energy storage material, and boiling and condensing pressures. Rankine cycle thermal efficiencies typically approach 90 percent of the Carnot efficiency corresponding to the same nominal boiling and condensing temperatures.

Assuming operation in an orbital mission, the solar input must, of course, supply both the boiler heat requirement and the heat input to the energy storage material for subsequent eclipse operation. This computation is performed in Block T and requires determination of the overall collection efficiency (mirror-absorber efficiency).

Assuming a cavity absorber, collection efficiency is a function of concentrator geometry, accuracy, orientation, and reflectivity as well as cavity aperture dimensions. Efficiency can be plotted as a function of the ratio of aperture diameter to theoretical solar image diameter in the focal plane as shown in Block L and Figure A5-4. Calculated data is provided, based on the paraboloidal Sunflower concentrator which uses a 50-degree 40-minute rim angle. An equivalent 1/2-degree angular surface deviation is considered within the state of the art for a petaline configuration employing aluminum honeycomb sandwich construction. Orientation accuracies of ±1/4 degree are considered achievable with existing orientation system designs. These angular errors will of course cause the focal image to be shifted away from the absorber aperture. The displacement is proportional to the focal length for a given rim angle and therefore will be more severe for a given angular error at increased concentrator diameter and focal length corresponding to increased distance from the Sun. To account for this variation, the angular deviations are normalized to the angle subtended by the solar disc at the given solar distance (AU).

Vacuum-evaporated aluminum film surfaces can achieve total reflectivities (integrated over solar spectrum) of slightly over 90 percent. Negligible data is currently available on surface degradation rates in space; however, severe damage is not anticipated. As a result, a

90 percent concentrator reflectivity at the end of one year in Earth orbit appears to be a reasonable estimate.

The fraction of total reflected energy which enters the cavity increases with increased aperture size; however, the absorber losses due to reradiation from the aperture also increase. The percentage of energy absorbed, therefore, reaches a maximum value at an aperture size that provides an optimum balance between the intercepted energy in the focal plane and the absorber reradiation losses in sunlight. Both the maximum collection efficiency and corresponding aperture diameter ratio can be determined from parametric data presented as shown in Block L. The aperture diameter can then be calculated as shown in Block M for a specific mirror geometry. Since the mirror diameter is not yet defined at this point in the calculation, an estimated value is provided from parametric data for similar collectors (Blocks J and K) (Figure A5-5) and an initial aperture diameter calculated (Block M). Blocks N and O determine the heat storage input requirement as a function of energy withdrawn by the boiler and radiation losses during solar eclipse.

For the petaline concentrator configuration, the outside diameter is a function of required frontal area and concentrator inside diameter. The former is calculated (Block U) as a simple function of the solar power input requirement and the available solar power per unit area at the spacecraft location. The inner diameter is related to absorber diameter by a factor (A) that takes into account the applicable fairing diameter and the number of petals required for the concentrator. Figure 3-28 illustrates the effect of varying the outside-to-inside diameter ratio on the number of petals required. The minimum inside diameter is limited by the absorber (shadow) diameter. The maximum inside diameter is limited by the launch configuration. Optimization of these parameters requires analysis of specific spacecraft configurations; therefore, a factor (A) of 1.5 is assumed for this study.

The absorber diameter is computed from Blocks P, Q, R, and S as a function of energy storage unit dimensions. The energy storage material weight is calculated in Block Q as a function of the energy stored during

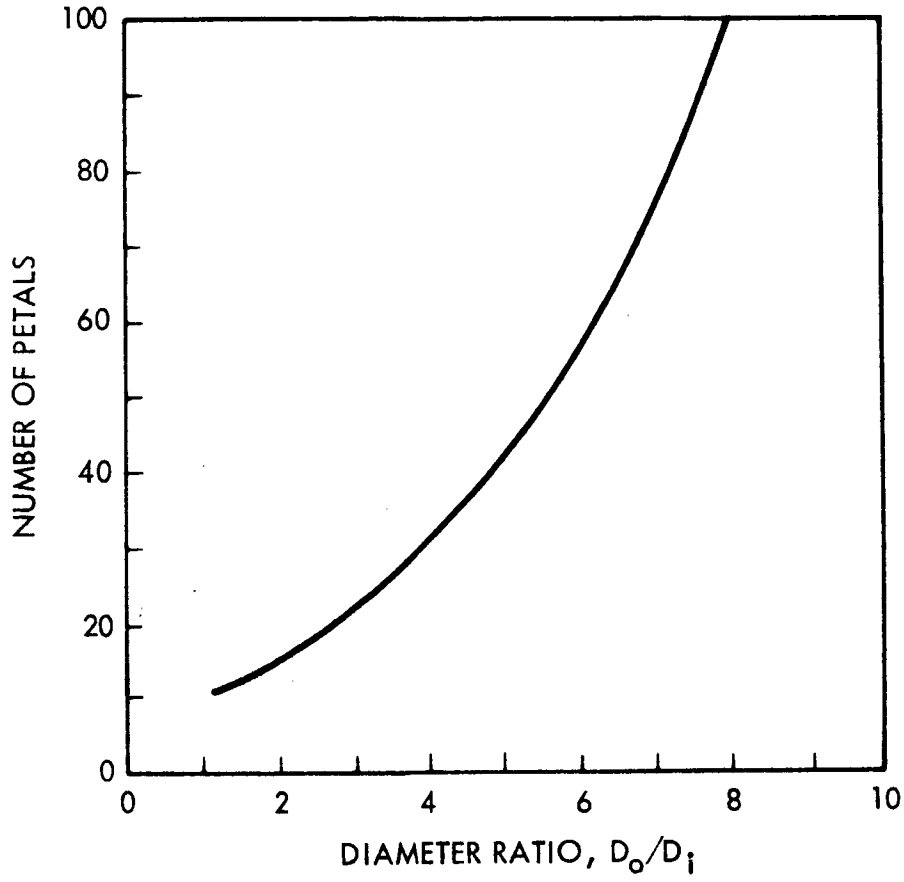

Figure 3-28. Required Number of Petals as a Function of the Ratio of Outside to Inside Concentrater Diameters

sunlight, the total enthalpy change of the material, and (assuming lithium hydride) the added material required to compensate for hydrogen diffusion losses during the mission.

The total enthalpy change is equal to the sum of the latent heat of fusion and the sensible heat addition (Block P) that represents the additional input required to account for the temperature variations of the energy storage material. For a 1250°F fusion temperature, the absorber surface temperature, based on Sunflower test data, can be assumed to cycle from 1250° to 1600°F.

If it is then further assumed that this temperature variation (350 degrees) also represents the change in average temperature of the storage material, the sensible heat addition can be computed (Block P), based on an average specific heat for the material at temperatures near the fusion temperature. For lithium hydride, this value is approximately 1.9 Btu/lb°F or 0.56×10^{-3} kwh/lb°F.

Outgassing and diffusion of hydrogen through the container walls at the elevated lithium hydride storage temperatures can be limited by proper selection of container materials and coatings. During mission durations of a year or more, however, the loss becomes significant in that 8 pounds of lithium hydride must be added to make up each pound loss of hydrogen.

The surface area required for the energy storage material (Block R) is determined from the volume of material, the heat transfer rate required into the boiler, and the corresponding material thickness based on its thermal conductivity. Variations in conductivity of lithium hydride with temperature and phase changes have not been successfully measured in the temperature ranges of interest. As a result, a value has been assumed equal to 0.69×10^{-3} kw/ft^2 °F/ft for both liquid and solid phases. The absorber diameter approximation (Block S) is based on a spherical configuration in which the absorbing area covers one-half of the internal surface.

Since the first concentrator diameter calculation is based on absorber and aperture diameters resulting from an estimated concentrator diameter (Block J), reiteration is now performed using the output of Block U to redetermine these parameters. The iterative process is continued unitl two successive computations yield the same concentrator diameter (Block V). This final value and its corresponding absorber diameter are two of the outputs that define the power supply size. In addition, the concentrator diameter is utilized in Blocks W and X to compute the focal length and concentrator depth, which constitude additional dimensional definition of the power supply.

The radiator-condenser and subcooler heat rejection per unit area are computed (Blocks AA and FF), based on the surface emissivity, rejection temperature, and radiation effectiveness factor η_r. The effectiveness factor takes into account double-sided versus single sided radiation as well as fin effectiveness criteria. Values of $\eta_r = 0.75$ appear reasonable for single-sided radiators based on existing designs. Thermal inputs from solar illumination or planet albedo are neglected in these simplified computations. The former input (solar) should usually be negligible since optimum packaging configurations normally place the radiator surfaces parallel to the solar vector. The second consideration (planet albedo) may constitute a significant radiator input dependent on the required orbital conditions.

The total subcooler heat rejection (Block BB) is assumed equal to the fluid subcooling heat load plus the total shaft power input to the accessories (pump, bearings and seals). The condenser heat rejection computation (Block CC) is based on balancing the system input (boiler) with the system outputs (heat radiated and electric power). Condenser and subcooler areas are then defined (Blocks DD and GG) by the required heat rejection rate and radiation capability per unit area. These two outputs of the computational flow diagram complete the dimensional criteria necessary to determine the power supply configuration and size.

Estimation of total power supply weight is based on parametric weight data for each major component and the supporting structure. These data have been obtained entirely from extrapolations of Sunflower type system designs.

The absorber-heat storage unit weight data is divided into a basic absorber-boiler weight exclusive of energy storage as a function of boiler input power, and heat storage unit weight as a function of heat storage material weight. These two values (Blocks KK and LL) are combined in Block MM to determine total unit weight. (See Figures A5-6 and A5-7.)

Concentrator weight (Block JJ) is determined from the required frontal area and typical weight per unit area criteria supplied by the mirror manufacturer. For paraboloidal concentrators of the size required for power supplies in the 1 to 10 kw range, a specific weight of 0.25 lb/ft^2 appears attainable.

Weight of the rotating units (turbine, generator and pumps) is given as a function of electric power output in Block II (See Figure A5-8). Similarly, controls weight and fluid inventory weight (mercury) are provided as functions of rated load in Blocks OO and NN, respectively. The total component weight (Block Y) is utilized to determine total support structure weight in Block PP. (See Figure A5-11.) The power supply weight is then the sum of structure and total component weight, as shown in Block Z, to complete the computations.

The outputs of the computation reflect a nonredundant power plant configuration. Severe size and weight penalties would appear to preclude the use of redundant solar collectors. It is most probable, however, that redundancy of rotating machinery and fluid-filled radiators is essential to achievement of satisfactory power plant reliability for normal mission durations (1 year minimum). The size and weight of the power plant, therefore, must be modified in proportion to the degree of component redundancy employed for a specific application.

E. POWER SOURCE CONTROL AND CONDITIONING

Such power sources as photovoltaic, solar thermoelectric, solar thermionic, and solar dynamic in the power range studied have electrical output characteristics that require external control and conditioning to assure the required voltage at the battery and power loads. In the case of photovoltaic and flat-plate thermoelectric sources, output voltage can be regulated by partially shunting a portion of the series-connected energy converter string. The shunt method results in minimum heat dissipation in the regulator at the time during the mission when the least amount of power loss can be afforded; the partial-shunt method results in a minimal value of maximum regulator dissipation. For thermionic and dynamic power sources, a partial-shunt control would create an undesirable change in the thermodynamic balance of the converters (see Appendix D). Therefore, these devices usually employ a full shunt (or parasitic load) to maintain optimized design point operating conditions continuously throughout the mission. The computation process for determining the size and performance of power source controls, described herein, is applicable to both partial and full-shunt regulators used on direct energy converters. Controls for the dynamic power sources are discussed in Section D.

Thermionic power sources in the power output range of 100 to 1000 watts consist of only a few series-connected energy converters. As a result, their output voltage is lower than required for high efficiency operation of electronic equipment and other spacecraft power loads. A boost-regulator, therefore, is inserted between the thermionic converter output and the system bus to transform the source voltage to a readily usable value. A computation procedure for a low-voltage input boost-regulator is presented to obtain preliminary system design information.

1. Power Source Controls

a. Design Approach

Three major functional units constitute the power control. They are:

1) Shunt Voltage Regulator Circuit

2) Load Control Logic Circuit

3) Monitoring Circuits

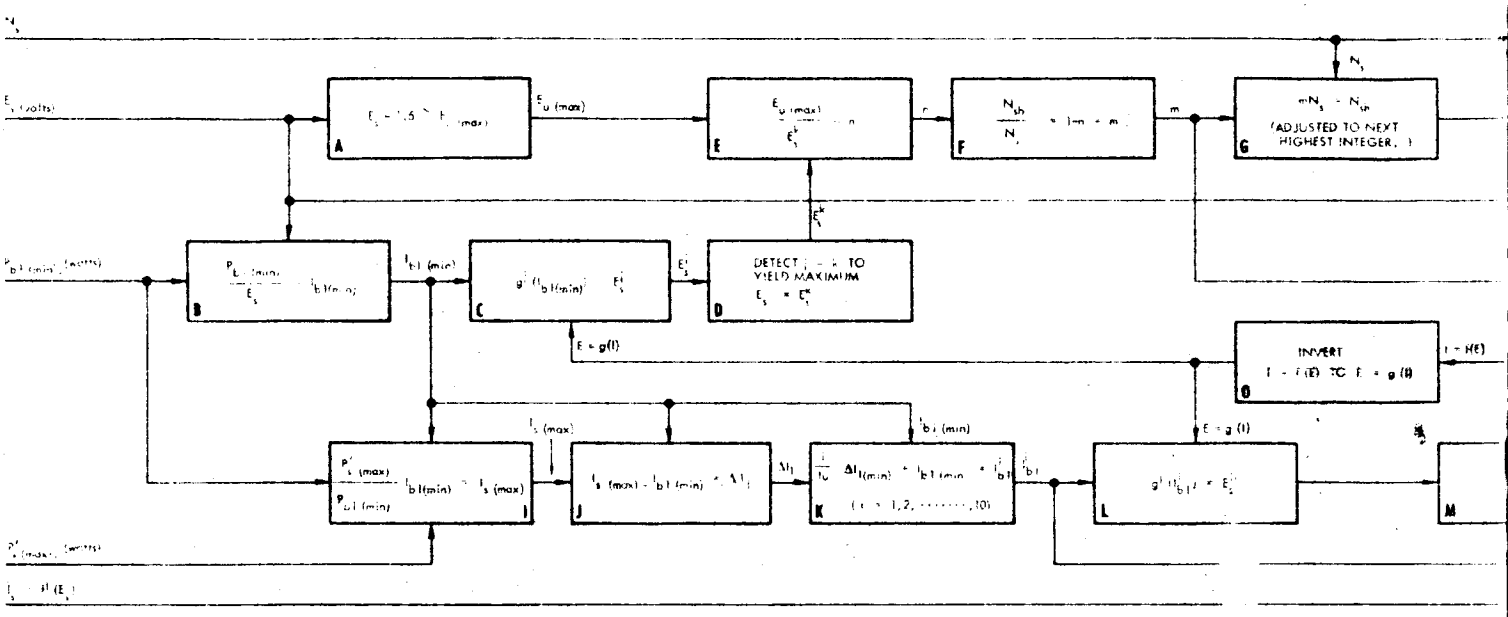

A
B
C
D
E
F
G
H
I
J
K
L
M
DETECT j = k TO YIELD MAXIMUM
(ADJUSTED TO NEXT HIGHEST INTEGER,)
INVERT
E = g(I)

Bus voltage is maintained by means of a shunt regulator operating on the power source. The shunt configuration was selected in preference to series regulators because of its very high efficiency at the design point where the greatest demand, relative to capacity, is made on the source. Redundancy may be used to a great extent in the shunt regulator circuit design. The basic shunt regulator configuration is being used successfully on several spacecraft (OGO, Relay). The partial-shunt regulator scheme was originally developed in 1961 for use in the OGO (Orbiting Geophysical Observatory) spacecraft. A similar configuration has been breadboarded and life-tested. Operating modes of the full-shunt and partial-shunt regulating techniques are compared in Figure 3-29. It may be seen that the maximum dissipation in the partial-shunt regulator is significantly less than the dissipation in the full-shunt regulator.

A shunt regulator configuration may be used for either the photovoltaic, flat-plate thermoelectric or the solar thermionic power sources. A block diagram showing the application of the shunt regulating technique to these power sources is given in the system block diagram of Section II.

As discussed in Section IIIB, the thermionic diode power source requires a full-shunt regulator. However, both the thermoelectric and photovoltaic sources are able to make use of the partial-shunt regulating scheme.

Operation of the shunt regulator is as follows. The source output voltage is sensed and compared to a reference voltage. The error voltage generated is amplified and used to control the current in the dissipative element (redundant transistors) shunting either the whole source or a portion of the source. This current changes the operating voltage of the shunted portion of the source, thereby controlling the total source voltage. The shaded area of Figure 3-29 represents the dissipation in the shunt element. Maximum shunt element dissipation also depends on the tap point selected.

The advantage of any shunt regulator operating from a current source is that it dissipates minimum power when power is not available (e.g., end of life). The unique advantage of the partial-shunt regulator is that it minimizes regulator heat dissipation when the source is new, while at the same time maintaining Class A regulation.

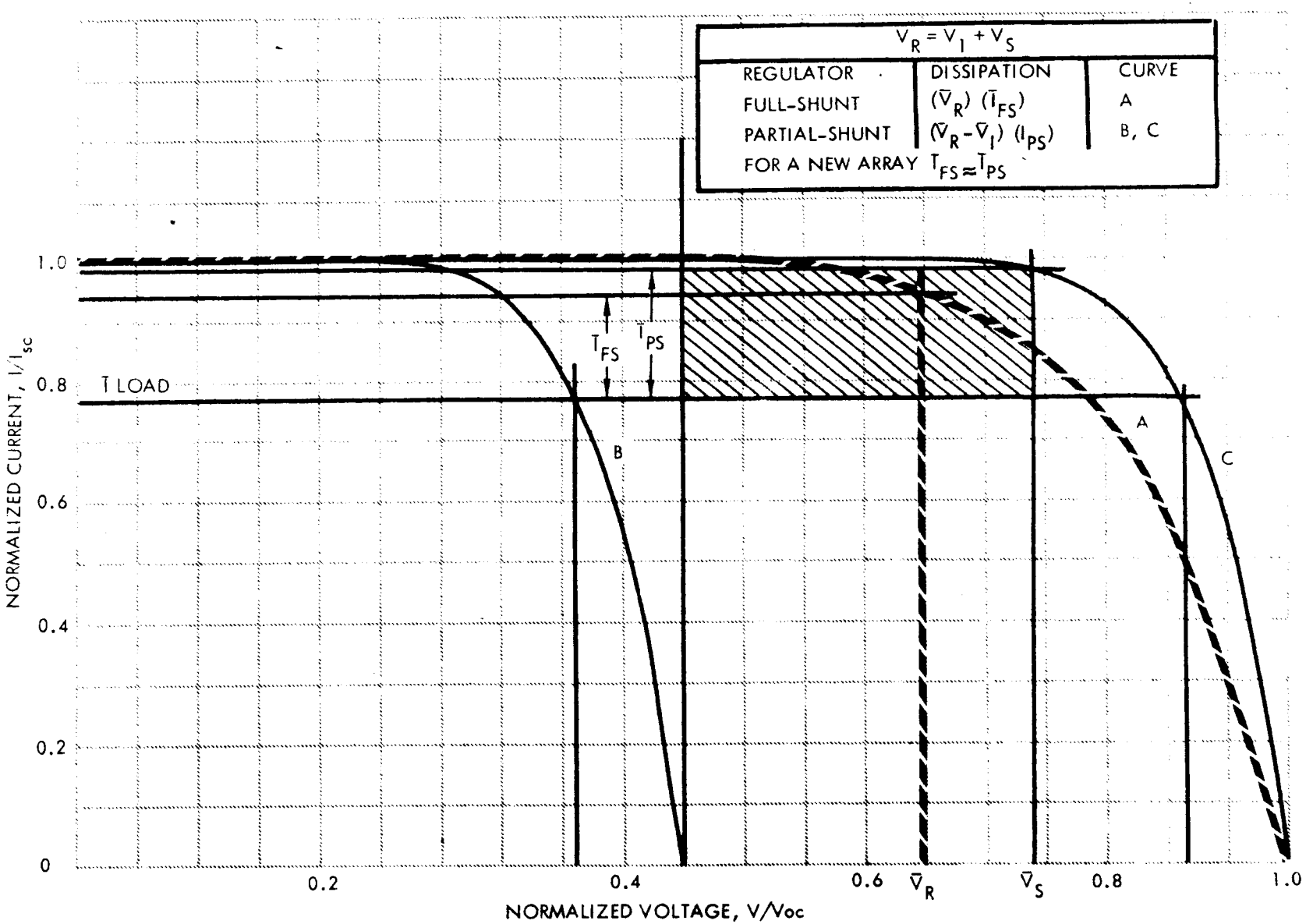

Figure 3-29. Operating Modes of the Full-Shunt and Partial-Shunt Regulators

Monitoring of voltages, currents, and temperatures within the electrical power system is performed with a minimum number of sensors. It is assumed, however, that the number of sensors increases as system power increases and that the power control equipment contains only the sense points necessary to determine the state-of-health of the system. Voltage sensing is accomplished by simple resistive dividers. Current sensing, using dc current transformers, provides maximum accuracy and minimum power loss. These dc current transformers are used on all STL designed statellites and have proven their space worthiness on the Nuclear Test Detection Satellite. Temperature measurements are made with thermistor elements in strategic locations. Thermistors are energized from constant-current sources.

Logic circuitry for load control consists of various sensors operating into solid-state trigger circuits, which in turn control latching relays. Again, it is assumed that the number of trigger circuits and relays increases as the system power level increases.

b. Development of Design Computation Process

The power control design computation diagram is shown in Figure 3-30. The following inputs are required for this computation:

N_s	Total number of series energy converters
E_s	Regulated value of source voltage
$P_{bl(min)}$	Minimum bus power required
$P'_{s(max)}$	Maximum available source power.
$I_s = f^j(E_s)$	Functional relation of source current available to source voltage, for various extremal conditions denoted by j.

Source voltage (E_s) enters the computation at Block A. This yields the maximum value of the unshunted source voltage, $E_{u(max)}$. E_s and the minimum value of bus voltage, $P_{b(min)}$, enter Block B and yield the minimum value of bus current, $I_{fl(min)}$. $I_{fl(min)}$ enters Block C and produces the corresponding value of source voltage E_s^j for various time-mission events, j. The series of values E_s^j enter Block D, which detects the maximum value (at j = k) of E_s^k. E_s^k and the source voltage (E_s) enter

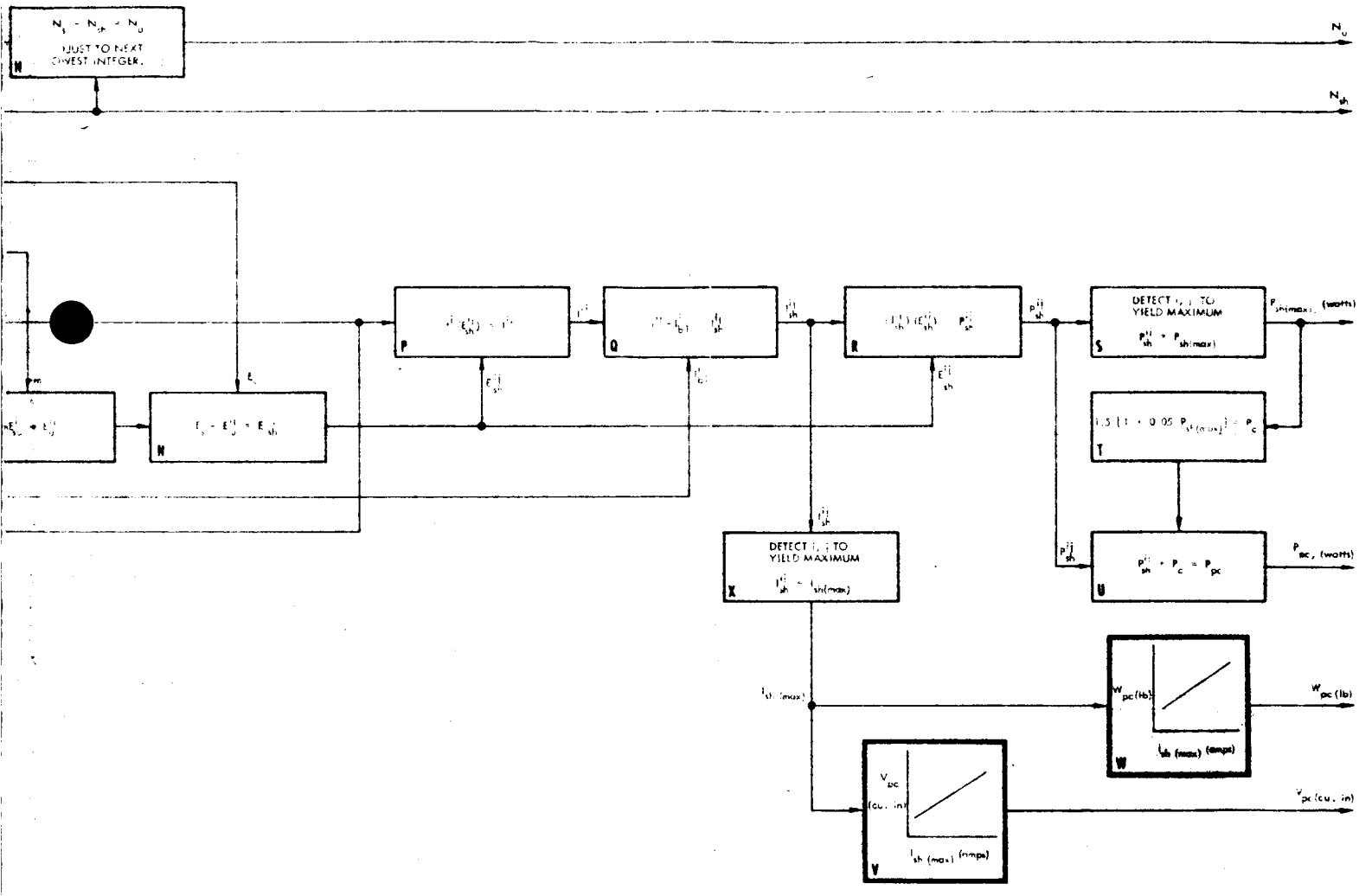

Figure 3-30. Power Control

Block E and give the ratio n (the fraction of unshunted series energy converters). Ratio n enters Block F which yields the shunted fraction, m. Ratio m and the value for N_s (from Source Calculation, Section II) enter Block G and produce output N_{sh}, the number of shunted series energy converters.

The number of total series energy converters, N_s, and the number of shunted series energy converters, N_{sh}, enter Block H and produce output N_u, the number of unshunted series energy converters.

Remaining calculations are given in abbreviated form below:

The sequence, Block I through Block R, accepts inputs of source voltage (E_s), minimum bus power $\left[P_{bl(min)}\right]$, minimum bus current $\left[I_{bl(min)}\right]$, maximum available source power $\left[P_{s(max)}\right]$, ratio m, and the functional relationship, $I_s = f^j(E_s)$. The output of Block I through Block R is P^{ij}_{sh}, the power dissipated in the shunt element for various values of I^i_{bl} and various time-mission events, j.

P^{ij}_{sh} enters Blocks S and U and the maximum value, $P_{sh(max)}$ is determined as an output.

$P_{sh(max)}$ enters Block T which yields P_c, the power dissipated in the monitor and control circuits. P_c and P^{ij}_{sh} enter Block U and yield the output Q_{pc}, the power dissipated in the power control unit.

$I_{sh(max)}$ enters both Block V (see the parametric data in Figure A4-1, and Block W (see the parametric data in Figure A4-2), which yield power control unit volume (V_{pc}) and weight (W_{pc}) respectively.

c. Computation Assumptions

Block A

Computation:

$$E_s - 1.5 \leqq E_{u(max)}$$

The value 1.5 volts dc is an approximation of the total voltage drop across two series silicon transistors in the saturated mode.

Block T

Computation:

$$1.5\left[1 + 0.05\, P_{sh(max)}\right] = P_c$$

This expression is derived from:

$$P_c = \frac{4\,P_{sh(max)}}{K_p} + \frac{P_{sh(max)}}{2\,K_p} + 1.5 \text{ watts}$$

where

$\frac{4\,P_{sh(max)}}{K_p}$ = The drive power required by the redundant quad shunt elements

$\frac{P_{sh(max)}}{2\,K_p}$ = The power required by redundant drive amplifier circuits

K_p = The shunt element power gain.

1.5 watts is a typical value for monitor circuit power loss

therefore

$$P_c = 4.5\,\frac{P_{sh(max)}}{K_p} + 1.5 \text{ and if } K_p = 20$$

$$P_c = 1.5\left[1 + 0.15\,P_{sh(max)}\right]$$

2. Boost-Regulator

a. Design Approach

A brief study has been conducted on boost regulators that are to be used in conjunction with a thermionic/battery power source. The purpose of this study was to determine boost regulator size, weight, and efficiency as a function of load power. A detail design analysis of the thermionic source would be required to determine source voltage. To eliminate this requirement, a basic thermionic generator of 3 vdc, 100-watt capability was assumed. Higher power sources are constructed by series-parallel combinations of this basic module, as given in Table 3-9. A crude correlation between source voltage and source power was also assumed and is given in Figure A4-3. The values in Table 3-9 and Figure A4-3 are used solely for the purpose of preliminary sizing of the boost regulator.

The boost regulator is designed to boost a regulated input voltage to an output voltage limited to the maximum battery charge voltage. Output regulation is proportional to input regulation as provided by a shunt

Table 3-9. Structure of Thermionic Diode Power Sources

P_s (watts)	N_s	N_p	E_s (vdc)
100	1	1	3
200	1	2	3
400	2	2	6
600	3	2	9
800	4	2	12
1000	5	2	15

regulator. The boost regulator contains provisions for controlling its output as a function of battery charge condition. The following component selection and design assumptions are made:

1) Transistors. Low voltage, high current, low saturation resistance germanium transistors. Base plate temperature is limited to 50°C.; h_{fe} = 40 min; I_c = 20 amps; $V_{ce(sat)}$ = 0.1 volt max; switching gain of 10 (used for a conservative guarantee of saturation and fast commutation); rise time $t_r \leq 20$ μsec; base drive voltage of 4 volts (used as a conservative approach to a constant current drive).

2) Rectifiers. Silicon rectifiers with a forward drop of 1.0 volt. (Efficiency could be improved if germanium transistors were used as rectifiers.)

3) Transformers. A power transformer efficiency of 90-95 percent; output voltage of 30 volts (efficiency will be 1 to 3 percent lower if output voltage is 20 volts); converter frequency of 1000 cps (size can be reduced if frequency is increased, but efficiency is simultaneously reduced, because transistor and transformer losses are nearly proportional to frequency).

Table 3-10 shows a summary of booster regulator losses, weight, and volume at power source levels of 100, 400, 600, and 1000 watts at the assumed source voltage given by Table 3-9.

b. Development of Design Computation Process

The boost regulator design computation flow diagram is shown in Figure 3-31. Required load bus power $\left[P_{b(max)}\right]$ and the assumed efficiency (η_o) are used in Block A of Figure 3-31 and to give the required source power P_s. P_s is used to enter Block B (Figure A4-3) and to

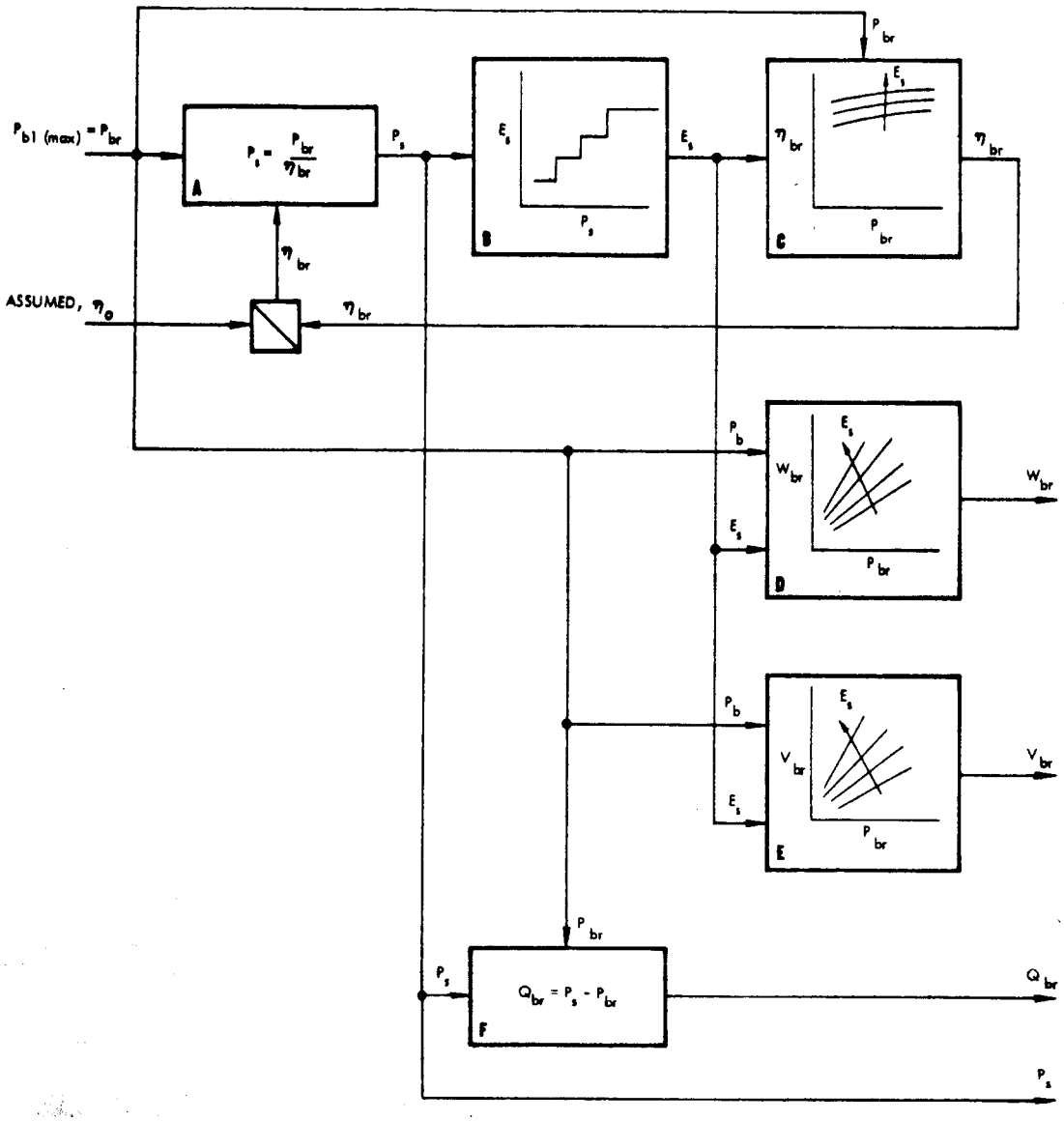

Figure 3-31. Boost Regulator Design Computation Flow Diagram

Table 3-10. Booster Regulator Power Losses

Input			Ratio	Boost-Regulator Losses				Output		Size	
Power P_s (watts)	Voltage E_s (volts)	Current I_s (amp)	$\frac{E_{br}-E_s}{E_{br}}$	Transistor (watts)	Driver (watts)	Transmitter (watts)	Rectifier (watts)	Power P_{br} (watts)	Efficiency η_{br} (percent)	Weight W_{br} (lb)	Volume V_{br} (in.^{3})
100	3	33.3	0.9	2.7	12.0	8.6	2.5	72	72	3.4	100
400	6	66.7	0.8	7.0	21.3	25.6	11.5	335	84	8.8	234
600	9	66.7	0.7	7.9	18.7	29.4	18.1	526	88	10.9	284
800	12	66.7	0.6	8.4	16.0	28.8	24.9	722	90	12.5	322
1000	15	66.7	0.5	8.3	13.4	25.0	31.7	922	92	13.0	332

yield source voltabe (E_s) $P_{b(max)}$ and P_s also enter Block F and this yields the regulator dissipation, Q_{br} Source voltage (E_s) and bus power $P_{b(max)}$ enter Block C (Figure A4-4), to give a value of efficiency, η_{br}, which replaces the assumed efficiency, η_o The computation is then repeated with the new value of efficiency. E_s and $P_{b(max)}$ also enter Blocks D and E, (Figures A4-5 and A4-6) to yield booster regulator weight, W_{br}, and booster regulator volume, V_{br}.

BIBLIOGRAPHY AND REFERENCE LIST

Section IIIA. Solar Photovoltaic Sources

3-1. Bichsel, H., Physical Review, 112, 1089 (1958), and unpublished calculations.

3-2. Brown, G. L., "The Effect of 1 Mev Electron Bombardment on the Optical Properties of Hoffman N-on-P Solar Cells and Covers," TRW/STL Report No. 8566-6007-RU000; 11 October 1963.

3-3. Denney, J. M., "Preliminary Flight Results Satellites 1963-14B, 1963-14C and 1963-30B," TRW/STL Report No. 8685-6005-KU000; 14 January 1964.

3-4. Denney, J. M. and R. G. Downing, "Charged Particle Radiation Damage in Semiconductors, VIII: The Electron Energy Dependence of Radiation Damage in Photovoltaic Devices," STL Report No. 8653-6025-KU000; 15 July 1963.

3-5. Denney, J. M., et al., "Charged Particle Radiation Damage in Semiconductors, V: Effect of 1 Mev Electron Bombardment on Solar Cells," STL Report No. 8653-6018-KU001; 11 February 1963.

3-6. Johnson, F. S., "The Solar Constant," J. Meteorology, Vol. 1, p. 431; 1954.

3-7. Klein, W. A., "The Reliability of Solar Arrays," paper presented at 1962 National Winter Convention on Military Electronics, IRE; 7 February 1962.

3-8. Luft, W. and J. Sonies, "The Effect of 1 Mev Electron Bombardment on the Electrical Characteristics of N-on-P Silicon Solar Cells and Cell-Cover Assemblies," TRW/STL Report 2315-6007-KU000; 11 February 1964.

3-9. Martin, J. H., J. W. Teener and E. L. Ralph, "Some Effects of Electron Irradiation and Temperature on Solar Cell Performance," 17th Annual Power Sources Conference; 21-23 May 1963.

3-10. Ralph E. L. and P. Berman, "Silicon Cell for Use in Concentrated Solar Energy," 17th Annual Power Sources Conference; 21-23 May 1963.

3-11. Wolf, M. and H. Rauschenbach, "Series Resistance Effects on Solar Cell Measurements," AIEE Conference Paper CP61-1006, Presented at Pacific General Meeting of AIEE, Salt Lake City, Utah; 23 to 25 August 1961.

Section IIIB. Solar Flat-Plate Thermoelectric Generator

3-12. Campana, R.J., "Status Report on General Atomic Flat-Plate Thermoelectric Space Power Systems," Report No. GA-3519, General Atomic Division of General Dynamics, San Diego, California; 5 October 1962.

3-13. Campana, R.J. and L.W. Perry, "Preliminary Design and Performance Evaluation Study of a 300-W(E) Long-Lived Thermoelectric Space Power Converter," Report No. GA-2336, General Atomic Division of General Dynamics, San Diego, California; 19 March 1962.

3-14. Campana, R.J. and J.B. Roes, "Preliminary Design and Performance Evaluation Study of a Solar Thermoelectric Flat Plate Generator," Report No. GA-1924, General Atomic Division of General Dynamics, San Diego, California; 5 January 1961.

3-15. Chang, S.S.L., Energy Conversion, International Series in Electrical Engineering, Prentice-Hall, Inc., Englewood Cliffs, New Jersey; 1963.

3-16. "Flat-Plate Solar Thermoelectric Conversion Panels," Final Report No. ASD-TDR-62-214, Aeronautical Systems Division, Dir/Aeromechanics, Flight Accessories Lab, Wright-Patterson AFB, Ohio; May 1962.

3-17. "Flat Plate Solar Thermoelectric Generator Orbital Experiment," Final Report No. ASD-TDR-63-479, Aeronautical Systems Division, AF Aeropropulsion Laboratory, Flight Vehicle Power Division, Wright-Patterson AFB, Ohio; May 1963.

3-18. Private Communication with Messrs. Pidd, Perry, Campana, and Haflinger of the General Atomic Division, General Dynamics, San Diego, California.

Section IIIC. Solar Thermonic Sources

3-19. "Advanced Solar Thermionic Generators," First Quarterly Technical Progress Report, Contract AF 33(657)-8947, General Electric; December 1962.

3-20. "Advanced Solar Thermionic Power Systems," ASD-TDR-62-877; December 1962.

3-21. Blake, F.A., "Calibration of Solar Concentrator for Use in Power System Research," ARS Paper No. 2528-62.

3-22. "Cavity Vapor Generator Program," ASD-TDR-62-899; December 1962.

3-23. "High Temperature Solar Thermionic Generators," First Quarterly Technical Report. Contract AF 33(657)-11169, Tapco Division, TRW, Inc., 15 August 1963.

3-24. Leovic, W.J., Mueller and G.G. Stevenson, "Performance Test of Cubical Cavity Solar Thermionic Generator," ARS Paper No. 2554-62.

3-25. "Long-Life Thermionic Converters for Solar Power Systems," ASD-TDR-62-1069; February 1963.

3-26. Mena, S.G. and J.H. Weinstein, "Recent Progress in the Development of Solar Thermionic Converters," presented at 1963 Thermionic Conversion Specialist Conference, Gatlinburg, Tennessee; October 1963.

3-27. Menetrey, W.R. and A. Smith, "Solar Energy Thermionic Conversion System," ARS Paper No. 2499-62.

3-28. Purdy, D.L., "Thermionic Cavity Generator Development," Power Systems for Space Flight, Academic Press, p. 791; 1963.

3-29. Purdy, D.L., "Thermionic Cavity Generator Development," ARS Paper No. 2572-62.

3-30. Rouklove, Peter, "Results on Laboratory Test of Thermionic Converters and Generators," presented at 1963 Thermionic Conversion Specialist Conference, Gatlinburg, Tennessee; October 1963.

3-31. Smith, A.H., "Thermionics: Auxiliary Power Application for Space," ASME 63-MD-54; May 1963.

3-32. "Solar Concentrator Development Status at TRW," Technical Memorandum 3345-68, Tapco Division, TRW, Inc.

3-33. "Solar Energy Thermionic Conversion System," Final Report for period 22 May to 22 November 1961, Contract JPL 950109, NASA7-100, Electro-Optical Systems, Inc.

3-34. "Solar Energy Thermionic Conversion System," Final Report for period 21 May 1961 to 12 November 1962, Contract JPL 950109, NASA7-100, Electro-Optical Systems, Inc.

3-35. "Solar Thermionic Electrical Power System," ASD-TDR-62-94; April 1962.

3-36. "Solar Thermionic Power Conversion System for Planetary Spacecraft," Report ER-4378, Tapco Division TRW, Inc; 17 March 1961.

3-37. "Stowage and Deployment Concepts for Solar Concentrators for Space Power Systems," Report ER-5364, Tapco Division, TRW, Inc; 24 May 1963.

3-38. "A Preliminary Vehicle Installation Study for Project Sunflower," 8th Symposium on Ballistic Missile and Aerospace Technology, Volume III, Academic Press, Inc., New York, N.Y.; 1961.

3-39. "A Study of Advanced Solar APU Systems," Final Technical Report SY-5183-R, The Garrett Corporation, AiResearch Manufacturing Division; 1 June 1960.

3-40. Boretz, J.E., "Survey of Space Power Systems," TM3604-20, Tapco Division, TRW, Inc; 31 January 1963.

3-41. "Energy Conversion Systems Reference Handbook," WADD Technical Report 60-1699; Syst 1960.

3-42. Heath, A.R., Jr., "Status of Solar Energy Collector Technology," ARS Paper 2331-62, NASA Langley Research Center; September 1962.

3-43. Investigation of a 3 kw Sterling Cycle Solar Power System, WADD TR 61-122.

3-44. Norman, L.W., "The Application of the Recuperated Brayton Cycle to Space Power Conversion Systems," AIAA Paper 63-220, AiResearch Manufacturing Company; June 1963.

3-45. Nowlin, W.D. and H.E. Benson, "Study of Umbrella-Type Erectable Paraboloidal Solar Concentrators for Generation of Spacecraft Auxiliary Power," NASA TN D-1368, Langley Research Center; August 1962.

3-46. Leon, Schipper, "Wright Optimization of a Solar or Nuclear Mechanical Conversion System," WADC Technical Note 59-180, Aeronautical Accessories Laboratory; June 1959.

3-47. "Solar Concentrator Development Status at TRW," Technical Memorandum 3345-68, Tapco Division, TRW, Inc.

3-48. "Space Power Systems," Lecture Notes, Course X494MN, UCLA; July 1961.

3-49. "Sunflower Power Conversion System - Quarterly Report," ER-4715, Tapco Division, TRW, Inc; September-November 1961.

3-50. "Sunflower Power Conversion System - Quarterly Report," ER-5044, Tapco Division, TRW Inc; June-August 1962.

3-51. "Sunflower Power Conversion System - Quarterly Report," ER-5163, Tapco Division, TRW, Inc; September-November 1961.

IV. ELECTROCHEMICAL SOURCES

A. PRIMARY SILVER-ZINC BATTERIES

Primary silver-zinc batteries are available in two basic varieties, the manually and the automatically activated. Both are dry charge batteries. The electrolyte is stored external to the cells and is dispensed to each cell immediately before use. The anode and cathode are completely formed, requiring no charging.

The automatically activated battery has the electrolyte stored within the battery package in a special reservoir equipped with a distribution manifold. A pyrotechnic gas generator builds up a pressure in the reservoir, breaks a frangible diaphragm, and forces the electrolyte into the cells. By means of an initiating electrical pulse, the battery can be activated remotely and automatically in a matter of seconds.

The manually activated battery is activated by pouring electrolyte through an opening at the top of each cell. Both types are variable in wet stand time, depending upon the number and thickness of cellulose separators used, the time required for activation being directly variable with the required wet stand time. In general, the cells, although of standard case size, are usually tailor-made to the desired application.

1. State of Development

Primary silver-zinc battery cells can be manufactured to contain up to 100 watt-hours per pound in the larger cell sizes, although it is somewhat difficult to achieve this level of power density in any but the largest and simplest of batteries.

Voltage regulation in a single discharge of a primary silver-zinc battery can be improved by heat treatment of the positive plates prior to assembly into the cell. This creates a high resistance layer of silver ^{I} oxide between the silver^{II} oxide and the metallic silver current collector and, in effect, drops the excess voltage internally. This lost energy appears as heat within the battery cell.

In the longer life forms, the primary battery may be used as a secondary battery for a limited number of discharges, but the voltage regulation initially available on the first discharge is not reproducible on recharge.

2. Systems Applications

The primary battery is designed for a single use and is thereafter discarded. The automatically activated types are generally applied to high energy short time applications in which instant readiness for use is a critical requirement.

The manually activated battery is applied where the requirement for instant readiness is not important, or where it is outweighed in importance by other factors, such as critical weight requirements, unavailability of an activating pulse, or a requirement for wet stand time that makes the design of an automatically activated battery difficult to implement due to the long filling time.

3. Development of the Design Computation Process

The computation process for the primary battery is designed to estimate the weight of a primary battery, either automatically activated or manually activated, feeding a bucking type regulator as shown in the block diagram of Figure 4-1. The steps of the calculation are as follows:

1) The calculation is initiated by dividing the total mission load power profile into n unequal time intervals Δt_i during which the power P_i delivered to the load is a constant (Block A*).

2) A value of overall converter efficiency, η is assumed, ($\eta = 0.8$).

3) A value of load voltage is derived from the load voltage requirements (E_L).

4) In order to provide for a voltage drop through the converter-regulator, 1 volt is added to the load voltage required. This provides a preliminary estimate of the terminal voltage of the battery (Block C).

Input, E_L

$$E_b = E_L + 1.0$$

Output, E_b

*The blocks referenced in Subsection IV. A are shown in Figure 4-1.

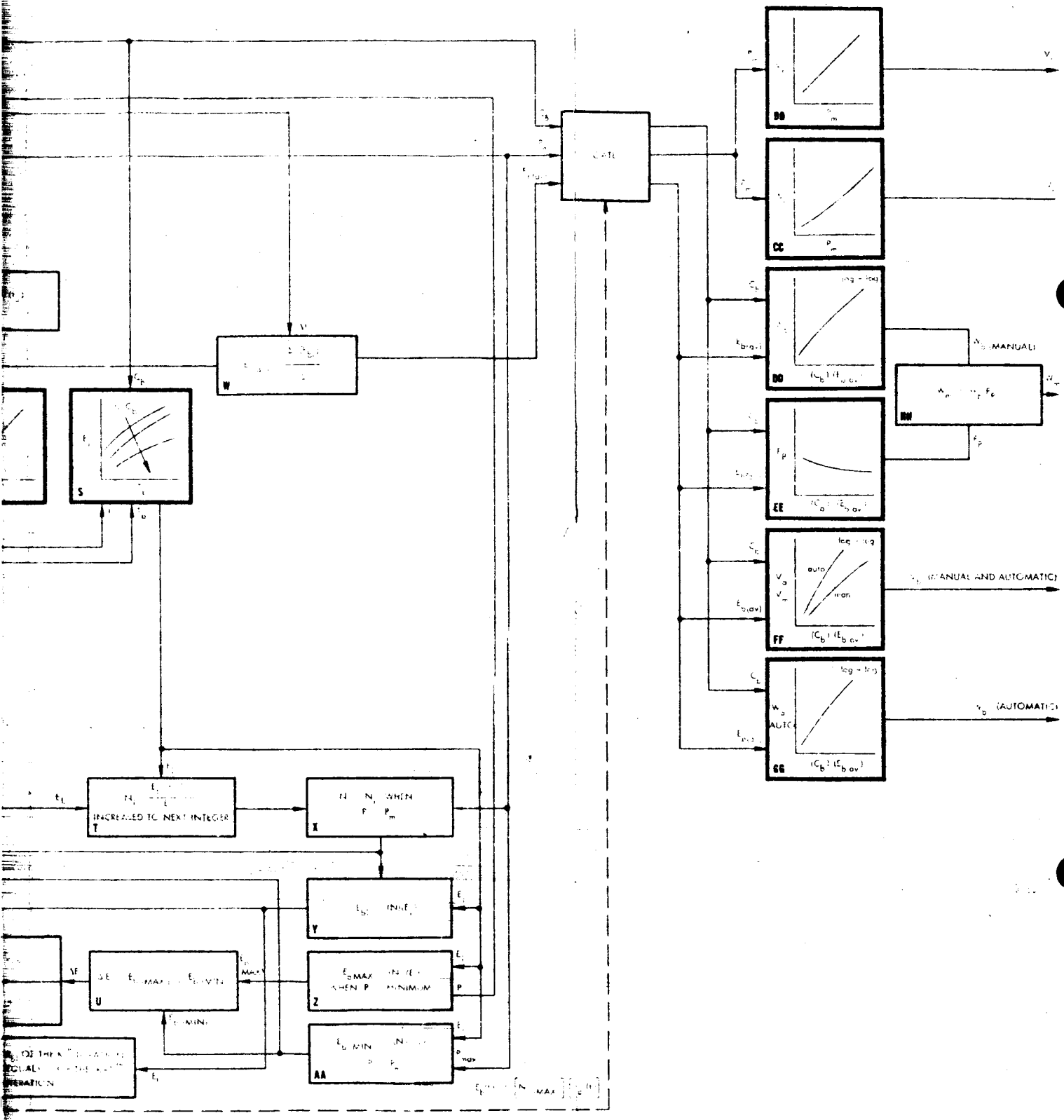

Figure 4-1. Primary Battery and Regulator Design Computation Flow Diagram

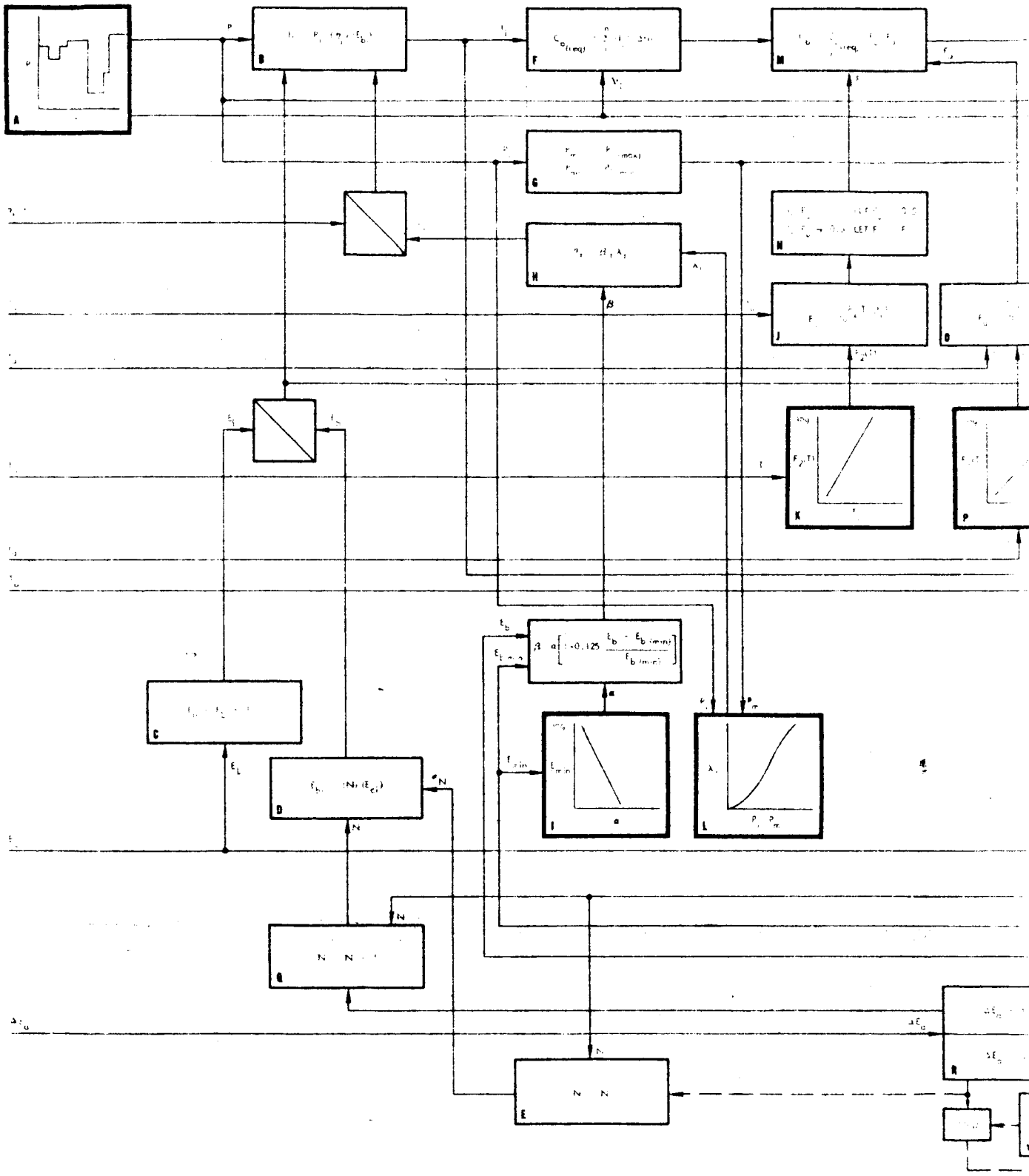
A
B
F
M
G
H
N
J
O
K
P
C
D
I
L
Q
E
R

5) The current I_i corresponding to P_i is calculated (Block B)

Input, P_i (from 1)

η (from 2)

E_b (from 3)

$$I_i = \frac{P_i}{\eta_i E_b}$$

Output, I_i

6) A preliminary estimate of total battery cell capacity required is obtained (Block F)

Input P_i, Δt_i (from 1)

I_i (from 5)

$$C_b\,(\text{req}) = \sum_{i}^{n} (I_i\,\Delta t_i)$$

Concurrently with these six steps of the program, the storage deterioration factors are calculated. Storage is divided into (a) unactivated or dry storage and (b) activated or wet storage. The wet storage period includes the total storage time between activation of the battery by introduction of the electrolyte and the end of the mission. Since the temperature of the activated storage affects deterioration rate, the temperature coefficient f_1 (T) is read out, assuming a constant storage temperature

7) Block P

Input, see Figure A6-1.

T_a - temperature of activated storage (original)

readout $f_1(T)$

Output, $f_1(T)$

8) The fraction of capacity remaining after activated storage is calculated (F_a) (Block O).

Input, $f_1(T)$ (from 7)

t_a - time of activated storage (original)

$$F_a = \left(1 - \frac{1}{10^{f_1(T)t_a}}\right)$$

Output, F_a

Similarly, the temperature coefficient, $f_2(T)$ and F_u are calculated for unactivated or dry storage.

9) Block K.

Input, Figure A6-2

T_u - unactivated storage temperature (original)

readout $f_2(T)$

Output, $f_2(T)$

10) Block J.

Input, $f_2(T)$ (from 9)

t_u - Time of activated storage (original)

$$F_u = \left(1 \quad \frac{1}{10^{f_2(T)t_u}}\right)$$

Output, F_u

Since loss of capacity in dry storage occurs because of thermal decomposition of the divalent silver oxides, which comprise only half the electrical capacity of the cell, F_u may not be less than 0.5.

11) Compare F_u, 0.5 (Block N)

Input, F_u (from 10)

If $F_u < 0.5$, let $F_u = 0.5$

If $F_u \overline{<} 0.5$, let $F_u = F_u$

Output, F_u

A preliminary estimate of installed capacity may now be made.

12) Block M.

Input, C_b (req) (from 6)

F_a (from 8)

F_u (from 10)

$$C_b = \frac{C_b \text{ (req)}}{F_a F_a}$$

Output, C_b

Based upon the preliminary capacity estimate, the load voltage of the individual battery cells is determined as a function of current and temperature.

13) Block S.

Input, I_i (from 5)

T_b (original)

C_b (from 12)

Read out E_i

The number of cells required to provide a plateau voltage equal to E_b is determined.

14) Block T.

Input, E_i (from 13)

E_L (Original)

$$N_i = \frac{E_L + 1.0}{E_i}$$

This value is increased to the next higher integer

Output, N_i (integer)

The minimum and maximum power levels are determined.

15) Block G.

Input, P_1, P_2 - - - P_n , P_i

Find P_{max}

Find P_{min}

Output, $P_{i(max)}$, $P_{i(min)}$

The maximum number of cells is found by readout of N_i (from 14), when P_i is a maximum. Input N_i (from 14) $P_{i\ max}$ (from 15)

16) Block Z.

$$N = N_i \ (P_i = P_{max})$$

The maximum and minimum battery voltages are calculated and the difference compared with the voltage range allowable at the input to the converter.

17) Blocks Y and Z.

Input, E_i (from 13)

N

$P_{i(max)}$

$P_{i(min)}$

$$E_{bi} = N\ E_i \qquad (P_i)$$

$$E_{b(max)} = N\ E_i \qquad \left[P_i = P_{i(min)}\right] \qquad \text{(Block Y)}$$

$$E_{b(min)} = N\ E_i \qquad \left[P_i = P_{i(max)}\right] \qquad \text{(Block Z)}$$

Output, $E_{b(max)}$, $E_{b(min)}$ E_{bi}

18) Block U.

Input, $E_{b(max)}$, $E_{b(min)}$ (from 17)

$$\Delta E = E_{b(max)} - E_{b(min)}$$

19) Block R.

Input, ΔE (from 18)

ΔE_a (original)

Compare $(\Delta E_a - \Delta E)$ 0

If $[\Delta E_a - \Delta E] \geq 0$, let N = N (Block E)

If $[\Delta E_a - \Delta E] < 0$, let N = N - 1 (Block Q

A reduction in the number of series cells reflects as a reduction in voltage, causing an increase in current and a consequent increase in capacity, resulting in improved regulation.

20) On the first iteration, no test can be made. On all subsequent integrations (Block V),

E_b of the Kth iteration and

E_b of the $K - 1^{th}$ iteration are equal

and

$$\Delta E_a - \Delta E \geq 0$$

the iterative portion of the calculation is complete and the weights and volumes are read out

The minimum design voltage of the converter is assumed to be equal to $E_{b(min)}$ and a converter efficiency factor, α, is read out.

21) Block I.

Input, $E_{b(min)}$ from 17 (Figure A 6-4).

Read out a

A converter efficiency factor, β, due to voltage drop through the converter is calculated.

22) Block JJ.

Input, α (from 21)

E_{bi}, $E_{b(min)}$, from 17

$$\beta = \alpha \left[1 - 0.125 \frac{E_{bi} - E_{b(min)}}{E_{b(min)}} \right]$$

Output β

A converter efficiency factor, λ, due to operation of the converter off the design power level is read out.

23) Block L.

Input, P_i (from 1), see Figure A6-5.

$P_{i(max)}$ (from 15)

$$\text{Read out } \lambda = F\left(\frac{P_i}{P_{i(max)}}\right)$$

Output, λ

A revised estimate of overall converter efficiency is obtained.

24) Block H.

Input, β (from 22)

λ (from 23)

$$\eta_i = \beta_i \lambda_i$$

Output, η_i (replaces η used in the last iteration)

25) A revised estimate of E_{bi} is obtained (Block B).

Input, E_i (from 13)

N (from 19)

$$E_{bi} = E_i N$$

Output, E_{bi}

Replaces E_{bi} used in last iteration

26) Using new E_{bi}, η_i,

Return to Step 5) for the next next iteration

27) Continue iterations until the criteria of Step 20 are satisfied (Block V).

28) Then Input, $P_{i(max)}$ (from 15)

Read out regulator volume and weight (Blocks BB, CC, Figure A6-6)

29) An average voltage is found (Block W)

Input, E_{bi} of the last iteration (from 17)

$$E_b(AV) = \frac{\sum_{i}^{n} E_{bi}}{n}$$

Output, $E_b(AV)$

30) Input, E_b (AV) (from 29)

C_b of the last iteration

Read out

Weight of unpackaged manually activated battery, (Block DD).

$W_b = f\ [C_b \times E_b(AV)]$ (Figure A6-7) (Block EE)

Packaging factor (Figure A6-8) $F_p = f\ [C_b \times E_b(AV)]$

Volume of batteries (Figure A6-9 and A6-10) $V_m,\ V_a = f\ [C_b \times E_b(AV)]$ (Block FF)

Weight of automatically activated battery (package) (Figure A6-11) $W_a = f\ [C_b \times E_b(AV)]$ (Block GG)

31) Calculate manually activated battery weight:

Input, F_p (from 30)

W_d (from 30)

$$W_m = W_b F_p$$

Output, W_m

B. SECONDARY SILVER-ZINC BATTERIES

The silver-zinc battery is the highest energy density electromechanical energy source presently available for practical use in aerospace applications. Its use as a secondary battery has somewhat restricted applicability because of the relatively small number of cycles available before deterioration or perforation of the separator or some other cause results in battery failure. The properties of the cells are variable between manufacturers and within the product lines of the individual manufacturers, since the thickness of cellophane separators, the number of layers of separator, and the thickness of the electrode are all varied by manufacturers to fit the requirements of the application in current density, storage life, number of cycles available, and so on.

1. State of Development

Silver-zinc secondary cells are in a fairly advanced stage of development and are now available from several manufacturers in both sealed and vented form with short life, high power density characteristics and long life, lower power density capability. They are capable of approximately ten full depth discharges followed by low rate (C/20 - C/40) charge, terminating at 1.9 to 2.0 volts per cell. For the purposes of this study, the longer life form of cell has been treated, although the higher power density form could be sized with this program if suitable data substitutions were made.

2. Systems Application

The most attractive application for the silver-zinc secondary is as the energy storage unit in a Mariner-Ranger type of mission, in which a few large blocks of power are required at widely spaced intervals. This permits full advantage to be taken of the high energy density available from the silver-zinc system and is not seriously affected by the two major shortcomings of the system: the low cycle life and the requirement for extremely low charging currents.

3. Development of Design Computation Process

The computation begins with the total mission power profile, which is divided into successive time intervals, Δt_i, during which the load power requirement, P_i, is a constant.

1) Divide the total mission into n unequal time intervals, Δt_i during which P_i is constant (Block A*).

The energy removed from or restored to the battery during each time interval is calculated. For this purpose, an available charging current from the primary energy source is assumed. The charge and discharge voltage are assumed to be identical and equal to the source voltage. While this is unrealistic from the standpoint of spacecraft design, its effect upon battery weight and sizing calculations is negligible.

2) Calculate energy flow into and out of battery (Block B).

Inputs, $P_i = P_1, P_2 \cdots P_n$

$\Delta t_i = \Delta t_1, \Delta t_2 \cdots \Delta t_n$

I_s = Primary source current

E_b = Battery voltage

Calculation (Block B):

$$\epsilon_I = (I_s E_b - P_i)\Delta t_i$$

Output, $\epsilon_i = \epsilon_1, \epsilon_2 \cdots \epsilon_n$

The energy withdrawn from or restored to the cell during each time interval is then grouped into successive intervals of charge and discharge by adding all successive energy blocks having the same sign, until a sign reversal occurs. Thus, if throughout time intervals $\Delta t_i, \Delta t_2 \cdots \Delta t_a$. the signs of $\epsilon_1, \epsilon_2 \cdots \epsilon_a$ are all negative, representing a discharge of the battery, and ϵ_{a+1} is positive representing a recharge, then the sum, Σ_1, of these energies represents the maximum depth to which the battery is discharged during the time interval $\Delta t_1 \rightarrow t_a$.

Similarly, the sum Σ_2 of these energies of positive sign $\epsilon_{a+1} - \epsilon_b$ represents the total energy restored to the battery during charge time interval $\Delta t_{a+1} - \Delta t_b$.

3) Calculate depth of discharge and recharge during each section of the mission (Block C).

*The blocks referenced in Subsection IV.B are shown in Figure 4-2.

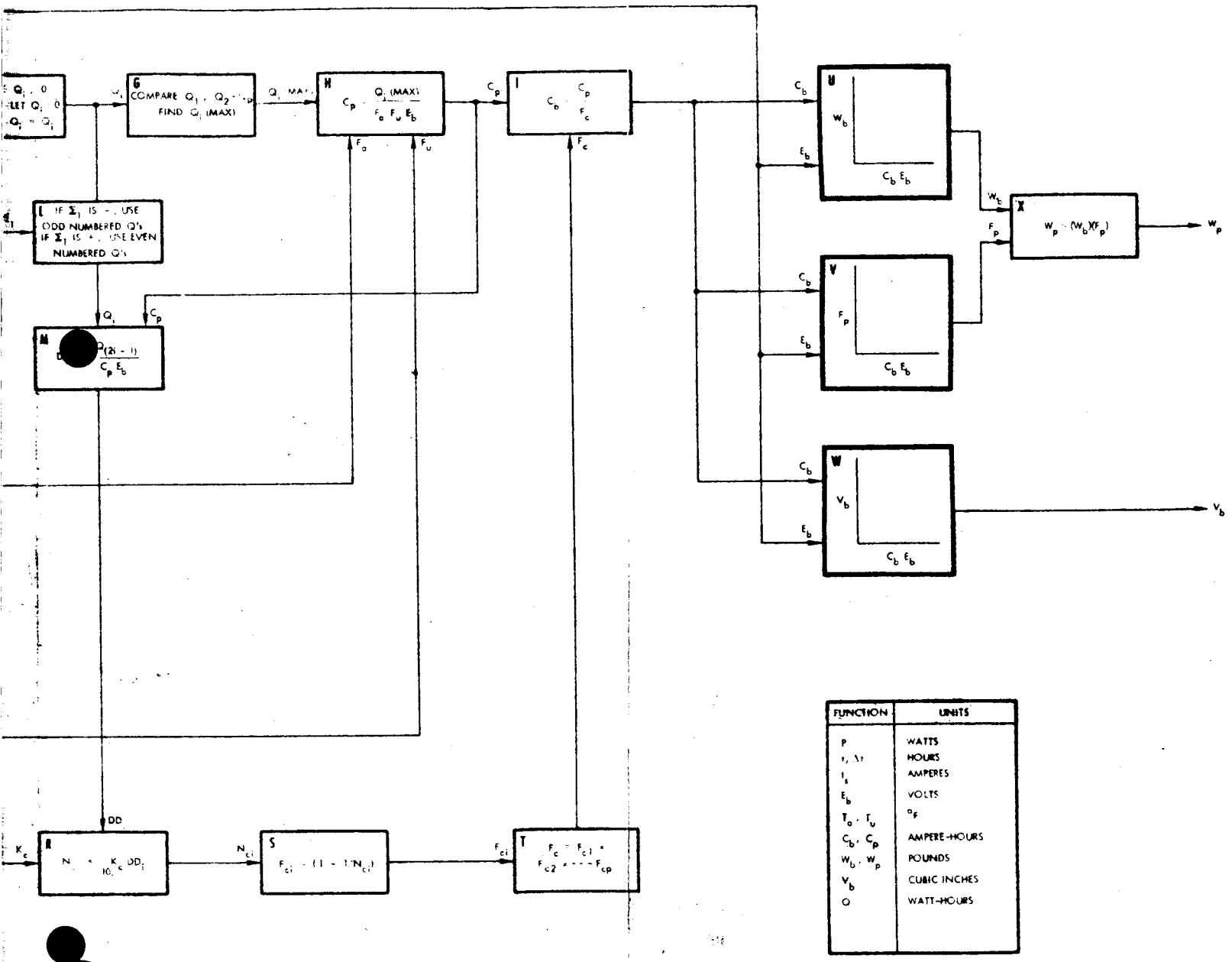

FUNCTION	UNITS
P	WATTS
t, Δt	HOURS
I_s	AMPERES
E_b	VOLTS
T_o, T_u	°F
C_b, C_p	AMPERE-HOURS
W_b, W_p	POUNDS
V_b	CUBIC INCHES
Q	WATT-HOURS

Figure 4-2. Secondary Silver-Zinc Battery Flow Diagram

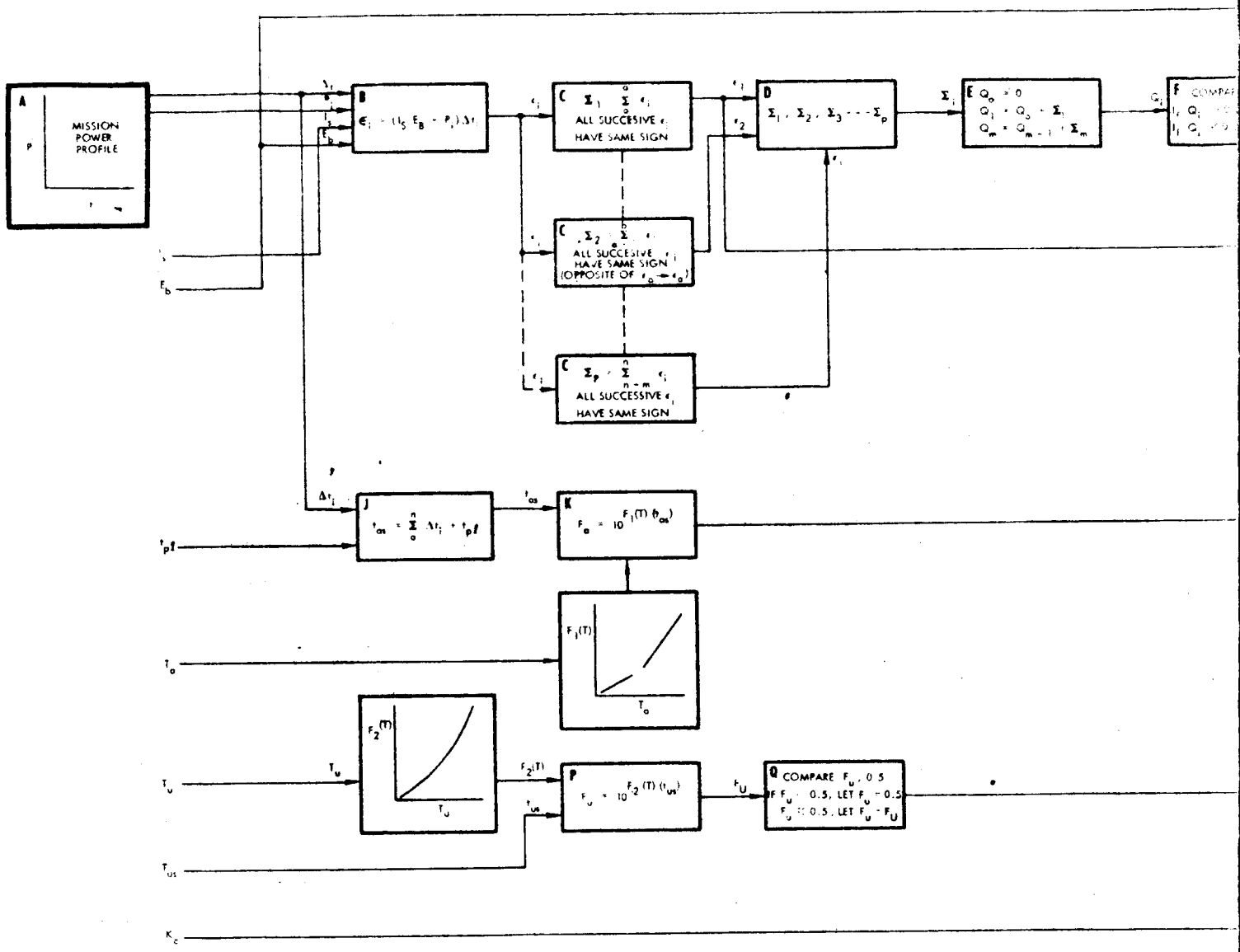

A
MISSION POWER PROFILE
B
C
ALL SUCCESIVE
HAVE SAME SIGN
D
E
F
ALL SUCCESIVE
HAVE SAME SIGN
(OPPOSITE OF
ALL SUCCESSIVE
HAVE SAME SIGN
J
K
P
Q
COMPARE

Input, ϵ_i (from 2)

$$\Sigma_1 = \sum_{t=0}^{t=a} \epsilon_i \text{ (all } \epsilon_i \text{ have the same sign)}$$

$$\Sigma_2 = \sum_{t_{a+1}}^{t=b} \epsilon_i$$

Output, $\Sigma_1, \Sigma_2 \cdots \Sigma_p$ (Block D)

The program now calculates the state of charge, Q, of the battery at the end of each charge and discharge period, using the state of full charge equal to zero as a reference.

4) Block E

When $t = 0$, let $Q = Q_o = 0$

The state of charge at the end of each charge or discharge period, i, is equal to the initial state of charge at the beginning of this period $+\Sigma_i$. However, the state of charge may never be allowed to exceed the fully charged battery capacity, $Q_o = 0$. Therefore, after each state of charge calculation, Q is tested against 0, and if it is found to be greater than 0, is readjusted to be 0.

5) Block E

Input, $\Sigma_1, \Sigma_2, \Sigma_3$ (from 3)

$$Q_o = Q \text{ (from 4)}$$

$$Q_1 = Q_o + \Sigma_1$$

$$Q_2 = Q_1 + \Sigma_2$$

$$Q_i = Q_{i-1} + \Sigma_i$$

Output, $Q_1, Q_2, Q_3, Q_4 = \theta \cdots Q_p$

6) Test Q_i versus 0 (Block F)

If $Q_i > 0$, let $Q_i = 0$

If $Q_i \leq 0$, let $Q_i = Q_i$

7) The maximum depth of discharge is found (Block G)

Compare Q_i, Q_2, $Q_3 \cdots Q_p$

Find Q_{min}

Concurrently with Steps 1) through 7) of the program, and independently of them, the storage deterioration factors are calculated. Storage is divided into unactivated, or dry, storage and activated, or wet, storage. The wet storage period includes the entire storage time between activation of the battery by introduction of the electrolyte and the end of the mission. Since the temperature of activated storage affects deterioration rate, the temperature coefficient $f_1(T)$ is read out, assuming a constant storage temperature.

8) Block N

Input, Figure A 7-1

T_a — Temperature of activated storage

Read out $f_1(T)$

Output, $f_1(T)$

9) The total time of activated storage is the sum of prelaunch and mission times (Block J)

Input, $\Delta t_1 \cdots \Delta t_n$

$t_{pl} \doteq$ Prelaunch time after activation

$$t_a = \sum_{o}^{h} \Delta t_i + t_{pl}$$

Output, t_a

10) The fraction of capacity remaining after activated storage, F_a, is calculated

Input, $f_1(T)$ from 8

t_a from 9

$$F_a = 10^{t_a f_1(T)}$$

Output, F_a

Similarly, the temperature coefficient $f_2(T)$ and F_u are calculated for unactivated, or dry storage.

11) Block O

Input, Figure A7-2

T_u — Unactivated storage temperature

Read out $f_2(T)$

Output, $f_2(T)$

12) Block P

Input, $f_2(T)$

t_u = time of unactivated storage

$F_u = 10^{t_u f_2(T)}$ = fraction of capacity remaining after unactivated storage

Output, F_u

However, loss of capacity occurs due to deterioration of the divalent silver oxides, which comprise only half the electrical capacity of the cell. F_u, therefore, may not be less than 0.5.

13) Compare F_u, 0.5 (Block Q)

If $F_u < 0.5$, let $F_u = 0.5$

If $F_u \geq 0.5$, let $F_u = F_u$

A preliminary estimate of capacity (C_p) may now be made, using Q_{min} from (7) and F_a and F_u.

14) Block H

Input, Q_{min} (from 7)

F_a (from 10)

F_u (from 13)

E_b (input)

$$C_p = -\frac{Q_{min}}{F_a F_u E_b}$$

Output, C_p

This preliminary estimate of capacity will be valid for 1 or 2 cycles of moderate depth of discharge. If, however, larger numbers of cycles are required, then a degradation factor based upon the number of cycle and the depth of discharge are also required. The program therefore calculates the depth of each discharge cycle, D_d, determines the number of cycles, N_c, which can be expected from the battery at that depth of discharge, and assumes a degradation due to one cycle equal to $1/N_c$. Then, the fractional capacity remaining equals $\left[1 - (1/N_c)\right]$.

Since only alternate Q's are states of charge at the end of discharge, the sign of Σ_1 is used to determine which are discharge and which are charge cycles.

15) Block L

If Σ_1 is negative, use odd numbered Q values.

If Σ_1 is positive, use even numbered Q values.

16) Calculate depth of discharge (Block M)

Input, $Q_1, Q_3, Q_5 \cdots Q_p$ or

$Q_2, Q_4, Q_6 \cdots Q_p$

C_p, E_b

$$D_{d1} = \frac{Q_1}{C_p E_b}, \quad D_{d2} = \frac{Q_3}{C_p E_b}, \quad D_{dn} = \frac{Q_{2n-1}}{C_p E_b}$$

17) Calculate number of cycles N_c expected at each depth of discharge (Block R)

Input, $D_{d1}, D_{d2}, D_{d3} \cdots D_{dk}, K_c$

$$N_{c1} = 10^{K_c D_{d1}}$$

Output, $N_{c1}, N_{c2} \cdots N_{ck}$

18) Calculate fraction of capacity retained after each cycle (Block S)

Input, $N_{c1}, N_{c2} \cdots N_{ck}$

$$F_{c1} = \left[1 - (1/N_{c1})\right]$$

19) Calculate overall fractional capacity (F_c) retained (Block T)

Input, F_{c1}, F_{c2}, $F_{c3} \cdots F_{ck}$

$$F_c = F_{c1} \times F_{c2} \times F_{c3} \cdots \times F_{ck}$$

Output, F_c

20) Calculate a final capacity (Block I)

Input, C_p, F_c

$$C_b = \frac{C_p}{F_c}$$

Output, C_b

21) Read out battery weight (unpackaged) and volume (Blocks U and W and Figures A7-3 and A7-4)

Input, C_b, E_b

Output, W_b, V_b

22) Read out packing factor (Block V and Figure A7-5)

Input, C_b, E_b

Output, F_p

23) Calculate packaged battery weight (Block X)

$$W_b \times F_p = W_p$$

4. Parametric Data Generation

Sources of parametric data for silver-zinc secondary batteries are as follows:

1) Parametric data on values were obtained from Yardney Electric Company Energy Data Book, SP5M82.

2) Battery weights were obtained from unpublished data provided by Electric Storage Battery Company.

3) Battery thermal deterioration rates were obtained by calculation from Mariner C battery data provided by the Electric Storage Battery Company.

4) Battery packaging factors are STL estimates based upon minimum-weight, open-frame packaging designs similar to OGO and 823 designs, which depend for rigidity of battery structure upon mounting on a rigid baseplate. These weight estimates do not allow support or translation of external loads through the battery structure.

C. SECONDARY SILVER-CADMIUM BATTERIES

When used in a secondary battery, the silver-cadmium cell has a somewhat greater specific power than its major competitor, the nickle-cadmium cell. Based upon cell weights, available specific power of from 25 to 30 watt-hours per pound are available.

Control of charge in a silver-cadmium battery depends on the characteristics of the silver electrode and the tolerable buildup of gas pressures within the cell. The maximum tolerable constantly applied voltage is presently believed to be a function of current and temperature and varies sufficiently with both parameters to defy any effort to develop a simple, single-valued limit that is universally applicable throughout the useful temperature-voltage-current range of the battery.

1. State of Development

At present, most silver-cadmium batteries are built with plastic encased cells whose tolerance to overpressure is limited. Because the maximum tolerable voltage is a function not only of temperature, but of current as well, this leads to difficulties in control of charge as well as problems in overall system reliability. Insufficient parametric data are presently available for application to the design of useful power systems over a wide range of powers, charge times and mission characteristics.

The useful life of the silver-cadmium battery has been extended recently to approximately one year, if the associated charge control problems can be solved and if battery charging rates are held to low levels. Additional improvement will require a significant advance in the state of the art, particularly in the area of separators, whose properties require an ionic permeability similar to that of cellophane but with lower deterioration rates.

2. Systems Application

Silver-cadmium batteries are best applied to multiple cycling use where the ratio of charge time to discharge time is fairly large, perhaps greater than 10:1. At lower ratios, the charging currents become high enough to cause difficulty in charge control, particularly with variable load levels. Silver-cadmium batteries are lighter in weight than the corresponding nickel-cadmium battery in sizes greater than 3 to 5

ampere-hours, and are nonmagnetic in character, which makes them most desirable for secondary power storage in satellites carrying magnetometers or other experiments that are sensitive to the presence of magnetic fields.

3. Development of Design Computation Process

The battery design computation logic shown in Figure 4-3 is directed toward the sizing of silver-cadmium batteries for cyclic use in aerospace vehicles and, at the same time, gives certain parametric output data regarding the minimum useful heat rejection capacity required in any spacecraft in which silver-cadmium batteries are applied in accordance with the basic assumptions defined in succeeding paragraphs.

To begin with, the program assumes that the worst operating condition for the battery is immediately obvious and needs no iterative computation. In the absence of this assurance, several likely sets of conditions may be tried and evaluated as "worst conditions." Having assumed a set of worst orbit or cycle conditions, the following input data are derived from the orbit condition and spacecraft mission:

a) Time of discharge = t_d

b) Time available for charge = t_c

c) Orbit period or repetitive cycle period = $t_p = t_d + t_c$

d) Average power required at the loads during discharge = P_L

e) Average voltage at the bus during discharge = E_b.

All the above input data are immediately derivable from a definition of the mission requirements of the power supply and are not a function of the power supply.

In addition, three preliminary estimates of the temperature of the battery must be made in order to begin the computation and should be selected with some thought. Although these estimates are automatically revised as the computation proceeds, the total computation time will be reduced if the original estimates are close to the final values. These estimates are as follows:

a) Battery temperature at the moment at which charging is terminated by the charge controller = T_{ec}

b) Battery temperature at the end of the daylight period of the orbit, or the charge period of the cycle = T_{ep}

c) Mean battery temperature = T_a

Unless solar inputs to the cooling system are large, T_{ec} will usually be higher than T_{ep}.

T_a will usually reflect the designer's wishes to maintain a fairly moderate battery temperature and can be estimated by taking the median temperature between T_{ep} and the temperature of the battery at the end of the discharge period.

Finally, the mission requirements will dictate the required number of cycles of operation. Following the empirical curve in Figure A8-1, the depth of discharge (DD) will be determined.

Using the above input data, listed again below, the computation is begun:

t_d	P_L	T_{ec}
t_c	E_b	T_{ep}
$t_p = t_d + t_c$	DD	T_a

1) Block C,* computation of required installed battery capacity.

Inputs, I_d (original)

t_d (original input)

DD (original input)

Computation:

$$C_b = \frac{(I_d)(t_d)}{DD}$$

Output, (C_b)

---

* The blocks referenced in Subsection IV C are shown in Figure 4-3.

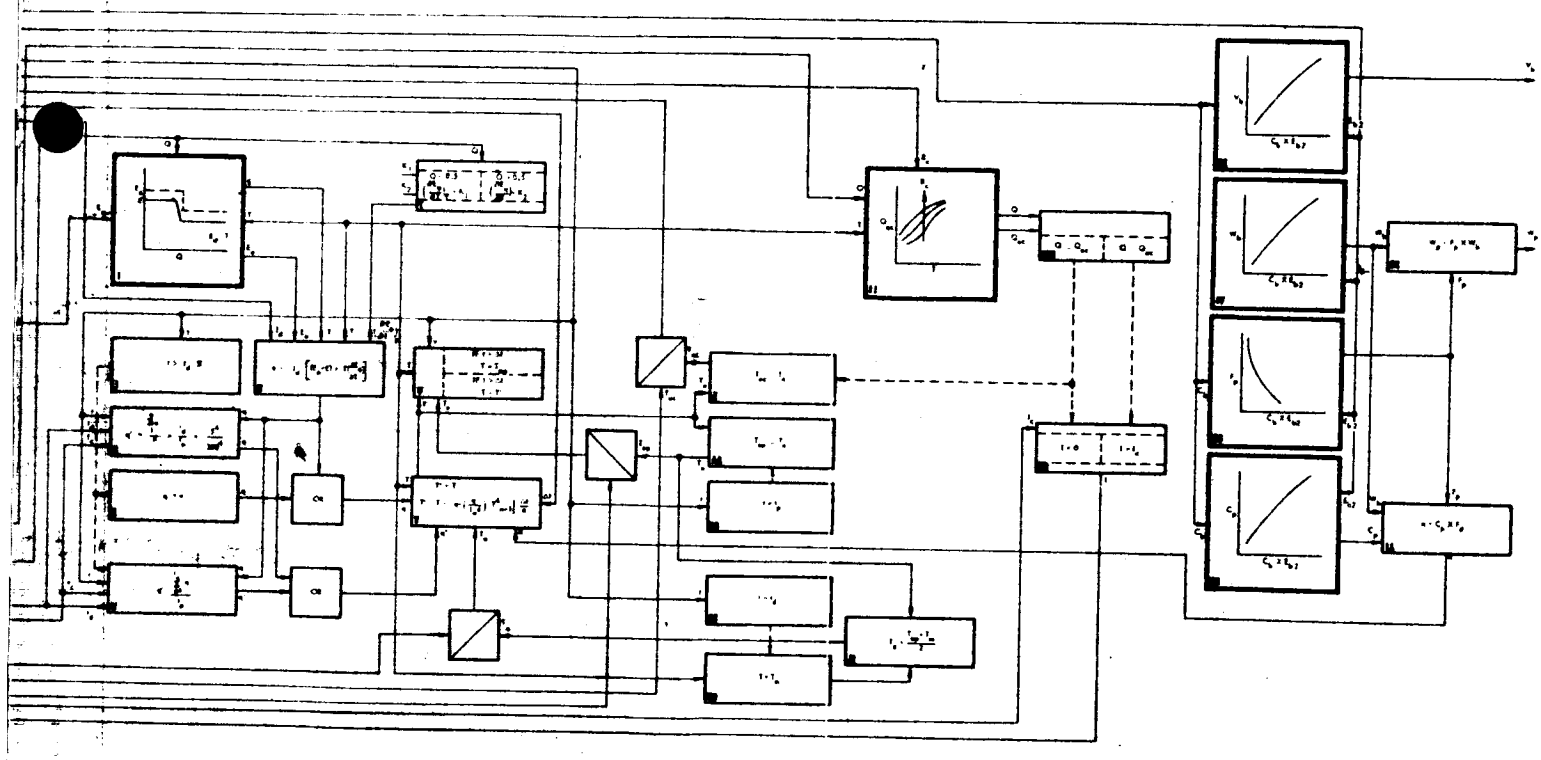

Figure 4-3. Silver-Cadium Secondary Battery Desig
Computation Flow Diagram

2) Block E, computation of hourly charge rate R_c.

The number of hours required to charge a battery having an installed capacity of (CBI) at an average charging current of (IBC)

Inputs, C_b (from block C)

I_c (original)

Computation:

$$R_c = \frac{C_b}{I_c}$$

Output, R_c

3) Block G, read out of maximum achievable state of charge from empirical data curves Q_{ec} (also see Figure A8-2).

Inputs, R_c (from E)

T_{ec} (original estimate)

Outputs, Q_{ec}

4) Block O, test to determine whether or not the battery is adequately charged.

Inputs, Q_{ec} (from G)

I_d (original)

t_d (original)

C_b (from C)

Two possible outputs:

Output 1,

$$Q_{ec} \geq \frac{I_d t_d}{C_b}$$

Output 1,

in which case, proceed to Step 5), or

Output 2,

$$Q_{ec} < \frac{I_d t_d}{C_b}$$

in which case, follow subroutine 4A through 4C

4A) Block D, compute increment of C_b (ΔCb)

Inputs, C_b (from C)
I_d (original)
t_d (original)
Q_{ec} (from G)

$$\Delta C_b = \frac{I_d t_d}{C_b} - Q_{ec}$$

Output, (ΔCb)

4B) Block F, increase in C_b

First a new (C_b) estimate is made,

$$C_b \text{ new} = C_b + (\Delta C_b) \text{ (from D)}$$

Prior estimates of (C_b) are eliminated and the new (C_b) is used in further computations.

4C) Iterate cyclically through C, E, G, O, D, F, etc., until the conditions of Block O are satisfied:

$$\text{i.e., } Q_{ec} = \frac{I_d t_d}{C_b}$$

Then proceed to Step 5.

At this point, a preliminary estimate of installed battery capacity is complete. If original temperature estimates are correct, or if low depths of discharge are used, it is to be expected that this estimate will not be changed significantly by further computation. However, because of the sensitivity of the battery to the temperature at the end of charge, the computation now proceeds into a new routine designed to define the

temperature variations in the battery as it goes through discharge-charge cycling. This is done by breaking the discharge-charge cycle into small time increments and accumulating the small temperature changes which occur during these discrete periods. It is assumed that all parameters remain constant throughout one increment of time.

Beginning with a battery of rated capacity, (C_b), which has been charged to a relative state of charge, Q_{ec} (dependent upon temperature (T_{ec}) which was assumed):

5) Block I, generation of time increment Δt. This initial time increment is triggered by satisfactory completion of Step 4.

6) Block Q, counting of time increments.

Input, Δt

$$t = n\Delta t$$

where n is the number of time increments which have been generated.

Output, Time (t)

7) Block R, determination of mission phase.

7A) If $t < t_d$, battery is discharging and

$$I = I_d$$

7B) If $t = t_d$, battery has just begun to charge and

$$I = +|I_c|$$

7C) If $t_d < t < t_p$, battery is still in the charging period and may either be charging or on open circuit, depending upon whether or not the charge controller has inhibited charging.

7D) If $t = t_p$, the cycle is complete. Since the discharge occurs first in this program, branch 7A ($t < t_d$) will be treated first.

Subroutine 7A, Battery discharge period, $I = |I_d|$

7A-1) Block W, Compute state of charge decrement (ΔQ).

Determines fraction of battery capacity removed during discharge at a current (I) = - I_d for a time period (ΔZ)

Inputs, Δt (from 5)

(I) (from 7A)

C_b (from 4)

Computation:

$$(\Delta Q) = \frac{(I)(\Delta t)}{C_b}$$

Output, ΔQ

7A-2) Block X, computation of battery state of charge.

Inputs, Q_{ec} (from G)
(ΔQ) (from 7A-1)

Computation:

$$(Q) = Q_{ec} + \sum_{nt}^{n\Delta t} \Delta Q$$

Output, (Q)

7A-3) Block H, computation of hourly discharge rate

Inputs, C_b (from 4)
I_d (original)

Computation:

$$R_d = \frac{C_b}{I_d}$$

Output, R_d

7A-4) **Block U, read battery temperature. On the first time increment, $t = \Delta t$, $T = T_{ep}$, since no better estimate has yet been made.**

Note: (Estimates in ^{o}K)

Output, (T)

7A-5) Block I, read out open circuit and closed circuit voltages from empirical data (also see Figures A8-3 through A8-11).

Inputs, (T)

(Q) (from 7A-2)

(R_d) (from 7A-3)

Outputs, E, E_o

7A-6) Block T, compare Q, 0.5.

If

$$Q<0.5, \left(\frac{\partial E_o}{\partial T}\right)_P = K_1$$

If

$$Q<0.5, \left(\frac{\partial E_o}{\partial T}\right)_P = K_2$$

Inputs, (Q) (from I)

0.5

Output, $\left(\frac{\partial E_o}{\partial T}\right)_P$

7A-7) Block N, estimate heat dissipation in the battery (q).

Inputs, (T) (from 7A-4)

I_d (original)

E_o (from 7A-5)

(E) (from 7A-5)

$\frac{\partial E_o}{\partial T}$ (from 7A-6)

Computation:

$$q = I_d\left(E_o - E + T\frac{\partial E_o}{\partial T}\right)$$

Output, (q),

Here, the computation logic recognizes that good estimates of spacecraft thermal control and heat rejection capacity may be unavailable. As a temporary measure, the program therefore generates a heat rejection capability by assuming that at one temperature, 80°F, the total heat generated by the battery during the discharge mode is exactly balanced by the ability of the spacecraft to reject this amount of heat during the entire cycle period (t_p). This represents a minimum heat rejection capability for the mission. Where spacecraft thermal rejection parameters are available, these should be substituted for computation Block K.

7A-8) Block K, computation of minimum heat removal rate from the battery (q)

Inputs, (q) (from 7A-7)

(Δt) (from 5)

(t) (from 6)

(t_d) (original)

(t_p) (original)

Computation:

$$q' = \left[\frac{\sum_{1}^{n} q}{n}\right] = \left[\frac{(t_d)}{(t_p)}\right]\left[\frac{T^4}{300^4}\right]$$

Output, (q')

7A-9) This subroutine computes battery heat capacity (K)

7A-9-1) Block HH, read out empirical battery specific heat capacity (C_p).

Inputs, (C_b) (from F)

(E_b) (original)

Output, (C_p)

7A-9-2) **Block FF, this step reads out unpackaged battery weight.**

Inputs (C_b) (from F)

(E_b) (original)

Outputs, (W_b)

7A-9-3) Block GG, this step reads out battery package factor (F_p).

Inputs, (C_b) (from F)

(E_b) (original)

Output, (F_p)

7A-9-4) Block LL, this step computes battery heat capacity (K).

Inputs, (C_p) (from 7A-9-1)

(W_b) (from 7A-9-2)

(F_p) (from 7A-9-3)

Computation:

$$\kappa = C_p W_b F_p$$

Output, stored, κ

7A-10) Block V, computation of battery temperature (T').

Note: In the absence of detailed knowledge of spacecraft characteristics, the simplest equation form for battery temperature is used. This assumes that the battery consists of a solid block of infinite thermal conductivity radiating to cold space and that there are no external inputs to the radiator at any time.) Where more detailed knowledge of spacecraft performance is available, it should be substituted for the relationships in Block V.

Inputs, (T) (from Block U) ($T = T_{ep}$ on the first run)

(q) (from 7A-7)

(q') (from 7A-8)

(Δt) (from 5)

(T_a) (assumed)(original)

(K) (from 7A-9)

Computation:

$$T' = T + \left[q - \frac{q'}{T_a^4} T^4 \right] \frac{\Delta t}{\kappa}$$

Output, (T')

7A-11) Block U, revision of battery temperature (T). (T') (from 7A-10) is read into Block U and becomes the new (T) which is used in all further computations.

This completes one computation run on battery discharge for $t = \Delta t$. When T' is substituted for T, a new time increment is generated in Block P and the computation of Steps 5) through 7A-11) repeated until $t = t_d$.

When $t = t_d$, the discharge is complete and a new subroutine begins in which the battery is recharged.

When $t = t_d$, battery temperature is read out and stored as the maximum battery temperature point, T_m.

7A-12) Read battery temperature (T)

Inputs, $(t) = (t_d)$ (from Block CC)

(T) (from Block DD)

Computation:

$$\text{Let } T_m = T$$

Output, (stored T_m)

Subroutines 7B-7C battery charging period

$$\text{If } t = t_d, \quad I = +|I_c|$$

7B-1) Block LB Computation of battery charge increment (ΔQ)

(Determines fraction of battery capacity restored to the battery at charge current (I_c) in a time increment (ΔZ)

Computation - Same as 7A-1

Output, (ΔQ)

7B-2) Block X, computation of battery state of charge (Q).

Input and computation (same as 7A-2)

Output, (Q)

7B-3) Block L, computation of heat dissipation in battery.

Input, $t = t_d$ (from J)

Computation:

$$q = 0$$

Output, (q)

7B-4) Block M, computation of heat removal rate from battery (q').

Inputs, $t = t_d$ (from J)

$$\sum_{1}^{n_d} q \text{ (from K)}$$

7B-5) Computation of battery heat capacity.

Use battery heat capacity computed in (7A-9)

7B-6) Computation of battery temperatures (same as (7A-10)

As before, when the new battery temperature (T) is generated, it replaces the last battery temperature in Block V and is used in the succeeding computations.

7B-7) Block U.

Input, (T') (from R-B)

Computation:

$$\text{Let } T = T'$$

7B-8) Generate next time increment, Δt.

Subroutine 7C. This subroutine substitutes for 7B when $t < t_d$, since after one or more increments of charge, the battery may have reached its maximum achievable state of charge at the temperature (T) and no further charging may take place. The program accomplishes this by comparing Q, as calculated in step 7B-2, with Qec (empirical data). If $Qec > Q$, further charging is permitted to continue and additional charge increments (ΔQ) are added to Q to increase the battery state of charge. Once $Q = Q_{ec}$, no further increments of charge are permitted to accumulate.

7C-1) Block II.

Note: This is identical with Block G (This step determines the battery maximum achievable state of charge) (also see Figure A8-2)

Inputs, (T) (from Block U)

(R_c) (from Block E)

Output, (Q_{ec})

7C-2) Block MM, comparison of the actual state of charge with the maximum achievable state of charge (Q).

Two outputs are possible:

If $(Q) < (Q_{ec})$, then $(I) = (I_c)$

If $(Q) \geq (Q_{ec})$, then $(I) = 0$

Computation continues as in 7B-1, 7B-2, 7B-3, 7B-4, 7B-5, 7B-6, 7B-7, 7B-8.

7C-3) When Q becomes equal to Q_{ec}, a new value of T_{ec} is read out.

Inputs, (T) (from V)
$(Q) = (Q_{ec})$ for the first time (from II)

Computation:

Let $T_{ec} = T$ (Block Z)

Output, (T_{ec})

New time increments are generated and the computation is repeated, until, finally, $t = t_p$.

At the end of the computation, when $t = t_p$, a new value of t_{ep} is read out and replaces the value previously stored.

8) Block AA.

Input, (T)
$(t = t_p)$

Computation:

Let $T_{ep} = T$

Output, (T_{ep})
(T_a)

11) Block JJ, a new average battery temperature is calculated and replaces the value previously stored.

Inputs, (T_{ep}) **(from AA)**
(T_m) **(from DD)**

Computation:

$$\text{Let } T_a = \frac{T_{ep} T_m}{2}$$

Output, (T_a)

10) The program compares the value of T_{ec} generated in step 7C-3, with the value previously stored. If $T_{ec} = T_{ec}$ (previously stored) no further iterations are necessary and capacity, weight, packing factor and other parameters may be read out (Step 13).

If $T_{ec} \neq T_{ec}$ (previous) the entire computation is repeated from Step 5.

11) Final data read out: $T_{ec} = T_{ec}$ previous.

11A) Read out C_b from Block F.

11B) Block EE, calculation of battery volume (also see Figure A8-12).

Input, (C_b) (11A)
(E_b) (original)

Output, (V_b)

11C) Block FF, calculation of unpackaged battery weight (W_b) (also see Figure A8-13).

Inputs, (C_b) (from 11A)
(E_b) (original)

Outputs, (W_b)
(F_p)

11D) Block GG, calculation of battery package factor (also see Figure A8-14).

Inputs, (C_b) (from 11A)
(E_b) (original)

Outputs, (F_p)
(W_p)

13E) Block KK, computation of packaged battery weight.

Inputs, (W_b) (from FF)

(F_p) (from GG)

Computation:

$$W_p = F_p W_b$$

Output, (W_p)

3. Parametric Data Generation

Sources of parametric data are as follows:

1) Battery cell voltage as a function of time, temperature and current are based upon discharge curves taken at STL and reported in STL Report No. 2314-6001-RU000, by J.J. Biess, W.T. Stafford, and W.H. Wright, May 1963 and upon unpublished data by W.T. Stafford.

2) Battery weight and volume relationships are derived from the Yardney Electric Company's Energy Data Handbook, Yardney Publication SP5M 82, "Compact Power by Yardney".

3) Maximum achievable state of charge relationships to current and temperature are derived from 1) and from "Interim Report, Silver-Cadmium Batteries," by W.T. Stafford, STL.

4) Heat capacity data on silver-cadmium batteries are generally unavailable. A single value of 0.714 watt-hour per watt-hour of capacity is based upon a single measured value of 221 Btu per pound of weight (unpublished data by W.T. Stafford).

4. Problem Areas

The major problem area in silver-cadmium battery technology is that of control of the charging process over wide ranges of battery current and temperature. Insufficient data are presently available for the development of such a wide-range charge control technique, although there are several approaches now under investigation at STL and elsewhere that show some promise of final achievement of this objective.

The silver-cadmium cell has an inherently poorer voltage regulation range than almost any other type of battery due to a combination of the low

voltage of the system itself and the two-step process of discharge characteristic of the silver-peroxide-oxide electrode. This makes it difficult to take advantage of the low impedance of a battery by floating the battery across the power line at all times and makes the design of power systems incorporating silver-cadmium batteries difficult.

The design computation program is applicable generally to cyclic programs of a repetitive nature, in which temperatures are unknown and in which the battery is allowed to reach thermal equilibrium. It may also be used with some modification for missions having nonrepetitive cycles in which the starting temperatures of the battery are known, but in this case, the accuracy of the program is dependent upon the accuracy to which the heat rejection properties of the spacecraft are known. This is of greatest importance in those missions in which long cruise periods exist during which the battery temperature is a function of the spacecraft thermal properties rather than a function of battery energy throughout.

5. Conclusions

Development of a program for sizing of silver-cadmium batteries involves simulation of the mission in time, temperature, and power level. In addition to the sizing of batteries, the following data are available within the present computer program:

1) An estimate of battery temperature, heat generation rates, and minimum acceptable cooling rates consistent with battery operation.

2) If data on actual spacecraft heat rejection properties are substituted for Blocks K through N, a simulated mission can be flown, which will develop heat generation and battery temperature transient data useful in the design of charge control systems.

3) Much of the data required for a complete design, particularly of the thermal interface, are not available. Direct measurements of heat generation rates as a function of current and of state of charge, thermal conductivity data, heat capacities, etc., are now nonexistent.

5. Recommendations

This design computation method is basically a refinement of the detailed design technique most useful in sizing the battery. It ignores,

however, the problem of battery charge control, which may be solved in one of several ways, depending upon mission requirements. It is the writer's opinion that this design computation technique could be expanded to include a selection of charge control technique and charge control parameters, but in order to implement this effectively, extensive cell property measurement must be undertaken.

It is recommended that battery property measurements be geared to the requirements of this design computation program. Such data will be useful in all silver-cadmium battery design efforts with or without benefit of the computer program.

Finally, it is recognized that the rapidly charging state of the art will cause rapid absolescence of the data provided, and of a few of the subroutines in the program. It is suggested that some effort be expended periodically in updating the program and data.

V. POWER CONDITIONING (INVERTERS)

A parametric study was conducted involving eight inverters (dc-ac) to determine their weight, volume, input current, and total power dissipation as a function of load, efficiency, and input voltage. The eight inverters are typed by permutations of phase, frequency, and regulation in the following manner:

	Description		
Type	Phase	Frequency	Regulation
1A	1	400	Regulated
1B	1	400	Unregulated
2A	3	400	Regulated
2B	3	400	Unregulated
3A	1	2400	Regulated
3B	1	2400	Unregulated
4A	3	2400	Regulated
4B	3	2400	Unregulated

A. STATE OF DEVELOPMENT

Inverters are produced with a variety of circuits, depending on requirements. In most cases, the end item is influenced by cost. Military applications, however, require reliability and often light weight, and space applications strive for even higher reliability and a minimum weight. To achieve a high reliability inverter, the design must employ a limited number of parts, all of them selected for proven performance and applied in a considerably derated manner.

The most complicated circuit in the inverter is the regulator. Many types of regulators have been developed, but for this study, a single type, which has the greatest efficiency at the higher power levels, was selected for all types of inverters investigated. Transistors have continued to improve, and power transistors with extremely fast rates of switching are known to be more efficient at the frequencies and power levels described here.

B. ASSUMPTIONS FOR DESIGN STUDY

All types of inverters described here are assumed to operate from a primary bus at a nominal voltage between 20 vdc and 30 vdc. The output potential may be as high as 250 volts peak. Ambient temperature is 0° to 45°C with a maximum internal temperature rise of 40°C in vacuum. Approximately 80 percent of the heat dissipation is removed through the base mounting. All inverters studied had a power range of 5 to 250 volts.

The simplified schematic in Figure 5-1 illustrates the general circuit used in the evolution of the parametric study. The regulating system is of the pulse-width modulator type in the input dc power circuit. An input susceptibility and interference filter (C1-L1-C2) precedes the pulse-width modulator (Q1). A power-integrator (CR1-L2-C3) follows, so as to smooth the pulses prior to dc-to-ac conversion by the power-switching transistors (Q2 and Q3) and impedance-changing transformer (T1). An oscillator supplies stable frequency drive to the switching transformers and to the regulator amplifier (Z1) that contains the dc-to-pulse converter. Flux integral is kept constant by feedback from a separate output winding into the amplifier containing a voltage comparator.

Figure 5-2 represents a package containing the principal parts in a three-phase regulated inverter, and Figure 5-3 illustrates a single-phase unregulated converter package.

C. DEVELOPMENT OF DESIGN COMPUTATION PROCESS

Figure 5-4, Inverter Design—Computation Flow Diagram, contains the essential steps in deriving the weight, W_i, volume, V_i, input current, I(P), and heat dissipation, Q_i in the process of optimizing any one of the eight types of inverters.

The computation begins with Block A of the flow diagram (Figure 5-4). The rated output power, P_r, of the inverter, based on the maximum steady-state load power required during the mission, is introduced. For the specified rated power required by the load, Function A (Figure A9-1 in Appendix A9) relates efficiency, η_o, for a specific inverter type to the specific weight, P_r/W. Dividing the specific weight into the rated power yields the weight as a function of efficiency $\left[W = f(\eta_o)\right]$.

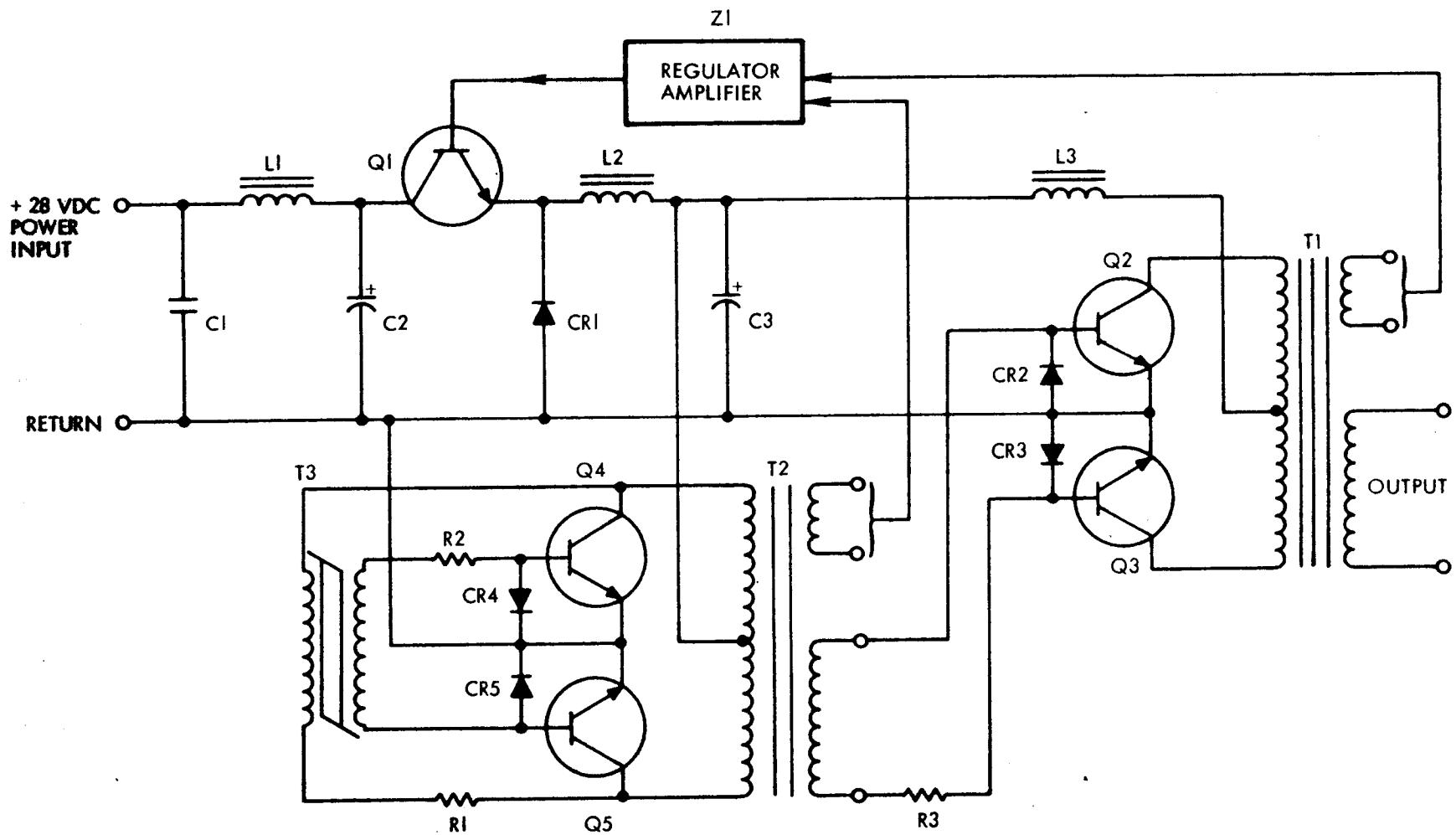

Figure 5-1. Regulated Single-Phase Inverter

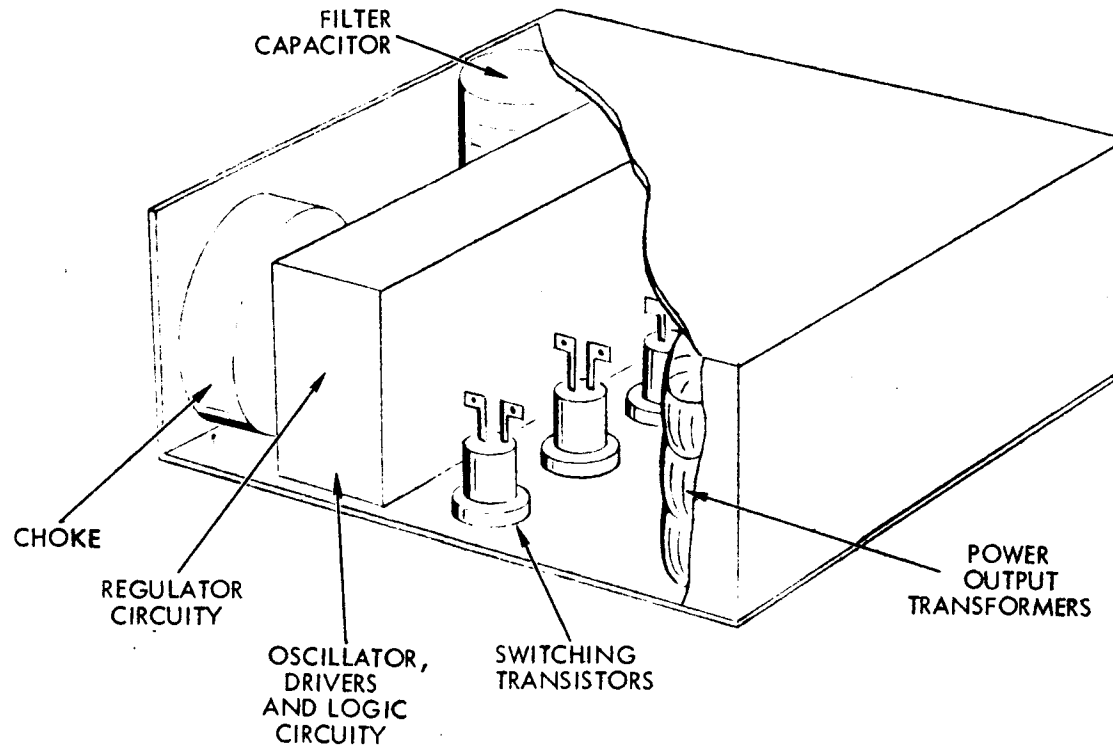

Figure 5-2. Regulated, Three-Phase Inverter (Type 2A, 4A)

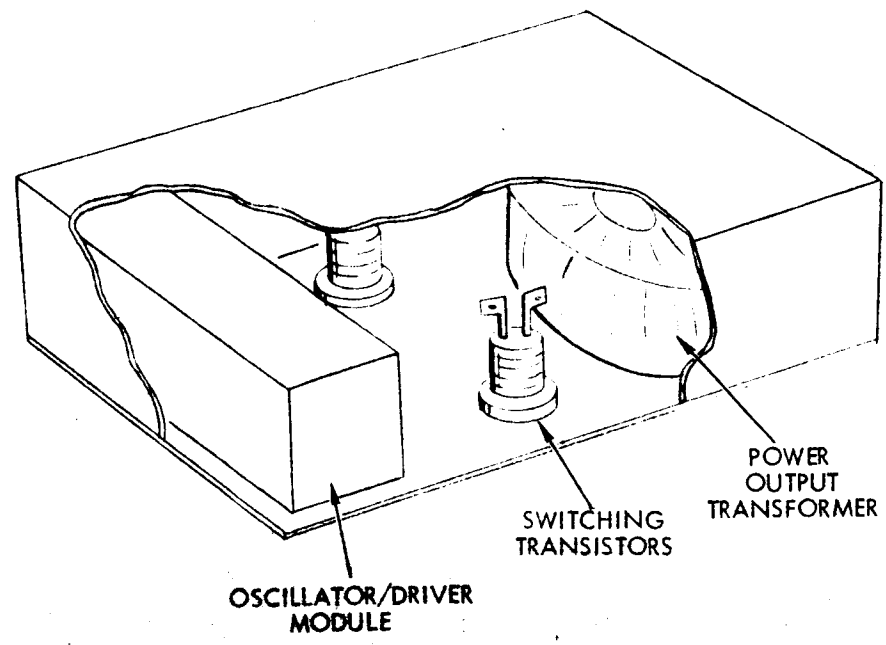

Figure 5-3. Unregulated, Single-Phase Inverter (Type 1B, 3B)

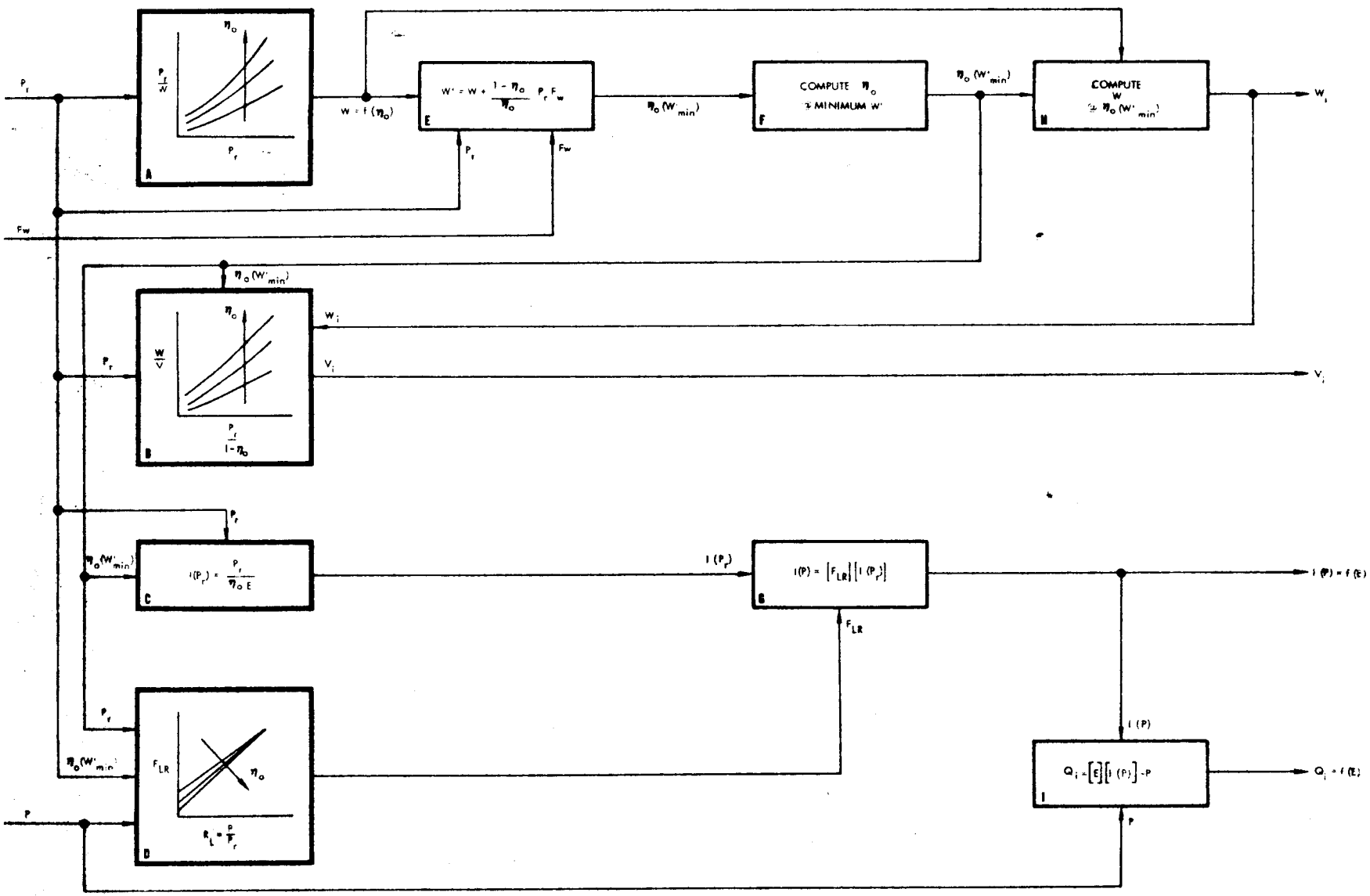

Figure 5-4. Inverter Design Computation Flow Diagram

Figure A9-1 contains a general equation for each inverter type and a table of constants. This will permit computation of any weight for any type of inverter between the efficiency limits of 50 to 100 percent and the power limits of 5 to 250 watts.

The weight of the inverter enters the computation Block E where it is combined with a weight term composed of a weight factor, F_w, which is the specific weight (lb/watt) of the system power supply. The initial inverter weight calculated at a given efficiency is thereby modified in such a manner as to compensate for the weight penalty paid elsewhere in the power system because of power dissipated within the inverter.

The computation process of Block F scans the varying efficiency of the inverter until a minimum corrected weight, W'_{min}, is obtained. This final efficiency is then reapplied to the parametric graph (or equation) of Block A, resulting in a new specific weight and, by division into the rated load power, an inverter weight, W_i.

Block B receives the optimum efficiency computed in Block F and the rated power. For the proper inverter type, Function F (Figure A9-2 in Appendix A9) provides the density, W/V. The density divided into the weight resulting from Block H computation produces the volume, V_i, of the optimum inverter.

Figure A9-2 also has a general equation and an associated table of constants, providing a solution for the range of efficiencies and rated power given.

In Block C, a fundamental calculation is made to determine the input current to the inverter at rated load at any input voltage. The efficiency is virtually constant for the type regulator used. Input current, therefore, is a function of input power and input voltage.

Block D introduces a correction factor for inverter loads less than rated. Function D (Figure A9-3 in Appendix A9) relates the load factor, F_{LR}, with the ratio of actual-to-rated loads at the optimum efficiency and with the specified inverter type. The corresponding value is a factor correcting the input current at rated load to a magnitude related to the actual load. The two factors resulting from Blocks C and D are combined in Block G to produce the function of input current at actual load to the input voltage.

Block I completes the process by computing the dissipation in the inverter.

The use of the Inverter Design Computation Flow Diagram is demonstrated with the sample calculation in Appendix B5.

VI. CONCLUSIONS AND RECOMMENDATIONS

This study has shown the feasibility of employing computer techniques for a step-by-step method of calculation and has provided strong indications of the possibility of performing complete mission simulations on electric power systems. The validity of this calculation method in the design of thermoelectric sources, inverters, and silver-cadmium batteries has been verified by test computer runs that show good agreement with existing hardware designs. The study has clearly disclosed gaps in the state-of-the-art and in available data, thus providing directions for future research and test effort.

The value of this report should be preserved by periodic updating. Revisions and expansion of its content should include the following areas:

- Power Sources: fuel cells, concentrator collectors, thermoelectric sources, Brayton cycle dynamic system.
- Thermal Storage.
- Electrochemical Energy Storage: nickel-cadmium batteries.
- Power Conditioning: converters, regulators.
- Power Control: series type.
- Reliability and Redundancy.

It is also recommended that: (1) research and development test efforts be conducted to upgrade the present data and to improve both the availability and usability of existing information; (2) that methods of system mission simulation be studied and devised; and (3) that the feasibility of broadening present computation procedures to cover wider ranges of missions and applications be investigated.

APPENDIX A1

SOLAR PHOTOVOLTAIC PARAMETRIC DATA*

*The blocks referenced in this appendix are shown in Figure 3-1.

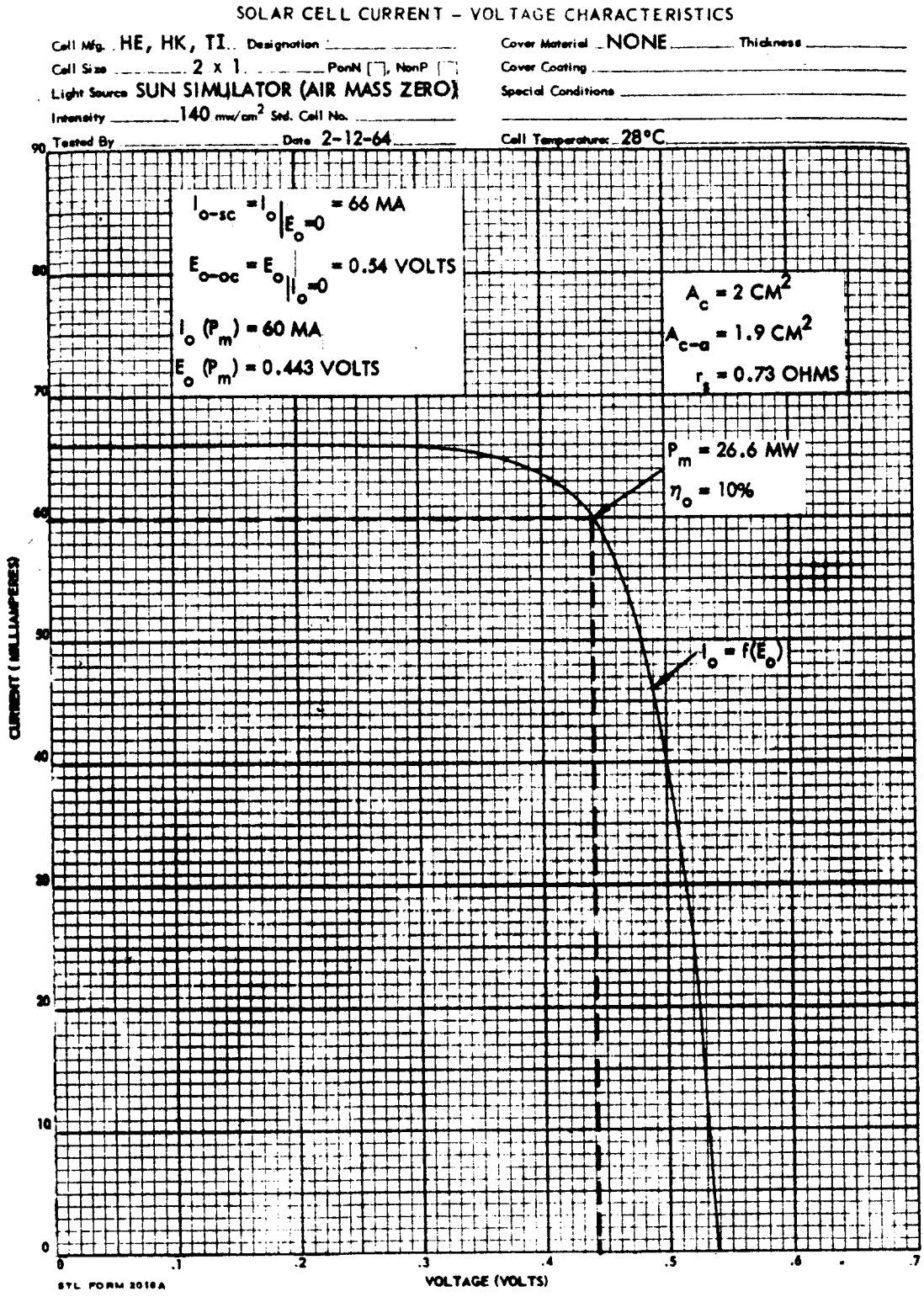

Figure A1-1. Solar Cell Current — Voltage Characteristics **(Block A)**

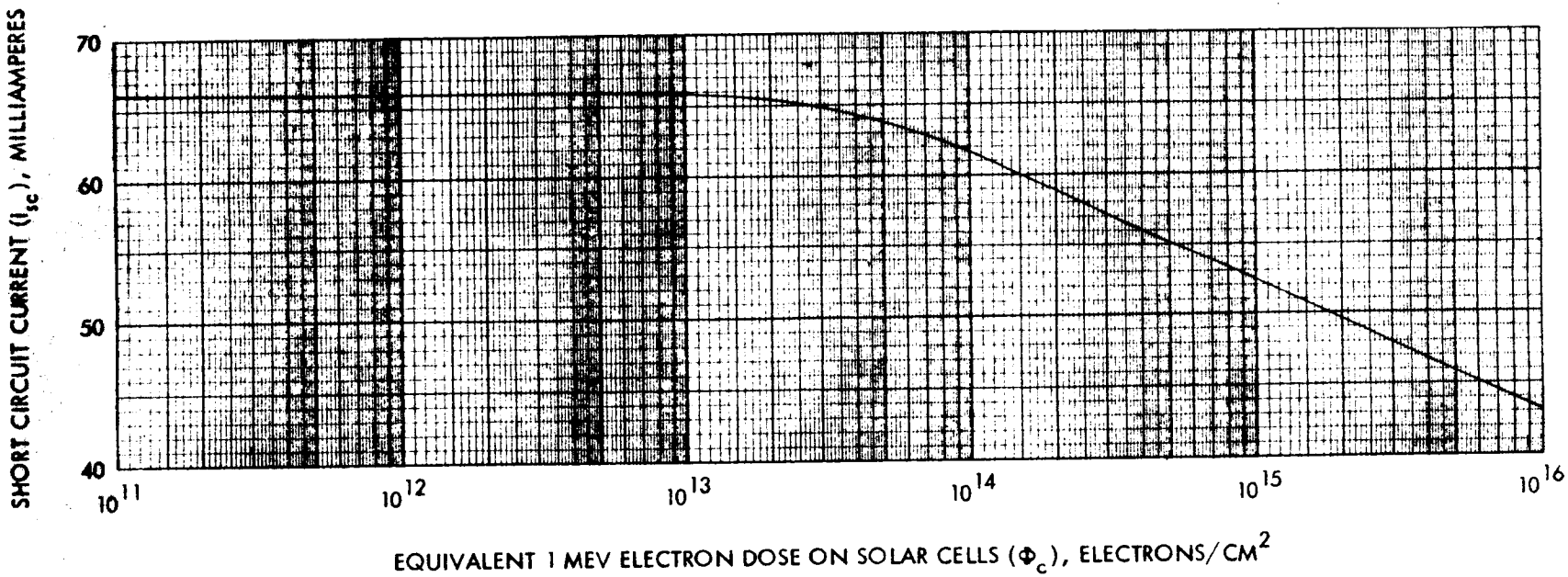

Figure A1-2. Solar Cell Short Circuit Current as a Function of Electron Dose (Block B) (Typical Characteristics)

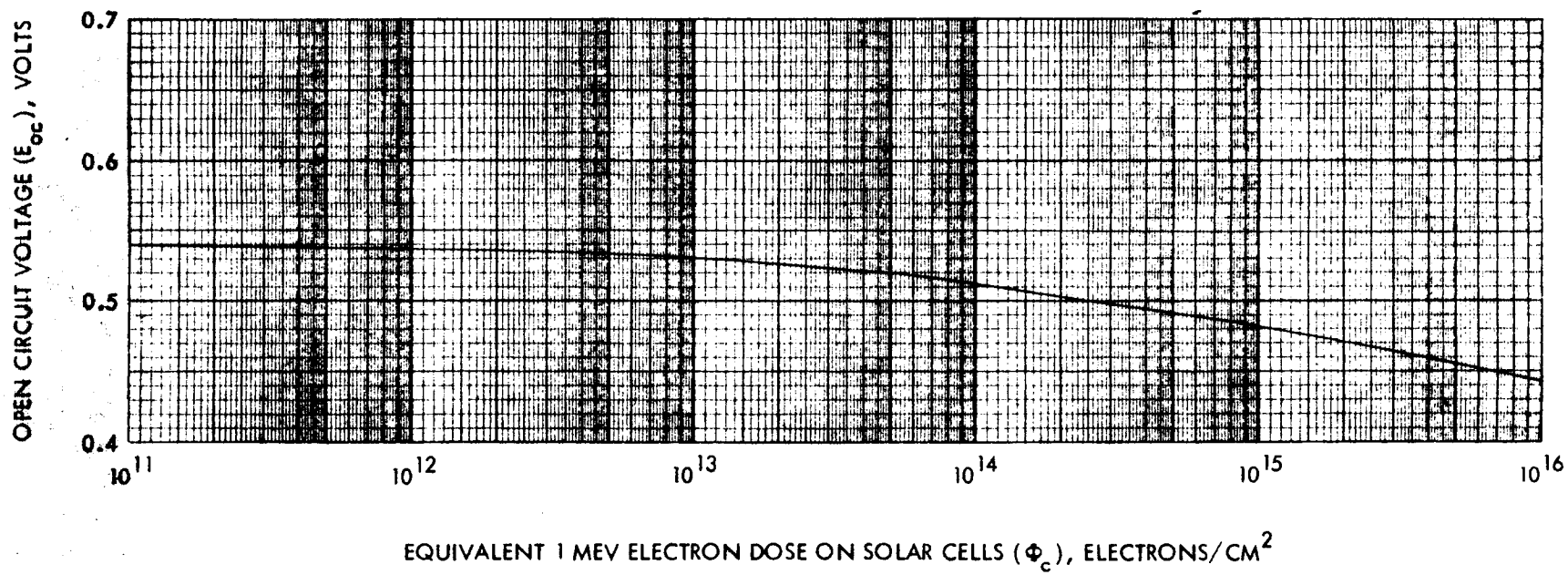

Figure A1-3. Solar Cell Open Circuit Voltage as a Function of Electron Dose (Block C) (Typical Characteristics)

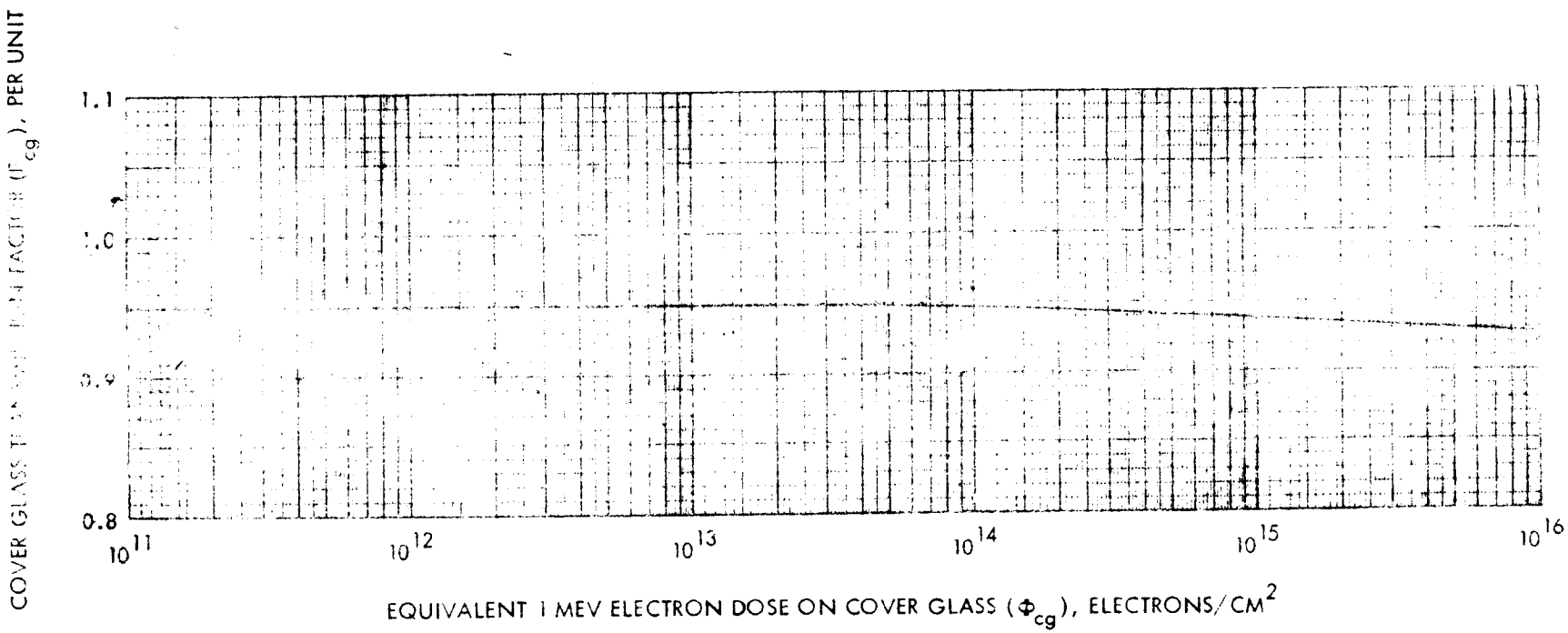

Figure A1-4. Solar Cell Cover Glass Transmission as a Function of Electron Dose (Block D)

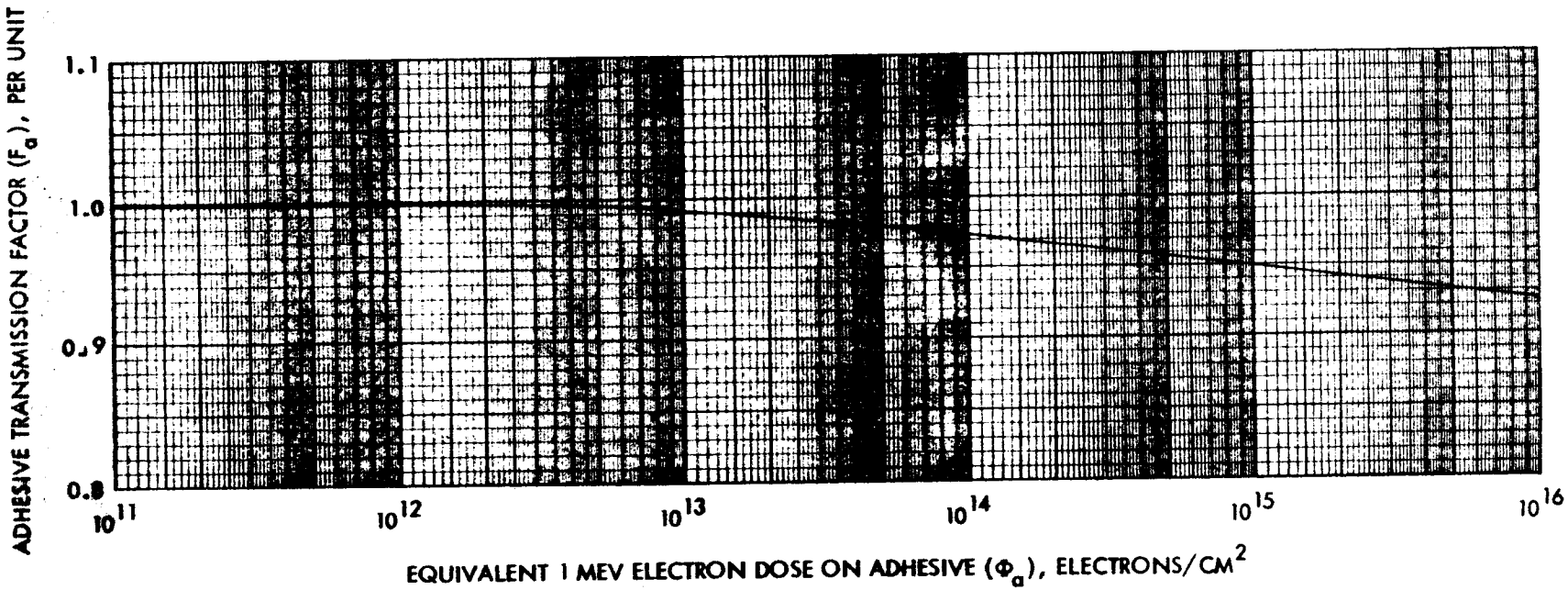

Figure A1-5. Solar Cell Adhesive Transmission as a Function of Electron Dose (Block E)

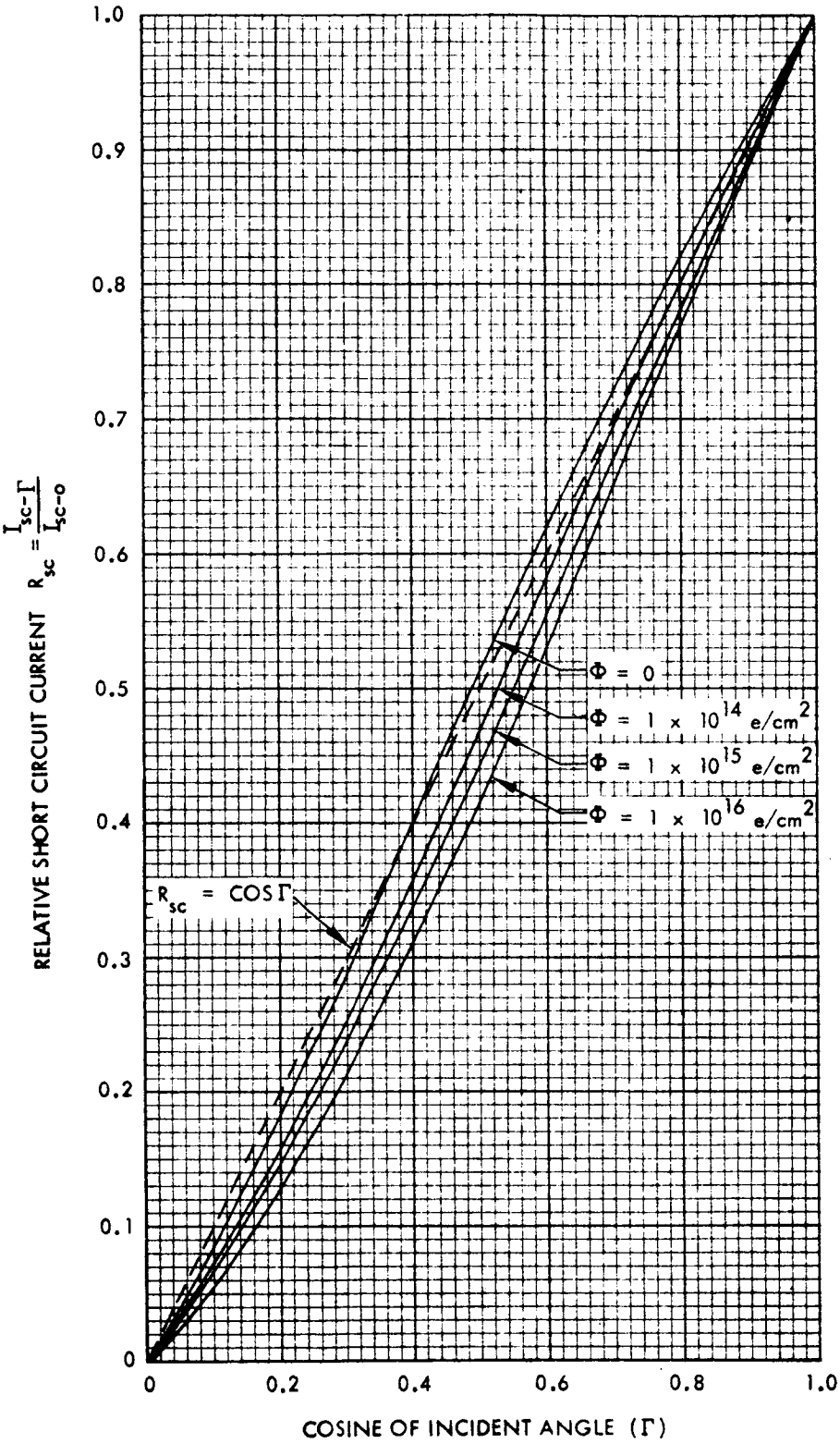

Figure A1-6. Short Circuit Current as a Function of Angle of Incidence (Block F)

APPENDIX A2

SOLAR THERMOELECTRIC PARAMETRIC DATA*

*The blocks referenced in this appendix are shown in Figures 3-11, 3-12 and 3-13.

DATA FURNISHED BY:

GENERAL ATOMIC
DIVISION OF GENERAL DYNAMICS
P.O. BOX 608, SAN DIEGO 12,
CALIFORNIA

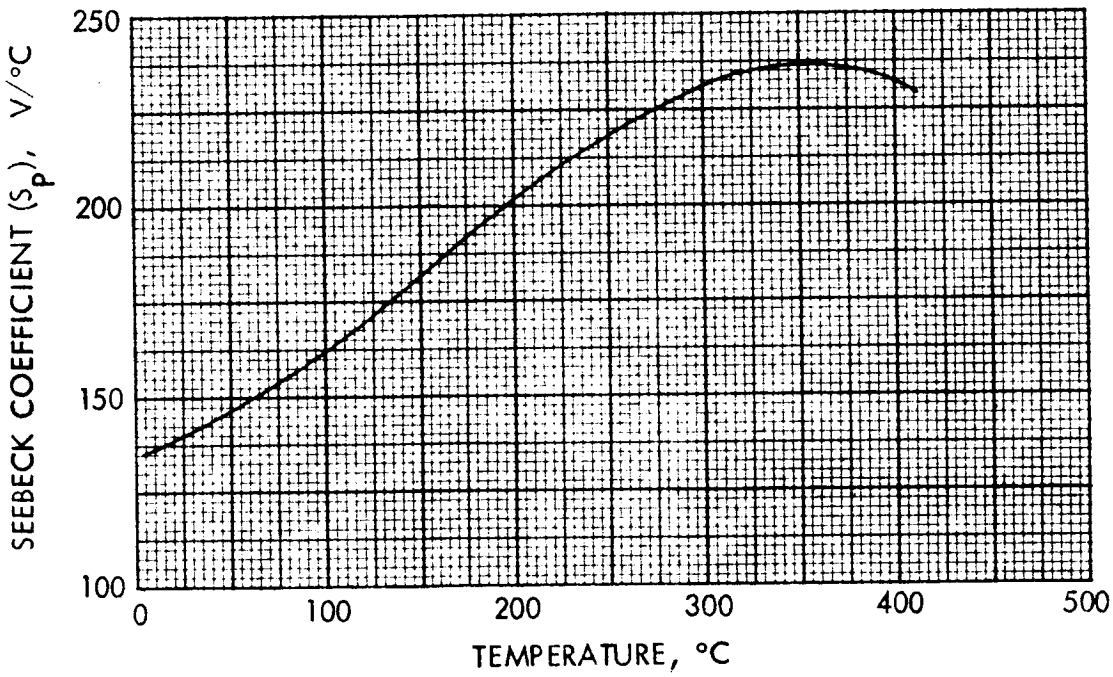

Figure A2-1. Seebeck Voltage, P-Type Elements (Block A)

DATA FURNISHED BY:

GENERAL ATOMIC
DIVISION OF GENERAL DYNAMICS
P.O. BOX 608, SAN DIEGO 12,
CALIFORNIA

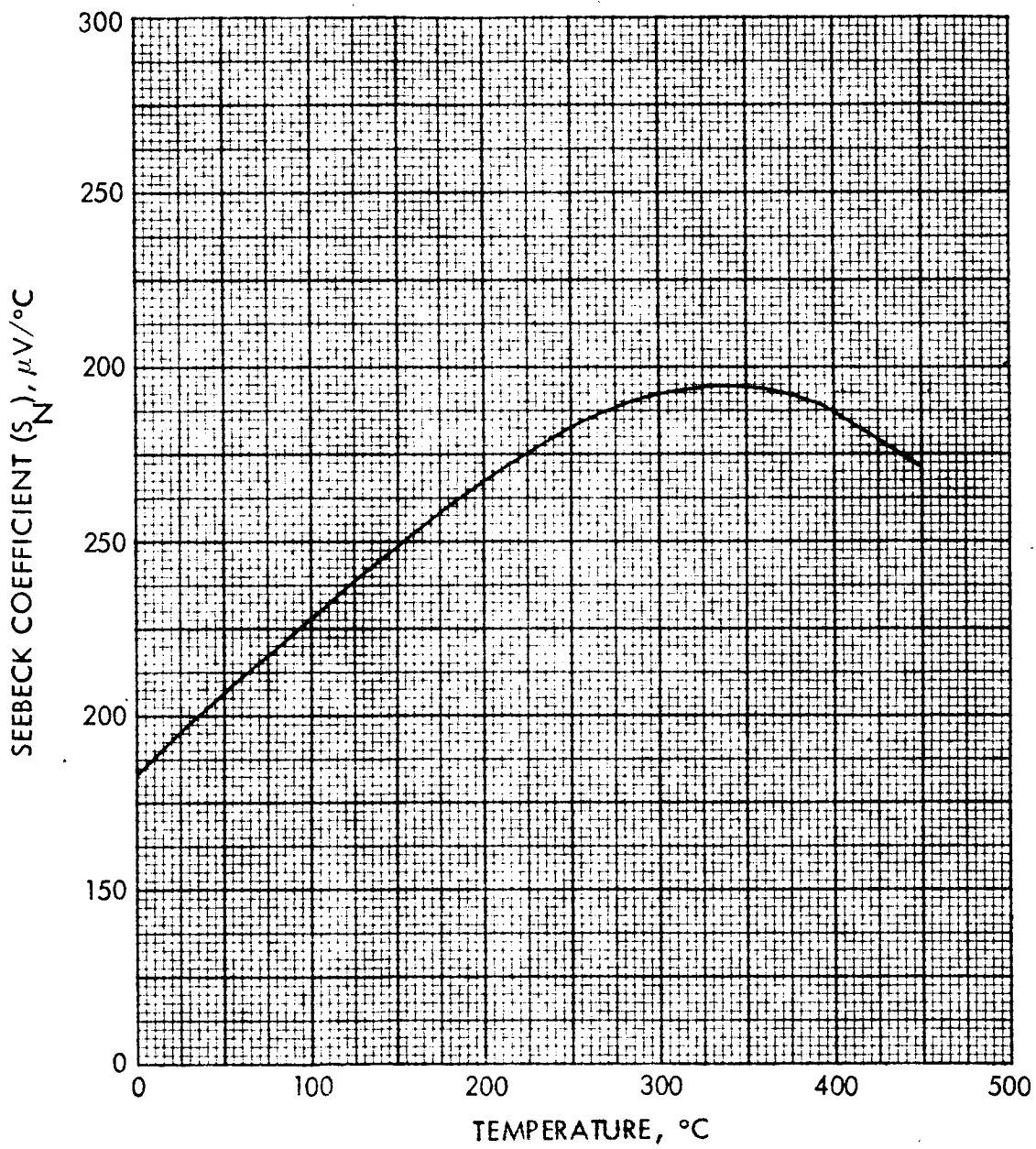

Figure A2-2. Seebeck Voltage, N-Type Elements (Block B)

DATA FURNISHED BY:

GENERAL ATOMIC
DIVISION OF GENERAL DYNAMICS
P.O. BOX 608, SAN DIEGO 12,
CALIFORNIA

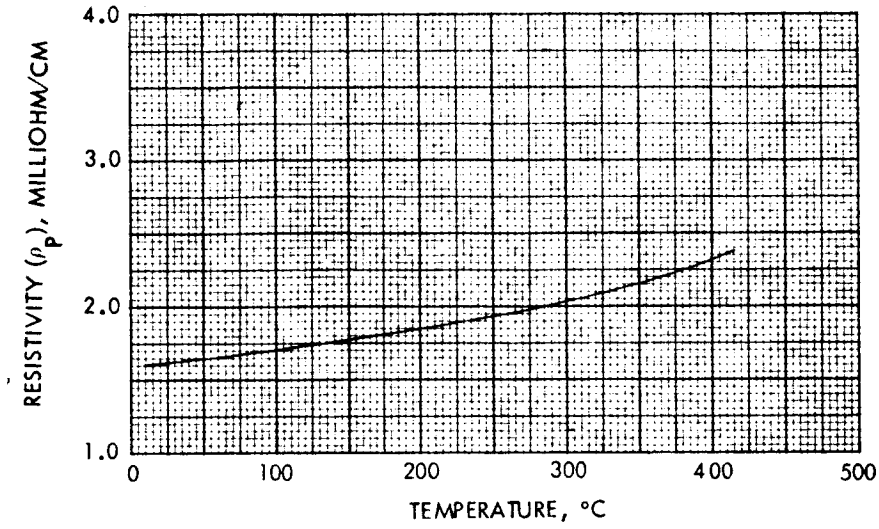

Figure A2-3. Electrical Resistivity, P-Type Elements (Block C)

DATA FURNISHED BY:

GENERAL ATOMIC
DIVISION OF GENERAL DYNAMICS
P.O. BOX 608, SAN DIEGO 12,
CALIFORNIA

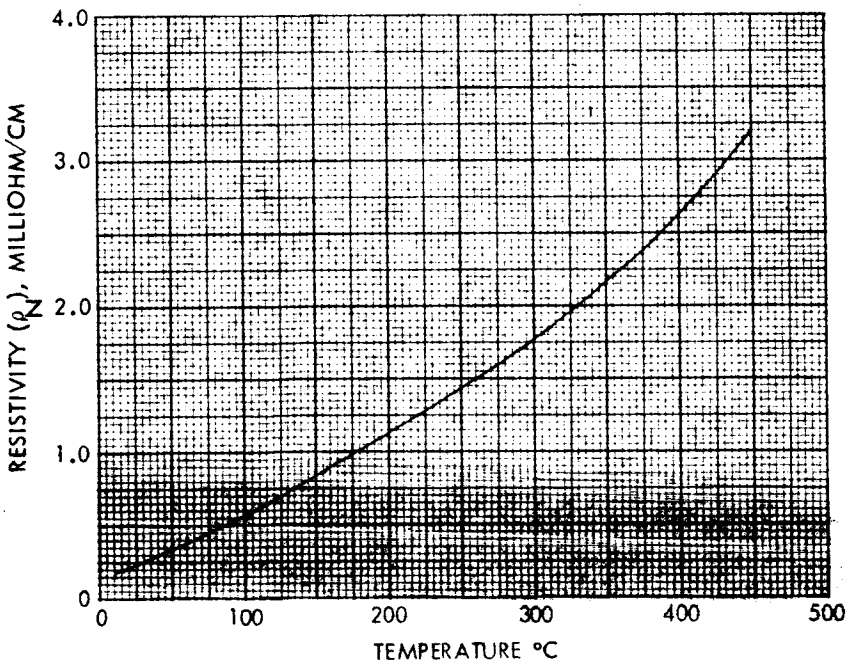

Figure A2-4. Electrical Resistivity, N-Type Elements (Block D)

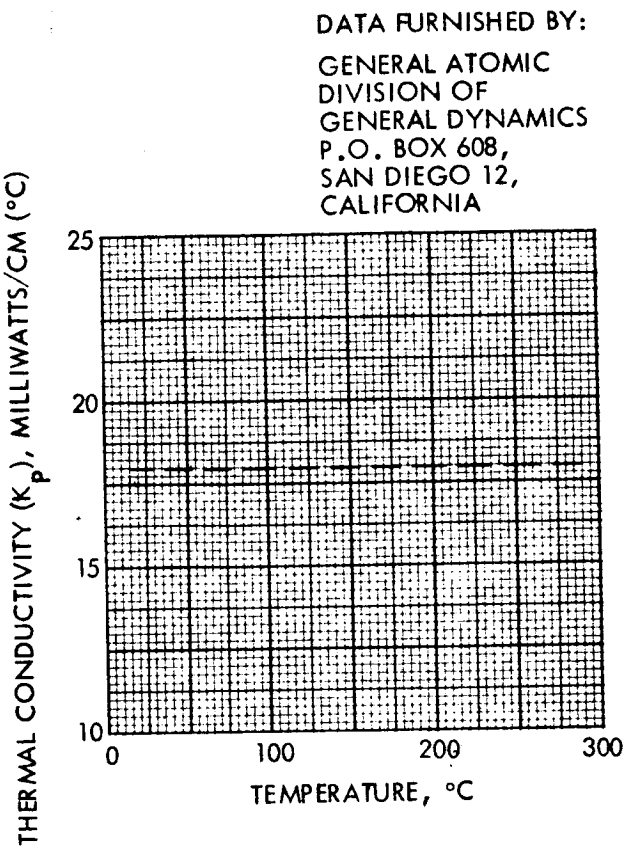

Figure A2-5. Thermal Conductivity, P-Type Elements (Block E)

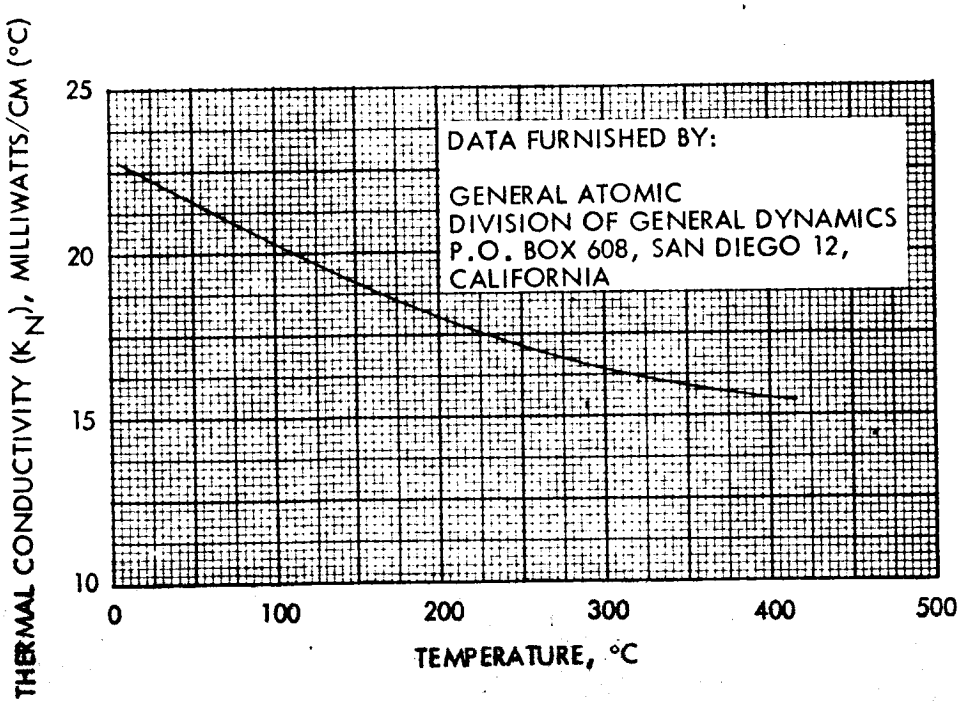

Figure A2-6. Thermal Conductivity, N-Type Elements (Block F)

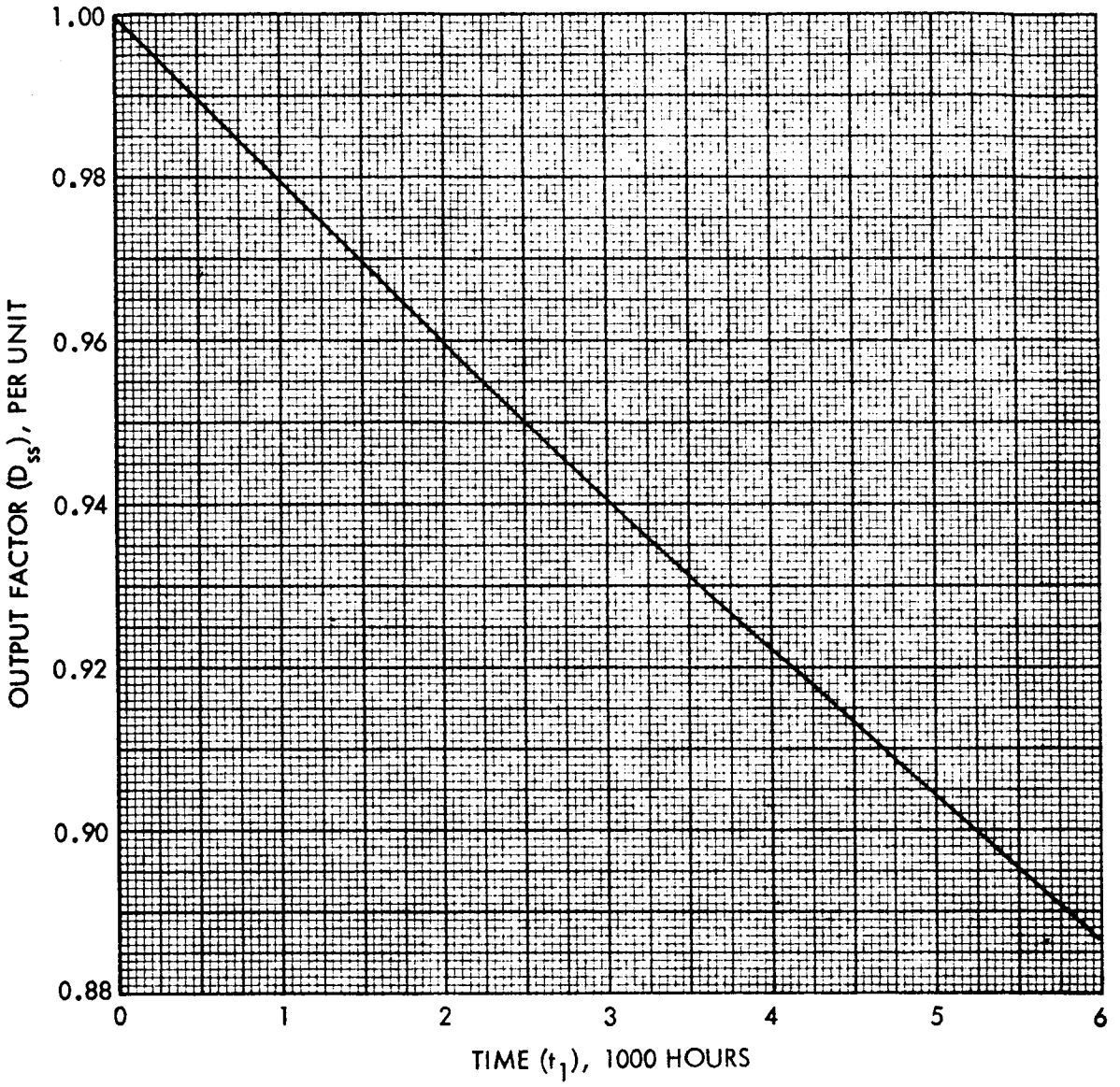

Figure A2-7. Steady State Degradation (Block G)

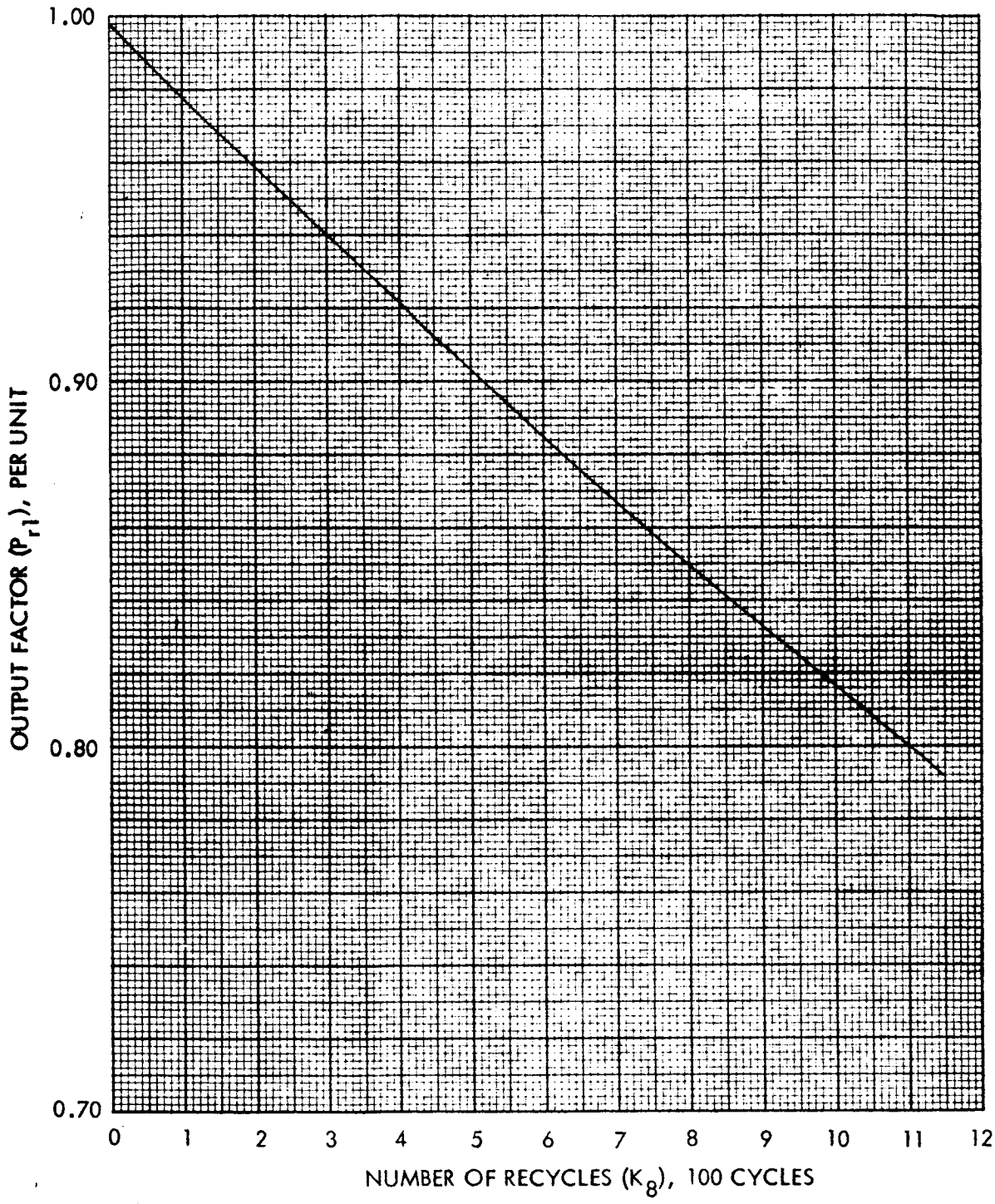

Figure A2-8. Thermal Recycling Degradation After Less Than 10^3 Hours at Steady State (Block H)

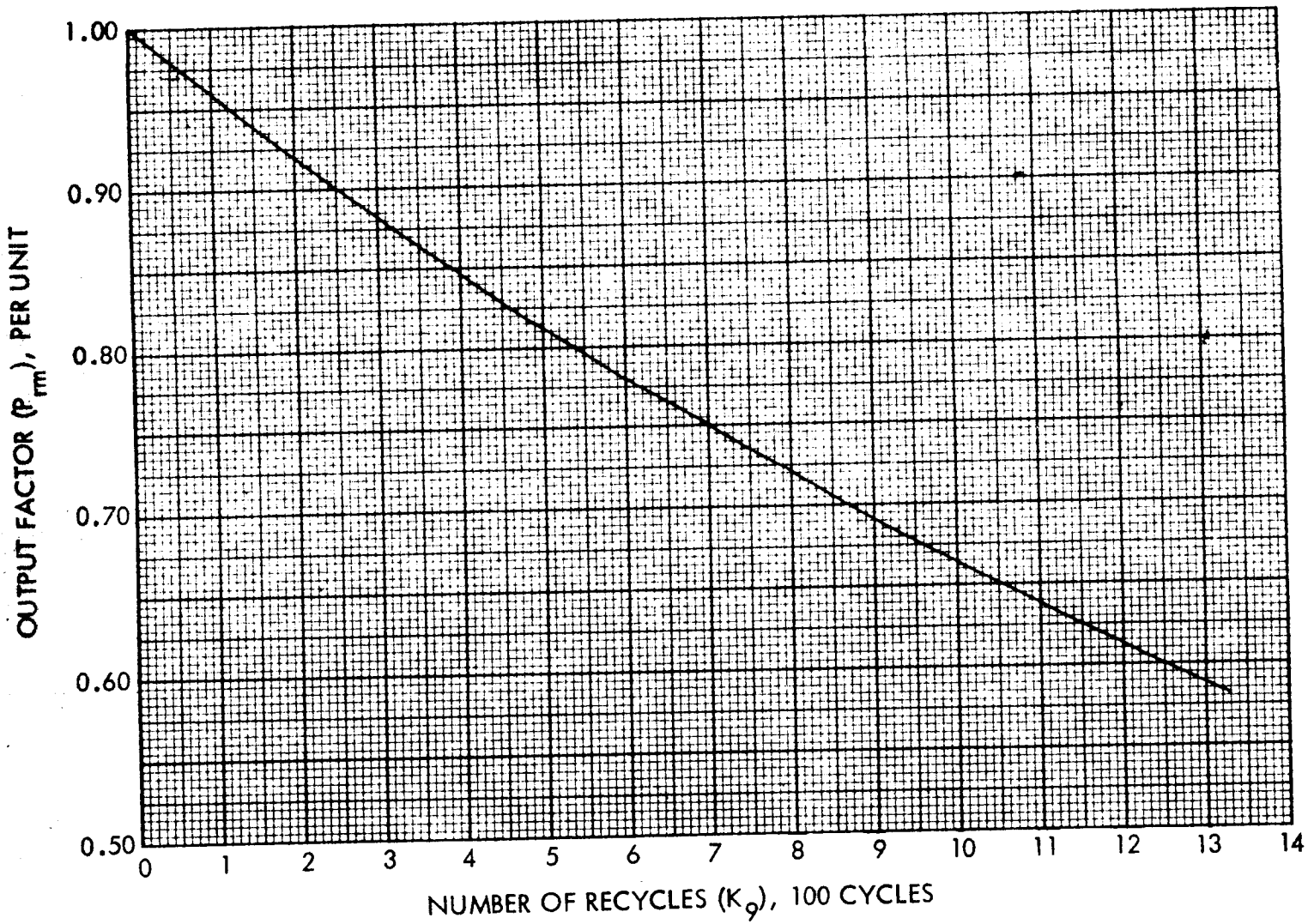

Figure A2-9. Thermal Recycling Degradation After Less Than 10^3 Hours at Steady State (Block I)

APPENDIX A3

SOLAR THERMIONIC PARAMETRIC DATA*

*The blocks referenced in this appendix are shown in Figure 3-24.

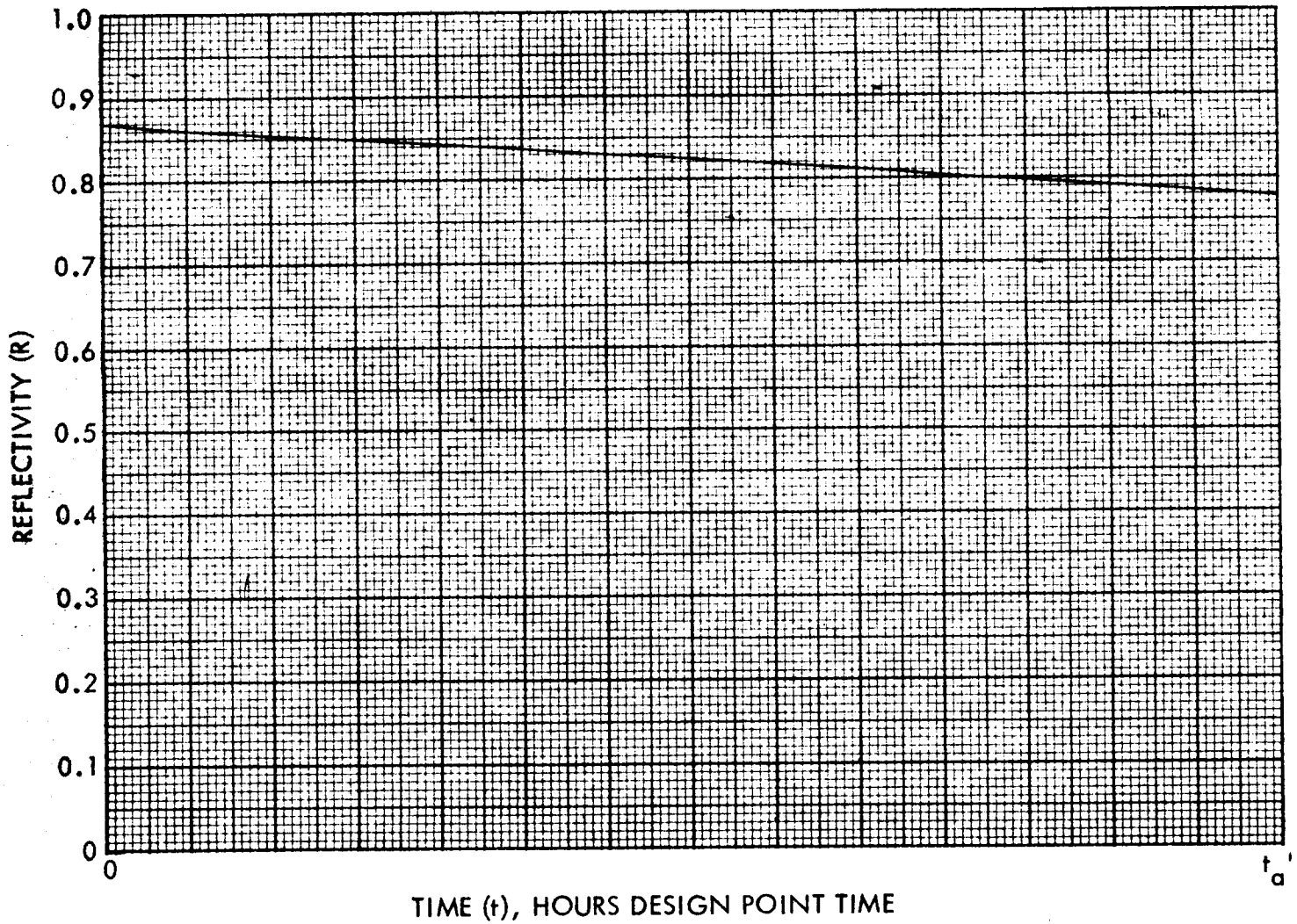

Figure A3-1. Reflectivity Versus Time, Solar Thermionic Function (Block A)

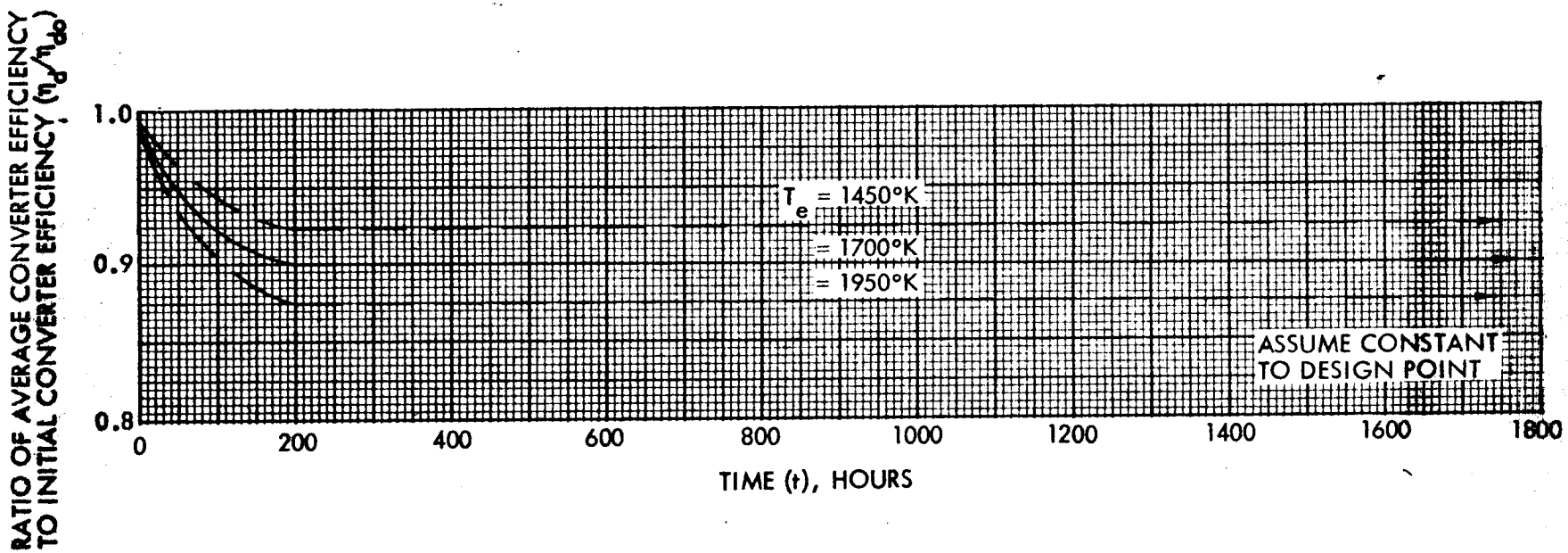

Figure A3-2. Ratio of Average Converter Efficiency to Initial Converter Efficiency Versus Time, Solar Thermionic Function (Block B)

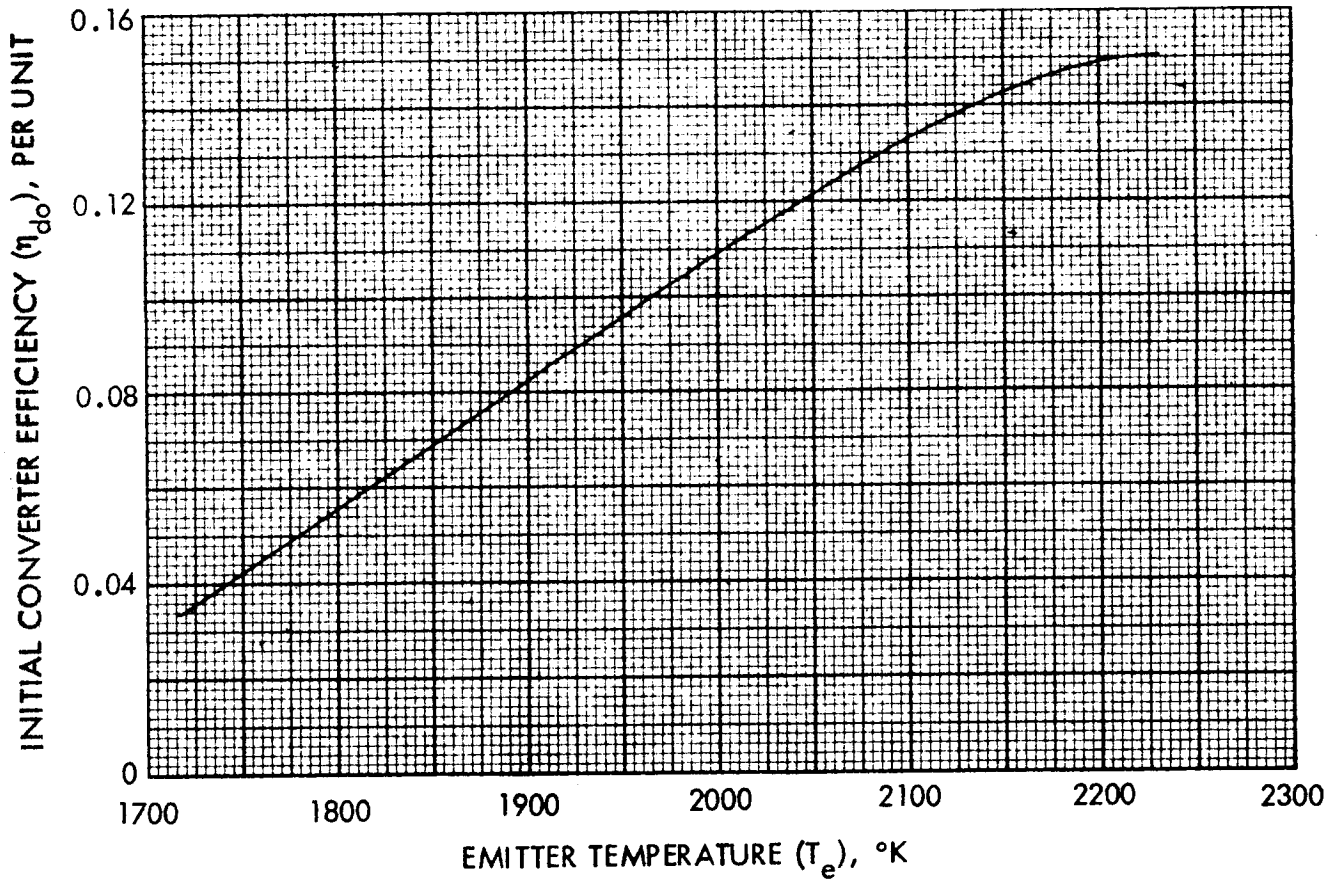

Figure A3-3. Initial Converter Efficiency Versus Emitter Temperature, Solar Thermionic Function (Block C)

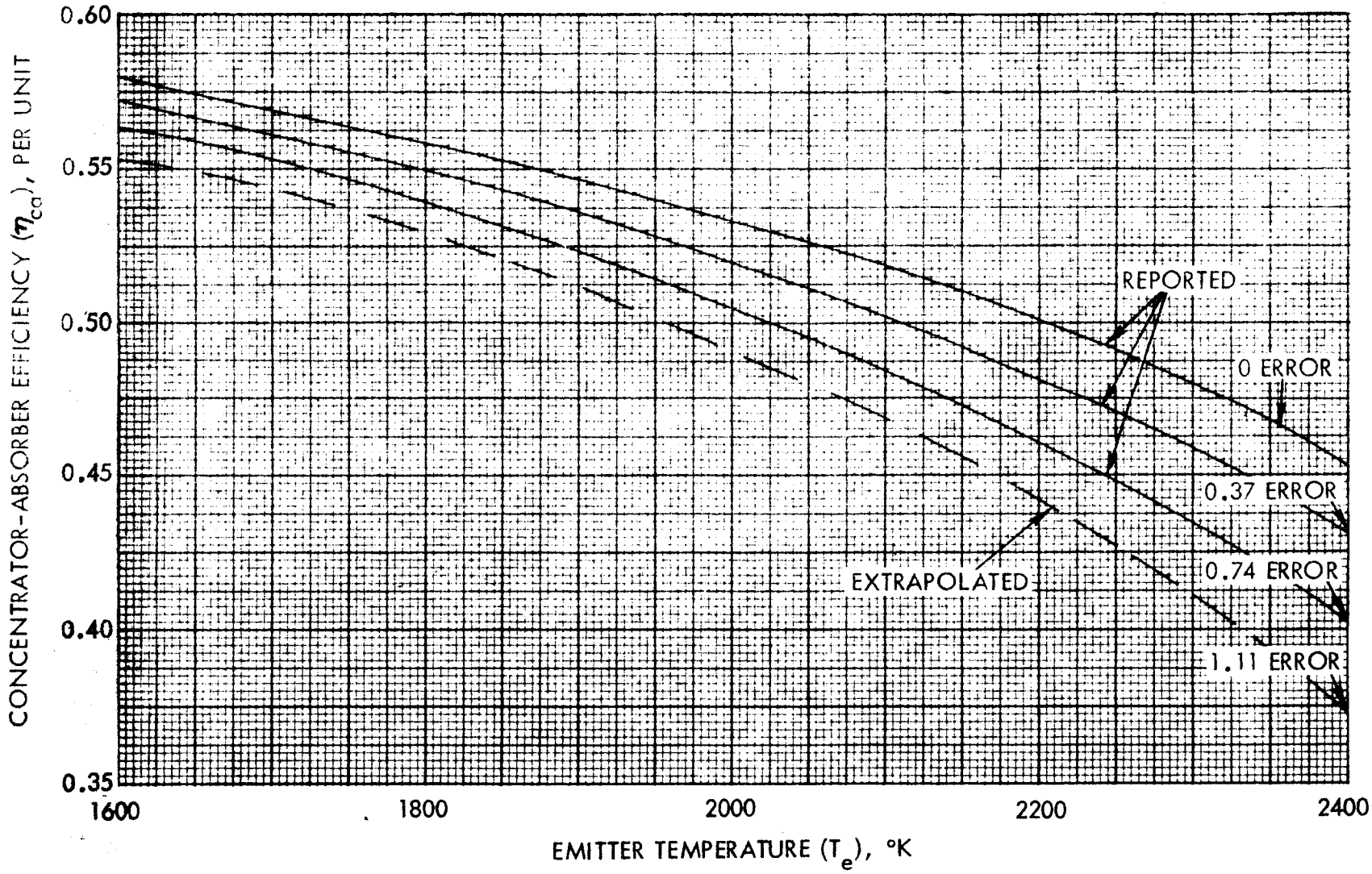

Figure A3-4. Concentrator-Absorber Efficiency as a Function of Emitter Temperature and Relative Orientation Error, Solar Thermionic Function (Block D)

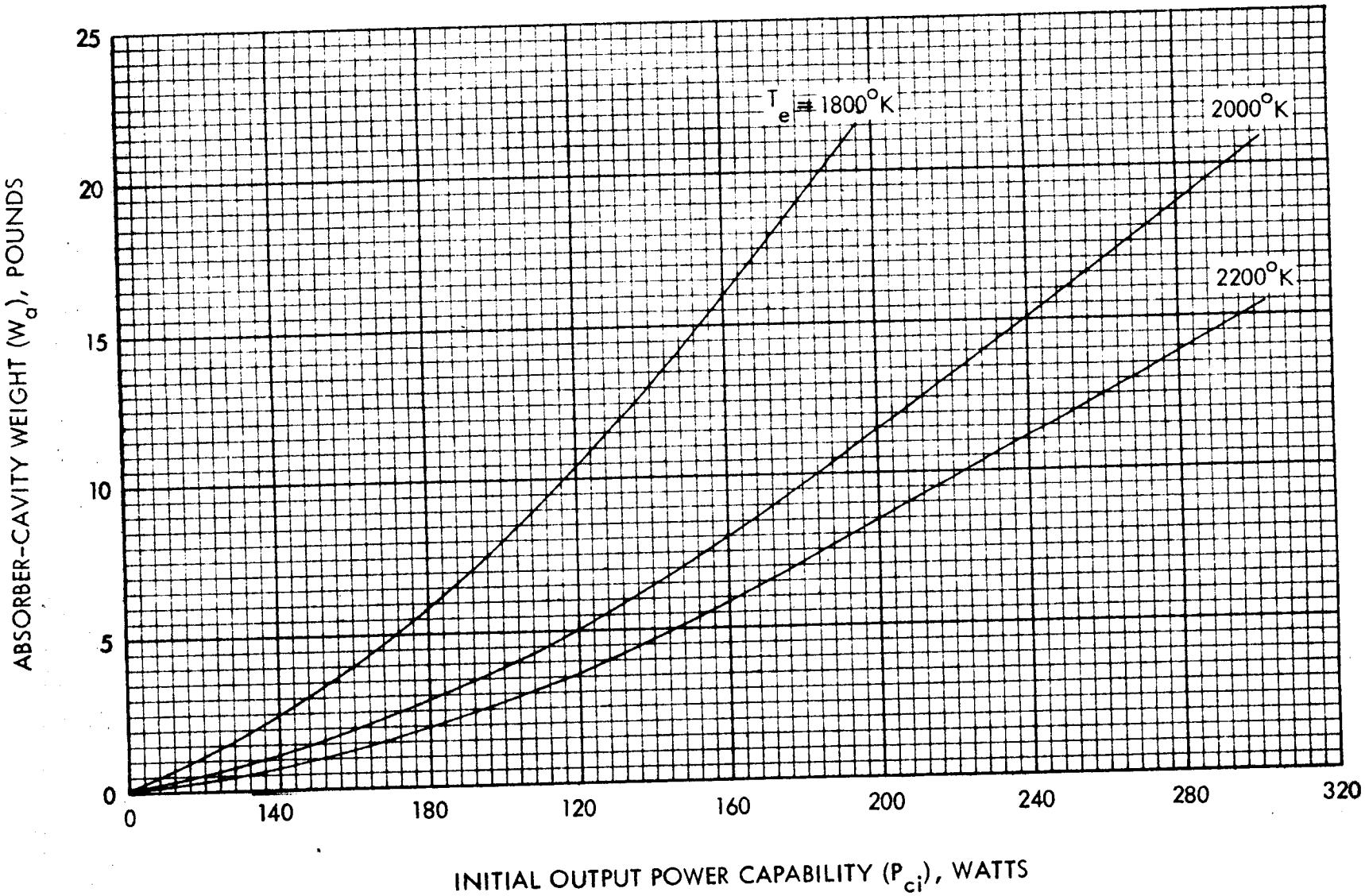

Figure A3-5. Weight of Absorber Cavity as a Function of Initial Power Capability and Emitter Temperature, Solar Thermionic Function (Block E)

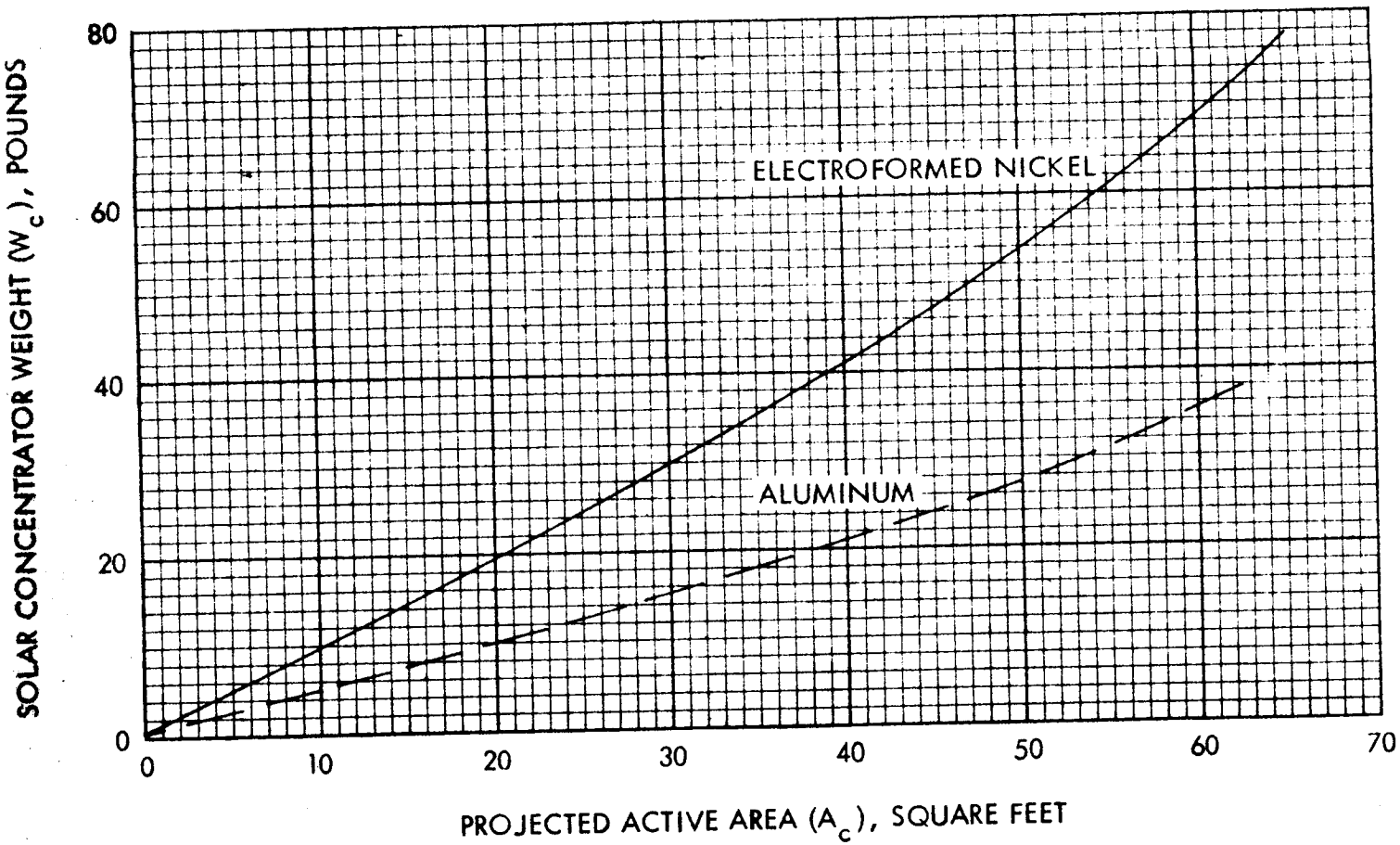

Figure A3-6. Weight of Solar Concentrator as a Function of Projected Active Area, Solar Thermionic Function (Block F)

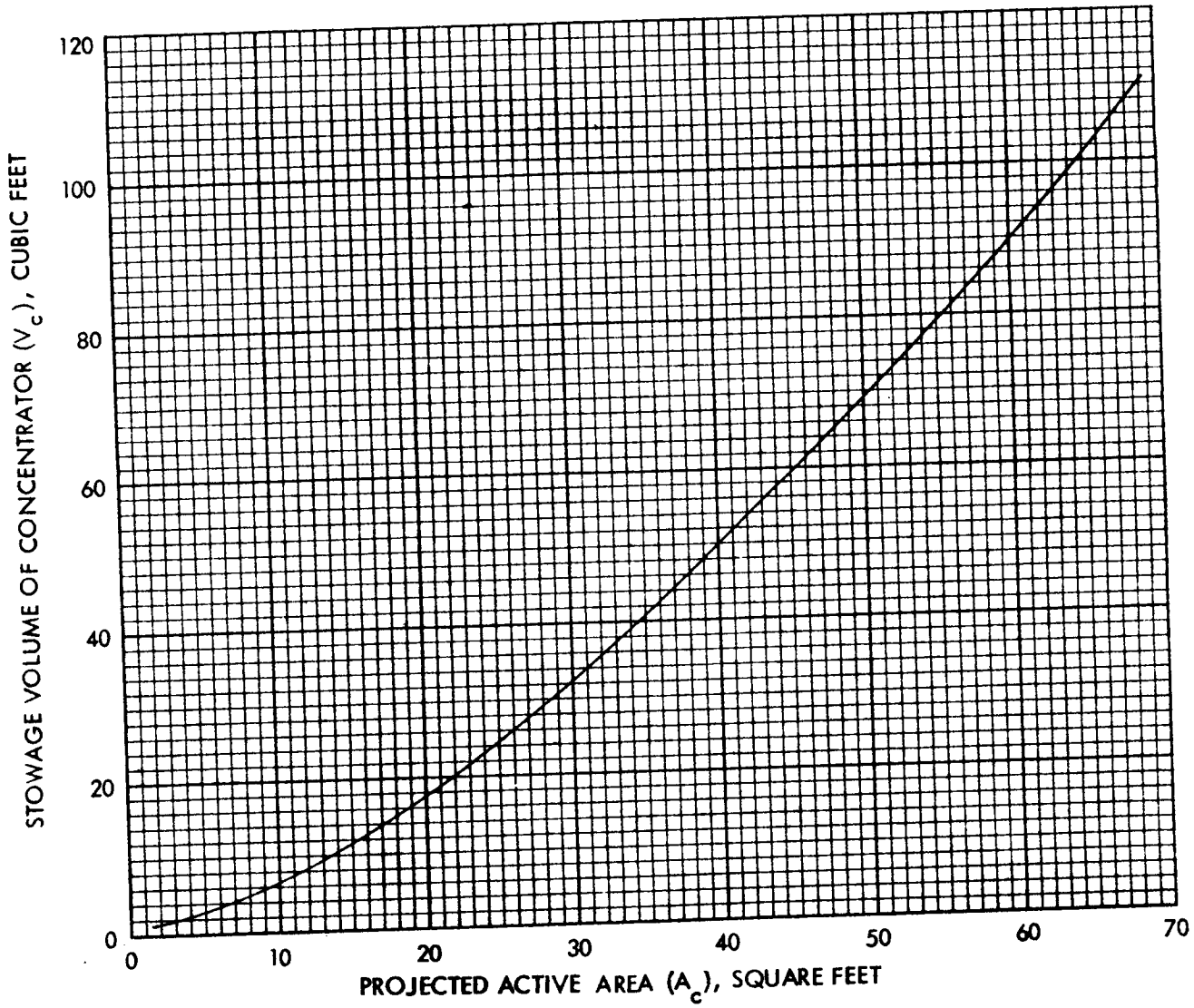

Figure A3-7. Stowage Volume of Concentrator as a Function of Projected Active Area, Solar Thermionic Function (Block G)

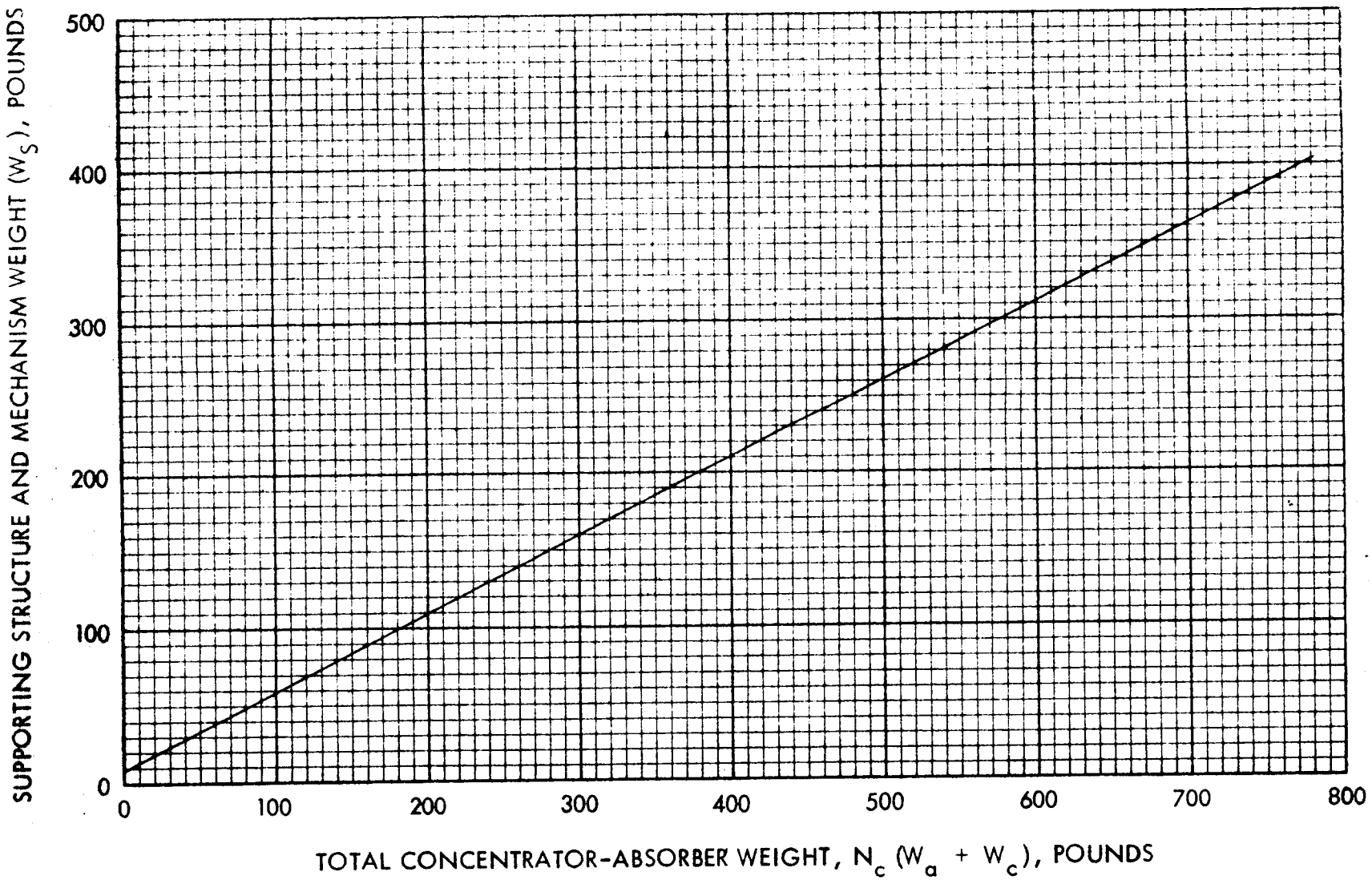

Figure A3-8. Weight of Supporting Structure and Mechanisms as a Function of Total Concentrator-Absorber Weight, Solar Thermionic Function (Block H)

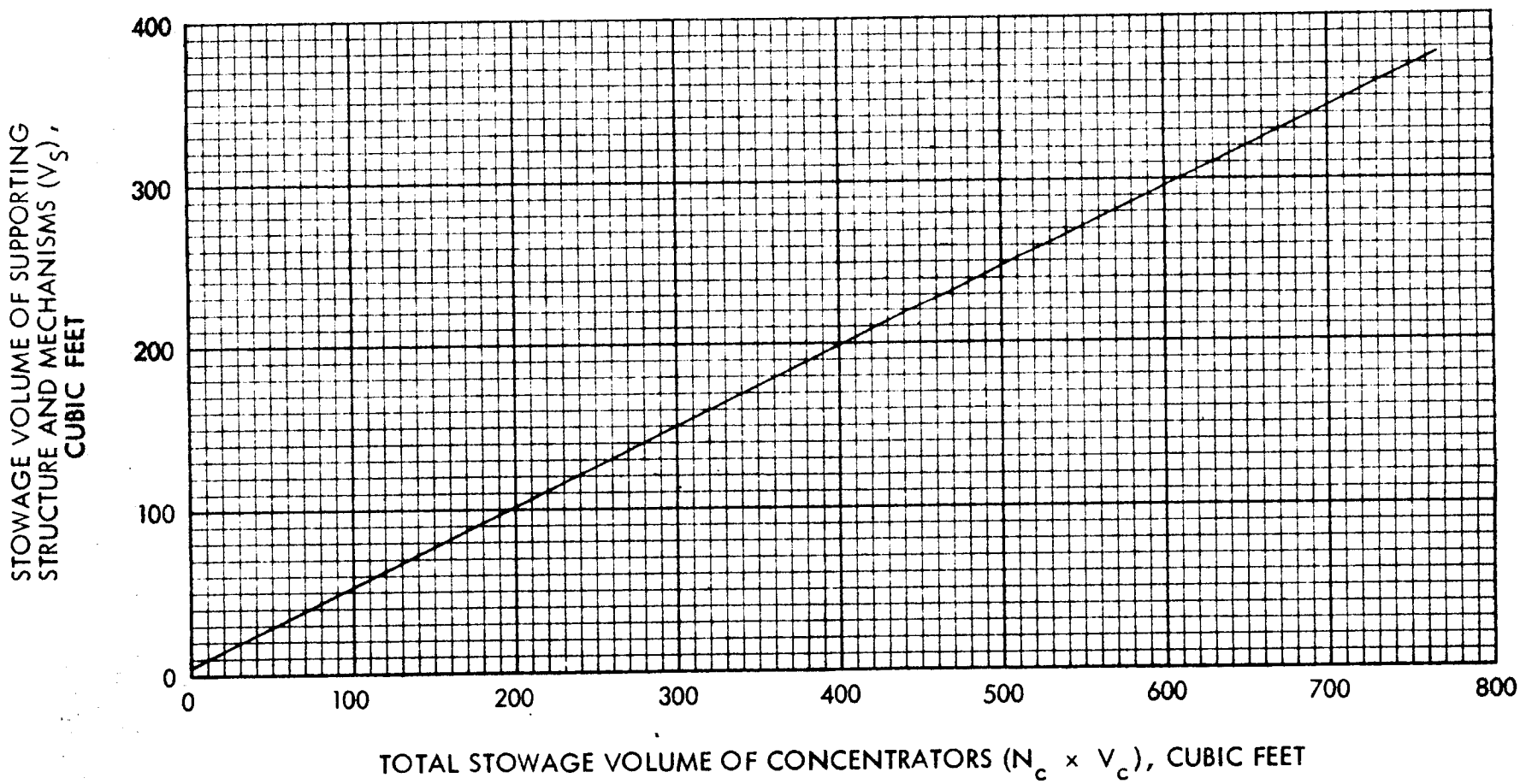

Figure A3-9. Stowage Volume of Supporting Structure and Mechanisms as a Function of Total Stowage Volume of Concentrators, Solar Thermionic Function (Block I)

APPENDIX A4

SOLAR POWER SOURCE CONTROLS PARAMETRIC DATA*

*The blocks referenced in this appendix are shown in Figure 3-30.

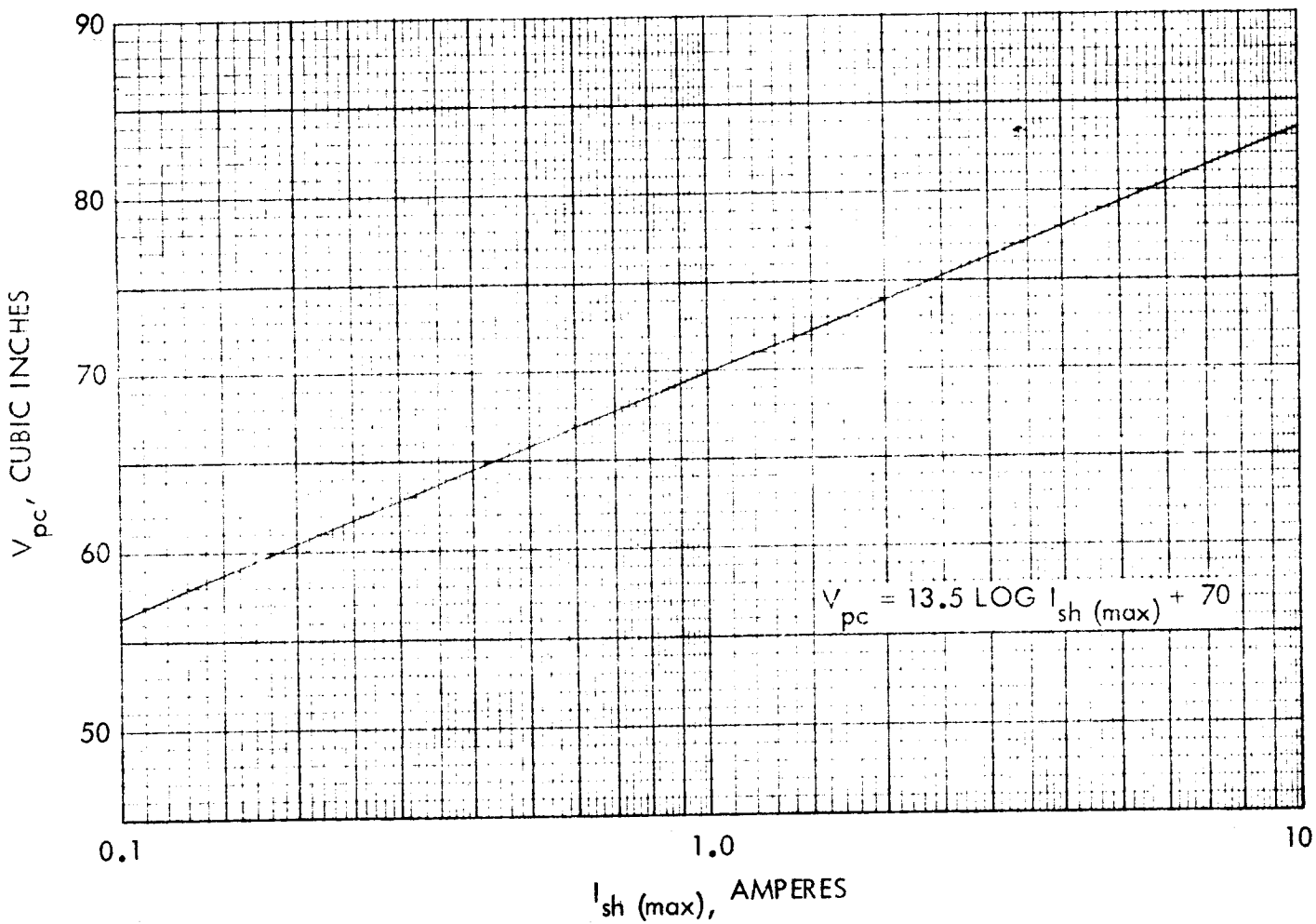

Figure A4-1. Power Control Volume as a Function of Shunt Current (Block A)

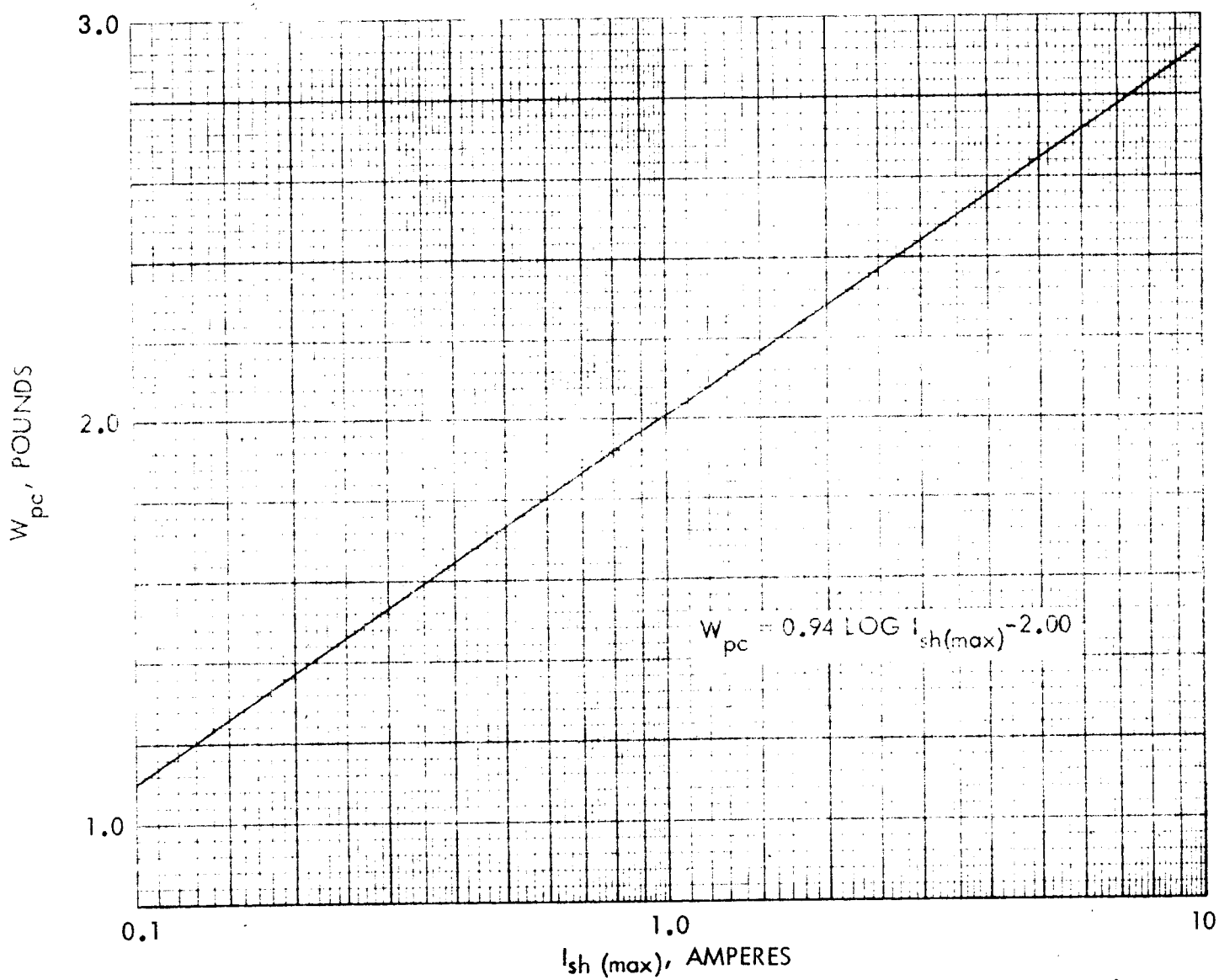

Figure A4-2. Power Control Weight as a Function of Shunt Current (Block W)

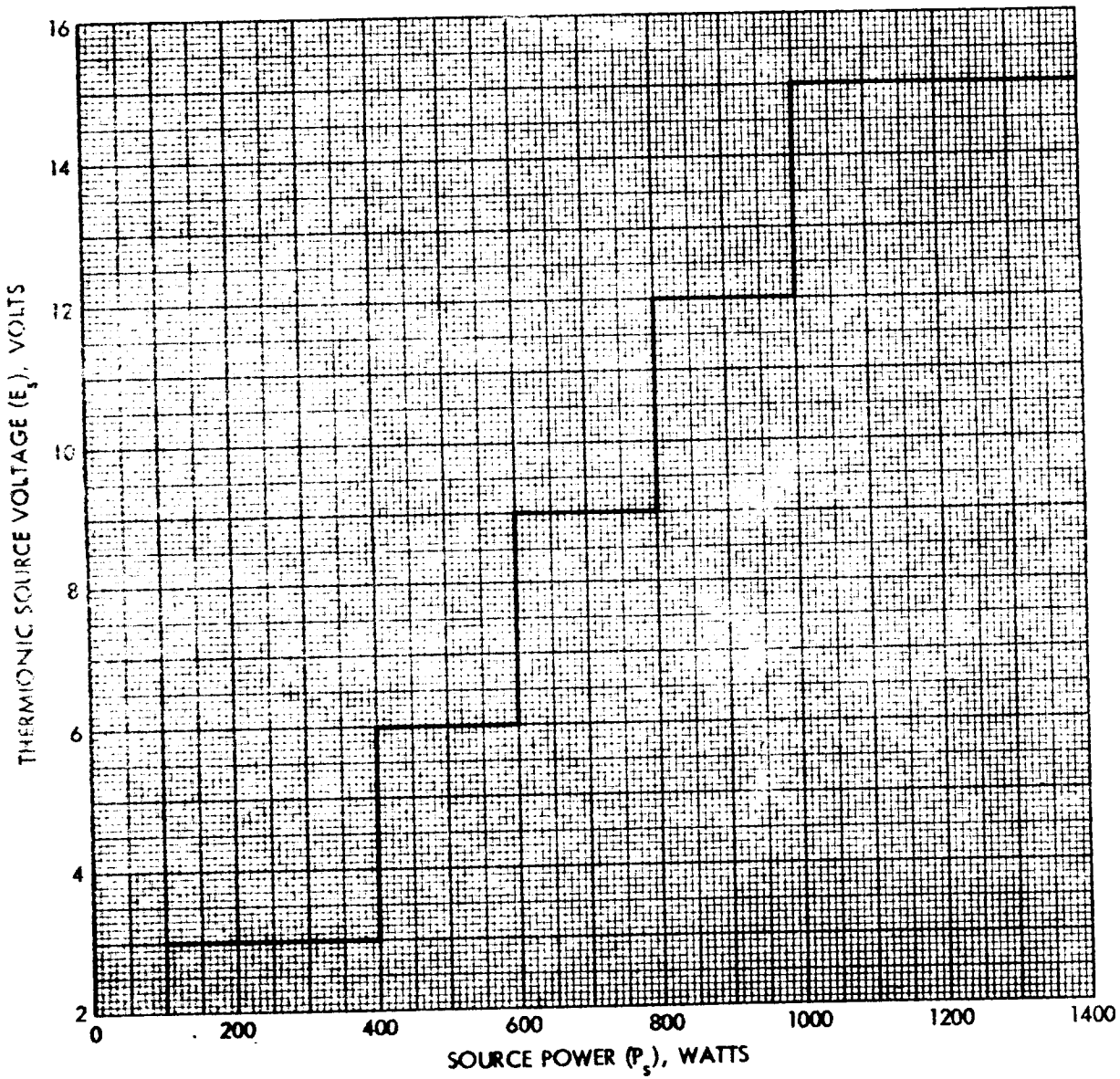

Figure A4-3. Assumed Thermionic Power Source Output Voltage as a Function of Output Power (Block B)

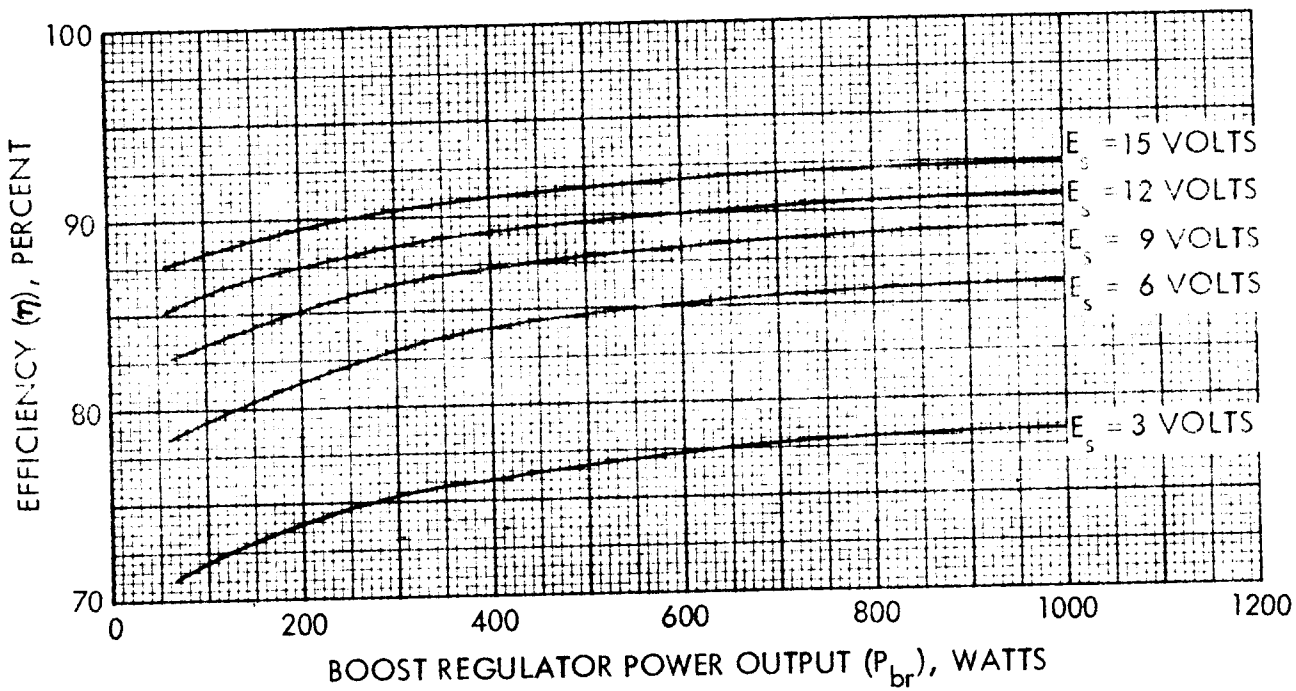

Figure A4-4. Boost Regulator Efficiency as a Function of Output Power and Input Voltage (Block C)

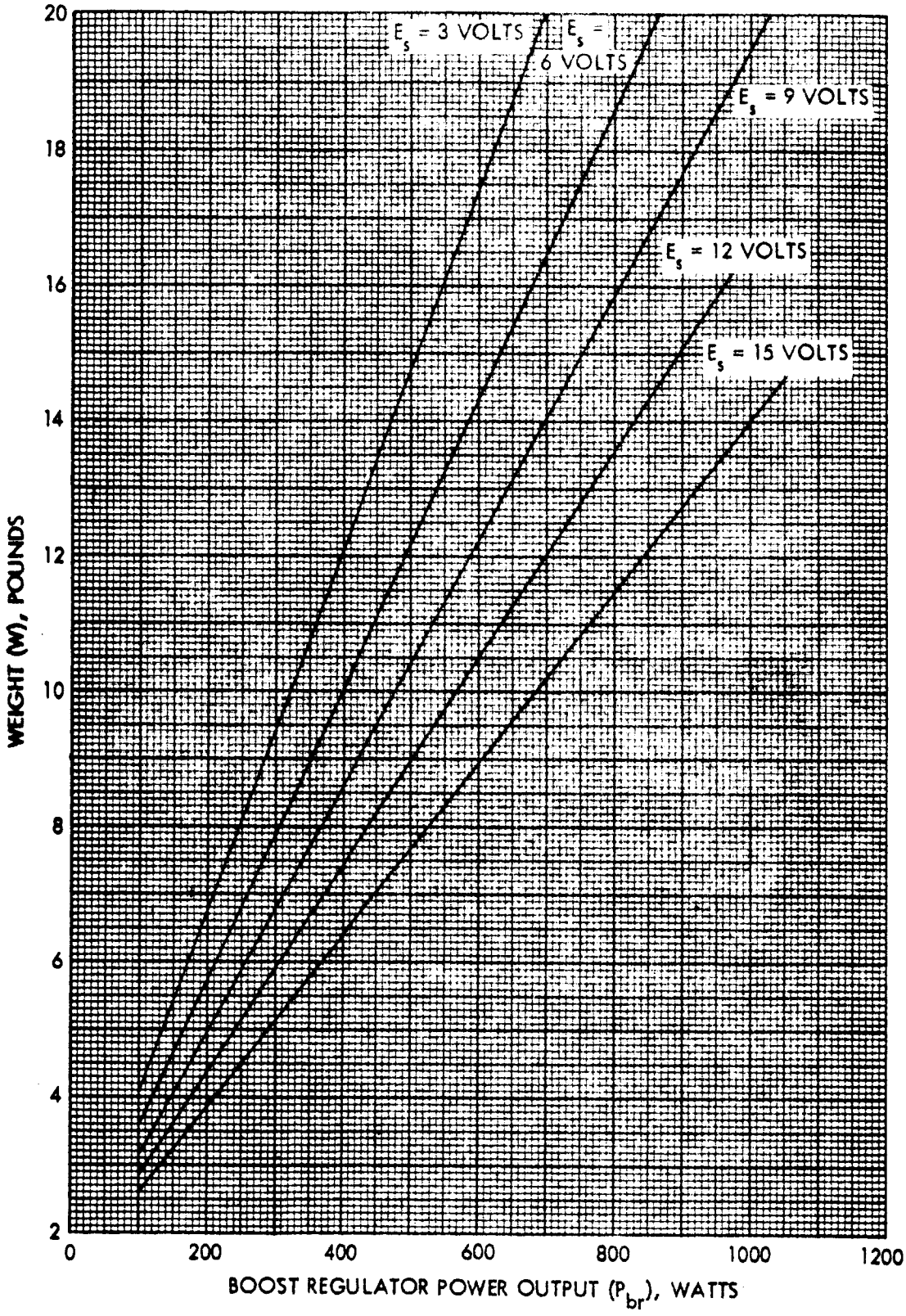

Figure A4-5. Boost Regulator Weight as a Function of Output Power and Input Voltage (Block D)

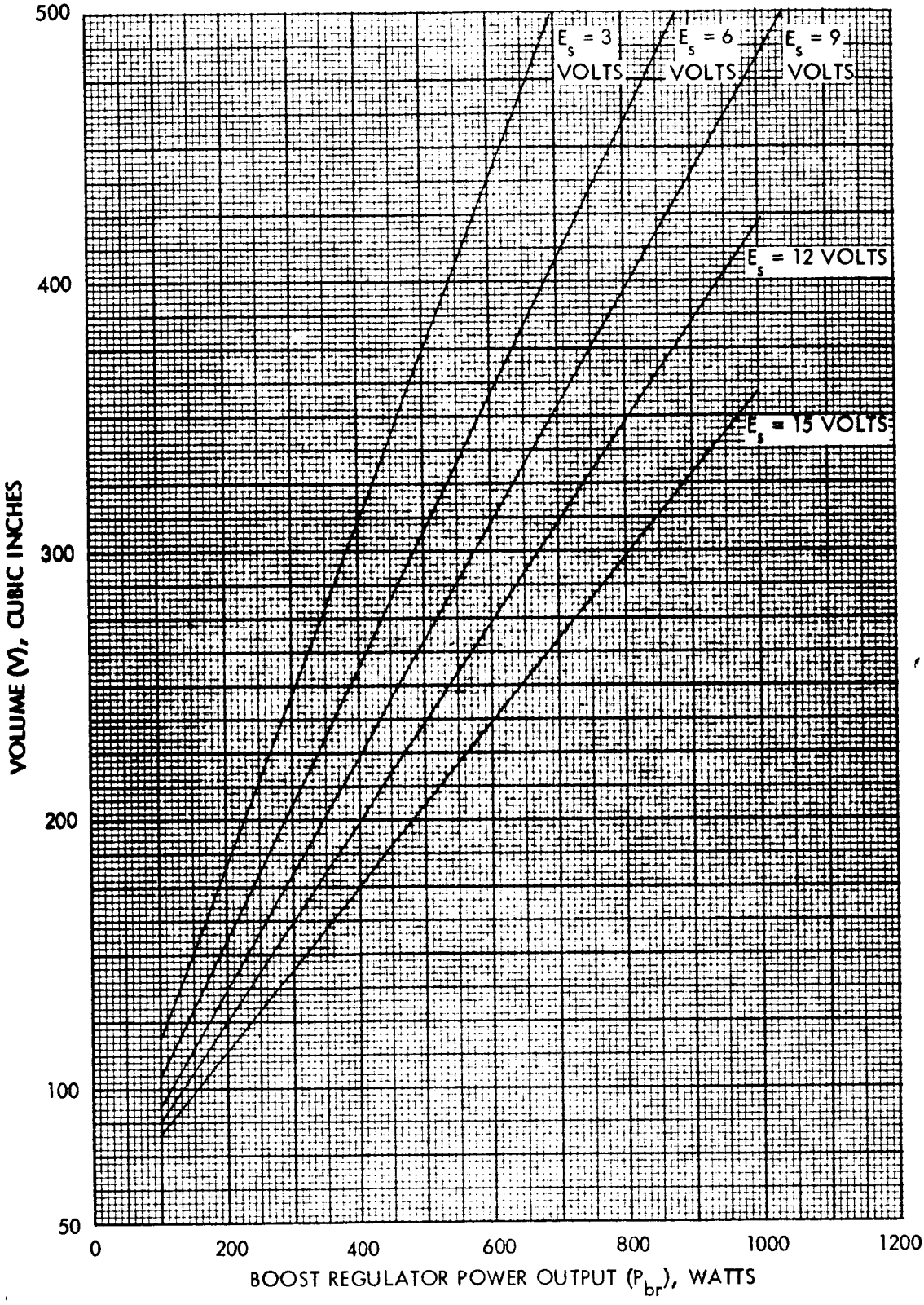

Figure A4-6. Boost Regulator Volume as a Function of Output Power and Input Voltage (Block E)

APPENDIX A5

SOLAR DYNAMIC POWER PLANT PARAMETRIC DATA*

*The blocks referenced in this appendix are shown in Figure 3-26.

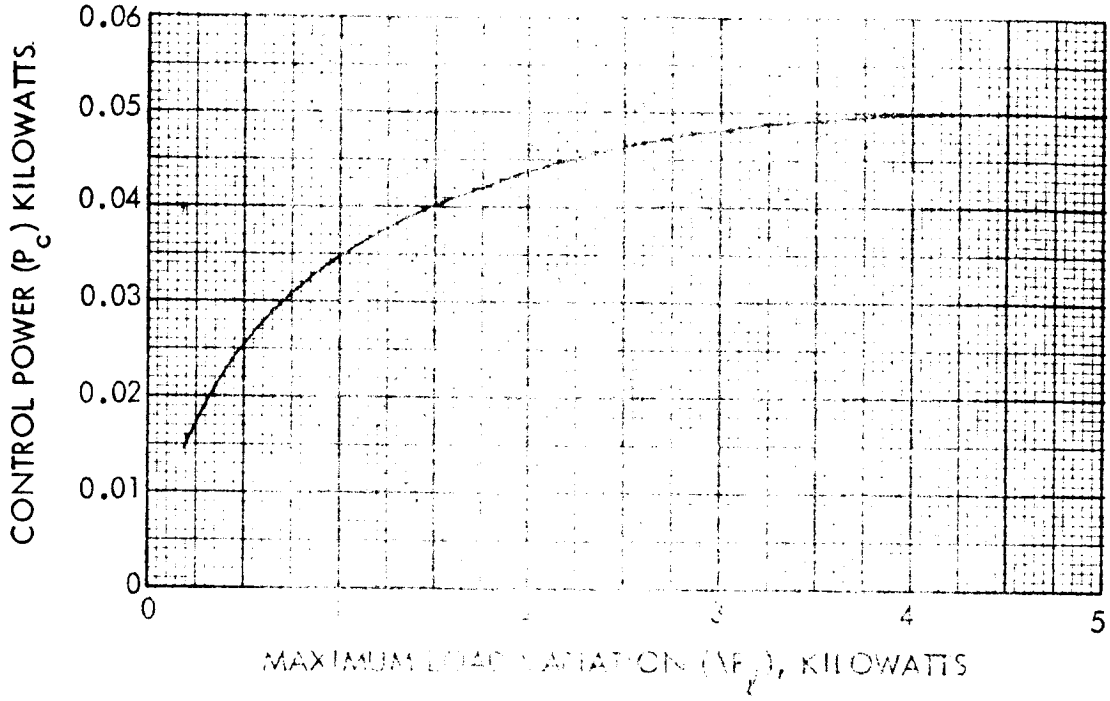

Figure A5-1. Estimated Power [illegible] for Control of Parasitic Load as a Function of Maximum Parasitic Load Power Dissipation (Block B)

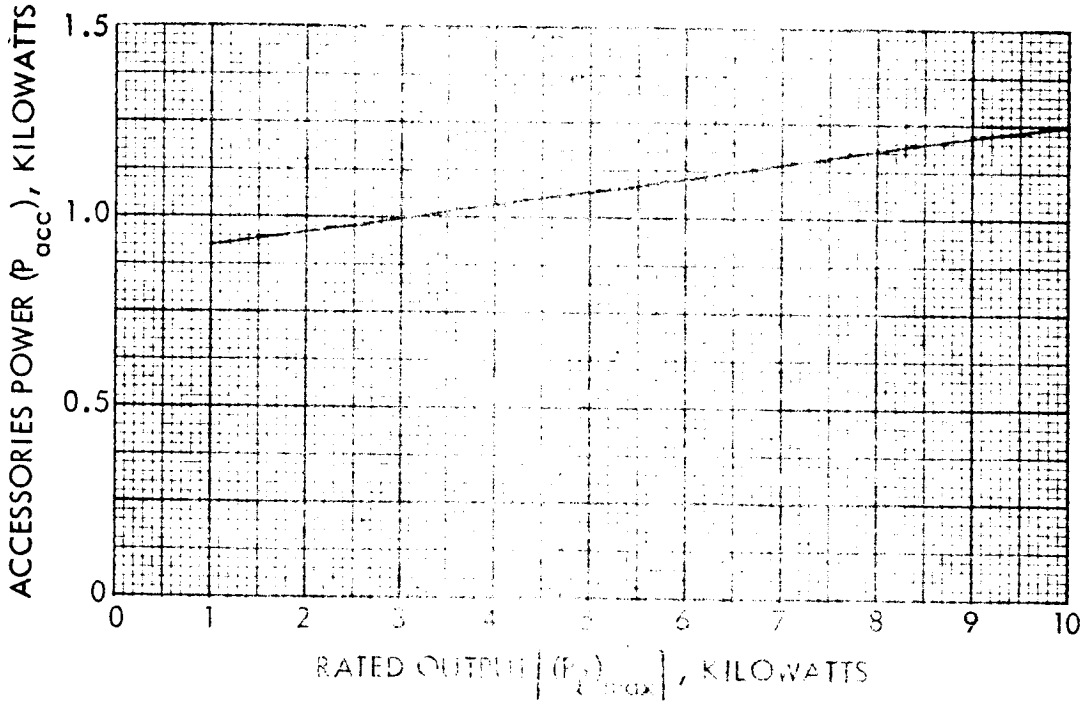

Figure A5-2. Accessories [illegible] Power as a Function of Rated Output for Mercury [illegible] Power Supply (Block E)

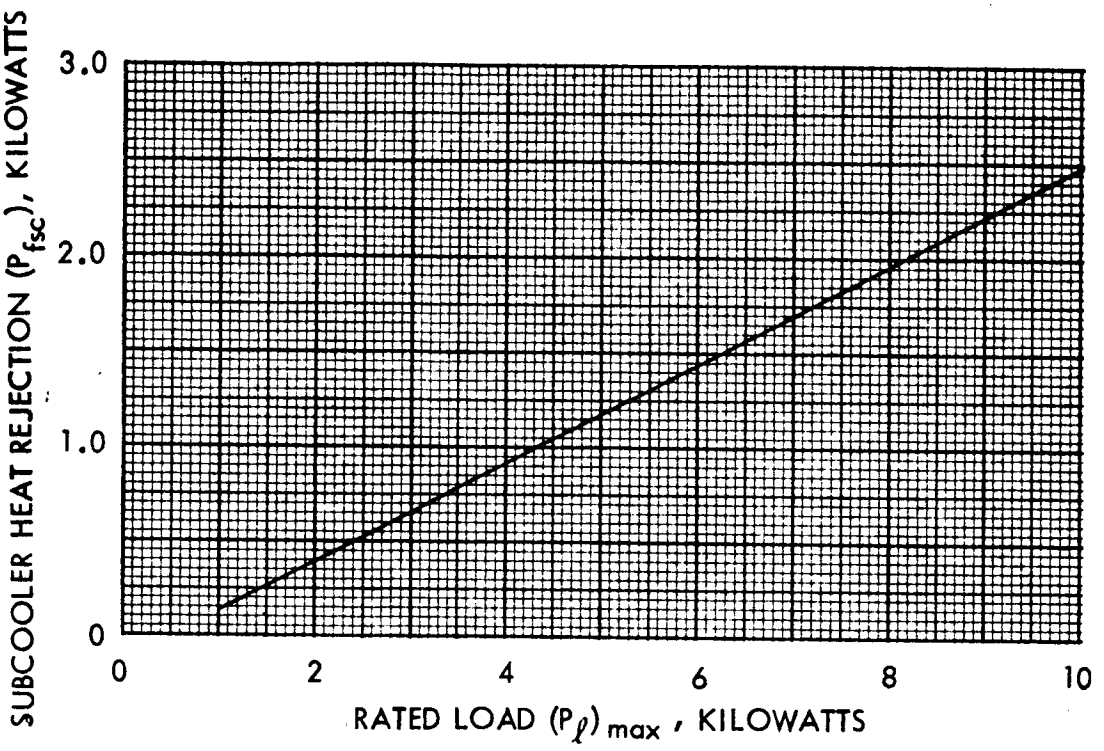

Figure A5-3. Fluid Subcooling Required as a Function of Rated Output for Mercury Rankine Power Supply (Block G)

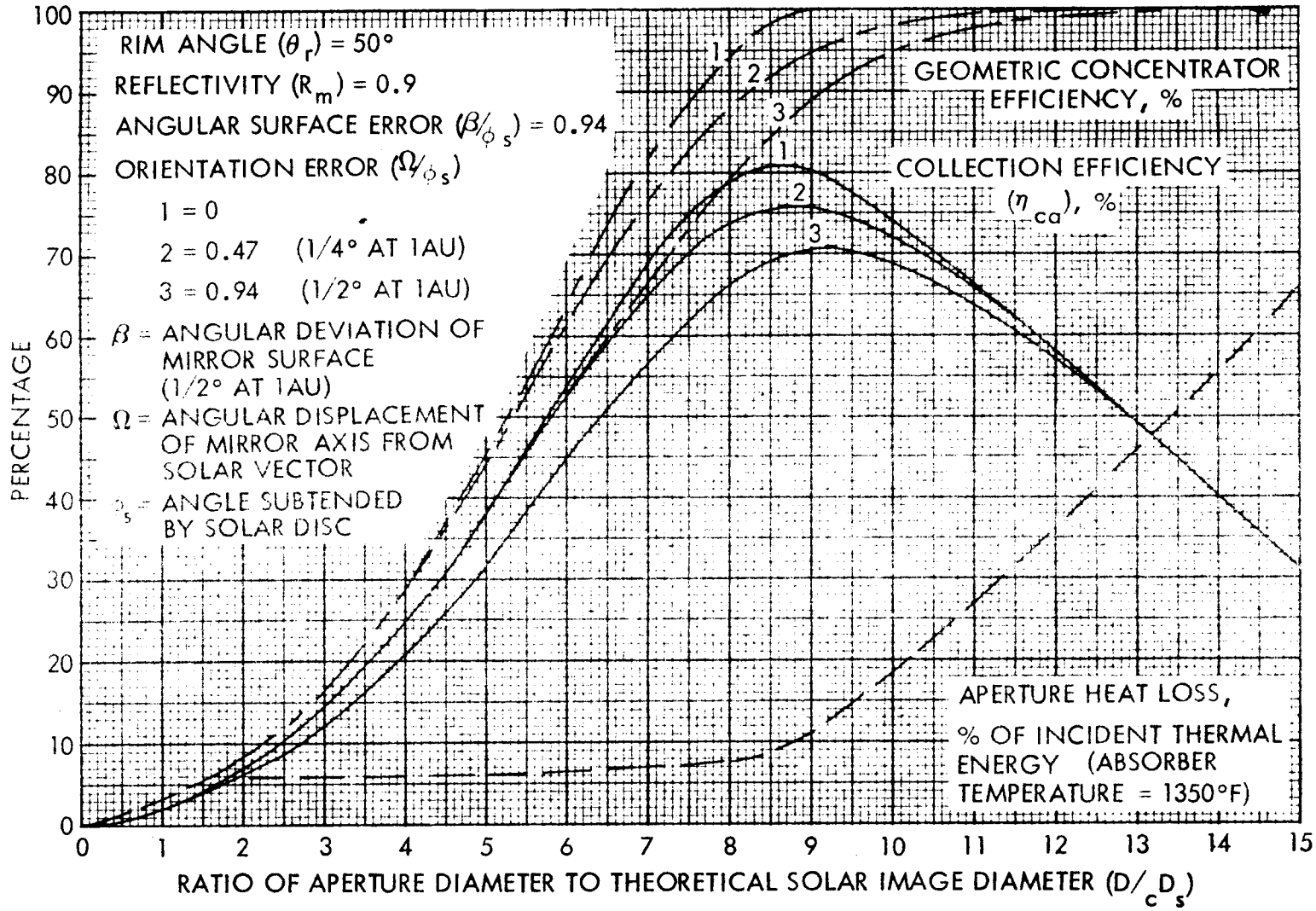

Figure A5-4. Collector Performance Characteristics as a Function of Concentrator Accuracy and Cavity Aperture Diameter (Block L)

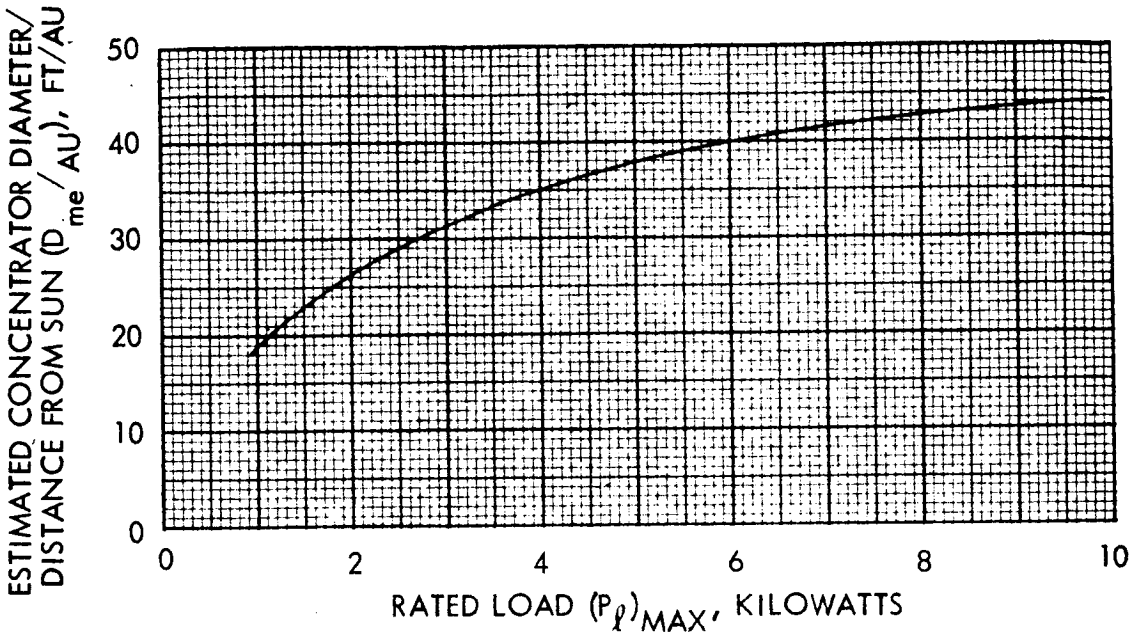

Figure A5-5. Estimated Concentrator Diameter Normalized to AU as a Function of Rated Output for Mercury Rankine Power Supply (Block J)

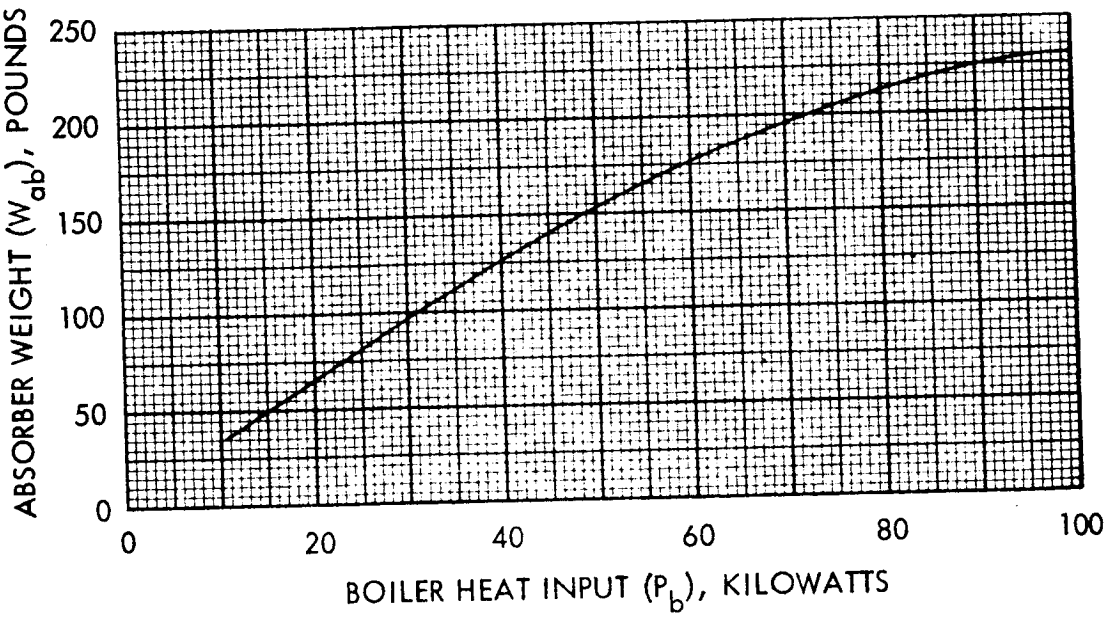

Figure A5-6. Estimated Absorber Weight Excluding Heat Storage Unit vs Boiler Heat Input Rate (Block KK)

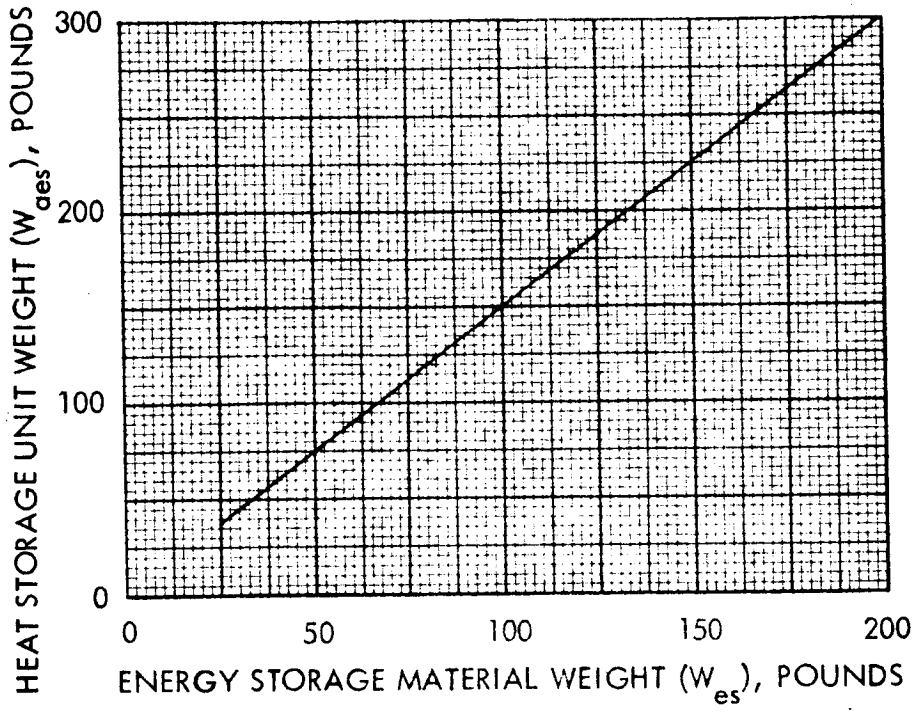

Figure A5-7. Total Heat Storage Weight as a Function of Energy Storage Material Weight (Block LL)

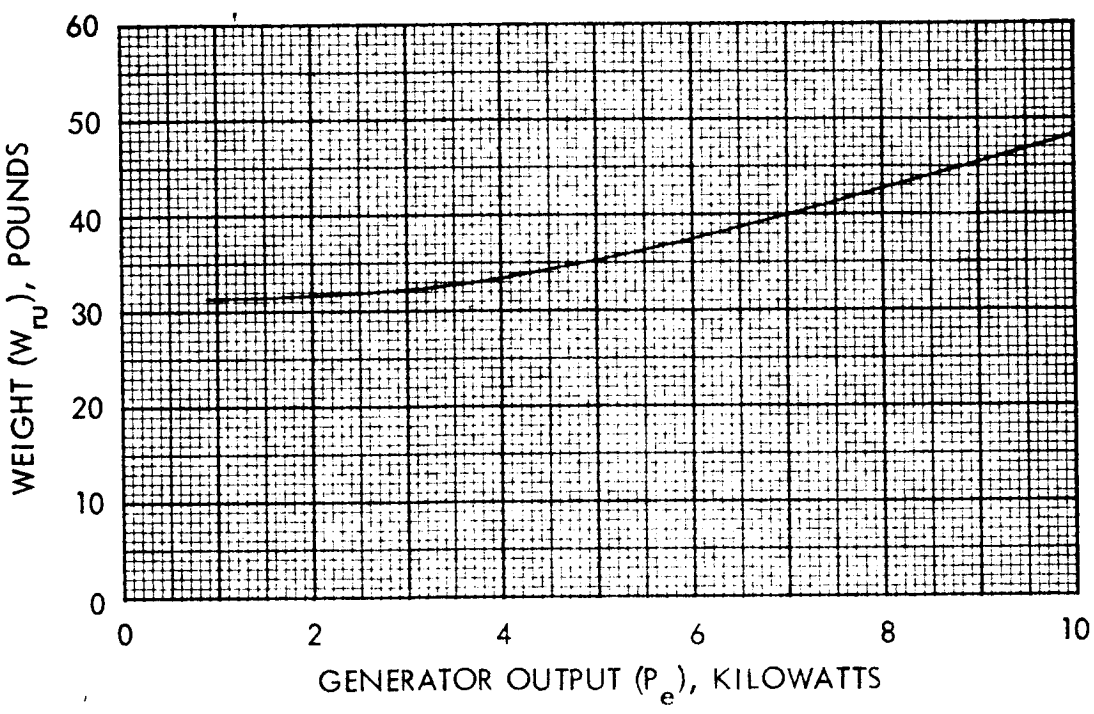

Figure A5-8. Weight of Rotating Unit (Generator, Turbine, and Pump) as a Function of Electrical Output (Block II)

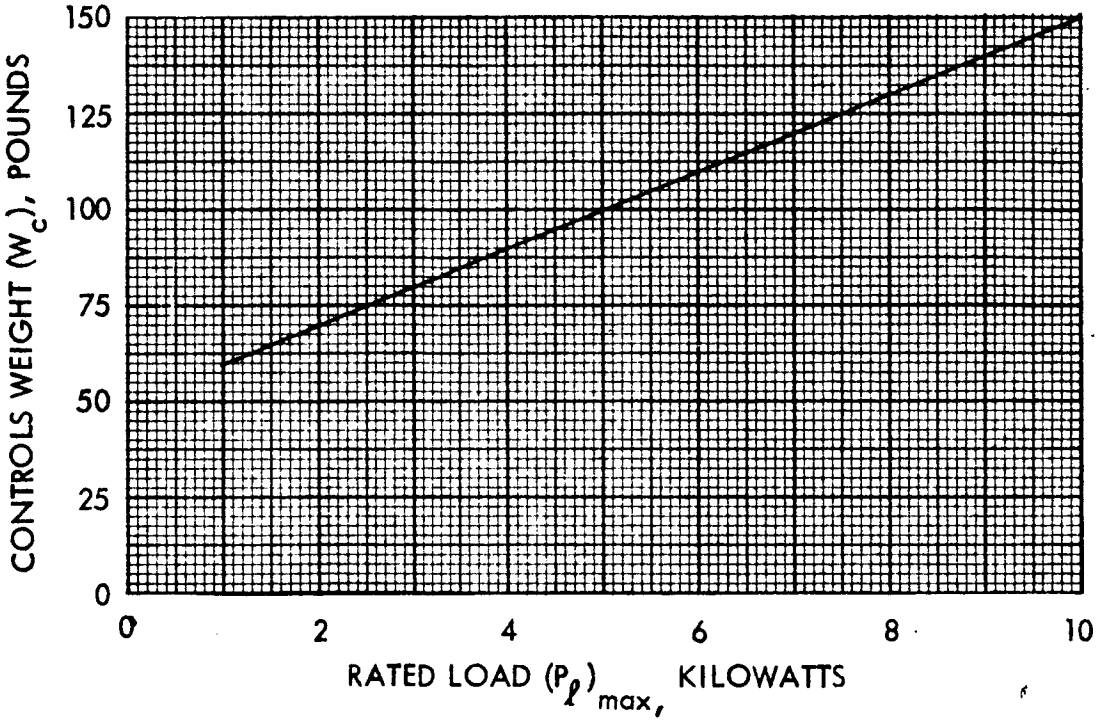

Figure A5-9. Estimated Weight of Control Equipment as a Function of Rated Output —Weight Includes Speed Control and Startup System —(Block OO)

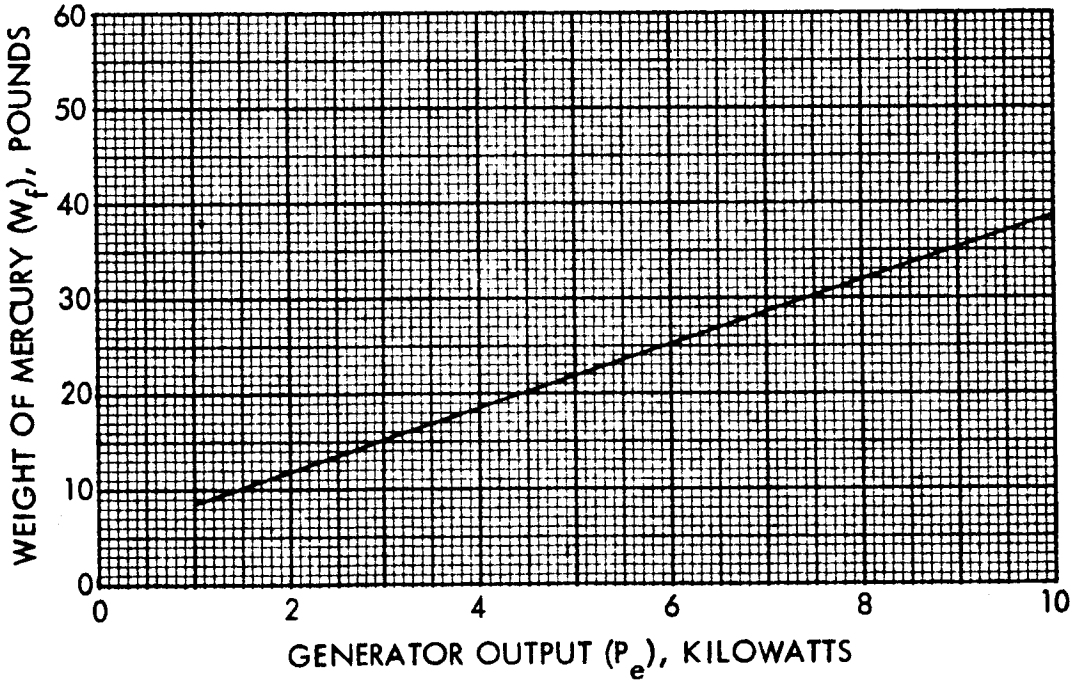

Figure A5-10. Fluid Inventory Weight for Mercury Rankine Power Supply as a Function of Generated Power (Block NN)

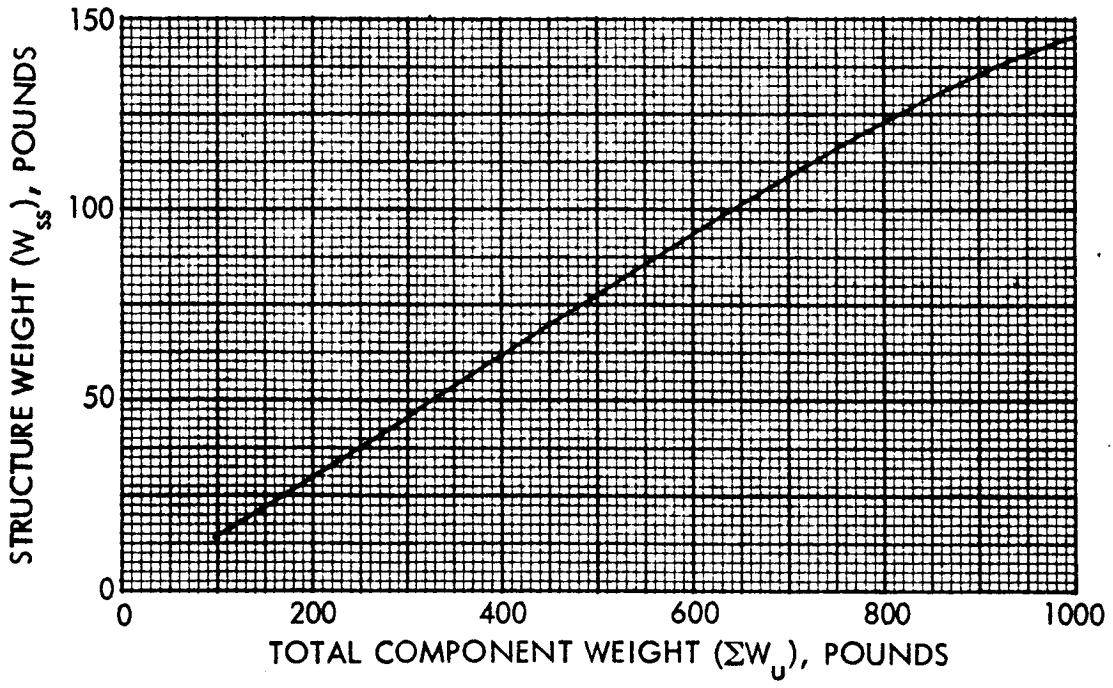

Figure A5-11. Support Structure Weight for Solar Dynamic Power Supply vs Total Weight of Components (Block PP)

APPENDIX A6

PRIMARY SILVER-ZINC BATTERY PARAMETRIC DATA*

*The blocks referenced in this appendix are shown in Figure 4-1.

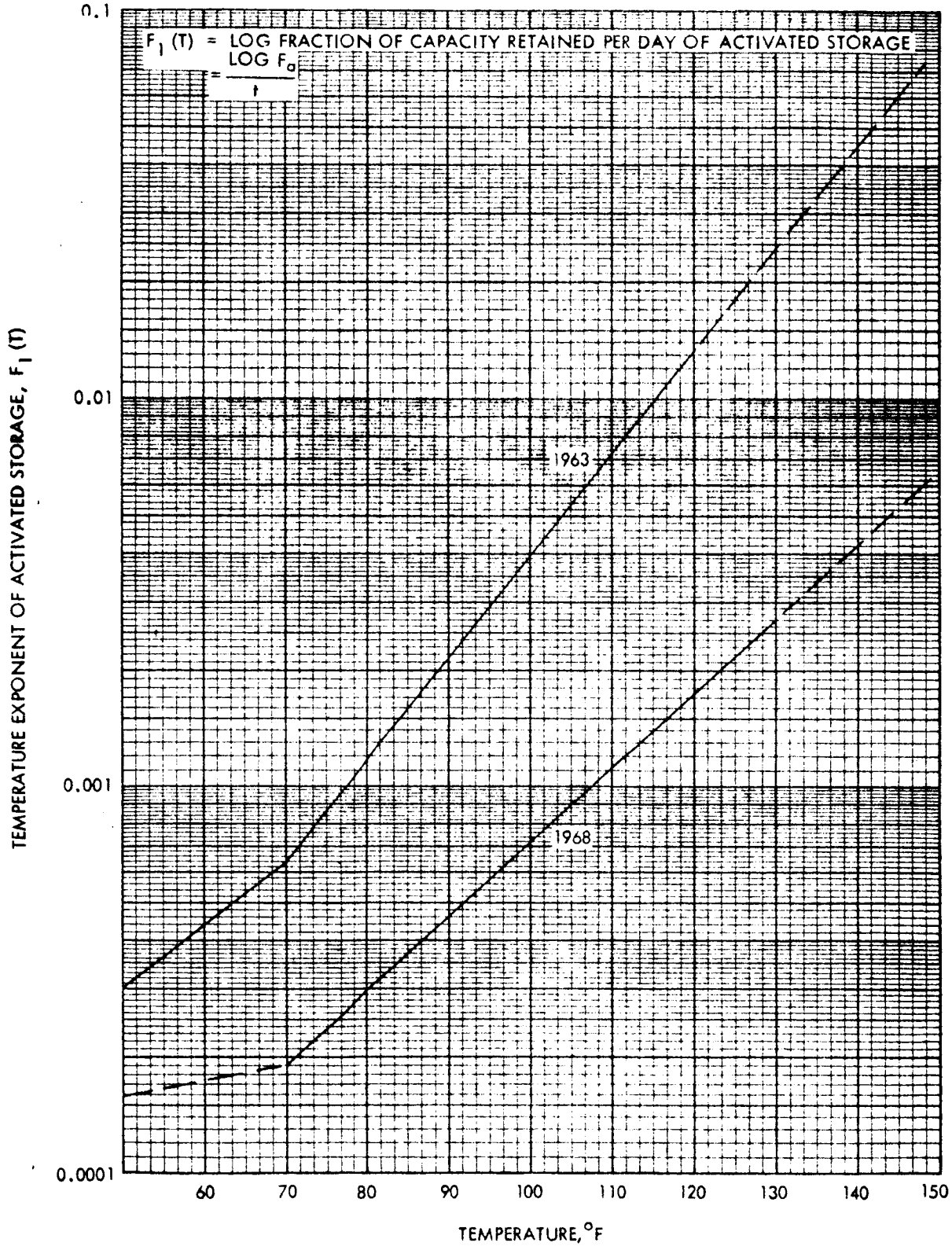

Figure A6-1. Temperature Exponent of Activated Storage Versus Temperature (Block P)

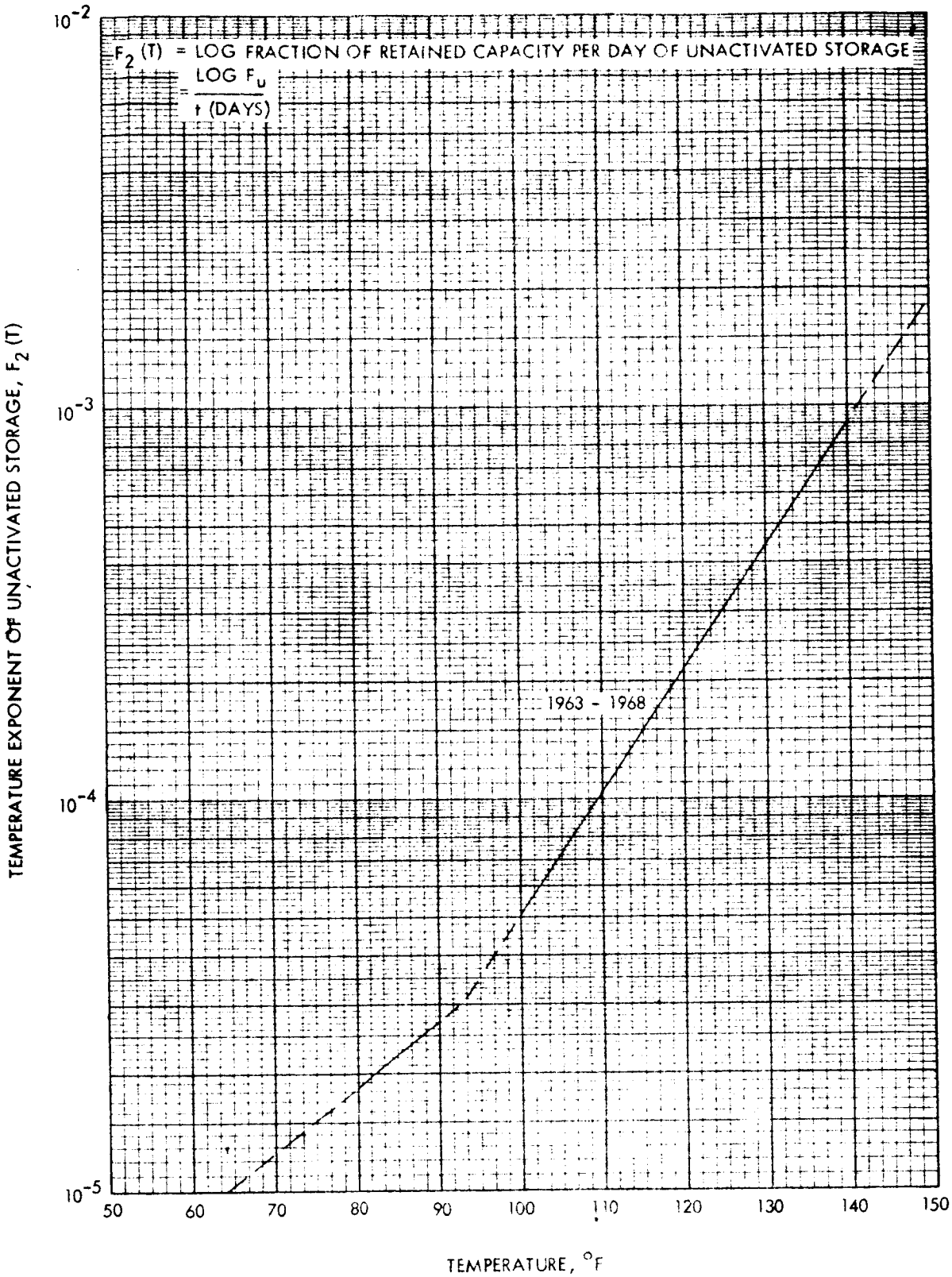

Figure A6-2. Temperature Exponent of Unactivated Storage Versus Temperature (Block K)

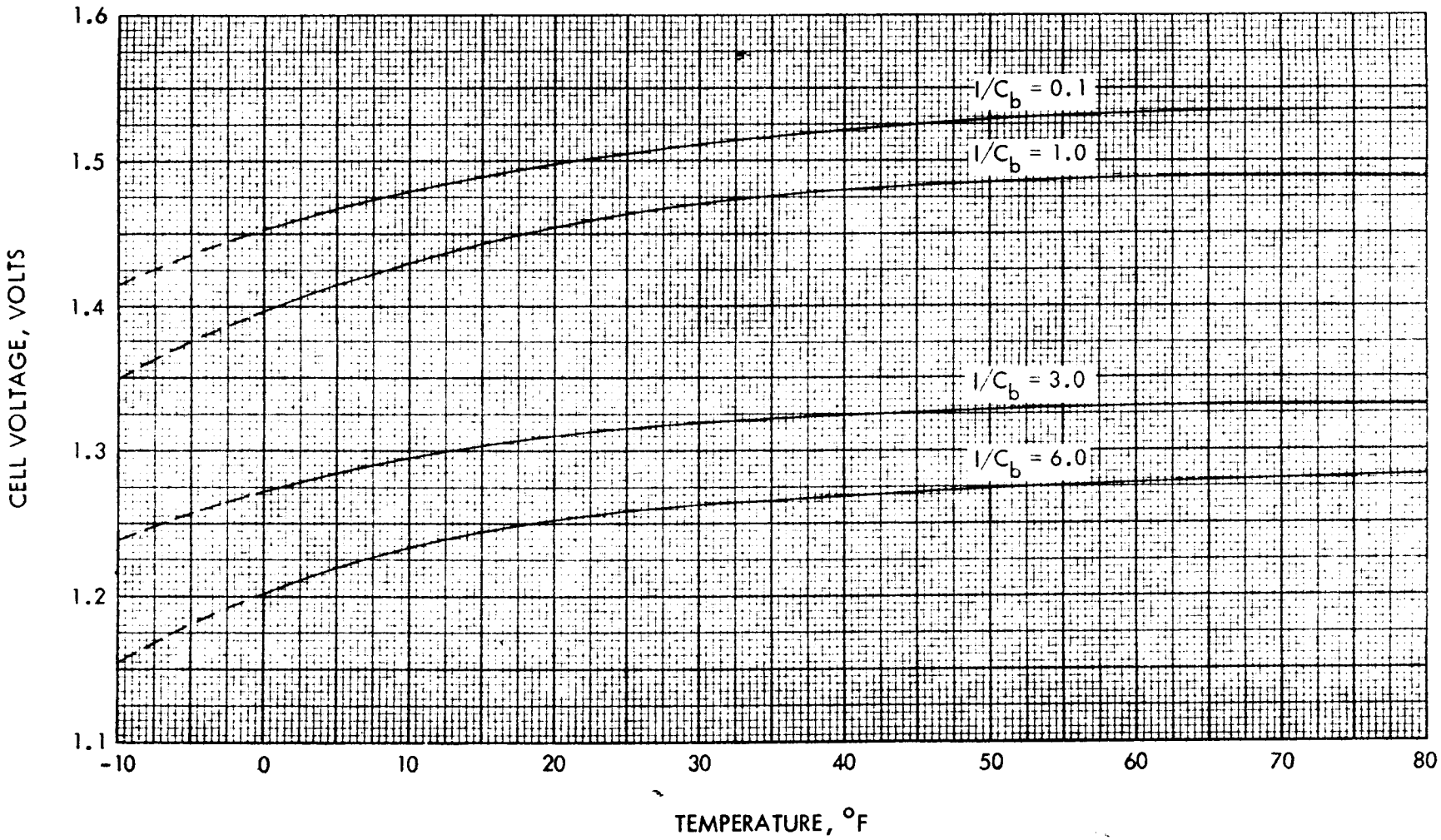

Figure A6-3. Cell Plateau Voltage as a Function of Discharge Rate and Temperature (Block S)

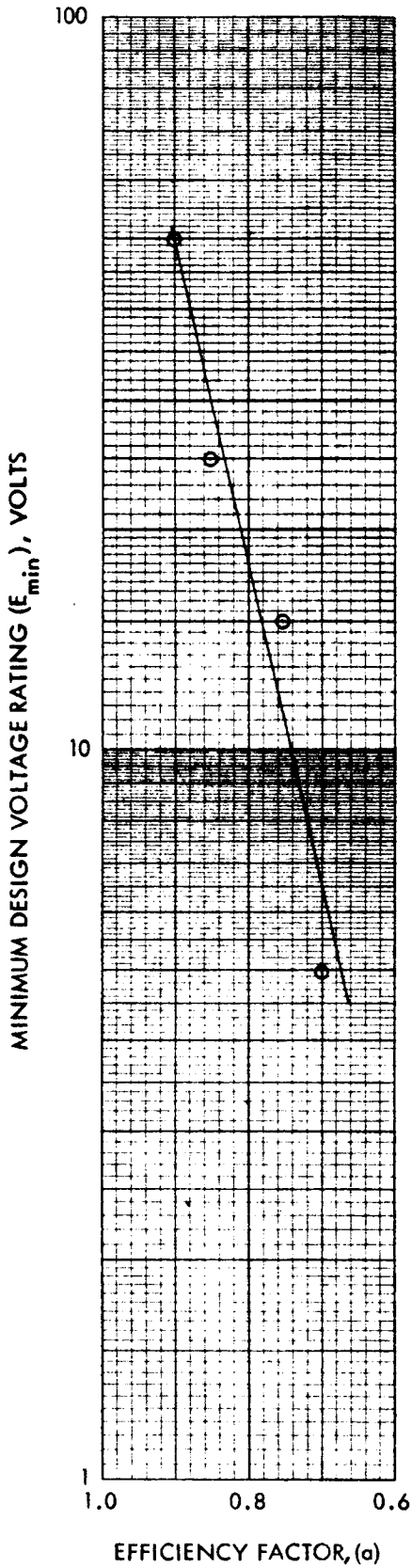

Figure A6-4. Converter Efficiency Factor, a, Versus Rated Design Voltage (Block I)

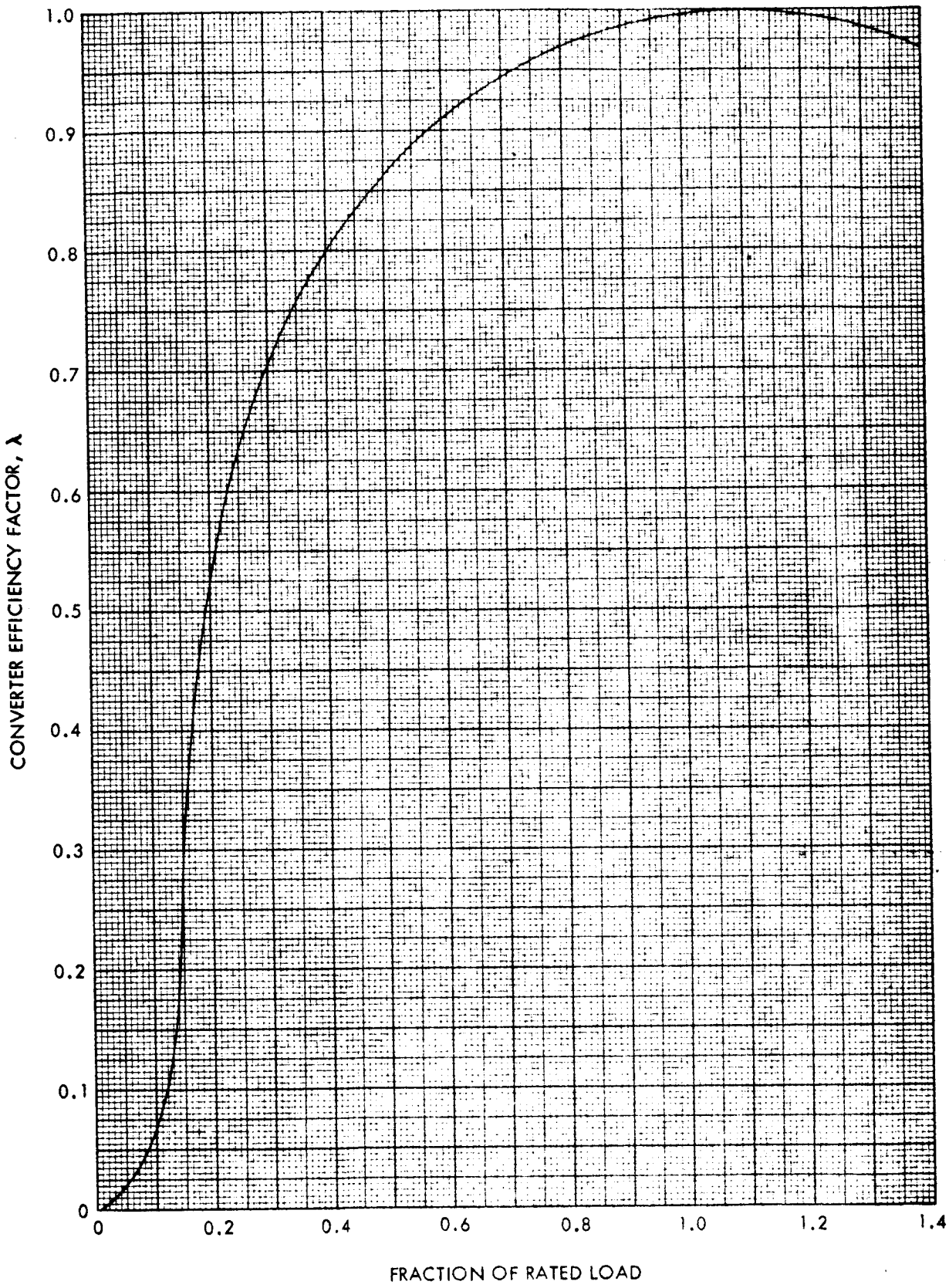

Figure A6-5. Converter Efficiency Factor, λ, as a Function of Rated Load (Block L)

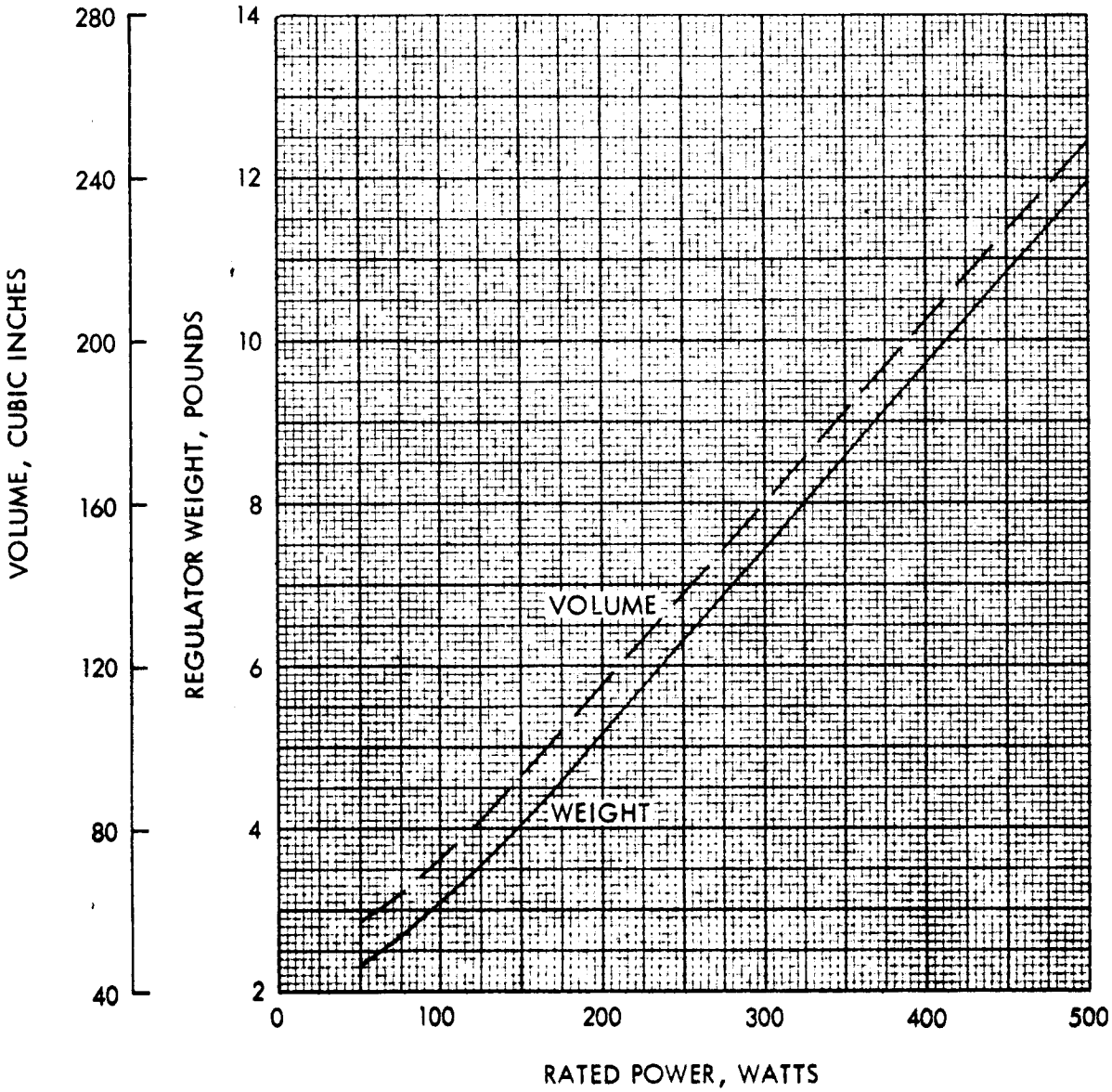

Figure A6-6. Converter Weight and Volume Versus Rated Power (Blocks BB and CC)

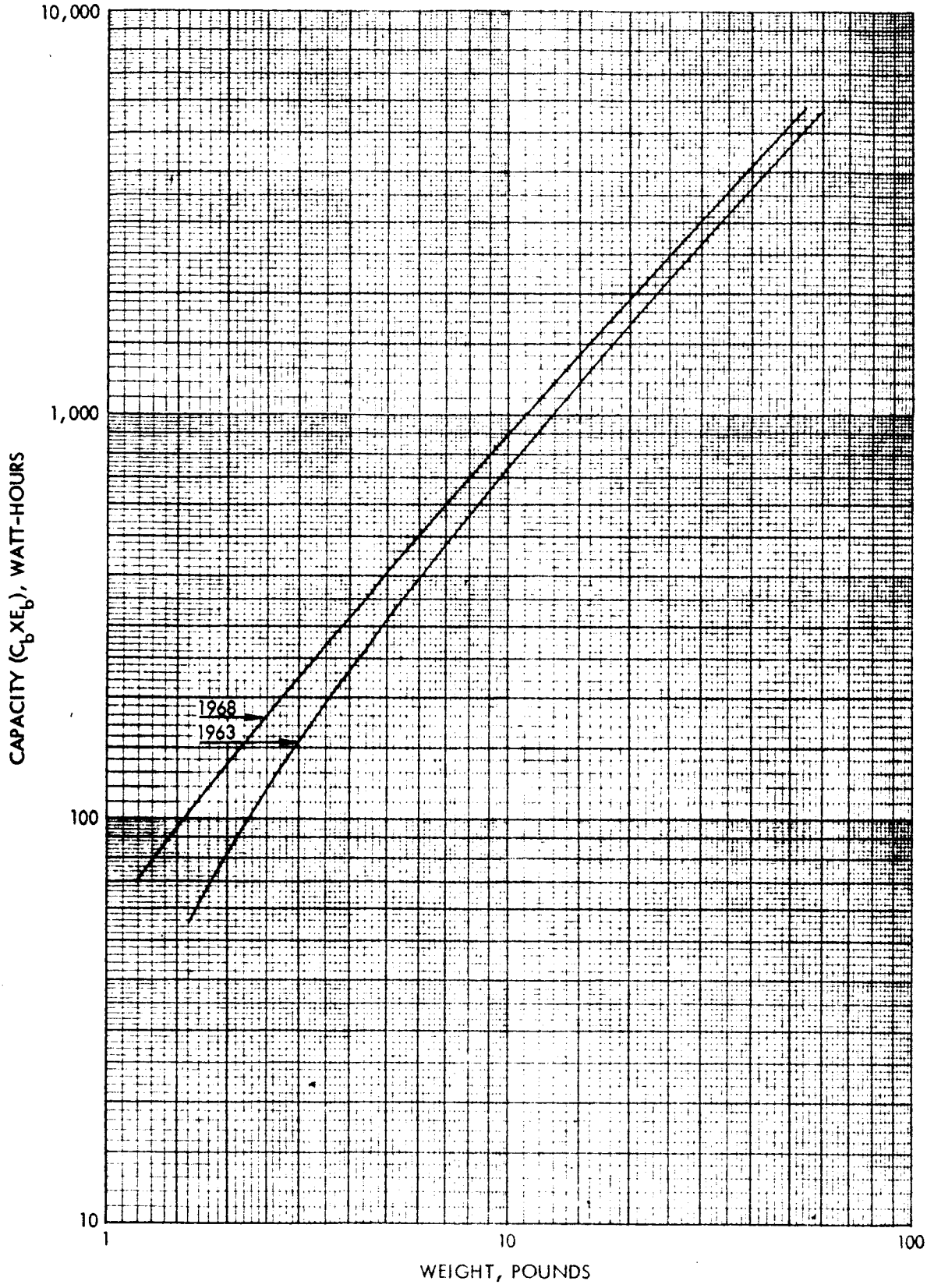

Figure A6-7. Capacity Weight Relationship of Manually Activated Primary Silver-Zinc Batteries (Block DD)

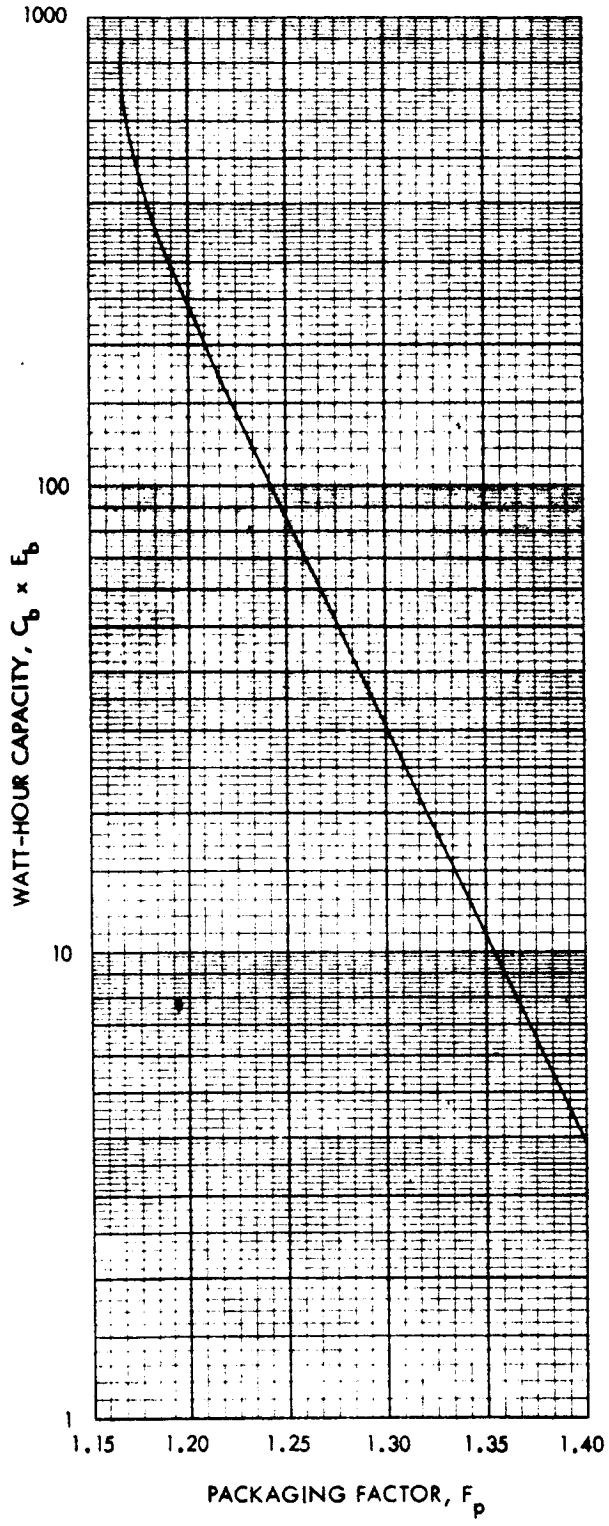

Figure A6-8. Battery Packaging Factor as a Function of Watt-Hour Capacity (Block EE)

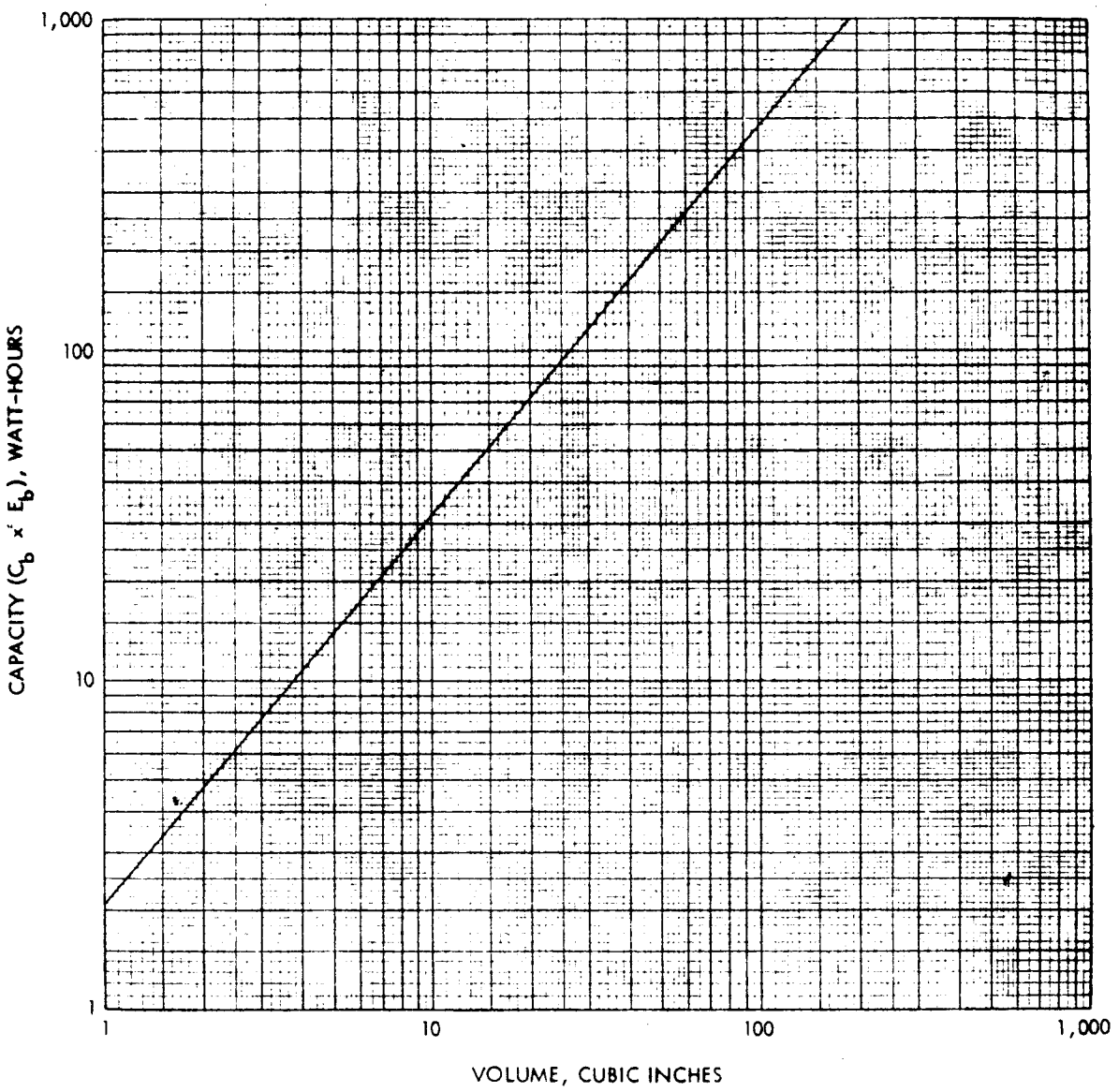

Figure A6-9. Capacity Volume Relationship of Manually Activated Primary and Sealed Secondary Silver-Zinc Batteries (Block GG)

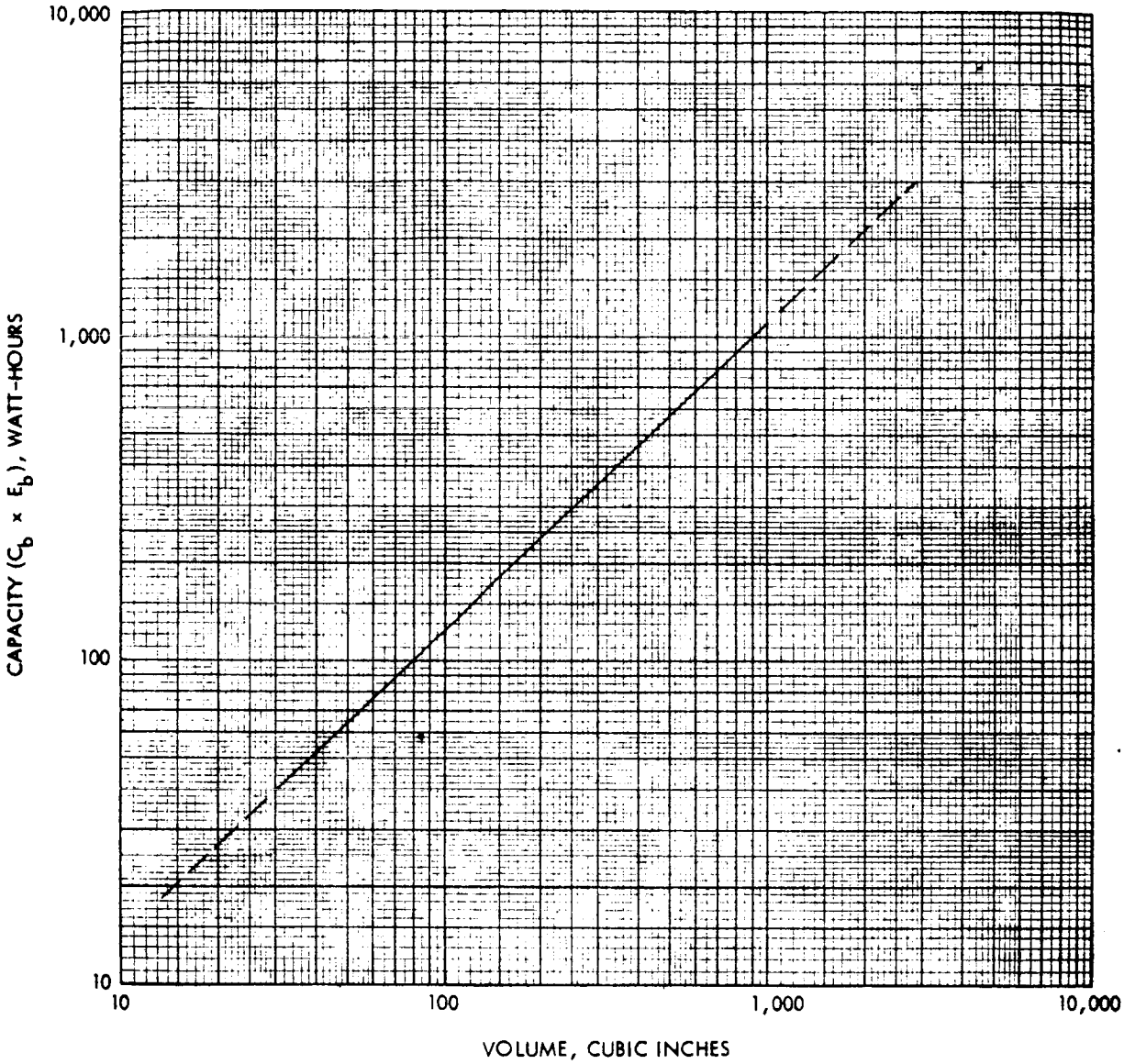

Figure A6-10. Volume Capacity Relationship of Automatically Activated Primary Silver-Zinc Batteries (Block GG)

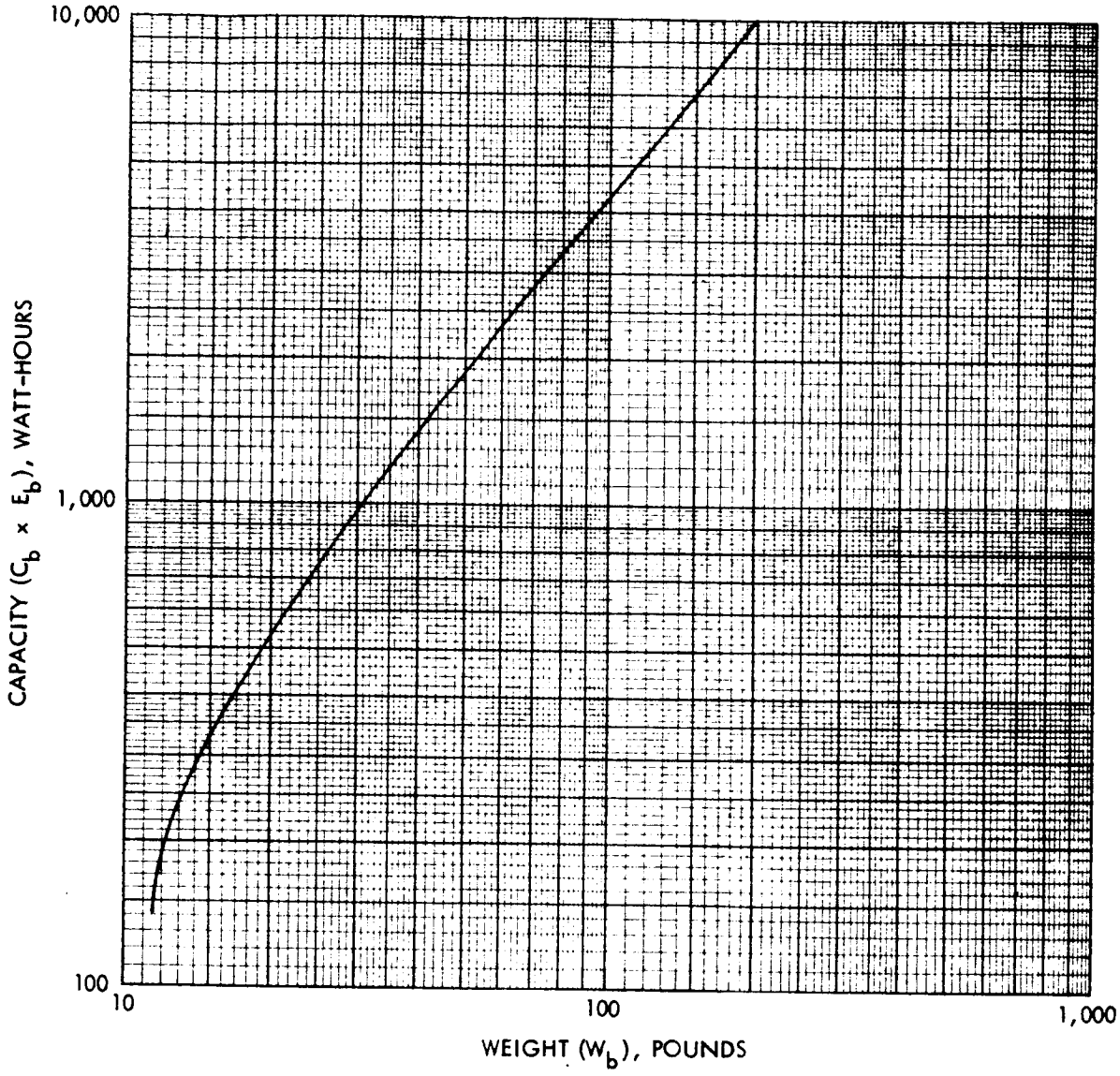

Figure A6-11. Capacity Weight Relationship of Packaged Automatically Activated Silver-Zinc Batteries (Block GG)

APPENDIX A7

SECONDARY SILVER-ZINC BATTERY PARAMETRIC DATA*

*The blocks referenced in this appendix are shown in Figure 4-2.

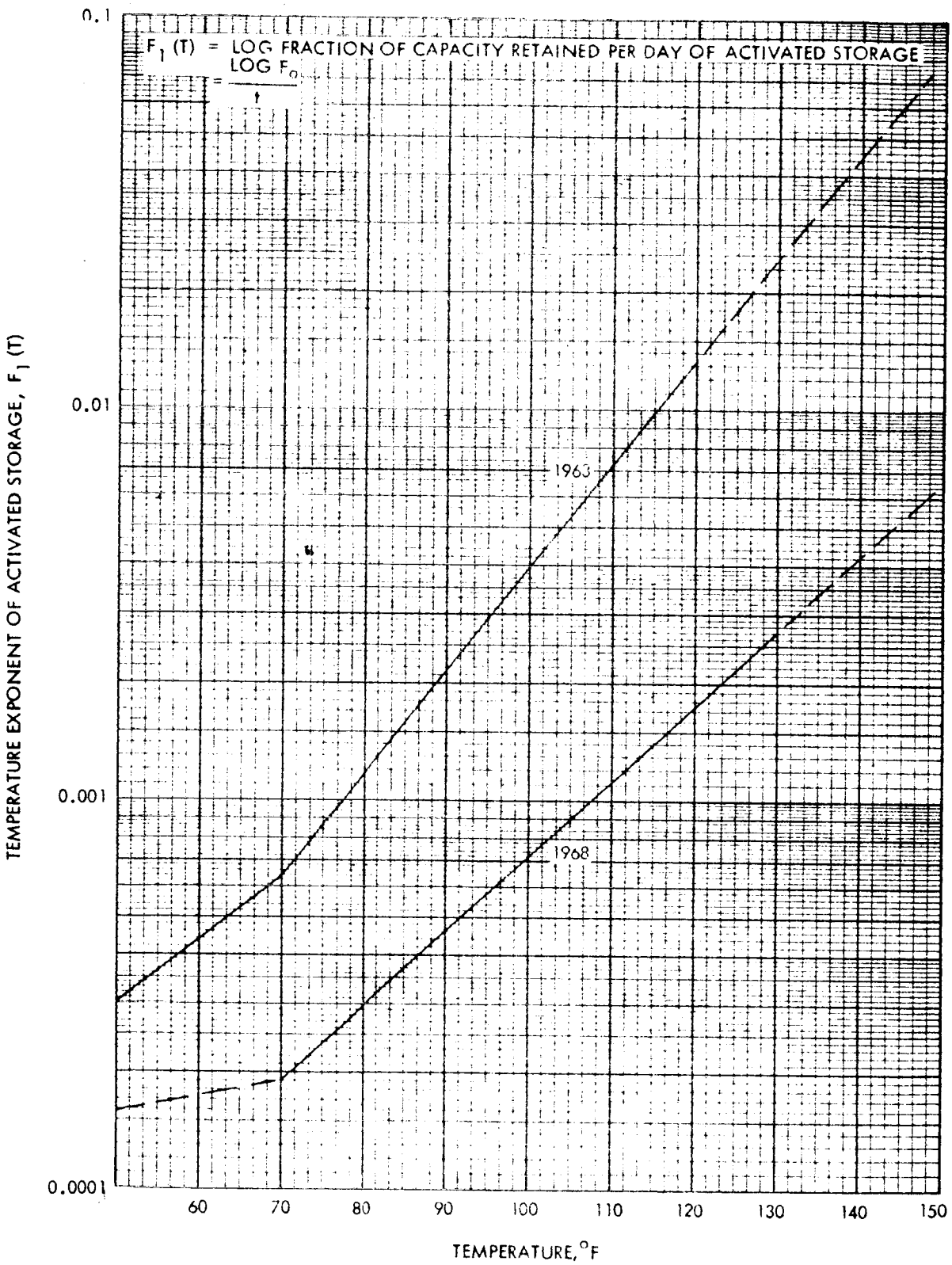

Figure A7-1. Temperature Exponent of Activated Storage Versus Temperature (Block N)

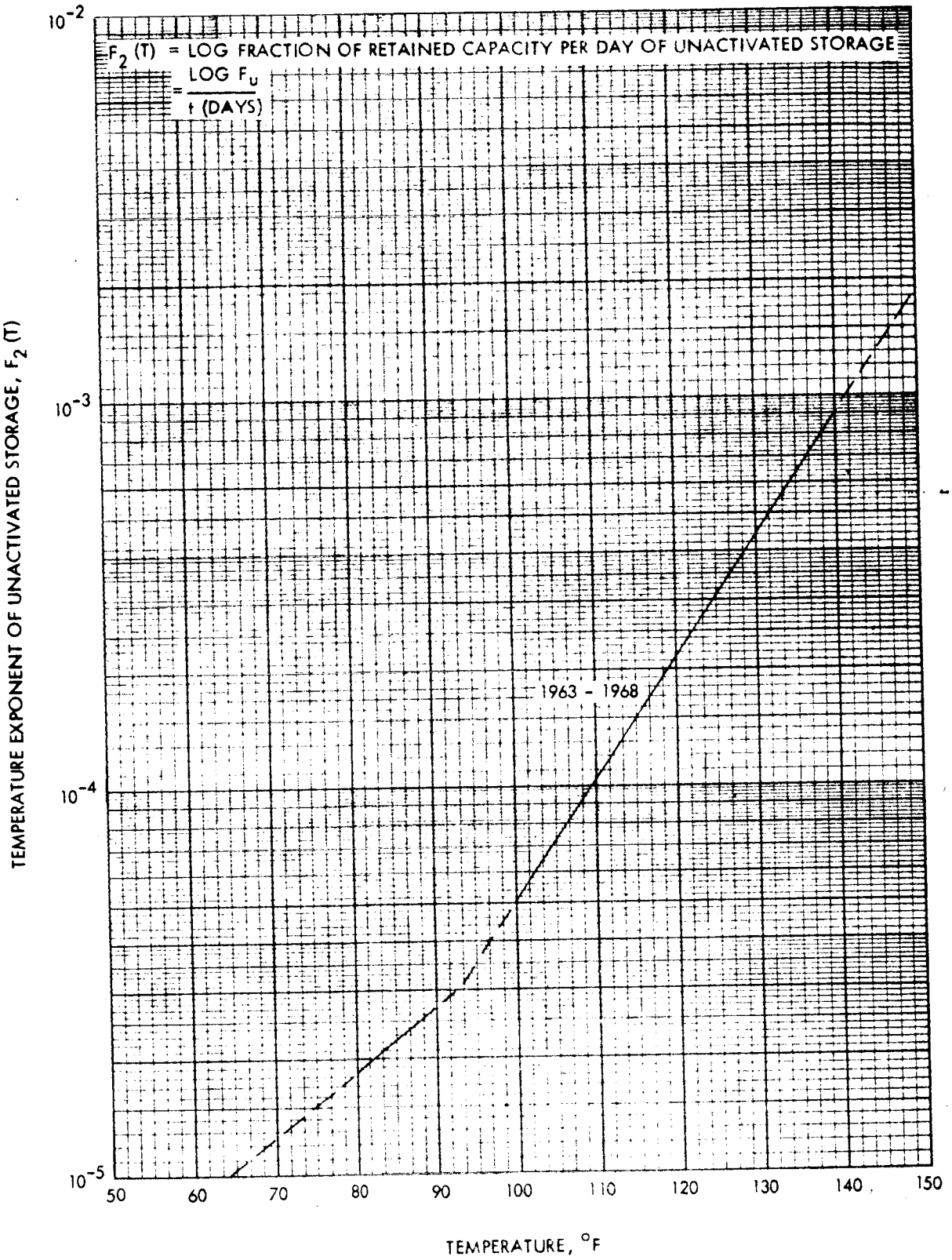

Figure A7-2. Temperature Exponent of Activated Storage Versus Temperature (Block O)

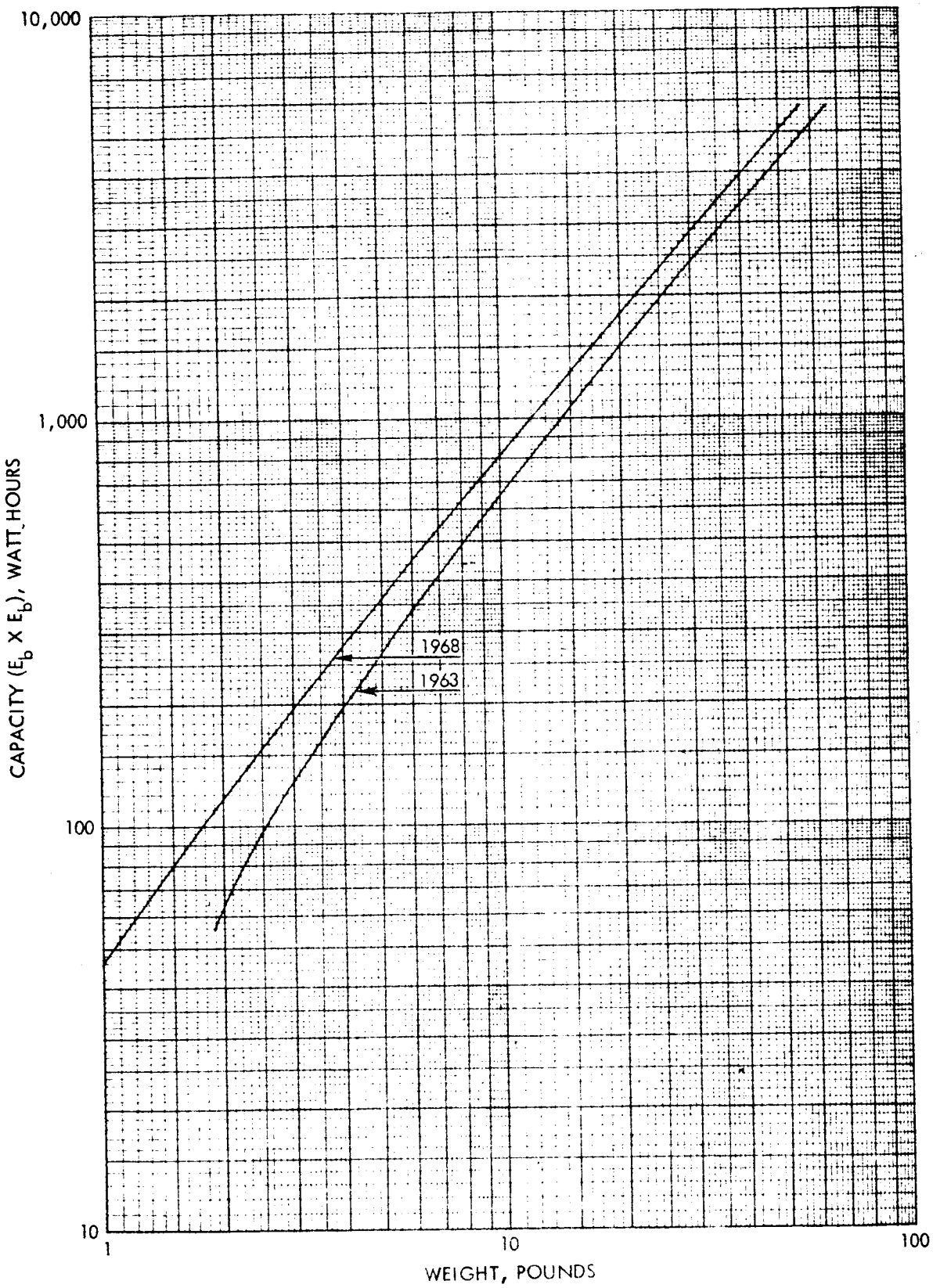

Figure A7-3. Capacity Weight Relationship of Sealed Secondary Silver-Zinc Batteries (Block U)

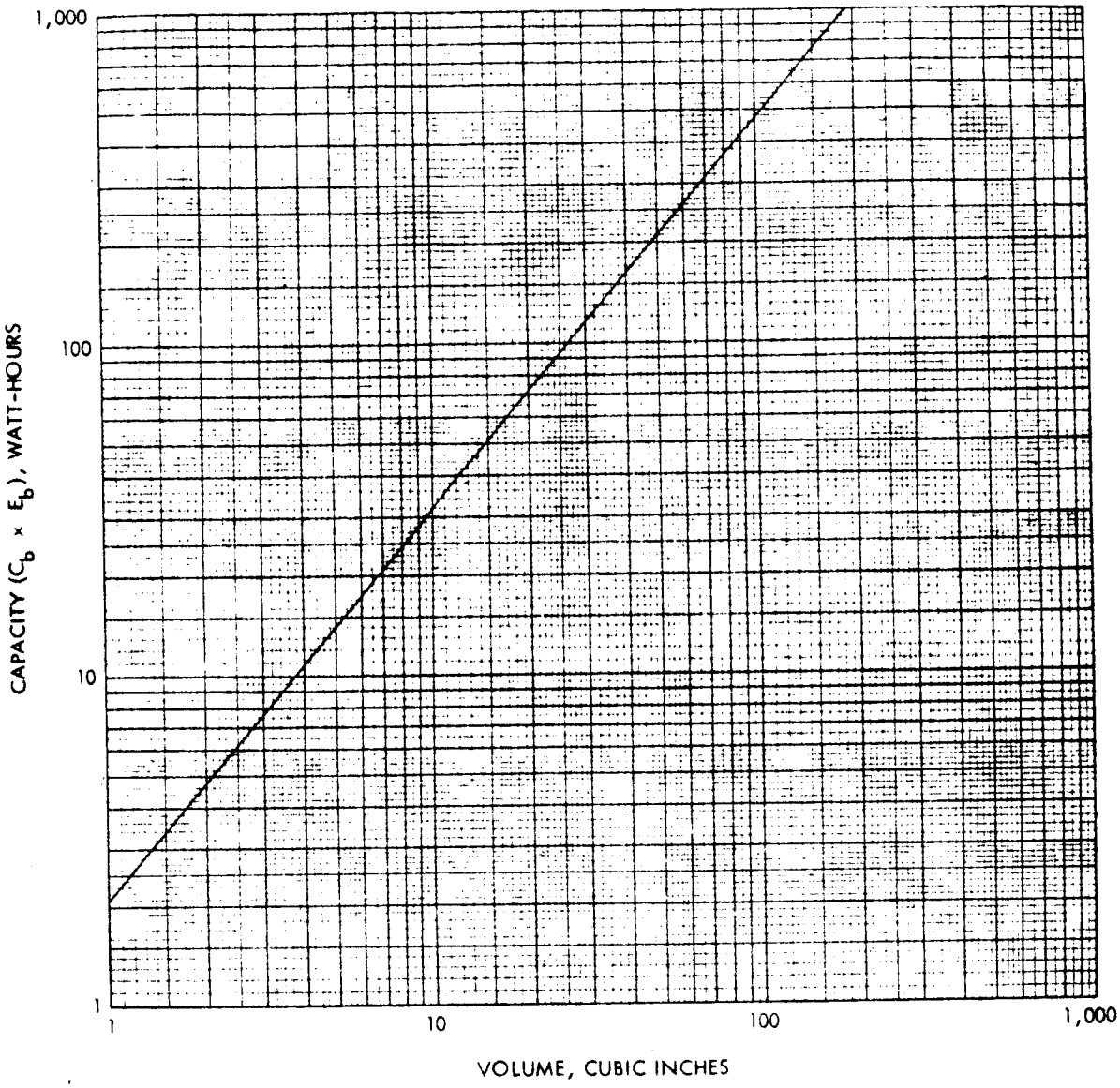

Figure A7-4. Capacity Volume Relationship of Manually Activated Primary and Sealed Secondary Silver-Zinc Batteries (Block W)

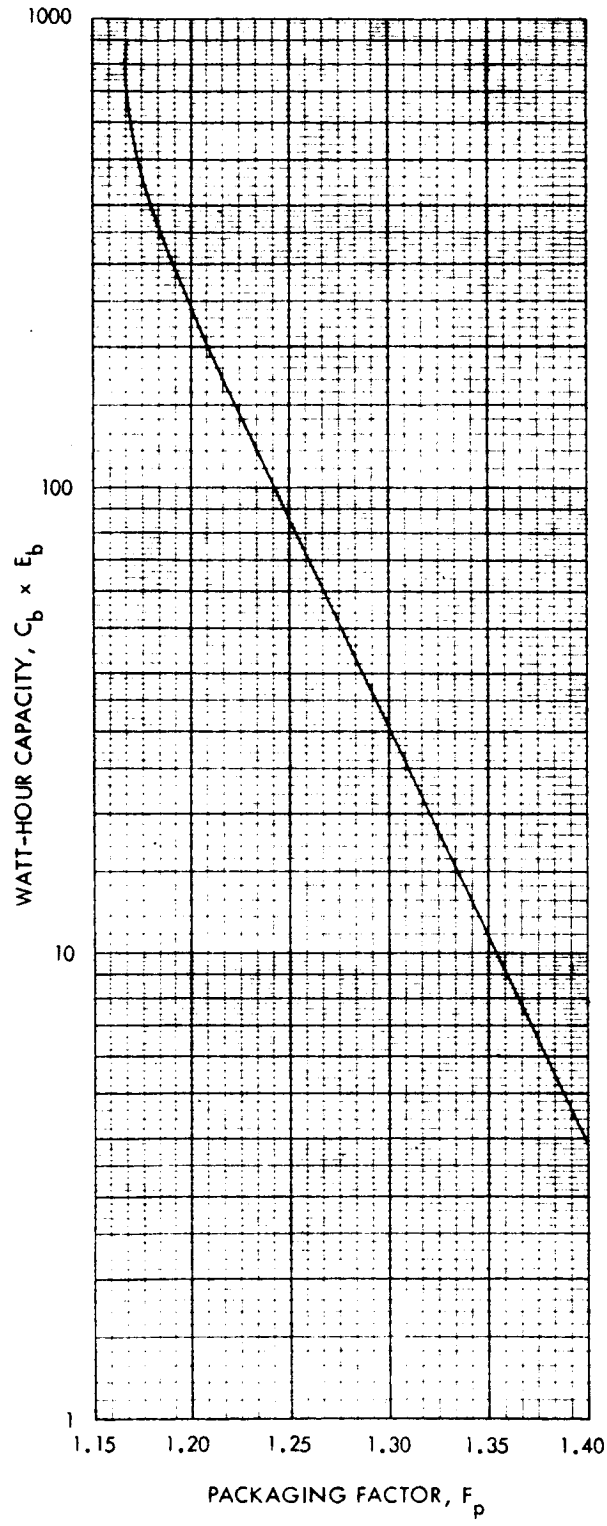

Figure A7-5. Battery Package Factor as a Function of Watt-Hour Capacity (Block V)

APPENDIX A8

SECONDARY SILVER-CADMIUM BATTERY PARAMETRIC DATA*

*The blocks referenced in this appendix are shown in Figure 4-3.

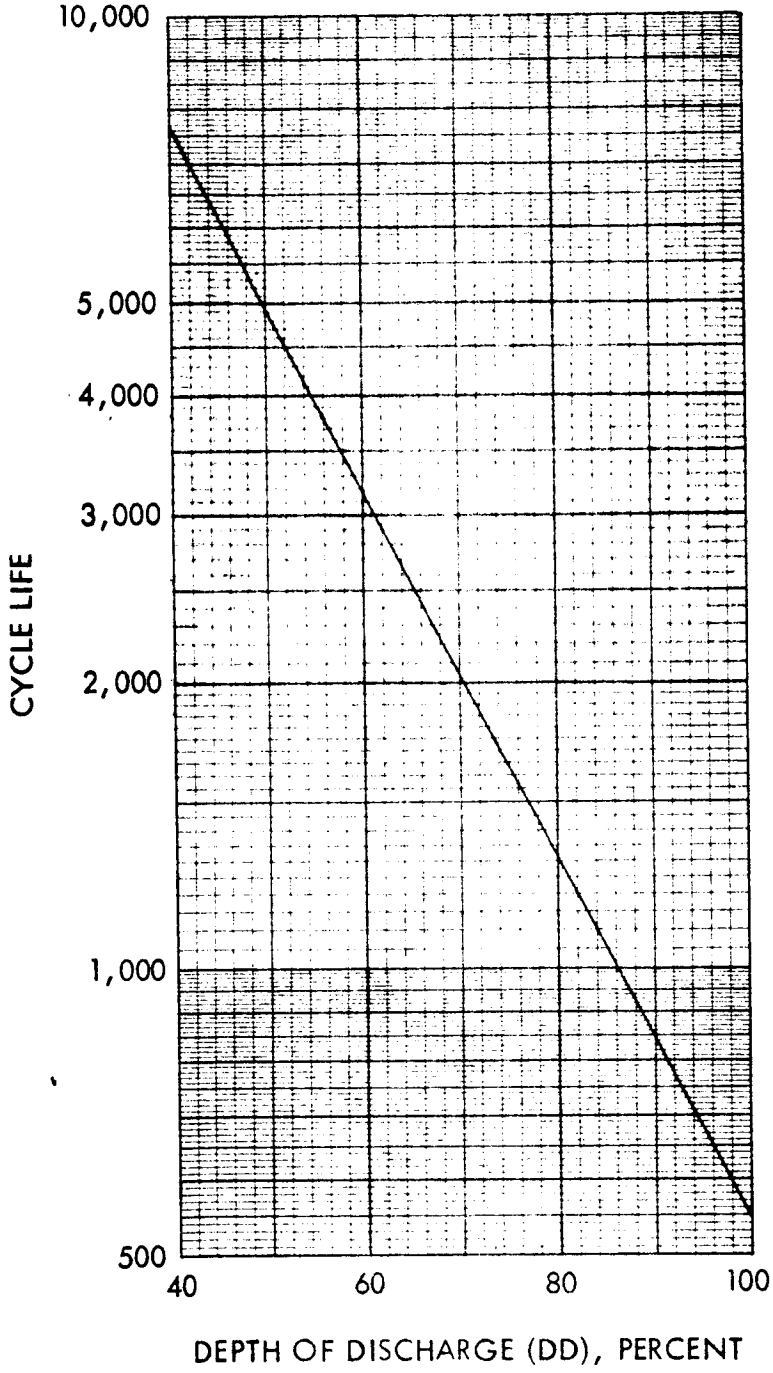

Figure A8-1. Depth of Discharge — Cycle Life Relationship of Silver-Cadmium Secondary Cells

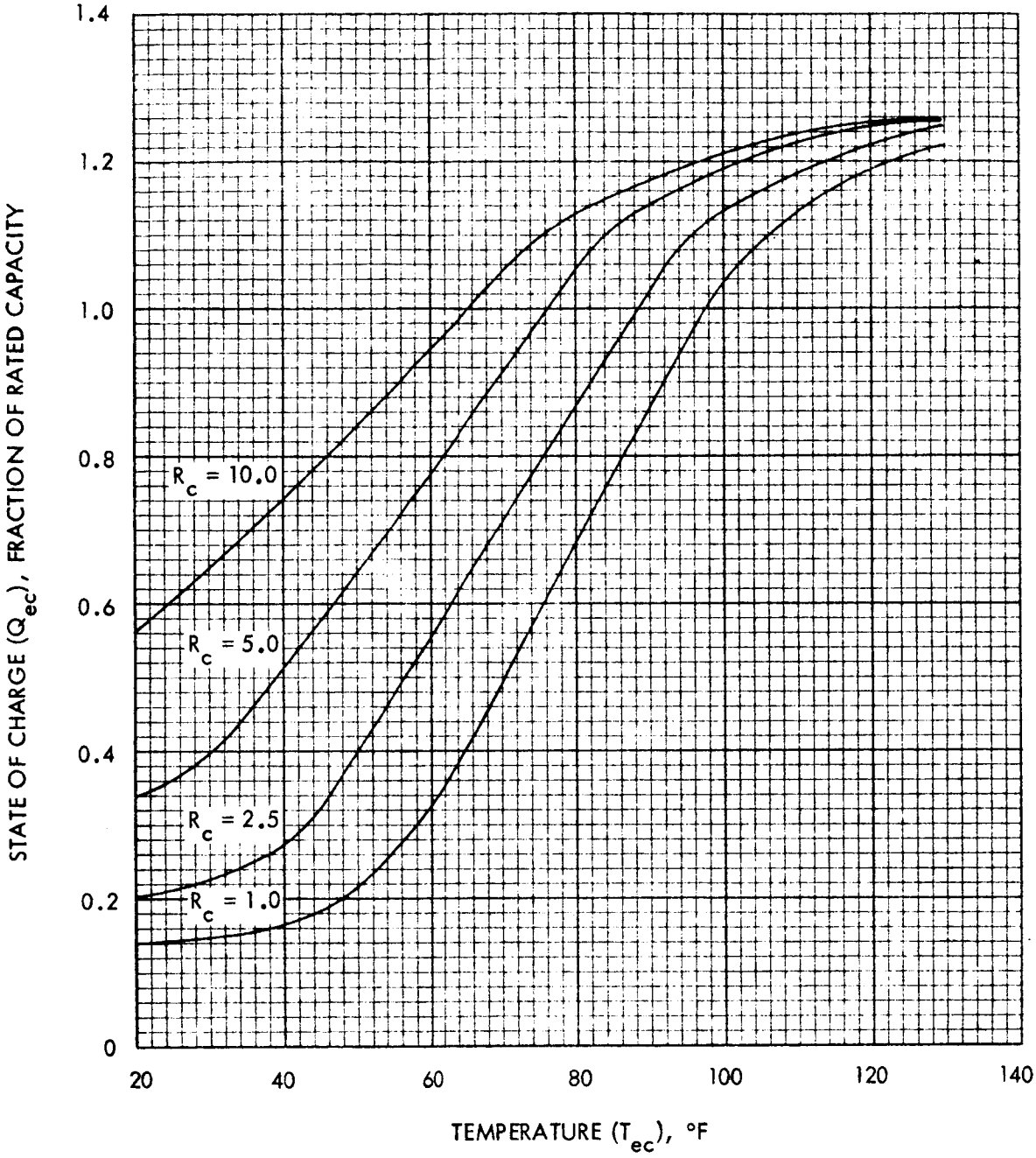

Figure A8-2. Maximum Achievable State of Charge vs Temperature, Charge Rate, a Parameter (Blocks G and II)

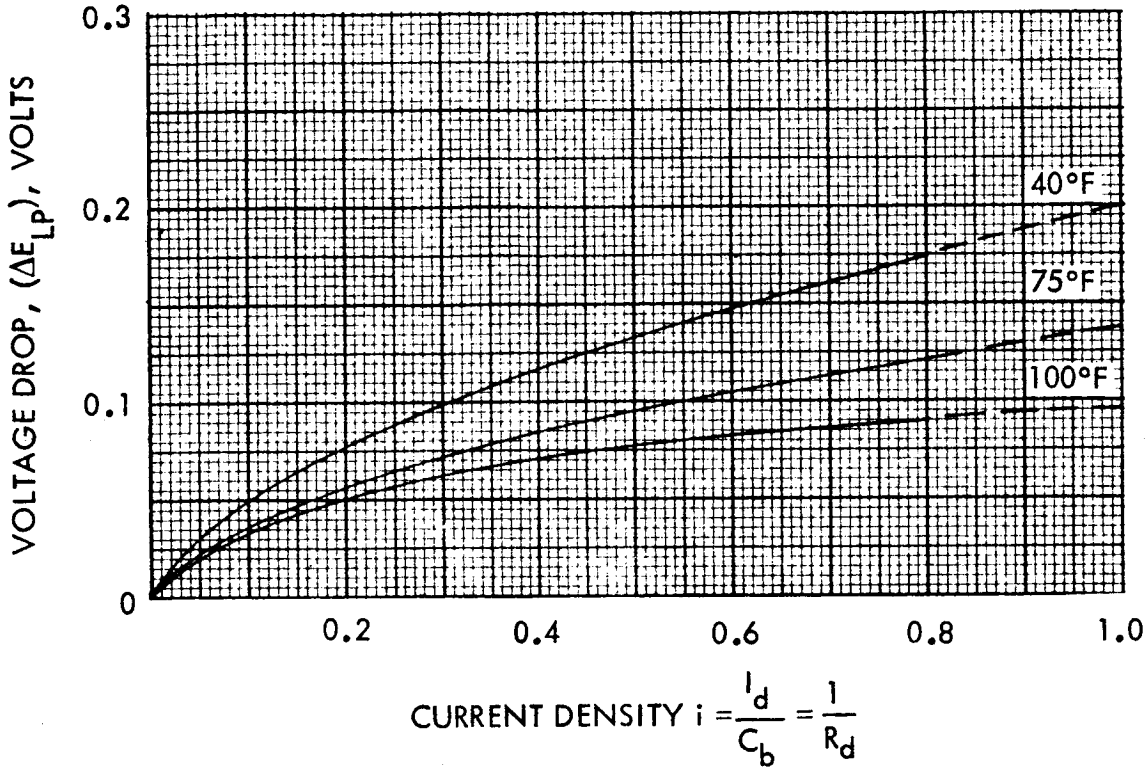

Figure A8-3. Secondary Silver-Cadmium Cells, Change in Lower Plateau Voltage with Discharge Current and Density (Block I)

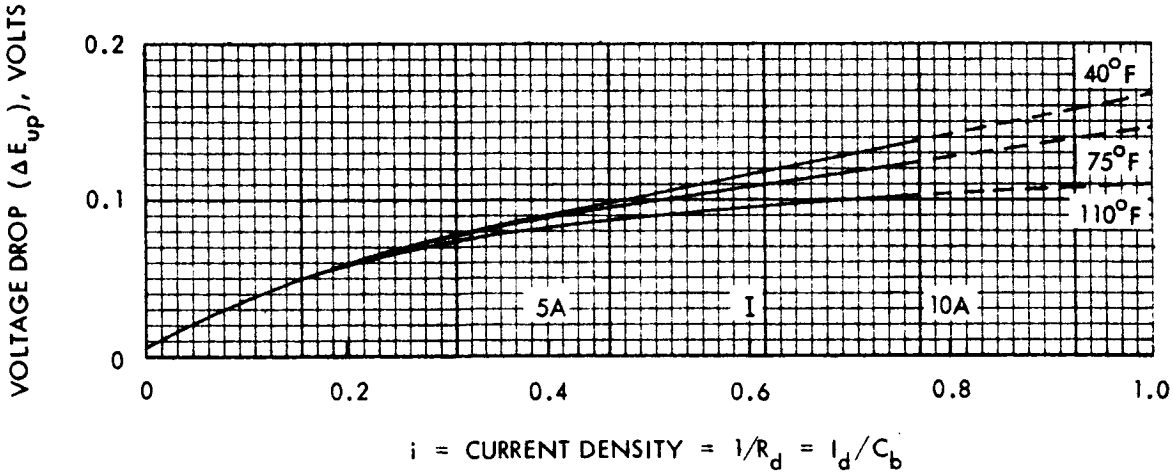

Figure A8-4. Change in Upper Plateau Voltage with Discharge Current Density (Block I)

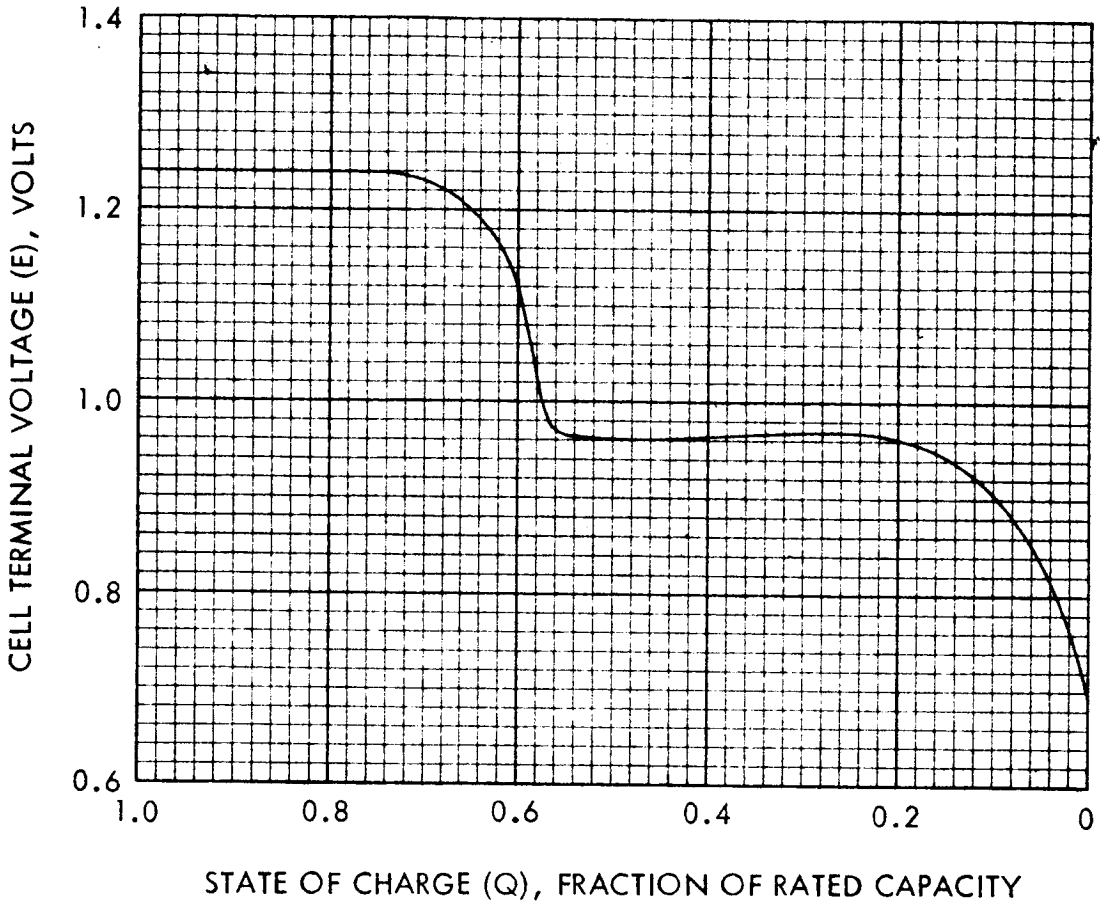

Figure A8-5. 50° F Silver-Cadmium Cell Voltage vs State of Charge (Block I)

Note:

See Figure A8-7 for the relationship between open circuit and closed circuit voltages.

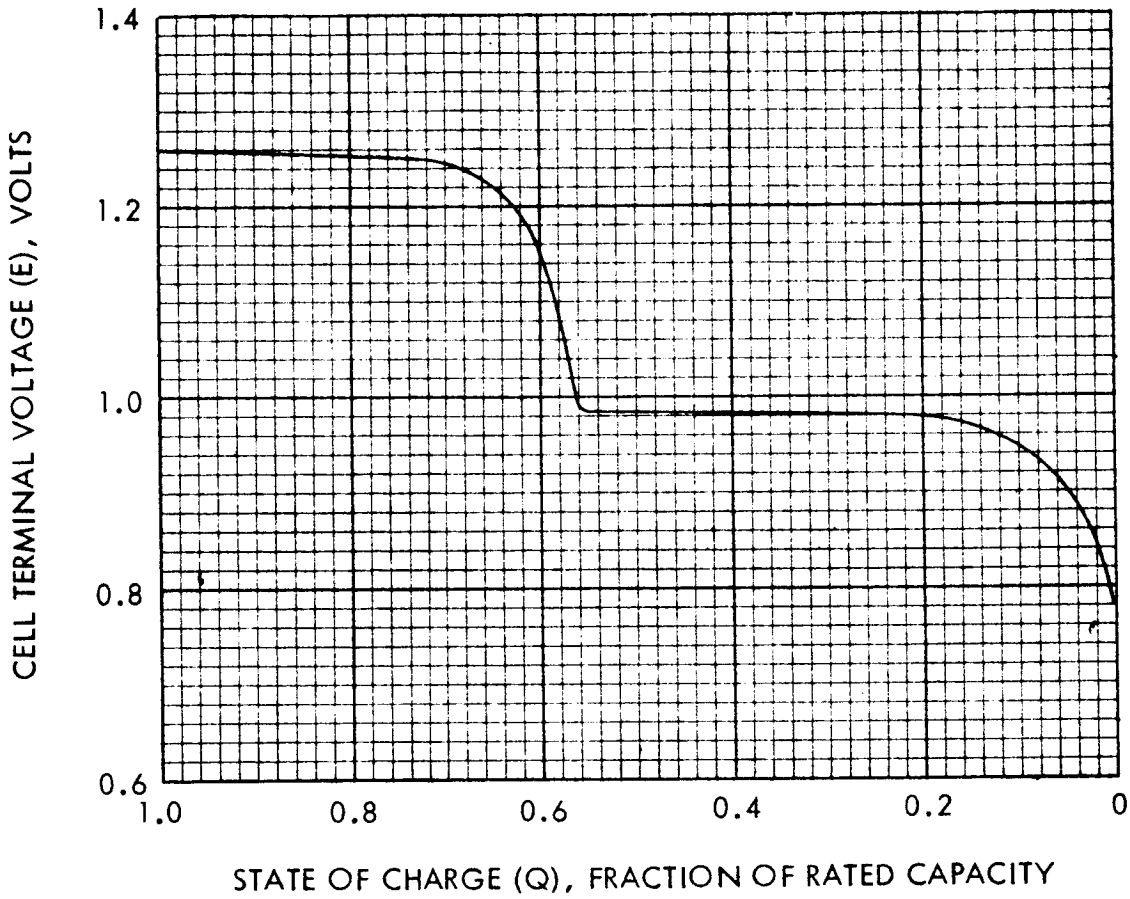

Figure A8-6. 60° F Silver-Cadmium Cell Voltage vs State of Charge (Block I)

Note:
See Figure A8-7 for the relationship between open circuit and closed circuit voltages.

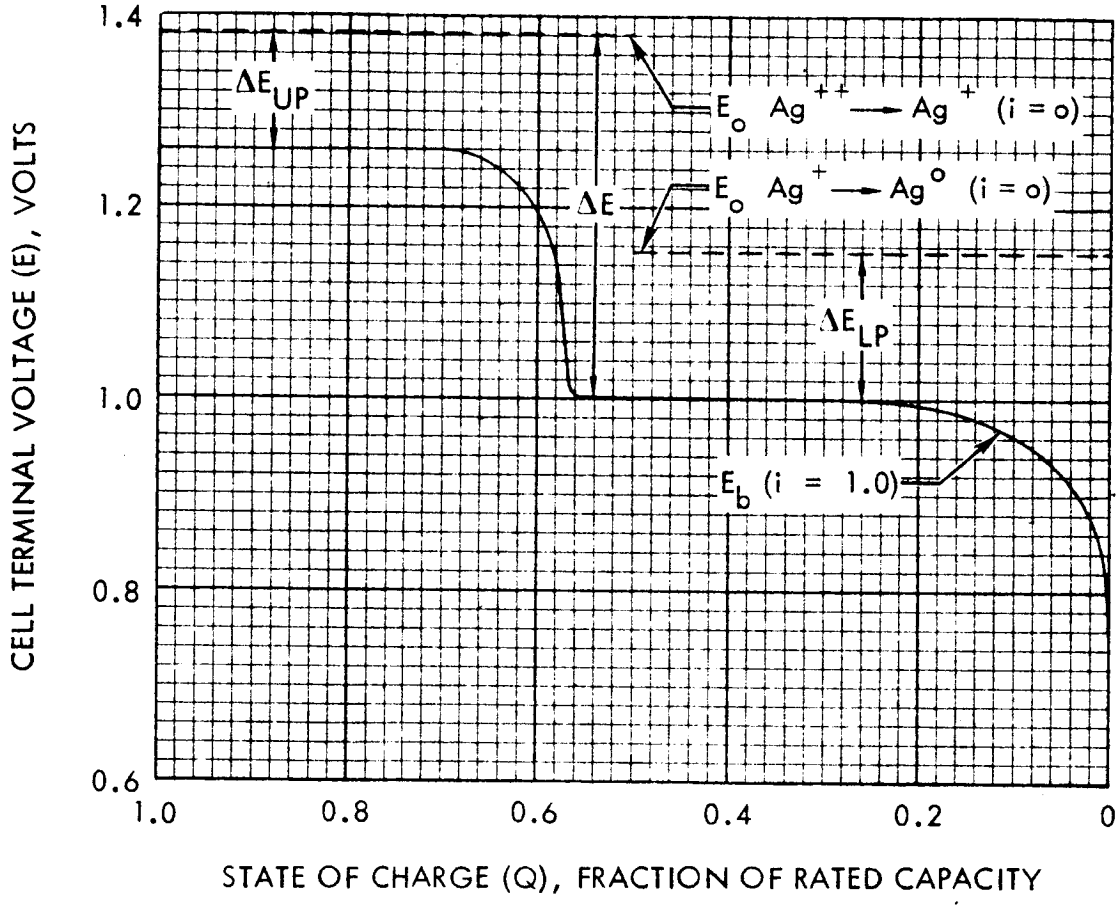

Figure A8-7. 70° F Silver-Cadmium Cell Voltage vs State of Charge (Block I)

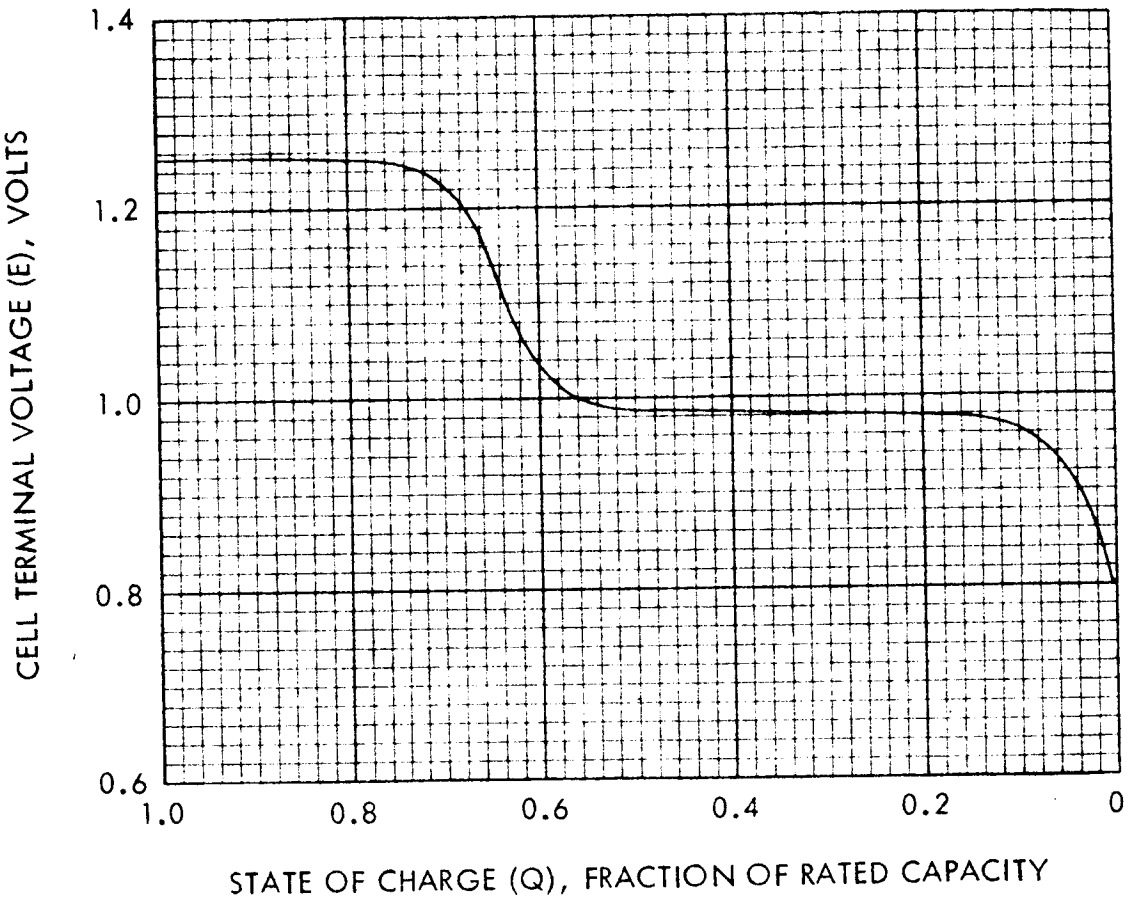

Figure A8-8. 80° F Silver-Cadmium Cell Voltage vs State of Charge (Block I)

Note:

See Figure A8-7 for the relationship between open circuit and closed circuit voltages.

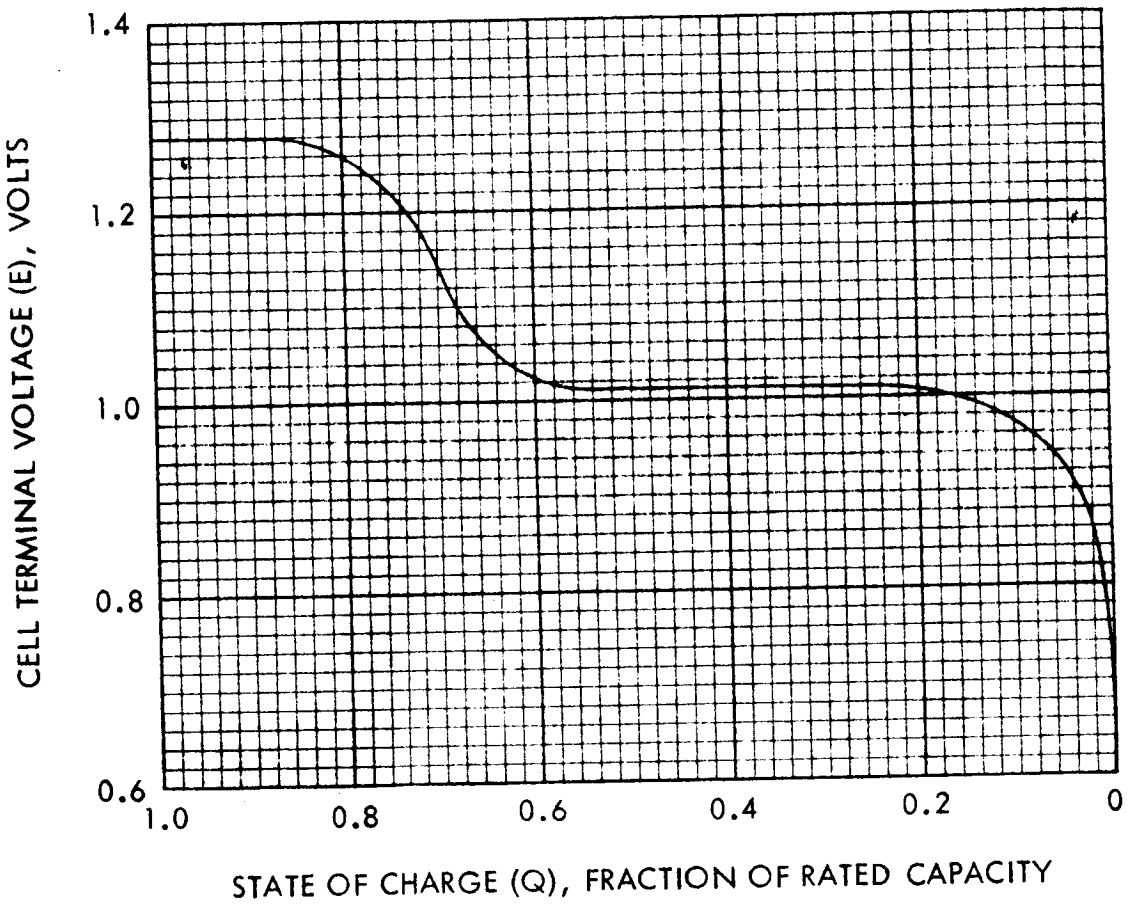

Figure A8-9. 90° F Silver-Cadmium Cell Voltage vs State of Charge (Block I)

Note: See Figure A8-7 for the relationship between open circuit and closed circuit voltages.

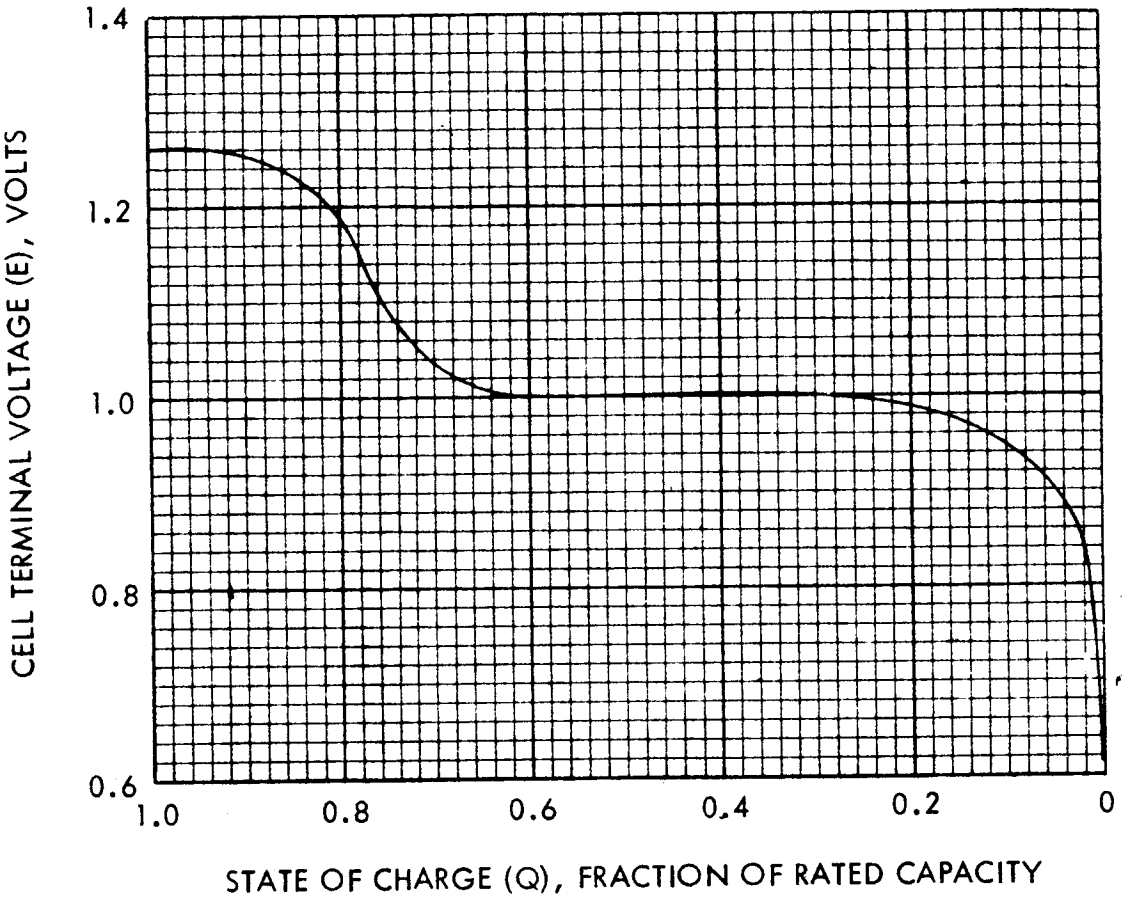

Figure A8-10. 100° F Silver-Cadmium Cell Voltage vs State of Charge (Block I)

Note:

See Figure A8-7 for the relationship between open circuit and closed circuit voltages.

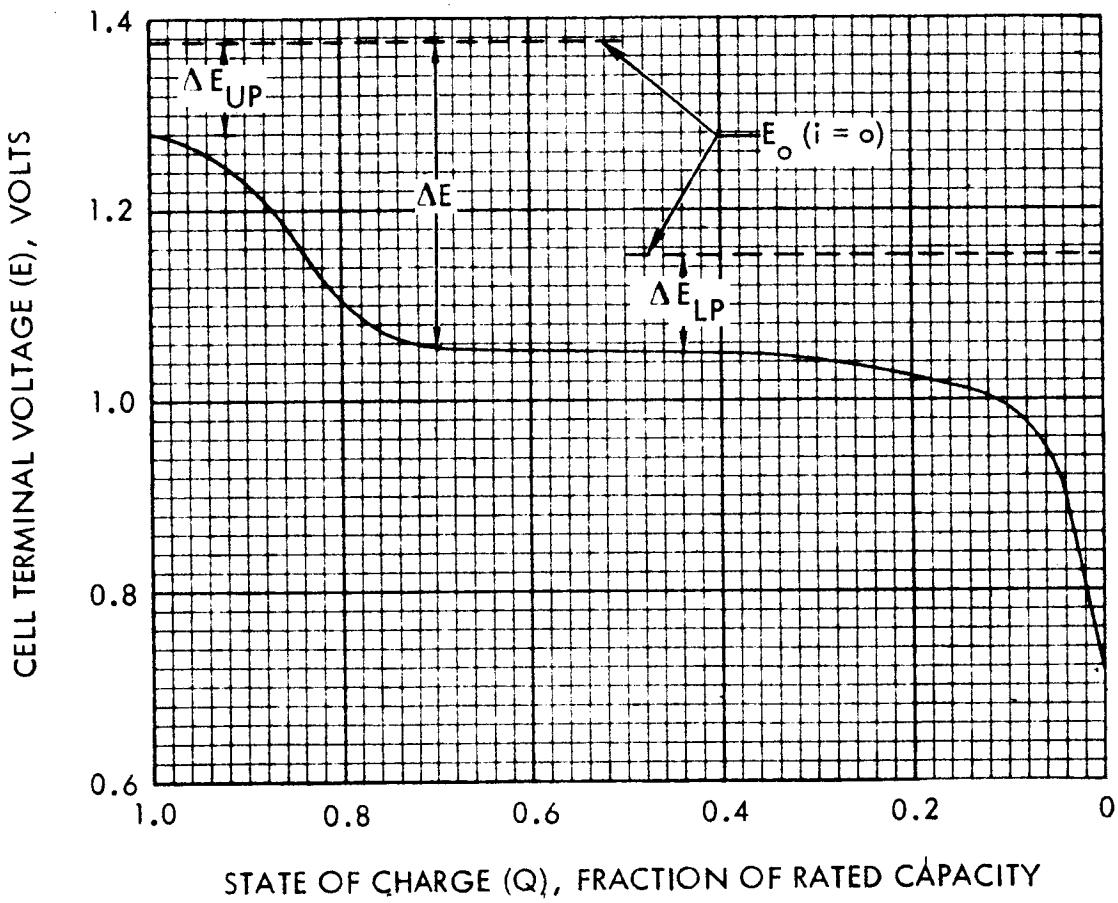

Figure A8-11. 110° F Silver Cadmium Cell Voltage vs State of Charge (Block I)

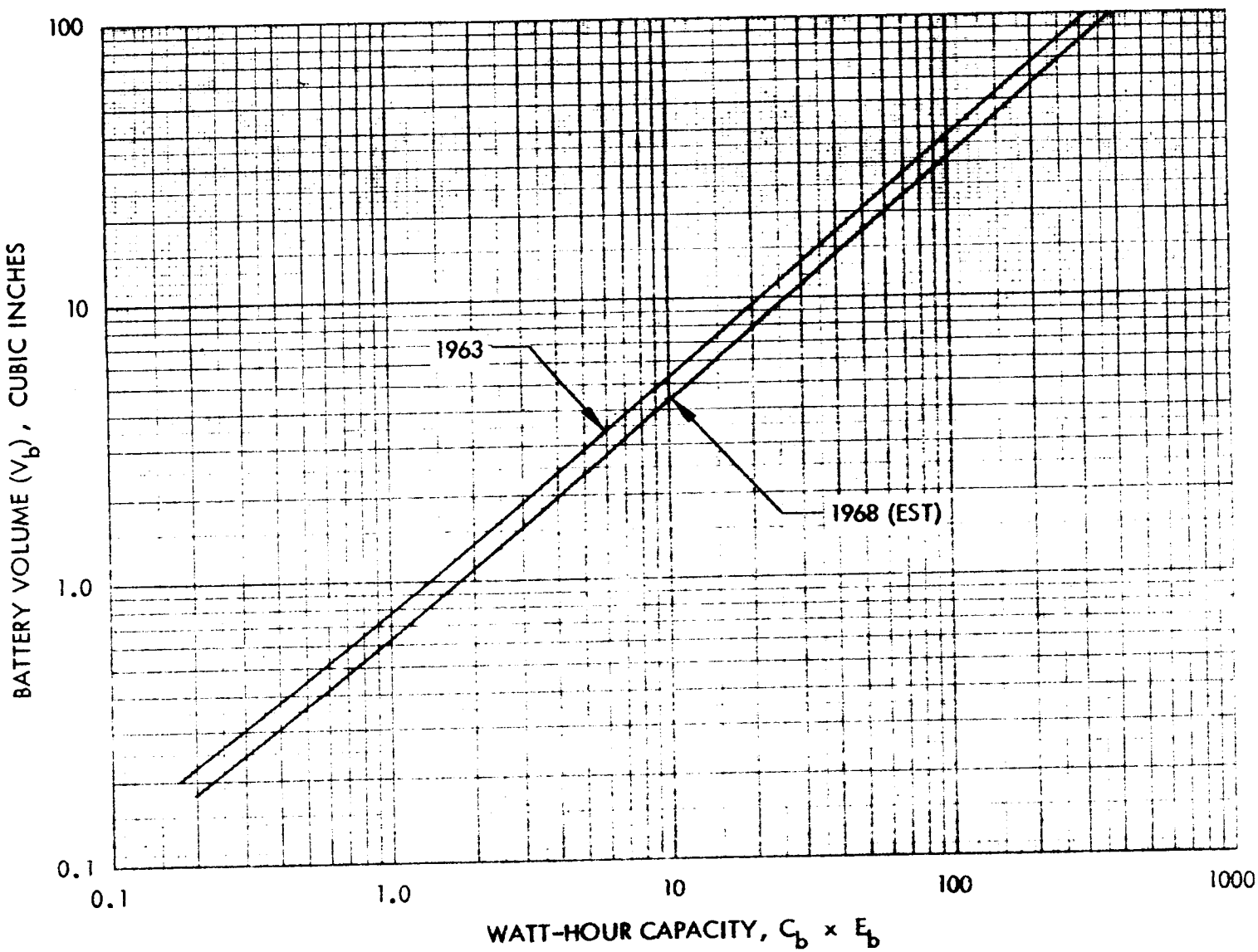

Figure A8-12. Silver-Cadmium Battery Volume as a Function of Capacity (Block EE

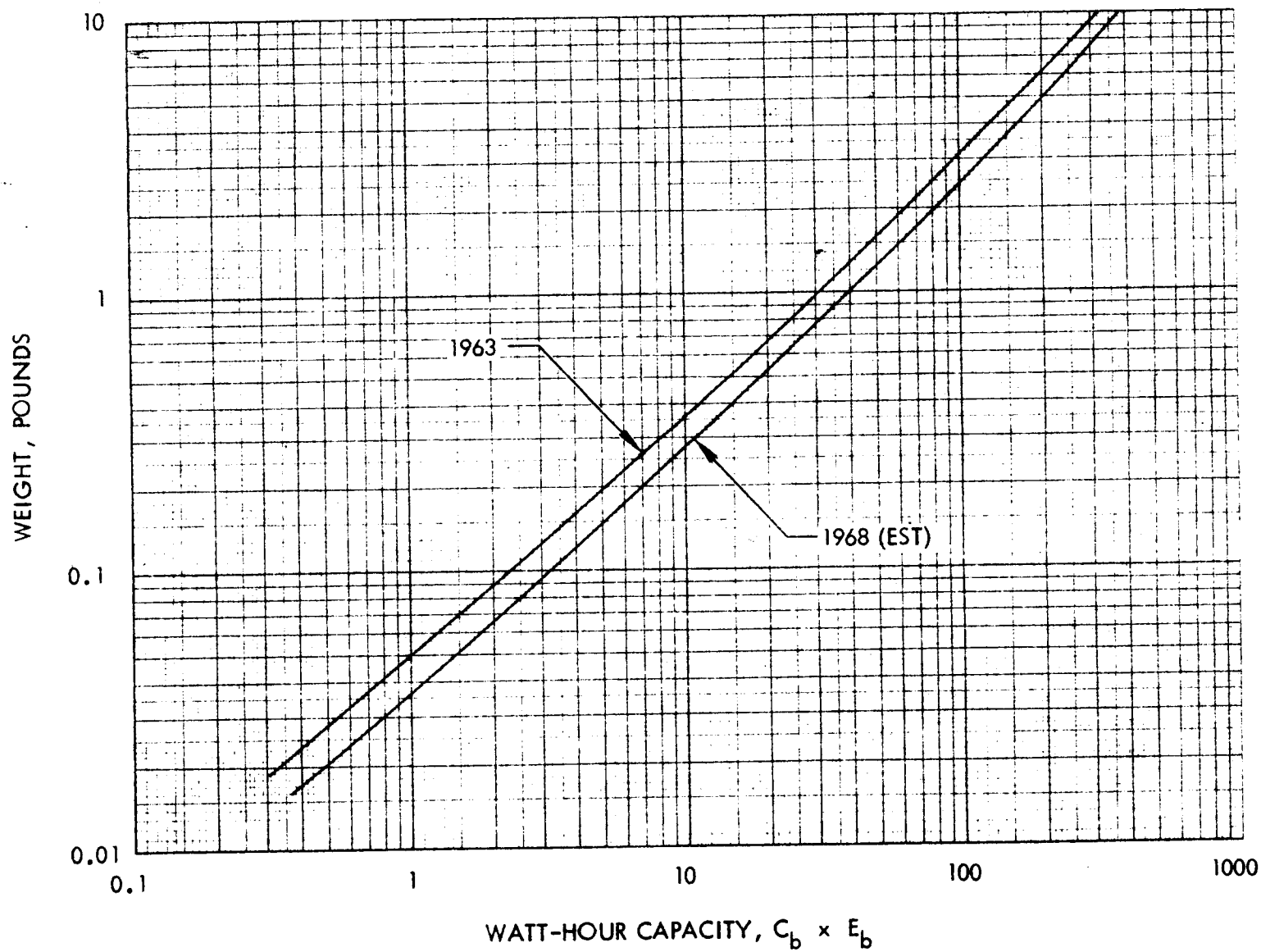

Figure A8-13. Silver-Cadmium Unpackaged Battery Weight as a Function of Capacity (Block FF)

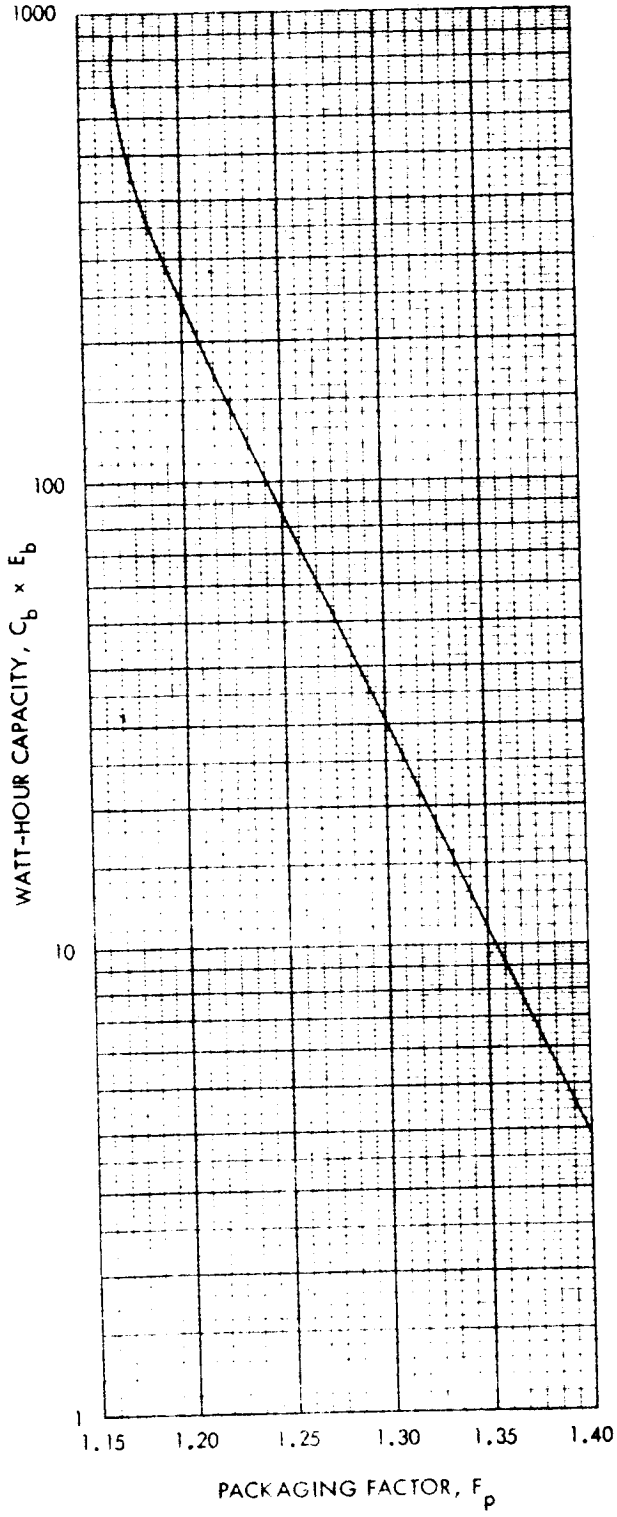

Figure A8-14. Battery Packaging Factor as a Function of Watt-Hour Capacity (Block GG)

APPENDIX A9

POWER CONDITIONING (INVERTERS) PARAMETRIC DATA*

*The blocks referenced in this appendix are shown in Figure 5-4.

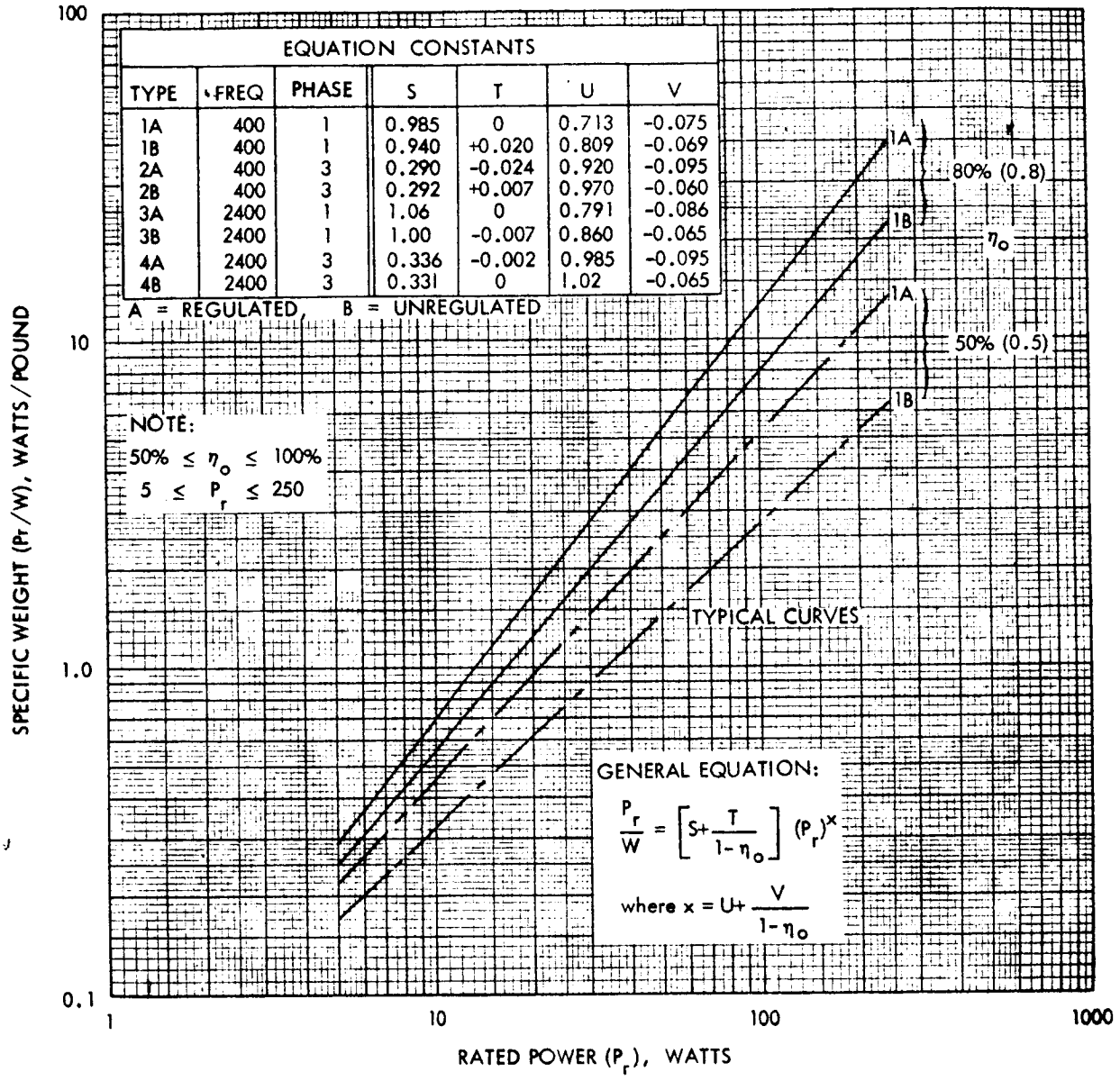

Figure A9-1. Power Per Unit Weight as a Function of Power Rating (Block A)

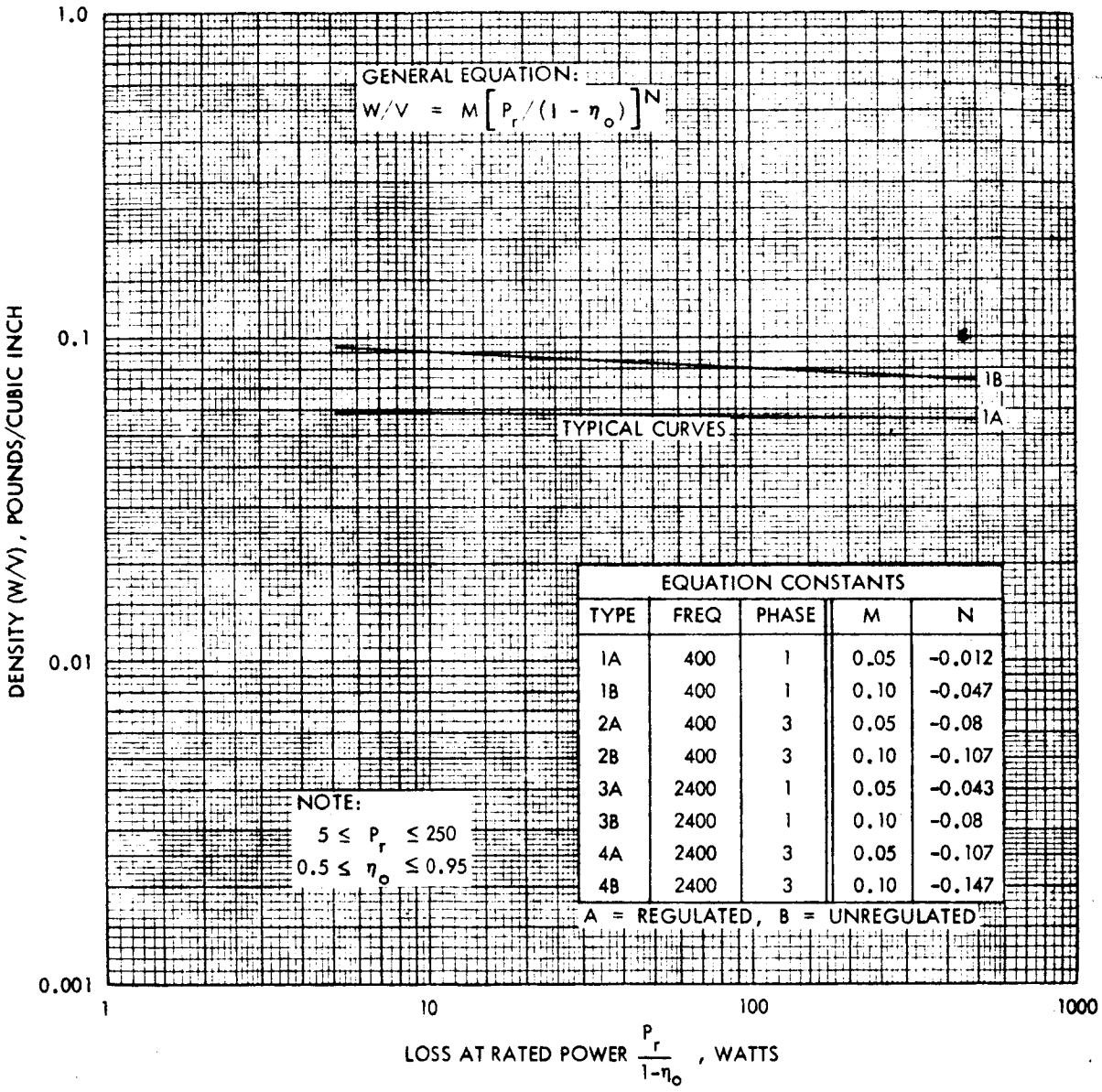

EQUATION CONSTANTS				
TYPE	FREQ	PHASE	M	N
1A	400	1	0.05	-0.012
1B	400	1	0.10	-0.047
2A	400	3	0.05	-0.08
2B	400	3	0.10	-0.107
3A	2400	1	0.05	-0.043
3B	2400	1	0.10	-0.08
4A	2400	3	0.05	-0.107
4B	2400	3	0.10	-0.147

A = REGULATED, B = UNREGULATED

Figure A9-2. Density as a Function of Power (Block B)

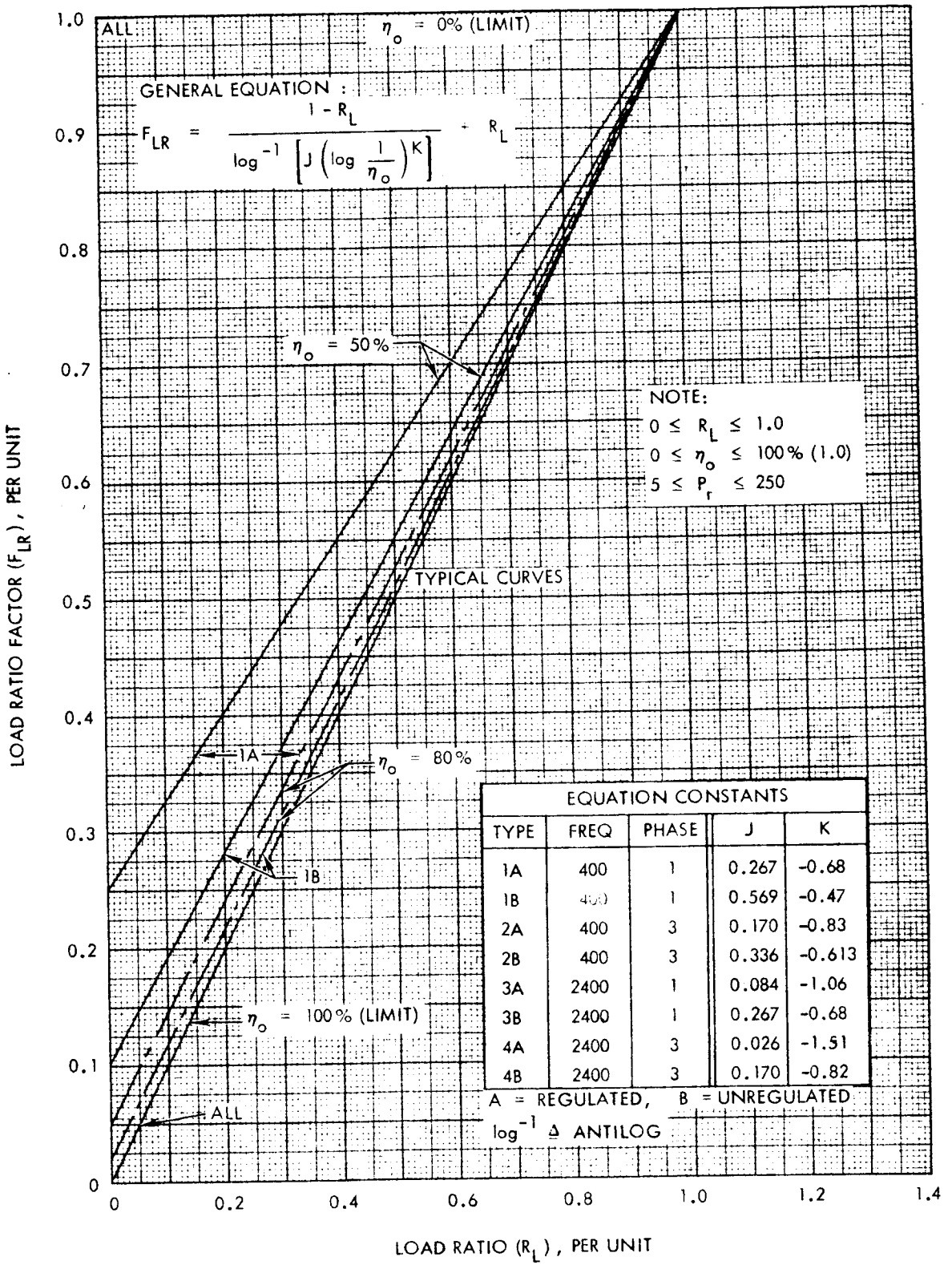

EQUATION CONSTANTS

TYPE	FREQ	PHASE	J	K
1A	400	1	0.267	-0.68
1B	400	1	0.569	-0.47
2A	400	3	0.170	-0.83
2B	400	3	0.336	-0.613
3A	2400	1	0.084	-1.06
3B	2400	1	0.267	-0.68
4A	2400	3	0.026	-1.51
4B	2400	3	0.170	-0.82

A = REGULATED, B = UNREGULATED

$\log^{-1} \triangleq$ ANTILOG

Figure A9-3. Load Ratio Factor as a Function of Load Ratio (Block D)

APPENDIX B1

SAMPLE CALCULATIONS FOR SOLAR PHOTOVOLTAIC SOURCES

Problem A: Design the solar array for a Mars oribiting vehicle, given the following:

P_s = 500 watts	AU = 1.67	Mission Life = 1 year
E_{sa} = 30.4 volts	$T_{sa} = 0^oC$	
I_{sa} = 16.8 amps	$T_{max} = 10^oC$	
E_s = 29.7 volts		

1. Determine Design Point Time with Respect to Launch

Assume that the design point for the solar array occurs at the end of life

$$t_d = 1 \text{ year} = 8736 \text{ hours}$$

2. Determine Particle Radiation Dose

The equivalent 1-Mev electron dose on solar cells, adhesive, cover material, etc., are determined by means of a separate calculation procedure. For initial design, assume:

$$\Phi_c' = 1 \times 10^{14} \text{ e/cm}^2$$

$$\Phi_a' = 1 \times 10^{14} \text{ e/cm}^2$$

$$\Phi_{cg}' = 1 \times 10^{14} \text{ e/cm}^2$$

3. Select Solar Cell

From solar cell current-voltage characteristics (Block A)* and other characteristics define:

I_{sc} = 66 ma	r_s = 0.73 ohms	ρ_{cg} = 2.6 gm/cm^3
E_{oc} = 540 mv	A_c = 2 cm^2	d_{cg} = 6 mils
$I(P_m)$ = 60 ma	A_{c-a} = 1.9 cm^2	
$E(P_m)$ = 443 mv	w_c/A = 0.11 gm/cm^2	

*Block letters in this appendix correspond to computation blocks in Figure 3-1.

4. Define Solar Array Configuration

$$A_{p(max)} = 30 \text{ ft}^2$$

$$\rho_{cb} = 2.4 \text{ gm/cm}^3$$

$$d_{cb} = 4 \text{ mils}$$

$$w_{h/A} = 0.08 \text{ gm/cm}^2$$

$$F_i = 0.95$$

$$F_p = 0.92$$

5. Calculate Radiation Current Degradation (Block K)*.

From Block B at $\Phi_c' = 1 \times 10^{14}$ e/cm^2, $I_{sc-\Phi} = 61.4$ ma. Therefore

$$\Delta I_\Phi = I_{sc-\Phi} - I_o\big|_{E_o=0}$$

$$= 61.4 \text{ ma} - 66.0 \text{ ma} = -4.6 \text{ma}$$

6. Determine I-V Curve due to Radiation Current Degradation (Block L).

Shift curve (Block A) along current axis by $\Delta I_\Phi = 4.6$ ma, or

$$I_1 = I_o + \Delta I_\Phi$$

$$= I_o - 4.6 \text{ ma}$$

Determine the open circuit voltage of the new curve $\left[I_1 = f(E_o)\right]$.

$$E_o\Big|_{I_1=o} = E_o\Big|_{I_o=4.6 \text{ ma}} = 537 \text{ mv}$$

7. Calculate Radiation Voltage Degradation (Block M).

From Block C at $\Phi_c' = 1 \times 10^{14}$ e/cm^2,

$$E_{oc-\Phi} = 512 \text{ mv}$$

---

*Figure B1-1 illustrates the results of computation steps 5 through 18.

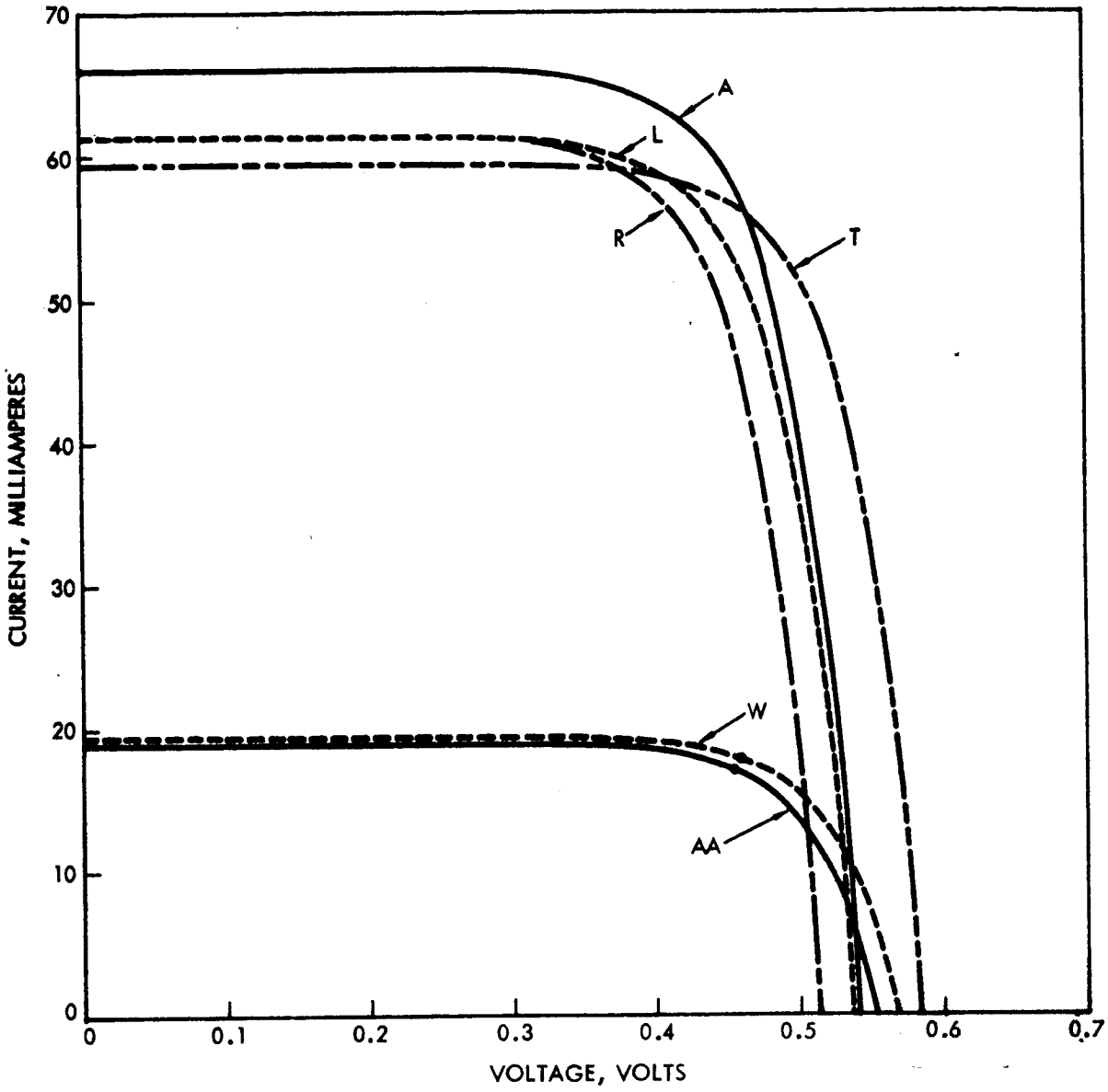

Figure B1-1. Solar Cell Current-Voltage Characteristics of Sample Calculations

Therefore,

$$\Delta E_{\Phi} = E_{oc-\Phi} - E_{o}\big|_{I_1=0}$$

$$= 512 \text{ mv} - 537 \text{ mv}$$

$$= -25 \text{ mv}$$

8. Determine I-V Curve due to Radiation Degradation (Block R).

Shift curve (Block L) along voltage axis by $\Delta E_{\Phi} = -25$ mv, or

$$E_1 = E_o + \Delta E_{\Phi}$$

$$= E_o - 25 \text{ mv}$$

9. Calculate Current Difference at Operating Temperature (Block S).

From Block N at $\Phi_c' = 1 \times 10^{14}$ e/cm^2

$$\beta_I/I_{sc} = 0.11\%/^{o}C$$

Thus,

$$\Delta I_T = I_1\big|_{E_1=0} \left(\beta_I/I_{sc}\right) \Delta T$$

From 6,

$$I_1\big|_{E_1=0} = I_o\big|_{E_o=22 \text{ mv}} + \Delta I_{\Phi} = 66.0 \text{ ma} - 4.6 \text{ ma} = 61.4 \text{ ma}$$

From Block O,

$$\Delta T = T_{sa} - T_o = 0^{o}C - 28^{o}C = -28^{o}C$$

and

$$\Delta I_T = 61.4 \text{ ma } (0.0011/^{o}C)(-28^{o}C) = -1.9 \text{ ma}$$

10. Effective Insolation on Solar Cells (Block P).

From Block G calculate the relative insolation

$$s = \frac{1}{(AU)^2}$$

$$= \frac{1}{(1.67)^2} = \frac{1}{2.79} = 0.358$$

From Block D at $\Phi_a' = 1 \times 10^{14}$ e/cm^2

$$F_a = 0.974$$

From Block E at $\Phi_{cg}' = 1 \times 10^{14}$ e/cm^2

$$F_{cg} = 0.948$$

From Block F at $\Gamma = 10$ deg and $\Phi_{cg}' = 1 \times 10^{14}$ e/cm^2

$$\cos \Gamma = \cos 10 \text{ deg}$$

and

$$R_{sc} = 0.986$$

Therefore, from Block P

$$s' = sR_{sc} F_{cg} F_a$$

$$= (0.358)(0.986)(0.948)(0.974)$$

$$= 0.326$$

11. Voltage Difference at Operating Temperature (Block U).

From Block Q and at $s' = 0.326$ (Step 10)

$$\beta_E = -2.45 \text{ mv}/^{\circ}\text{C}$$

From 9,

$$\Delta T = -28^{\circ}\text{C}$$

12. I-V Curve due to Operating Temperature (Block T).

Shift curve (Block R) along current axis by $\Delta I_T = -1.9$ ma and along voltage axis by $\Delta E_T = 69$ mv, or

$$I_2 = I_1 + \Delta I_T = I_o + \Delta I_\Phi + \Delta I_T$$

$$= I_1 - 1.9 \text{ ma} = I_o - 4.6 \text{ ma} - 1.9 \text{ ma} = I_o - 6.5 \text{ ma}$$

$$E_2 = E_1 + \Delta E_T = E_o + \Delta E_\Phi + E_T$$

$$= E_1 + 70 \text{ mv} = E_o - 25 \text{ mv} + 69 \text{ mv} = E_o + 44 \text{ mv}$$

and

$$I_2\Big|_{E_2=0} = I_1\Big|_{E_1=-69 \text{ mv}} + \Delta I_T = 61.4 \text{ ma} - 1.9 \text{ ma} = 59.5 \text{ ma}$$

13. Current Difference due to Insolation (Block V).

From 12,

$$I_2\Big|_{E_2=0} = 59.4 \text{ ma}$$

and from 10,

$$s' = 0.326$$

Therefore,

$$\Delta I_s = (s' - 1)\, I_2\Big|_{E_2=0}$$

$$= (0.326-1)(59.4 \text{ ma}) = (-0.674)(59.4 \text{ ma}) = -40.0 \text{ ma}$$

14. Voltage Difference due to Insolation (Block X).

From 13,

$$\Delta I_s = -40.0 \text{ ma}$$

$$\Delta E_s = -I_s \Delta I_s$$

$$= -(0.73\Omega)(-40.0 \text{ ma}) = 29 \text{ mv}$$

15. <u>I-V Curve due to Insolation (Block W).</u>

Shift curve (Block T) along current axis by $\Delta I_s = -40.0$ ma and along voltage axis by $\Delta E_s = 29$ mv, or

$$I_3 = I_2 + \Delta I_s = I_o + \Delta I_\Phi + \Delta I_T + \Delta I_s$$

$$= I_2 - 40.0 \text{ ma} = I_o - 46.5 \text{ ma}$$

$$E_3 = E_2 + \Delta E_s = E_o + \Delta E_\Phi + \Delta E_T + \Delta E_s$$

$$= E_2 + 29 \text{ mv} = E_o + 73 \text{ mv}$$

16. <u>Current and Voltage Difference due to Panel Assembly (Block Z).</u>

Determine the maximum power point of curve (Block W) and its current and voltage (Block Y).

$$I_3(P_{max}) = 17.6 \text{ ma}$$

$$E_3(P_{max}) = 460 \text{ mv}$$

Calculate with $F_i = 0.95$

$$\Delta I_i = -I_3(P_m)\left[1 - \sqrt{F_i}\right]$$

$$= -17.6 \text{ ma}(1 - \sqrt{0.95})$$

$$= -17.6 \text{ ma } (1 - 0.974)$$

$$= -17.6 \text{ ma } (0.026) = -0.5 \text{ ma}$$

$$\Delta E_i = -E_3(P_m)\left[1 - \sqrt{F_i}\right]$$

$$= -460 \text{ mv } (0.026) = -12 \text{ mv}$$

17. I-V Curve of Installed Solar Cell (Block AA).

Shift curve (Block W) along current axis by $\Delta I_i = -0.5$ ma and along voltage axis by $\Delta E_i = -12$ mv, or

$$I = I_3 + \Delta I_i = I_o + \Delta I_\Phi + \Delta I_T + \Delta I_s + \Delta I_i$$

$$= I_3 - 0.5 \text{ ma} = I_o - 47.0 \text{ ma}$$

$$E = E_3 + \Delta E_i = E_o + \Delta E_\Phi + \Delta E_T + \Delta E_s + \Delta E_i$$

$$= E_3 - 12 \text{ mv} = E_o + 61 \text{ mv}$$

18. Maximum Power Output of Installed Solar Cell (Block BB).

Determine the maximum power point of curve (Block AA) and its current and voltage.

$$I(P_{max}) = 17.0 \text{ ma}$$

$$E(P_{max}) = 455 \text{ mv}$$

19. Number of Series and Parallel Cells in Solar Array (Block CC).

From 18 and at $E_{sa} = 30.4$ volts and $I_{sa} = 16.8$ watts

$$N_p' = \frac{I_{sa}}{I(P_m)}$$

$$= \frac{16.8 \text{ amp}}{17.0 \text{ ma}} (1000 \text{ ma/amp}) = 988 \text{ cells in parallel}$$

$$N_s = \frac{E_{sa}}{E(P_m)}$$

$$= \frac{30.4 \text{ volts}}{0.455 \text{ volts}} = 66.8 \text{ cells}$$

Increase to next higher integer such that $N_s = 67$ cells in series.

20. Cell Operating Voltage (Block DD).

$$E_{op} = \frac{E_{sa}}{N_s}$$

$$= \frac{30.4 \text{ volts}}{67 \text{ cells}} = 454 \text{ mv/cell}$$

21. Cell Operating Current (Block EE).

From curve (Block AA) at E_{op} = 454 mv, determine

$$I_{op} = 17.1 \text{ ma}$$

and

$$I'_{sa} = I_{op} N'_P$$

$$= (17.1 \text{ ma})(988 \text{ cells}) = 16.9 \text{ amperes}$$

22. Array Reliability Enlargement (Block MM).

By means of a seperate reliability calculation, determine the anticipated array current at t_d. For initial design at time t_d and N'_P, assume:

$$I''_{sa}\Big|_{N'_P} = 0.95\, I'_{sa}$$

$$= 0.95\,(16.9 \text{ amp}) = 16.1 \text{ amperes}$$

and that

$$I''_{sa}\Big|_{N_P} = I_{sa} = 16.8 \text{ amperes}$$

Thus,

$$N_P = \frac{I_{sa}}{I''_{sa}\Big|_{N'_P}} N'_P$$

$$= \frac{16.8a}{16.1a}(988) = 1032 \text{ cells in parallel}$$

and

$$I'_{sa} = I_{op} N_P$$

$$= (17.1 \text{ ma})(1032) = 17.6 \text{ amperes}$$

23. Number of Cells in Solar Array (Block FF).

From 19 and 22

$$N_{sa} = N_s N_P$$

$$= (67)(1032) = 69,144 \text{ cells per array}$$

24. Area of Solar Array (Block GG).

From 3, 4 and 23

$$A_{sa} = \frac{N_{sa} A_c}{F_p}$$

$$= \frac{(69,144)(2 \text{ cm}^2)}{0.92} \left(\frac{1}{929} \text{ ft}^2/\text{cm}^2\right) = 162 \text{ ft}^2$$

25. Determine Solar Cell Physical Parameters (Block LL).

From 3 and 4 using Block H calculate

$$w_c = w_c/A \times A_c$$

$$= (0.11 \text{ gm/cm}^2)(2 \text{ cm}^2) = 0.22 \text{ gm}$$

$$w_{cg} = \rho_{cg} \times A_{c-a} \times d_{cg}$$

$$= (2.6 \text{ gm/cm}^3)(1.9 \text{ cm}^2)(6 \text{ mils})\left(\frac{2.54}{1000} \frac{\text{cm}}{\text{mil}}\right) = 0.075 \text{ gm}$$

$$w_{cb} = \rho_{cb} \times A_c \times d_{cb}$$

$$= (2.4 \text{ gm/cm}^3)(2 \text{ cm}^2)(4 \text{ mils})\left(\frac{2.54}{1000} \frac{\text{cm}}{\text{mil}}\right) = 0.049 \text{ gm}$$

$$w_h = w_h/A \times A_c$$

$$= (0.08\ gm/cm^2)(2\ cm^2)\ 0.16\ gm$$

and

$$w_c' = w_c + w_{cg} + w_{cb} + w_h$$

$$= 0.22\ gm + 0.075\ gm + 0.049\ gm + 0.16\ gm = 0.51\ gm/cell$$

$$= (0.51\ gm)(\frac{1}{453.6}\frac{lb}{gm}) = 1.13 \times 10^{-3}\ lb$$

26. Determine Solar Array Structural Parameters (Block JJ).

From 4 and 24 calculate Block HH

$$n_p = \frac{A_{sa}}{A_{p(max)}}$$

$$= \frac{162\ ft^2}{30\ ft^2} = 5.4\ panels$$

Adjust to 6 panels and calculate Block II

$$A_p = \frac{A_{sa}}{n_p}$$

$$= \frac{162\ ft^2}{6} = 27\ ft^2$$

For initial design, assume the use of only "Primary Panels" such that from data (Block JJ) at 27 ft^2

$$W_s/A = 0.516\ lb/ft^2$$

27. Weight of Solar Array (Block KK).

From 23, 24, 25 and 26 calculate

$$W_{sa} = W_s/A \times A_{sa} + w_c' \times N_{sa}$$

$$= (0.516\ 16/ft^2)(162\ ft^2) + (0.00113\ lb)(69,144)$$

$$= 83.6\ lb + 78.1\ lb = 161.7\ lb$$

or

$$\frac{161.7\ lb}{500\ watts} = 323\ lb/_{kw}$$

and

$$\frac{161.7\ lb}{162\ ft^2} = 1.0\ lb/ft^2$$

$$\frac{500\ watts}{162\ ft^2} = 3.08\ watts/ft^2$$

28. Solar Plant Power Output with Zero Cell Failures (Block PP).

From 22 at $E_s = 29.7$ volts and $I_{sa}' = 17.6$ amp, calculate

$$P_s' = E_s\ I_{sa}'$$

$$= (29.7\ volts)(17.6\ amp) = 523\ watts$$

Problem B: Determine power output of the designed solar array in near earth space just after launch:

$E_{sa} = 30.4$ volts	$t = 0$
$E_p = 29.7$ volts	$AU = 1.0$
$T_{sa} = 50^oC$	$\Phi = 0$

5'. Radiation Current Degradation (Block K). From Block B at $\Phi_c' = 0$,

$$I_{sc-\Phi} = 66\ ma$$

and therefore

$$\Delta I_\Phi = 0$$

7'. Radiation Voltage Degradation (Block M). At $\Phi_c' = 0$,

$$E_{oc-\Phi} = 540 \text{ mv}$$

and therefore

$$\Delta E_{\Phi} = 0$$

9'. Current Difference at Operating Temperature (Block S). From Block O,

$$\Delta T = 22^{o}C$$

with $\Phi_c' = 0$,

$$\left(\beta_I / I_{sc}\right) = 0.055\%/^{o}C$$

and therefore

$$\Delta I_T = I_1 \Big|_{E_1 = o} \beta_I / I_{sc} \, \Delta T = 66 \text{ ma } (0.00055/^{o}C)(22^{o}C) = 0.8 \text{ ma}$$

10'. Effective Insulation on Solar Cells (Block P). From Block G

$$s = \frac{1}{(AU)^2} = \frac{1}{(1.0)^2} = 1$$

From Block O at $\Phi_a' = 0$,

$$F_a = 1.0$$

From Block E at $\Phi_{cg}' = 0$,

$$F_{cg} = 0.95$$

and from Block F at $\Gamma = 10^{o}$ and $\Phi_{cg}' = 0$,

$$\cos \Gamma = \cos 10^{o} = 0.985$$

and

$$R_{sc} = 0.987$$

Therefore, from Block P

$$s' = s \, R_{sc} \, F_{cg} \, F_a = (1.0)(0.987)(0.95)(1.0) = 0.938$$

11'. Voltage at Operating Temperature (Block U).

Since $\Delta T = 22^{\circ}C$, and $s' = 0.938$,

$$\beta_E = -2.47 \text{ mv}/^{\circ}C$$

Therefore

$$\Delta E_T = \beta_E \Delta T = (-2.47 \text{ mv}/^{\circ}C)(22^{\circ}C)$$

$$= -54 \text{ mv}$$

12'. I-V Curve Due to Operating Temperature (Block T').

Shift curve (Block A) along current axis by $\Delta I_T = 0.8$ ma and along voltage axis by $\Delta E_T = -54$ mv, or

$$I_2 = I_o + \Delta I_\Phi + \Delta I_T = I_o + 0.8 \text{ ma}$$

$$E_2 = E_o + \Delta E_\Phi + \Delta E_T = E_o - 55 \text{ mv}$$

and

$$I_2\Big|_{E_2=0} = I_o\Big|_{E_o=67 \text{ mv}} + \Delta I_T = 66.0 \text{ ma} + 0.8 \text{ ma} = 66.8 \text{ ma}$$

13'. Current Difference Due to Insolation (Block V). From 12',

$$I_2\Big|_{E_2=0} = I_o\Big|_{E_o=0} = 66 \text{ ma}$$

and from 10',

$$s' = 0.938$$

Therefore,

$$\Delta I_s = (s'-1)\, I_2\Big|_{E_2=0} = (0.938-1)(66.8 \text{ ma}) = (-0.062)(66.8 \text{ ma})$$

$$= -4.1 \text{ ma}$$

14'. Voltage Difference due to Insolation (Block X). From 13',

$$\Delta I_s = 4.1 \text{ ma}$$

$$\Delta E_s = -r_s \Delta I_s = -(0.73\Omega)(-4.1 \text{ ma}) = 3 \text{ mv}$$

15'. I-V Curve Due to Insolation (Block W').

Shift curve (Block T) along current axes by $\Delta I_s = -4.1$ ma and along voltage axis by $\Delta E_s = 3$ mv, or

$$I_3 = I_o + \Delta I_\Phi + \Delta I_t + \Delta I_s = I_o + 0.8 - 4.1 = I_o - 3.3 \text{ ma}$$

$$E_3 = E_o + \Delta E_\Phi + \Delta E_t + \Delta E_s = E_o - 54 \text{ mv} + 3\text{mv} = E_o - 51 \text{ mv}$$

16'. Current and Voltage Difference Due to Panel Assembly (Block Z).

Determine the maximum power point of curve (Block W').

$$I_3(P_m) = 56.0 \text{ ma}$$

$$E_3(P_m) = 395 \text{ mv}$$

Calculate with $F_i = 0.95$

$$\Delta I_i = -I_3(P_m)\left[1 - \sqrt{F_i}\right] = -(56.0 \text{ ma})(0.026) = -1.5 \text{ ma}$$

$$\Delta E_i = -E_3(P_m)\left[1 - \sqrt{F_i}\right] = -(395 \text{ mv})(0.026) = 10 \text{ mv}$$

17'. I-V Curve of Installed Solar Cell (Block AA').

Shift curve (Block W') along axis by $\Delta I_i = -1.5$ ma and along voltage axis by $\Delta E_i = 10$ mv, or

$$I = I_3 - 1.5 \text{ ma} = I_o = 4.8 \text{ ma}$$

$$E = E_3 - 10 \text{ mv} = E_o - 62 \text{ mv}$$

21'. Cell Operating Current (Block EE).

From (Block AA) at $E_{op} = 454$ mv (Result of 20) determine

$$I_{op} = 23.2 \text{ ma}$$

and

$$I_{sa}' = I_{op} N_p$$

$$= (23.2 \text{ ma})(1050) = 24.4 \text{ amperes}$$

28'. <u>Solar Plant Power Output (Block PP).</u>

$$P'_s = E_s I_{sa}'$$

$$= (29.7 \text{ volts})(24.4 \text{ amp}) = 725 \text{ watts}$$

APPENDIX B2

SAMPLE CALCULATIONS FOR THERMOELECTRIC SOURCES

This appendix contains sample calculations for a flat-plate solar thermoelectric generator to be used for a 100-watt (el) Mars mission.

A. ELECTRICAL THERMAL CHARACTERISTICS PER COUPLE *

The manufacturer's recommended values are:

Hot junction (T_h) temperature = $473^{\circ}K$

Cold junction (T_c) temperature = $288^{\circ}K$

These values are used to obtain mean values between temperatures for the following:

1) Seebeck voltage (P element) $S_{\bar{P}}$ (Figure A2-1)
2) Seebeck voltage (N element) $S_{\bar{N}}$ (Figure A2-2)
3) Electrical resistivity (P element) $\rho_{\bar{P}}$ (Figure A2-3)
4) Electrical resistivity (N element) $\rho_{\bar{N}}$ (Figure A2-4)
5) Thermal conductivity (P element) $K_{\bar{P}}$ (Figure A2-5)
6) Thermal conductivity (N element) $K_{\bar{N}}$ (Figure A2-6)

These values may be calculated from the representative integrals, or a first order approximation may be made by obtaining 10 values between T_c and T_h and averaging them. For this calculation, the latter method was employed, since input data was provided as approximate only. Results of averaging are as follows:

$$S_{\bar{P}} = 170\ \mu\text{-volts}/^{\circ}C$$

$$S_{\bar{N}} = 130\ \mu\text{-volts}/^{\circ}C$$

The mean Seebeck voltage, per couple, is obtained by adding the two

$$S_m = S_{\bar{P}} + S_{\bar{N}} = 300\ \mu\text{-volts}/^{\circ}C$$

*Refer to Figure 3-11 for Computation Flow Diagram

Electrical resistivity of the elements comprising a couple are:

$$\rho_{\overline{P}} = 1.75 \text{ milliohms/cm}$$

$$\rho_{\overline{N}} = 0.73 \text{ milliohms/cm}$$

and the respective mean values of thermal conductivity are

$$K_{\overline{P}} = 0.018 \text{ w/cm}^{\circ}\text{C}$$

$$K_{\overline{N}} = 0.021 \text{ w/cm}^{\circ}\text{C}$$

Additional input from the manufacturer provides the following data on thermoelectric element sizing

$L = L_P = L_N = 0.270$ cm of length

$K_1 = 13.5 \text{ cm}^{-1}$ length-to-cross section area of "p" element

From these data, the cross section area of the "p" element is calculated

$$\sigma_P = \frac{L_P}{K_1} = \frac{0.27}{13.5} = 0.02 \text{ cm}^2$$

Next, the figure of merit (θ) is calculated

$$\theta_{mean} = \frac{\left(T_h + T_c\right) S_m^2}{2\left[\sqrt{K_{\overline{P}}\,\rho_{\overline{P}}} + \sqrt{K_{\overline{N}}\,\rho_{\overline{N}}}\right]^2}$$

$$= \frac{(473 + 288)\left(3 \times 10^{-4}\right)^2}{2\left[\sqrt{(0.018)(1.75 \times 10^{-3})} + \sqrt{(0.021)(0.73 \times 10^{-3})}\right]^2}$$

$$= 0.377$$

From the figure of merit, the matching factor, M_o, can be determined

$$M_o = (1 + \theta)^{1/2} = (1.377)^{1/2} = 1.175$$

Employing the matching factor, M_o, the temperature differential, and Seebeck voltage, the voltage per couple is calculated

$$V_c = \left(T_h - T_c\right) S_m \frac{M_o}{1 + M_o} = (187)(3 \times 10^{-4}) \frac{1.175}{2.175}$$

$$= 0.030 \text{ volt/couple}$$

A mathematical comparison between thermal conductivities and electrical resistivities of the "n" and "p" elements permits a calculation of the optimized "r" value. This is the balance of conversion within a couple.

$$r = \sqrt{\frac{K_{\bar{N}}/\rho_{\bar{P}}}{K_{\bar{P}}/\rho_{\bar{N}}}} = \sqrt{\frac{(0.021)(1.75 \times 10^{-3})}{(0.018)(0.73 \times 10^{-3})}} = 1.67$$

The cross section area of the "p" element was calculated earlier; with the value of "r" known, the cross section area of the "n" element is calculated

$$\sigma_N = \frac{\sigma_P}{r} = \frac{0.02}{1.67} = 0.012 \text{ cm}^2$$

While this value is not in complete agreement with the manufacturer's listed area (0.010 cm^2), it is within the tolerance limits for manufacturer. These elements are hot-pressed and sintered, resulting in a product which is neither 100 percent density nor matching in size.

With both element cross section areas known as well as the previously determined electrical resistivities, "r" value and common element length, then the internal resistance (R_{ci}) of the couple may be calculated

$$R_{ci} = \frac{L}{\sigma_P} \left(\rho_P + r\rho_N\right) = \frac{0.27}{0.02} (1.75 \times 10^{-3} + 1.67)(0.73 \times 10^{-3})$$

$$= 0.040 \text{ ohm/couple}$$

Knowing the couple voltage and resistance as well as the matching factor, M_o, the couple current, I_c, may be determined as follows:

$$I_c = \frac{V_c}{R_{ci} M_o} = \frac{0.030}{(0.040)(1.175)} = 0.638 \text{ amp/couple}$$

The theoretical power/couple, P_{tc}, is then calculated from voltage and current

$$P_{tc} = V_c I_c = (0.030)(0.638) = 0.0191 \text{ watt (el)/couple}$$

However, realistic power rating of a thermoelectric array must include the contact resistance at hot and cold junctions of each element. This resistance, usually provided by the manufacturer as a constant, is designated R_c and is estimated at 5 percent of R_{ci} for this calculation

$$R_c = 0.05 R_{ci} = 2.5 \times 10^{-3} \text{ ohm}$$

but there are four contacts per couple; therefore, the total contact resistance is 4 times R_c or 0.01 ohm/couple.

The resistance used to calculate the current and hence, theoretical power, did not take into account the power loss due to load resistance, $R_{\ell c}$

$$R_{\ell c} = V_c/I_c = \frac{0.03}{0.638} = 0.047 \text{ ohm/couple}$$

Power per couple may now be recalculated in a more realistic manner, incorporating the contact resistance and load resistance of a couple as follows:

$$P_{\ell c} = P_{tc}\left(\frac{R_{\ell c}}{R_{\ell c} + 4R_c}\right) = 0.0191\left(\frac{0.047}{0.047 + 0.010}\right)$$

$$= 0.0157 \text{ watt (el)/couple}$$

On those thermoelectric generators containing a heat supply, such as radioisotope, the thermal input to the couples may be adjusted to comply with and therefore provide the electrical power in watts as calculated.

However, solar power requires that a suitable collector surface be provided in order to meet the required operating temperatures at hot and cold junctions. Before this can be determined, an examination of the heat flow through a couple must be made. This includes the Peltier-Thompson effect, conducted heat, and Joulean heating.

1. Heat Input Per Couple

There are three ways that heat may be expended after entering a couple:

a) Peltier-Thompson Effect on Hot Side

$$Q_{pth} = \left(S_m\right)\left(T_h\right)\left(I_c\right)$$

$$= \left(3 \times 10^{-4}\right)(473)(0.638) = 0.091 \text{ watt/couple}$$

b) Heat Conducted Through Couple

$$Q_{ch} = \frac{\left(T_h - T_c\right)\left(\sigma_{\overline{P}} K_{\overline{P}} + \sigma_{\overline{N}} K_{\overline{N}}\right)}{L}$$

$$\doteq \frac{(187)\left[(0.02)(0.018) + (0.012)(0.021)\right]}{0.270} = 0.422 \text{ watt/couple}$$

c) Joulean Heating/Couple. In addition to the heat introduced into a couple, a portion of the converted electrical power is reconverted back to heat by resistance through the couple.

$$Q_j = \frac{I_c^2 R_{ci}}{2} = \frac{(0.638)^2(0.040)}{2} = 8.14 \times 10^{-3} \text{ watt/couple}$$

The net heat input per couple may be calculated in the following manner:

$$Q_1 = Q_{pth} + Q_{ch} + Q_j$$

$$= 0.091 + 0.422 - 0.008 = 0.505 \text{ watt/couple}$$

2. Heat Output Per Couple

The heat output per couple may be determined similarly. Heat from the same three sources will emerge at the cold end of a couple.

a) Peltier-Thompson Effect-Cold Side:

$$Q_{ptc} = (S_m)(T_c)(I_c)$$

$$= (3 \times 10^{-4})(288)(0.638) = 0.055 \text{ watt/couple}$$

b) Conducted Heat Per Couple. This value is the same as that calculated for the conducted heat passing through the hot end of the couple.

$$Q_{ch} = 0.422 \text{ watt/couple}$$

c) Joulean Heating Per Couple. This value is the same as that calculated for Joule heat production at the hot end of the couple.

$$Q_j = 8.14 \times 10^{-3} \text{ watt/couple}$$

Therefore, heat rejection, per couple, may be expressed as

$$Q_2 = Q_{ptc} + Q_{ch} + Q_j$$

$$= 0.055 + 0.422 + 0.008 = 0.485 \text{ watt/couple}$$

Knowing the amount of heat entering a couple at the hot side and the amount of heat leaving the cold side, the electrical conversion (theoretical power/couple) is expressed as the difference between the two values

$$P_{tc} = Q_1 - Q_2$$

$$= 0.505 - 0.485 = 0.020 \text{ watt electrical/couple}$$

This value of theoretical power per couple compares favorably with the earlier calculation based upon electrical properties, within the limit of accuracy of input data.

B. HEAT BALANCE AND PANEL DESIGN *

The foregoing calculations have identified the electrical characteristics one may expect from a thermoelectric couple, provided a certain hot and cold temperature differential is established. Since the thermal energy from the sun is to be used to power the flat-plate array, sufficient absorber area must be provided if the required temperatures are to be met. It is the purpose of the present calculations, therefore, to identify absorber/radiator area.

Based on manufacturer's flat-plate design and recommended hot and cold temperatures, the absorber temperature (T_a) and radiator temperature (T_r) are calculated as follows:

Manufacturer's Input:

$$T_h = 473^oK$$

$$K_2 = 5^oK$$

$$T_a = T_h + K_2$$

$$T_a = 473^oK + 5^oK = 478^oK$$

Manufacturer's Input:

$$T_c = 288^oK$$

$$K_3 = 5^oK$$

$$T_r = T_c - K_3$$

$$T_r = 288^oK - 5^oK = 283^oK$$

Because the hypothetical mission is in Mars orbit, the solar intensity at that distance will be less than at earth. We calculate Mars solar intensity as follows:

Mission Input:

$$S_e = 0.140 \text{ watt/cm}^2$$

$$AU_d = 1.667$$

*Refer to Figure 3-12 for Computation Diagram

$$S_d = \frac{S_e}{\left(AU_d\right)^2} = \frac{0.140 \text{ watt/cm}^2}{(1.667)^2} - 0.050 \text{ watt/cm}^2$$

Because not all the heat absorbed by the absorber surface travels through the thermoelectrics, it is necessary to calculate that portion which radiates directly from absorber to radiator. To do so, one determines the net heat flow from two reflectors: the underside of the absorber and the inside of the radiator, as they face each other. Using the manufacturer's data the net emissivity is calculated.

Manufacturer's Input:

$$\epsilon_{ai} = 0.04$$

$$\epsilon_{ri} = 0.04$$

$$\epsilon_n = \frac{1}{\frac{1}{\epsilon_{ai}} + \frac{1}{\epsilon_{ri}} - 1} = \frac{1}{\frac{1}{0.04} + \frac{1}{0.04} - 1} = 0.02$$

By employing the data obtained above and additional manufacturer's input, we attempt to calculate the required absorber area for the hot and cold junction temperatures assumed.

Manufacturer's Input:

$$\upsilon_a = 0.88$$

$$\epsilon_a = 0.04$$

σ_{sb} = Stefan-Boltzmann Constant

$$A = \frac{Q_2 + I_c V_c}{S_d \upsilon_a - \sigma_{sb}\left[\epsilon_a T_a^4 + \epsilon_n \left(T_a^4 - T_r^4\right)\right]}$$

$$A = \frac{0.485 + 0.019}{(0.05)(0.88) - 5.71 \times 10^{-12}\left[(0.04)(478^4) + 0.02\,(478^4 - 283^4)\right]}$$

$$= 18.67 \text{ cm}^2/\text{couple}$$

Having calculated the area necessary to collect the required thermal energy for the couple, including internal losses, that portion which is directed at, but not retained by, the absorber must be determined. This loss is the reradiated heat and is calculated as follows:

$$Q_{rr} = (A)\left(\epsilon_a\right)\left(\sigma_{sb}\right)\left(T_a^4\right)$$

$$= (18.67)(0.04)(5.71 \times 10^{-12})(478^4) = 0.222 \text{ watt (th)/couple}$$

Similarly, it is necessary to determine the amount of heat radiated directly from the undersurface of the absorber to the inner surface of the radiator. This heat does not pass through the couple and is essentially wasted but must be accounted for.

$$Q_{trc} = \sigma_{sb}\left(T_a^4 - T_r^4\right) A\,\epsilon_n$$

$$= (5.71 \times 10^{-12})(478^4 - 283^4)(18.67)(0.02) = 0.097 \text{ watt (th)/couple}$$

By summation of heat losses and heat passage through the couple, the net heat input per thermocouple module may be determined

$$Q_a = Q_1 + Q_{rr} + Q_{trc}$$

$$= 0.446 + 0.222 + 0.097 = 0.765 \text{ watt (th)/couple module}$$

It now becomes necessary to test the manufacturer's recommended operating temperatures for the hot and cold junction of a couple. This may be done by recalculating the radiator temperature ($T_{r'}$) first, and then the cold junction temperature, as follows:

Electrical-Thermal Calculations:

$I = 0.638$ amp
$V = 0.030$ volt

Heat Balance and Panel Design:

$$A = 18.67 \text{ cm}^2$$

$$S_d = 0.050 \text{ watt(th)/cm}^2$$

$$Q_{rr} = 0.222 \text{ watt (th)/couple}$$

Manufacturer's Input:

$$\epsilon_r = 0.90$$

$$\upsilon_a = 0.88$$

Constant:

$$\sigma_{sb} = 5.71 \times 10^{-12}$$

$$T_{r'} = \sqrt[4]{\frac{AS_d\upsilon_a - Q_{rr} - IV}{A\epsilon_r \sigma_{sb}}}$$

$$= \sqrt[4]{\frac{(18.67)(0.05)(0.88) - 0.222 - 0.019}{(18.67)(0.9)(5.71 \times 10^{-12})}}$$

$$= 278^{\circ}\text{K radiator temperature (based on area)}$$

From the adjusted radiator temperature, $T_{r'}$, the adjusted cold junction temperature of the couple (T_c) is obtained in the following manner:

Manufacturer's Input:

$$K_3 = 5^{\circ}\text{K}$$

$$T_{c'} = T_{r'} + K_3$$

$$= 278 + 5 = 283^{\circ}\text{K cold junction temperature (based on area value)}$$

Comparing this cold junction temperature value with the manufacturer's recommended value, it is found that the manufacturer's value is 5°K too high. This means that the calculated power per couple cannot be obtained with the initially chosen values of hot and cold junction temperature. Therefore, an iterative calculation becomes necessary.

The adjusted cold junction temperature of 238°K will be used, together with the original value of the hot junction temperature, 473°K.

In examining the 5-degree decrease in cold junction temperature upon Seebeck voltage, thermal conductivity, and electrical resistivity, it is found that no measurable change is required. The curves are not accurate to more than 5 degrees differential; therefore, the originally calculated terms will be retained.

$$S_m = 300\ \mu\text{-volts}/^{\circ}C$$

$$\rho_{\overline{P}} = 1.75 \text{ milliohms/cm}$$

$$\rho_{\overline{N}} = 0.73 \text{ milliohm/cm}$$

$$K_{\overline{P}} = 0.018 \text{ w/cm}^{\circ}C$$

$$K_{\overline{N}} = 0.021 \text{ w/cm}^{\circ}C$$

This temperature correction does, however, result in a change in the figure of merit, $\theta'_{mean} = 0.374$ as compared to the original 0.377. Similarly, the matching factor, M_o changes $M'_o = 1.172$ as compared to an original 1.175. And, voltage per couple changes $V'_c = 0.031$ volt/couple, as compared to an original 0.030 volt/couple. Because the thermal conductivities and electrical resistivities did not change, the comparison factor, "r", will not change. $r = 1.67$ as before, and $\sigma_N = 0.012\ cm^2$ as before ("N" element diameter), and $R_{ci} = 0.040$ ohm/couple as before (internal resistance/couple); however, a change is expected in I_c, the current per couple, to $I'_c = 0.659$ amp/couple as compared to the original 0.638 which results in a change in theoretical power/couple P_{tc}, $P_{tc} = 0.0204$ watt (el)/couple as compared to an original 0.0191. The load resistance, R_{Lc}, does not change despite changes in voltage and current, $R_{Lc} = 0.047$ ohm/couple as before. However, the load power per couple P_{Lc}, will be expected to change, $P'_{Lc} = 0.0168$ watt (el)/couple as compared to an original 0.0157.

Because all heat transfer calculations were predicated upon temperatures, they will be expected to change. Peltier-Thompson effect on the hot side will change to Q'_{pth} 0.094 watt (th)/couple as compared to an original

0.091 and heat conducted through the couple, Q_{ch}, will increase to Q'_{ch} 0.433 watt (th)/couple as compared to an original 0.422. Likewise, Joulean heating/couple is expected to increase as Q'_j 8.68×10^{-3} watt (th)/couple as compared to an original 8.14×10^{-3}. These changes result in an increase in Q_1, the net heat input to a couple $Q'_1 = 0.518$ watt (th)/couple as compared to an original 0.505. The net heat output per couple will change, likewise. Peltier-Thompson effect at the cold side, Q_{ptc} changes to $Q'_{ptc} = 0.056$ watt (th)/couple as compared to an original 0.055. Therefore, the net heat rejection of a couple, Q_2, may be recalculated $Q'_2 = 0.498$ watt(th)/couple as compared to an original 0.485.

Recalculating theoretical power from a heat balance, $P_{tc} = 0.020$ watt (el)/couple is obtained, which is the same as the original value and agrees quite well with the recalculated theoretical power based upon current and voltage. Having recalculated the electrical and thermal factors, based upon the revised cold junction temperature, $T_{c'}$, the collector/radiator area needed to supply heat for these conditions to prevail is recalculated

$$A' = \frac{Q'_2 + I'_c V'_c}{S_d \upsilon_a - \sigma_{sb}\left[\epsilon_a T_a^4 + \epsilon_n\left(T_a^4 - T'^4_{r'}\right)\right]}$$

$$= \frac{498 + 0.02}{(0.050)(0.88) - 5.71 \times 10^{-12}\left\{(0.04)(478)^4 + (0.02)\left[(478)^4 - (278)^4\right]\right\}}$$

$= 19.18$ cm^2/couple module compared to 18.67 originally.

Using a revised collector/radiator area, the reradiated heat from this surface is recalculated as $Q'_{rr} = 0.228$ watt (th)/couple as compared to an original 0.222. Similarly, the internal radiative heat loss will be expected to increase to $Q'_{trc} = 0.101$ watt (th)/couple as compared to 0.097 originally. The revised net heat input to a couple module may then be recalculated

$$Q'_a = Q'_1 + Q'_{rr} + Q'_{trc}$$

$$= 0.518 + 0.228 + 0.101 = 0.847 \text{ watt(th)/couple}$$

as compared to the original 0.765.

Finally, to test the validity of the calculations based upon the revised cold junction temperature value, radiator temperature as a function of collector/radiator area is recalculated:

$$T_{r'} = \sqrt[4]{\frac{A'S_d \upsilon_a - Q'_{rr} - I'V'}{A' \epsilon_r \sigma_{sb}}}$$

$$= \sqrt[4]{\frac{(19.18)(0.05)(0.88) - 0.228 - 0.02}{(19.18)(0.9)(5.71 \times 10^{-12})}}$$

$$= 278.7^{\circ}K \text{ radiator temperature}$$

This value compares very favorably with the value calculated over the one assumed originally, being less than 1 degree different. Therefore, the system may be considered to be in thermodynamic balance and all power values are valid for temperatures employed.

It is now possible to return to the computational flow diagram and calculate the thermal efficiency of the couple module defined above.

Iteration:

$$I'_c = 0.659 \text{ amp}$$

$$V'_c = 0.031 \text{ volt}$$

$$A' = 19.18 \text{ cm}^2$$

Mission:

$$S_d = 0.050 \text{ w/cm}^2$$

$$N_{th} = \frac{I'_c V'_c}{S_d A} = \frac{(0.659)(0.031)}{(0.05)(19.18)}$$

$$= 2.1 \text{ percent conversion efficiency at Mars orbit distance}$$

Since all parameters governing the sizing of the flat-plate array have been defined, weight and dimension can be discussed. The flat-plate module is composed of five separate components whose weights will be determined individually.

Manufacturer's Input:

$K_4 = 0.0079\ g/cm^2$

$K_5 = 0.043\ g/cm^2$

$K_r = 0.0079\ g/cm^2$

a) Absorber weight/couple (W_{ac}):

$$W_{ac} = (A)(K_4)$$

$$= (19.18)(0.0079) = 0.152 \text{ gram/couple}$$

b) Structural weight/couple (W_{sc}):

$$W_{sc} = (A)(K_5)$$

$$= (19.18)(0.043) = 0.825 \text{ gram/couple}$$

c) Radiator weight/couple (W_{rc}):

$$W_{rc} = (A)(K_r)$$

$$= (19.18)(0.0079) = 0.152 \text{ gram/couple}$$

Although expressions have been developed for calculating the weights of the "N" and "P" elements from their dimensions and relative densities, this method will not be used here. Since the manufacturer has not provided density data, his value for the weight of a couple as given will be used. Therefore, $W_N + W_P = 0.026$ gram/couple (including shoes). The modular weight (W_{mc}), per couple, may then be calculated as follows:

Mission:

$P_d = 100$ w(el)

$$W_{mc} = W_{ac} + W_{sc} + W_p + W_N + W_{rc}$$

$$= 0.152 + 0.825 + 0.026 + 0.152$$

$$= 1.155 \text{ gram/couple module}$$

The modular enlargement factor, N_1, is next determined.

Heat Balance and Panel Design:

$$P'_{1c} = 0.0168 \text{ w/cple}$$

$$N_1 = \frac{P_d}{P'_{1c}}$$

$$= \frac{100}{0.0168} = 6000 \text{ (the number of couples required to provide 100 w(el).}$$

If the enlargement factor is applied to the modular weight, per couple, the modular weight of the panel, W_m is obtained.

$$W_m = (N_1)(W_{mc})$$

$$= (6000)\ (1.155) = 6930 \text{ grams}$$

However, in order for the panel to be folded during launch and to unfold and orient during the mission, support structure is needed. This equipment has been estimated (by the manufacturer) to be 1.36 times the weight of the panel it must support. Therefore, where the modular support weight equals W_{ms}

Manufacturer's Input:

$$K_6 = 1.36$$

$$W_{ms} = (K_6)\ (W_m)$$

$$= (1.36)\ (6930) = 9425 \text{ grams}$$

The array is composed of the panel plus the support structure. Its weight is calculated to be

$$W_a = W_m + W_{ms}$$

$$W_a = (6930) + (9.425) = 16,355 \text{ grams (or) } 16.36 \text{ kilograms}$$

The array area A_a is composed of the active area of the collector plates, plus dead space between plates that is not used for energy collection but is part of the support structure.

Manufacturer's Input:

$$K_a = 1.01$$

$$A_a = (K_a)(N_1)(A)$$

$$= (1.01)(6000)(19.18) = 116,230 \text{ cm}^2 = 11.62 \text{ meter}^2/\text{array}$$

C. MISSION INFLUENCE ON PANEL OVERSIZING *

The array developed in the preceding parts of this appendix provides a power supply of a size and weight that, without degradation, will provide the required 100 watts (el) for the Mars mission. However, environmental factors have been shown to adversely affect the longevity and power level of thermoelectric elements, particularly the "P" legs. In this part of the appendix, such degradation factors as the following will be factored into the sizing:

1) Thrusting shock and vibration
2) Steady-state operation
3) Recycling after short-term steady-state operation
4) Recycling after long-term steady-state operation.

In addition, pointing accuracy will be considered as a factor affecting power. For this study, the conditions of a Mars mission will be assumed:

1) Liquid propellent launching
2) Minimal number earth orbits before escape trajectory introduced
3) 210 days travel time, Earth-Mars
4) Five months in Mars orbit (100 orbits total)
5) 100 watts (el) required at end of life.

The degradation effects will be taken in chronological order:

1) Shock and Vibration Damage (D_t) Due to Thrusting. Based upon limited testing under development contract, the thermoelectric module manufacturer has indicated that the effect will be low, provided the folded module is properly positioned within the shroud. He expects a 3 percent degradation in power from thrusting breakage, based upon his testing. $D_t = 1 - 0.03 = 0.97$ thrusting factor.

*Refer to Figure 3-13 for Computation Flow Diagram

2) Steady-State Degradation Loss (D_{ss}) (Figure A2-7). During the entire active life of the mission, the thermocouples will be subjected to operational loss that is a function of time at temperature. This phenomenon has been observed by all users of thermocouples and must be assumed to occur here, although no manufacturer input is available for this study. Therefore, the degradation value has been assumed to be 2 percent/1000 hours of operation, and a graph has been plotted to reflect this effect.

Mission Input:

Earth-Mars time, 5040 hours

Using the steady-state degradation curve, for the interplanetary flight time, results in: D_{ss} = 0.94 steady-state degradation factor.

3) Recycling after Short-Term (1000 Hours) Steady-State Operation ($D_{r\ell 1}$) (Figure A2-8). Because the Earth-Mars mission will take longer than 1000 hours, this degradation effect will not manifest itself. However, it has been included to permit the user flexibility in assessing the flat-plate solar thermoelectric generator for any mission.

4) Recycling after Long-Term (> 1000 Hours) Steady-State Operation (D_{rml}) (Figure A2-9). This form of degradation will be introduced into the hypothetical Mars mission since with 210 days (5040 hours) interplanetary travel time, the generator will operate "full time," then go into a Mars orbit. During orbit, thermal cycling will occur between light and dark time. The appropriate graph in the appendix may be employed to obtain the degradation anticipated after Mars orbit is completed. Since Mars orbiting will take place during five months (1000 orbits), degradation will be cumulative. The thermoelectric manufacturer has indicated that thermal cycling after more than 1000 hours steady-state would be considerably more injurious than cycling after fewer hours of steady-state operation. However, no experimental data is available to describe the effect. For that reason, an estimated 4 percent power decrease per 100 cycles has been used for the plot. The degradation effect may then be approximated as follows:

Mission Input:

1000 cycles

$$D_{rml} = 0.66 \text{ (from graph)}$$

In the foregoing calculations of thermoelectric power from solar heat, it was assumed that the panel would be oriented normal to the sun and able to take advantage of solar density at a given distance. This may not actually be achievable; however, in assessing pointing angle error it is

assumed that Orbiting Geophysical Observatory (OGO) accuracy is valid. Here, the net error will not exceed ±5 degrees. Using the reduction in power as the cosine of the error angle, a curve has been plotted expressing the pointing accuracy (P_{pa}) correction factor in the following manner:

$P_{pa} = 1 - \cos \Gamma$.

OGO Input:

$\Gamma = \pm 5$ degrees

From the curve (Figure A2-10) we find that a 5-degree error would give the following pointing accuracy factor: $P_{pa} = 0.996$ (from graph). So long as the pointing error is kept to less than 10 degrees, the error value is within the limit of the solar density and therefore negligible.

The array enlargement factor (N_2) is a summation of all mission degradations as they collectively affect the enlargement of the flat-plate generator to meet mission requirements. It may be expressed as follows:

$$N_2 = \frac{1}{(D_t)\,(D_{ss})\,(D_{rml})\,(P_{pa})}$$

$$= \frac{1}{(0.97)\,(0.94)\,(0.66)\,(0.996)}$$

$$= 1.668 \text{ array enlargement factor for mission}$$

The flat-plate generator may now be enlarged in order to provide for the corrected array area (A_{ca}) and the corrected array weight (W_{ca}) connected with the mission as follows:

Heat Balance and Panel Design:

$$A_a = 11.62 \text{ meters}^2$$

$$A_{ca} = (N_2)\,(A_a)$$

$$= (1.668)(11.62) = 19.37 \text{ meters}^2 \ (208.4 \text{ ft}^2)$$

Heat Balance and Panel Design:

$$W_a = 16.36 \text{ kilograms}$$

$$W_{ca} = (N_2)(W_a) = (1.668)(16.36) = 27.28 \text{ kilograms } (60.15 \text{ lb})$$

The foregoing sizing will deliver 100 watts(el) at end of mission and is, therefore, capable of providing considerably more power at any time prior to end of mission. The greatest power capability of the generator would be immediately after launch. This value may be calculated as follows where P_{el} equals power after earth launch:

$$P_{el} = (N_2)(P_d)(D_t)(P_{pa})$$

$$P_{el} = (1.668)(100)(0.97)(0.996)$$

$$P_{el} = 161.15 \text{ watts (el)}$$

The panel area has been designed to operate at hot and cold temperatures compatible with a solar density observable at 1.667 AU distance from the Sun (Mars). If design power is to be provided at any time (t) where the spacecraft is at less than 1.667 AU, then a tilt must be introduced to the panel orientation with the sun to provide 0.050 watts(th)/cm^2 at all times. To obtain the correction tilt, ψ, the following calculation is made:

Mission Input:

$$AU_x = 1 \text{ AU}$$

$$AU_d = 1.667 \text{ AU}$$

$$\cos \psi = \left(\frac{AU_x}{AU_d}\right)^2$$

$$\cos \psi = \left(\frac{1}{1.667}\right)^2 = 0.6000$$

ψ = 51.3 degrees of tilt to the sun required

Therefore, if one is to obtain power at earth orbit, or just after earth launch as hypothesized above, an inclination of 51.3 degrees from normal is required to obtain P_{el} 161.15 watts(el). It is possible to obtain greater power than this value; however, to do so requires that less inclination be employed. This would increase the hot junction temperature and introduce a new set of thermoelectric characteristics into the calculation. Therefore, power would not be predictable.

APPENDIX B3

SAMPLE CALCULATIONS FOR SOLAR THERMIONIC SOURCES

For this computation, the following assumptions are made concerning input requirements:

- P_L = 500 watts (including source heater and control power and boost regulator losses). In computing P_L add a minimum of 10 minutes to the length of eclipse for warm up time.
- Mars orbit; therefore, the design AU is 1.67 AU
- Maximum orientation error of 6 minutes
- Maximum active projected area of concentrator corresponds to 9-foot mirror
- Maximum percent shadowing of active concentrator projected area, 5 percent
- Steady-state emitter temperature, 1900°K
- Design life, 1 year

The functions required for inputs to the program can now be generated, using the data given in Appendix A3 and described in the blocks shown in Figure 3-24 in the body of the report.

Function A

$R = 0.78$ (assumed)

Function B

$n_d/n_{do} = 0.9 - 0.01 \times 2 = 0.88$ (corrected from 1700 to 1900°K)

Function C

$n_{do} = 0.082$ at 1900°K

Function D

$$\phi_e = \frac{6}{16.125/1.67} = 0.621 \text{ at } 1900^\circ K$$

at $1900^{\circ}K$ and $\phi_e = 0.621$, the concentrator-absorber efficiency is extrapolated

$$n_{ca} = 0.523 + \frac{(0.74 - 0.621)}{(0.74 - 0.37)} \times 0.015$$

$$= 0.523 + \frac{0.119}{0.37} \times 0.015$$

$$= 0.523 + 0.005$$

$$n_{ca} = 0.528$$

Other inputs

$$n_s = 1 - 0.05 = 0.95$$

$$S_d = \frac{130}{1.67^2} = 46.6 \text{ watts/ft}^2$$

$$A_{cm} = \frac{9^2 \times \pi}{4} = 63.5 \text{ ft}^2$$

The first computation is

$$n_{do} \times (n_d/n_{do}) \times n_{ca} \times n_s \times S_d \times R$$

$$= 0.082 \times 0.88 \times 0.528 \times 0.95 \times 46.6 \times 0.78 = 1.32 \text{ watts/ft}^2$$

The total area required is then

$$A_T = \frac{P_L \text{ watts}}{1.32 \text{ watts/ft}^2} = \frac{500}{1.32} = 379 \text{ ft}^2$$

The number of concentrators can now be determined.

$$N_c \cong \frac{A_T}{A_{cm}} = \frac{379}{63.5} = 5.97$$

The nearest greater integer is 6.0, therefore

$$\boxed{N_c = 6.0}$$

The actual concentrator area is then,

$$A_c = \frac{A_T}{N_c} = \frac{379}{6} = \boxed{63.1 \text{ ft}^2}$$

This area corresponds to a concentrator having an active diameter of D where

$$D = \sqrt{\frac{63.1 \times 4}{\pi}} = \sqrt{80.3} = 8.86 \text{ ft}$$

This would be the minimum number of concentrators and the minimum area of concentrator that would meet the power requirements. The actual choice would probably be six 9-foot mirrors if the 9-foot mirror was already available.

The initial capability of the thermionic source would be

$$P_{ci} = \frac{500}{0.88} = 568 \text{ watts}$$

The initial capability of the generators is then

$$P_{ci} = P_{ci}/N_c = \frac{568}{6} = \boxed{96.5 \text{ watts}}$$

The weight of the generator can be computed from Function E. A Curve for 1900°K must first be generated. At 2000°K and 172 watts, the generator would weight 9.0 pounds. At the same power rating at 1900°K, the weight of the generator would be increased by the ratio of the initial connecter efficiency n_{do} at 2000°K to that at 1900°K as obtained from Function C. Therefore

$$W_a \text{ at } \begin{matrix} 172 \text{ watts} \\ 1900^\circ K \end{matrix} = 9.0 \times \frac{0.11}{0.082} = 12.1 \text{ pounds}$$

Since the weight varies as the 1.5 power of P_{ci}, the weight of the generator would then be

$$W_a \text{ at } \begin{matrix} 96.5 \text{ watts} \\ 1900^\circ K \end{matrix} = 12.13 \times \left(\frac{96.5}{172}\right)^{1.5} = 5.1 \text{ pounds}$$

The weight of the electroformed nickel concentrator is obtained from Function F

$$W_c = 19.7 \times \left(\frac{63.1}{20.5}\right)^{1\ 1/6} = 19.7 \times 3.71 = 73.1 \text{ pounds}$$

The concentrator-generator unit weight is then

$$W_a + W_c = 5.1 + 73.1 = 78.2 \text{ pounds}$$

The total concentrator-generator weight is then

$$N_c(W_a + W_c) = 6 \times 78.2 = 468 \text{ pounds}$$

The structure weight required from the concentrator-generator units is found from Function H to be

$$W_s = 468 \times 0.51 + 7 = 238 + 7 = 245 \text{ pounds}$$

Therefore, the total source weight is

$$W_T = N_c(W_a + W_c) + W_s = 468 + 245 = 713 \text{ pounds}$$

or

$$\text{rounded off} = \boxed{710 \text{ pounds}}$$

The stowage volume of each concentrator-generator unit is found from Function G to be

$$V_c = 17.9 \times \left(\frac{63.1}{20.5}\right)^{1.5} = 17.9 \times 5.41 = 97.0 \text{ ft}^3$$

The total stowage volume of concentrator-generator units is then

$$N_c \times V_c = 6 \times 97.0 = 581 \text{ ft}^3$$

The stowage volume of the structure is found from Function I to be

$$V_s = 581 \times 0.5 = 291 \text{ ft}^3$$

Therefore, the total stowage volume of the source is now:

$$V_T = N_c \times V_c + V_s = 581 + 291 = \boxed{872\ ft^3}$$

The program output information is indicated by the figures enclosed in squares.

The actual power available to the system, including source electrical controls and losses in a boost regulator, is found by subtracting 5 watts (1 watt for each converter) for each generator from the total load power. This figure is then 500—6 x 5 = 470 watts.

This power would be available at voltages of 3, 6, 9, and 15 volts, depending on the series-parallel arrangement chosen for interconnecting the generators.

APPENDIX B4

SAMPLE CALCULATIONS FOR SOLAR DYNAMIC POWER PLANTS

Assumptions	Computations
$(P_1)_{max} = 1.0$ kw $(P_1)_{min} = 0.5$ kw	A.* Load Variation $\Delta P_1 = (P_1)_{max} - (P_1)_{min} = 1.0 - 0.5 = 0.5$ kw
	B. Control Power $P_c = 0.025$ kw
	C. Generator Output $P_e = (P_1)_{max} + P_c = 1.0 + 0.025 = 1.025$ kw
$\eta_g = 0.85$	D. Generator Input $P_g = P_e/\eta_g = 1.025/0.85 = 1.21$ kw
	E. Accessories Power $P_{acc} = 0.93$ kw
	F. Turbine Output $P_t = P_g + P_{acc} = 1.21 + 0.93 = 2.14$ kw
	G. Fluid Subcooling Heat Rejection $P_{fsc} = 0.12$ kw
$F_c = 0.9$ $T_c = 1060^{\circ}R$ $T_h = 1560^{\circ}R$	H. Thermal Efficiency $\eta_{th} = F_c \left(1 - \frac{T_c}{T_h}\right) = (0.9)(1 - 1060/1560) = 0.29$

*Letter designations in this appendix correspond to computation blocks in Figure 3-26.

Assumptions	Computations
$\eta_t = 0.45$	I. <u>Boiler Output</u> $P_b = \frac{P_t}{\eta_t \eta_{th}} + P_{fsc} - (P_g - P_e)$ $= \frac{2.14}{(0.45)(0.29)} + 0.12 - (1.21 - 1.025)$ $= 16.4 + 0.12 - 1.21 + 1.025 = 16.3$ kw
	J. <u>Estimated Concentrator Diameter</u> $D_{me}/AU = 18$ ft/AU
AU = 1.0 (300 mi earth orbit)	JA. $D_{me} = 18$ ft
	K. $D_m = D_{me} = 18$ ft
$\beta = 30$ min $R_m = 0.9$ $\Omega = 15$ min $\phi_s = 32$ min $\theta = 50$ deg	L. <u>Collection Efficiency</u> Angular surface error $= \beta/\phi_s = 30/32 = 0.94$ Orientation error $= \Omega/\phi_s = 15/32 = 0.47$ $\eta_{ca} = 0.76$ at $D_c/D_s = 9$
	M. <u>Aperture Diameter</u> $D_c = \frac{D_c}{D_s}\left[\frac{(D_m \tan 1/2\ \phi_s)(1 + \cos\theta_r)}{2 \sin\theta_r}\right]$ $= (9)(18 \tan 16 \text{ min } (1 + \cos 50 \text{ deg})/(2 \sin 50 \text{ deg})$ $= (9)(18)(0.00465)(1.643)/(2)(0.766) = 0.81$ ft

Assumptions	Computations
$\epsilon_c = 1.0$	N. Power Loss During Eclipse
$T_{ac} = 1560^oR$ (avr. during eclipse)	$P_{re} = 1/4\ \epsilon_c \sigma \pi D_c^2 T_{ac}^4$
$\sigma = 0.507 \times 10^{-12}$ kw/ft^2 $^oR^4$	$= (0.25)(0.507 \times 10^{-12})(\pi)(0.81)^2(1560)^4$
	$= 1.56$ kw
$t_e = 0.582$ hr	O. Energy Storage Input Power
$t_s = 1.0$ hr	$P_{es} = \frac{t_e}{t_s}(P_b + P_{re}) = 0.582\ (16.3 + 1.56) = 10.4$ kw
$C_p = 0.557 \times 10^{-3}$ kw-hr/lb^{o}F	P. Sensible Heat Addition
$(\Delta T_{es})_{1-s} = 350^oF$	$\Delta H_{tes} = C_p\left(\Delta T_{es}\right)_{1-s} = (0.557 \times 10^{-3})(350)$
	$= 0.195$ kw-hr/lb
W_{hd} = 10 percent additional	Q. Energy Storage Material Weight
$H_{fes} = 0.322$ kw-hr/lb	$W_{es} = \frac{P_{es} t_s}{H_{fes} + \Delta H_{tes}} + W_{hd} = 1.1\left[\frac{(10.4)(1.0)}{0.322 + 0.195}\right]$
	$= 22.1$ lb
$K_{es} = 0.69 \times 10^{-3}$ kw/ft^2 ^oF/ft	R. Energy Storage Surface Area
$\rho_{es} = 40$ lb/ft^3	$A_{es} = \sqrt{\frac{P_b W_{es}}{K_{es}\rho_{es}\Delta T_{es}}} = \sqrt{\frac{(16.3)(22.1)}{(0.69 \times 10^{-3})(40)(200)}}$
$\Delta T_{es} = 200^oF$	$= \sqrt{65} \qquad = 8.05$ ft^2

Assumptions	Computations
	S. Absorber Diameter $D_a = \sqrt{\frac{2\,A_{es}}{\pi}} = \sqrt{\frac{(2)(8.05)}{3.14}} = \sqrt{5.13} = 2.25$ ft
	T. Solar Input $P_s = \frac{P_b + P_{es}}{\eta_{ca}} = \frac{16.3 + 10.4}{0.76} = 35.1$ kw
$A = 1.5$ $C_s = 0.13$ kw/ft^2	U. Calculated Concentrator Diameter $D_{mc} = \sqrt{\frac{4P_s}{\pi C_s} + \left(AD_a\right)^2} = \sqrt{\frac{(4)(35.1)}{(\pi)(0.13)} + \left[(1.5)(2.25)\right]^2}$ $= \sqrt{344 + 11.5} = \sqrt{356} = 18.9$ ft
	V. Begin Iteration $D_{mc} \neq D_m$, $18.9 \neq 18.0$ $\left(D_{mc}\right)_1 \neq \left(D_m\right)_0$, $18.9 \neq 18.0$
	M. Aperture Diameter $D_c = (9)(18.9)(0.00465)(1.643)/(2)(0.766)$ $= 0.85$ ft
	N. Power Loss During Eclipse $P_{re} = (0.25)(0.507 \times 10^{-12}(\pi)(0.85)^2(1560)^4$ $= 1.74$ kw
	O. Energy Storage Input Power $P_{es} = 0.582(16.3 + 1.73) = 0.582$ $(18.0) = 10.5$ kw

Assumptions	Computations
	Q. Energy Storage Material Weight $W_{es} = 1.1\left[\frac{(10.5)(1.0)}{0.517}\right] = 22.3$ lb R. Energy Storage Surface Area $A_{es} = \sqrt{\frac{(16.3)(22.3)}{(0.69 \times 10^{-3})(40)(200}} = \sqrt{65.6} = 8.1\ ft^2$ S. Absorber Diameter $D_a = \sqrt{\frac{(2)(8.1)}{\pi}} = \sqrt{5.16} = 2.27$ ft T. Solar Input $P_s = \frac{16.3 + 10.5}{0.76} = \frac{26.8}{0.76} = 35.3$ kw U. Calculated Concentrator Diameter $D_{mc} = \sqrt{\frac{(4)(35.3)}{(\pi)(0.13)} + \left[(1.5)(2.28)\right]^2}$ $= \sqrt{346 + 12} = \sqrt{358} = 18.9$ ft V. Comparison of calculated concentrator diameter with previous calculation $\left(D_{mc}\right)_{n=2} = 18.9\ \left(D_{mc}\right)_{n=1} = 18.9$ D_m = Concentrator Diameter = $\boxed{18.9\ ft}$ D_a = Absorber Diameter = $\boxed{2.3\ ft}$

Assumptions	Computations
	W. Focal Length $f = \frac{D_m (1 + \cos \theta_r)}{4 \sin \theta_r} = \frac{18.9(1.643)}{4(0.766)} = \boxed{10.1 \text{ ft}}$
	X. Concentrator Depth $H_m = D_m^2 / 16 f = (20)^2/(16)(10.7)$ $= \boxed{2.05 \text{ ft}}$
$\eta_r = 0.75$ (single-side radiation) $\epsilon_r = 0.09$	AA. Condenser Heat Rejection/Unit Area $(P/A)_{rc} = \eta_r \epsilon_r \sigma T_c^4$ $= (0.75)(0.9)(0.507 \times 10^{-12})(1060)^4$ $= 0.44 \text{ kw/ft}^2$
	BB. Subcooler Heat Rejection $P_{rsc} = P_{fsc} + P_{acc} = 0.12 + 0.93 = 1.05 \text{ kw}$
	CC. Condenser Heat Rejection $P_{rc} = P_b - P_g - P_{rsc} = 16.3 - 1.21 - 1.05$ $= 14.0 \text{ kw}$
	DD. Condenser Area $A_{rc} = P_{rc}/(P/A)_{rc} = 14.0/0.44 = \boxed{31.8 \text{ ft}^2}$
$T_{sc} = 960^\circ$	FF. Subcooler Heat Rejection/Unit Area $(P/A)_{rsc} = \eta_r \epsilon_r \sigma T_{sc}^4$ $= (0.75)(0.9)(0.507 \times 10^{-12})(960)^4$ $= 0.29 \text{ kw/ft}^2$

Assumptions	Computations
	GG. Subcooler Area
	$A_{rsc} = P_{rsc}/(P/A)_{rsc} = 1.05/0.29 = \boxed{3.6\ ft^2}$
$K_{wr} = 1.0\ lb/ft^2$	EE. Condenser Weight
	$W_{rc} = K_{wr} A_{rc} = (1.0)(31.8) = 31.8\ lb$
	HH. Subcooler Weight
	$W_{rsc} = K_{wr} A_{rsc} = (1.0)(3.6) = 3.6\ lb$
	II. Rotating Unit Weight
	$W_{ru} = 31.5\ lb$
$K_{wm} = 0.25\ lb/ft^2$	JJ. Concentrator Weight
	$W_m = K_{wm} P_s/C_s = (0.25)(35.3)/0.13 = 68\ lb$
	KK. Absorber - Boiler Weight
	$W_{ab} = 55\ lb$
	LL. Heat Storage Unit Weight
	$W_{aes} = 32\ lb$
	MM. Absorber-Heat Storage Unit Weight
	$W_{ahs} = W_{ab} + W_{aes} = 55 + 32 = 87\ lb$
	NN. Fluid Inventory Weight
	$W_f = 9\ lb$

Assumptions	Computations
	OO. Control Weight $W_c = 60$ lb Y. Total Weight of Units $\Sigma W_u = W_{rc} + W_{rsc} + W_{ru} + W_m + W_{ahs} + W_f + W_c$ $= 32 + 4 + 32 + 68 + 87 + 9 + 60 = 292$ lb PP. Support Structure Weight $W_{ss} = 45$ lb Z. Power Supply Weight $W_{ps} = \Sigma W_u + W_{ss} = 292 + 45 = \boxed{337 \text{ lb}}$

PRELIMINARY POWER PLANT CONFIGURATION ANALYSIS

Based on the above sample calculation, a preliminary 1-kw power plant configuration is depicted in Figure B4-1. Since specific vehicle dimensions constitute a major constraint in determination of stowed and deployed power plant configurations, this figure serves only to illustrate application of the dimensional criteria resulting from the design computation.

APPENDIX B5
SAMPLE CALCULATIONS FOR INVERTERS

Problem: Determine the weight, volume, and heat dissipation of a 400-cps, single-phase, regulated inverter (Type 1A), given the following:

$$P_r = 133 \text{ watts}$$

$$P = 133 \text{ watts and } 100 \text{ watts}$$

$$E = 26.5 \text{ volts}$$

$$F_w = 0.25 \text{ lb/watt}$$

1. Weight as a Function of Efficiency (Block A)*

Input

$$P_r = 133 \text{ watts}$$

Inverter Type IA

Computation:

$$\frac{P_r}{W} = S + \frac{T}{1 - \eta_o} (P_r)^x \quad \text{(from Figure A9-1)}$$

where

$$x = U + \frac{V}{1 - \eta_o}$$

results in the following:

η_o	$\frac{P_r}{W}$ (watts/lb)	W (lb)
0.5	15.5	8.6
0.6	13.0	10.2
0.65	11.5	11.6
0.7	9.6	13.9
0.75	7.5	17.7
0.8	5.2	25.6
0.9	0.835	159.0

*Block letters cited in this appendix correspond to computation blocks in Figure 5-4.

2. Optimum Efficiency (Block F)

Equation (Block E)

$$W' - W + \frac{1 - \eta_o}{\eta_o} P_r F_w$$

and

$$F_w = 0.25 \text{ lb/watt}$$

modifies results of Step 1 and results in the following:

o	$\frac{1 - \eta_o}{\eta}$	W' (lb)
0.5	1.0	41.9
0.6	0.67	32.5
0.65	0.54	29.6
0.7	0.43	28.2 (optimum)
0.75	0.33	28.7
0.8	0.25	33.9
0.9	0.111	162.7

Therefore

$$\eta_o (W'_{min}) = 0.7 \text{ and } W' = 28.2 \text{ lb}$$

3. Inverter Weight (Block A)

With $\eta_o (W'_{min}) = 0.7$, the inverter weight using Function A is

$$W_i = \boxed{14.3 \text{ lb}}$$

4. Inverter Volume (Block B)

With $\eta_o (W'_{min}) = 0.7$; $W_i = 14.3$ lb; $P_r = 133$ watts and using equation

$$\frac{W}{V} = M \left(\frac{P_r}{1 - \eta_o}\right)^N \quad \text{(from Figure A9-2)}$$

$$= 0.05 \left(\frac{133}{0.3}\right)^{-0.012} = 0.58 \text{ lb/in}^3$$

and the volume results in

$$V_i = \frac{14.3 \text{ lb}}{0.0538 \text{ lb/in}^3} = \boxed{248 \text{ cu in}}$$

5. Rated Input Current (Block C)

With $\eta_o (W'_{min}) = 0.7$; $P_r = 133$ watts and $E = 26.5$ volts

$$I(P_r) = \frac{P_r}{\eta_o E} = \frac{133}{(0.3)(26.5)} = \boxed{7.2 \text{ amperes}}$$

6. Load Ratio Factor (Block O)

With $\eta_o (W'_{min}) = 0.7$; $P_r = 133$ watts and $P = 100$ watts

$$R_L = \frac{P}{P_r} = \frac{100}{133} = 0.75$$

and

$$F_{LR} = \frac{1 - R_L}{\log^{-1}\left[J\left(\log \frac{1}{\eta_o}\right)\right]^K} + R_L \quad \text{(from Figure A9-3)}$$

$$= \frac{1 - 0.75}{\log^{-1}\left[0.267\left(\log \frac{1}{0.7}\right)\right]^{-0.68}} + 0.75$$

7. Input Current (Block G)

$$I(P) = \left[F_{LR}\right] \left[I(P_r)\right]$$

at

$P = 100$ watts

$$I(P) = (0.7784)(7.2 \text{ amp}) = \boxed{5.6 \text{ amperes}}$$

8. <u>Heat Dissipation</u> (Block I)

$$Q_i = \boxed{E}\ \boxed{I(P)} - P$$

at 133 watts

$$Q_i = (26.5 \text{ volts})(7.2 \text{ amp}) - 133 \text{ watts}$$

$$= 191 \text{ watts} - 133 \text{ watts} = \boxed{58 \text{ watts}}$$

at 100 watts

$$Q_i = (26.5 \text{ volts})(5.6 \text{ amp}) - 133 \text{ watts}$$

$$= 149 \text{ watts} - 100 \text{ watts} = \boxed{49 \text{ watts}}$$

9. <u>Efficiency</u>

at 133 watts

$$\eta = \frac{133}{(7.2)(26.5)} = \boxed{0.70}$$

at 100 watts

$$\eta = \frac{100}{(5.6)(26.5)} = \boxed{0.67}$$

APPENDIX C

CURRENT-VOLTAGE RELATIONSHIPS ANTICIPATED FOR A SOLAR FLAT-PLATE THERMOELECTRIC MODULE

Current and voltage derived from thermoelectrics may be anticipated only if the system is in thermodynamic equilibrium. Any environmental changes tending to cool or heat the radiator rapidly would result in subsequent increases or decreases in output characteristics. Such conditions would prevail during a planetary orbit, where sudden darkness or sunlight would be experienced. Similarly, a single current-voltage curve would be inadequate for a mission where grossly changing solar input would be experienced, unless, as we have shown, a means is employed to provide constant Q to the panel by correction tilting of the vehicle panel.

As shown in Figure C-1, for a hypothetical earth orbit, the designed operating point, T_1, would provide a given current and voltage to meet a required power level. If the load becomes such as to short circuit the generator and voltage approaches zero, the current profile tends to flatten, delivering less than might be expected. This is due to cooling at the hot junction. Similarly, when the load current approaches zero, the voltage (approaching open circuit) increases from a decrease in Peltier cooling on the hot side, delivering greater than anticipated voltage.

The importance of the curve lies in the fact that temporary changes in hot side temperature (due to load change) do not materially affect the panel output. If the panel should receive an increased (or decreased) Q input either from misorientation or off-course geometry, then the current-voltage relationship would follow a curve paralleling that shown in the figure.

For example, a design will be obtained for a particular solar input and a hot junction temperature value. Earth orbit will be used.

Then

$$S = 0.140 \text{ w/cm}^2$$

$$T_1 = 475^\circ K$$

$$T'_1 = 480^\circ K$$

The constants of the couple are

$$K = 2 \times 10^{-3} \text{ w/}^{o}\text{K}$$

$$R = 0.0484 \text{ r}$$

$$S_m = 342 \times 10^{-6} \text{ v/}^{o}\text{K}$$

The collector emissivity $\epsilon_1 = 0.04$.

The collector to radiator emissivity $\epsilon_n = 0.04$.

The radiator emissivity $\epsilon_z = 0.9$

Assuming a cold junction temperature of $T_2 = 290^{o}\text{K}$, $T_2' = 285^{o}\text{K}$.*

Then solving for area per couple

$$A = \frac{0.595\,(290 \times 342 \times 10^{-6}) + 2 \times 0.185 + 0.006}{0.88 \times 0.140 - 5.71\,(0.08 \times 5.3 \times 10^{10} - 0.04 \times 0.60 \times 10^{10})} \times 10^{-12}$$

$$= \frac{0.079 + 0.37 + 0.006}{0.1}$$

$$= 4.55 \text{ cm}^2$$

Solving for a revised T_2'

$$T_2' = 4\sqrt{\frac{4.55 \times 0.123 - 4.55 \times 5.3 \times 5.71 \times 4 \times 10^{-4} - 0.020}{0.9 \times 4.55 \times 5.71 \times 10^{-12}}}$$

$$= 214^{o}\text{K}$$

---

*Then

$\theta_m = 0.432$

$M_o = 1.2$

$V = 0.0345$ volt

$i = 0.595$ amp

$Vi = 20.5$ mw

$\Delta T = 185^{o}\text{K}$

$\overline{T} = 382^{o}\text{K}$

Using this value for T_2', $T_2 = 220^oK$

$$\Delta T = 270^oK$$

$$\theta_m = 0.402$$

$$M_o = 1.19$$

$$V = 0.0503 \text{ v}$$

$$i = 0.873 \text{ a}$$

$$P = 0.044 \text{ w}$$

Then a new area will be calculated

$$A' = \frac{0.873\,(220 \times 342 \times 10^{-6} + 0.05) + 2 \times 0.270 + 0.018}{0.123 - 5.71 \times 10^{-12}\,(0.08 \times 5.3 \times 10^{10} - 0.04 \times 0.215 \times 10^{10})}$$

$$= \frac{0.873 \times 0.125 + 0.54 + 0.018}{0.123 - 0.024}$$

$$A' = \frac{0.667}{0.099} = 6.75 \text{ cm}^2$$

Checking T_2' for this area

$$T_2' = 4\sqrt{\frac{6.75 \times 0.123 - 6.75 \times 5.3 \times 5.71 \times 4 \times 10^{-4} - 0.044}{6.75 \times 0.9 \times 5.71 \times 10^{-12}}}$$

$$= 4\sqrt{\frac{0.83 - 0.082 - 0.044}{0.348 \times 10^{10}}}$$

$$= 213^oK$$

which is only 2^oK low, so the area should be correct as well as T_2' which $\approx 213^oK$.

If the electrical operating point were changed, a problem to encounter would be the resulting equilibrium temperature and operating point. In considering the two possible extremes, short circuit and open circuit, a relationship is required to handle the balance. From previous work

$$A(1 - r)S = A6\epsilon_1 T_1'^4 + A6\epsilon_n(T_1'^4 - T_2'^4)$$

$$+ K(T_1 - T_2) + i(T_2 S_m + V) + \frac{1}{2} i^2 R$$

$$A6(\epsilon_n + \epsilon_1)T_1^4 + KT_1 = A(1 - r)S + A6\epsilon_n T_2'^4$$

$$+ KT_2 - i(T_2 S_m + V) - \frac{1}{2} i^2 R$$

Assuming T_2' is constant, a new T_1' can be found for each i and V. Using the values obtained previously

$$6.75 \times 5.71 \times 0.08 \times 10^{-12}\ T_1'^4 + 2 \times 10^{-3}\ T_1$$

$$= 6.75 \times 0.123 + 2 \times 10^{-3} \times 218 + 6.75 \times 5.71 \times 10^{-12} \times 0.04$$

$$\times\ 2.13^4 \times 10^8 - i\ (218 \times 342 \times 10^{-6} + V + 0.0242i)$$

$$0.308 \times 10^{-11}\ T_1'^4 + 2 \times 10^{-3}\ T_1$$

$$= 0.83 + 0.432 + 0.003 + i(0.0745 + V + 0.0242i)$$

$$= 1.265 + i(0.0745 + V + 0.0242i)$$

When i = 0, solve for T_1', T_1, assume

$$T_1' = 525^\circ K$$

$$T_1 = 520^\circ K$$

$$0.308 \times 10^{-11} \times 7.6 \times 10^{10} + 2 \times 0.520 = 1.265$$

$$0.234 + 1.040 = 1.274 \approx 1.265 \text{ watts (th)}$$

Therefore, that $T_1 = 520^\circ K$ is a fair approximation for T_1. At this temperature

$$V_{oc} = 342 \times 10^{-6} \times 302$$

$$= 0.103 \text{ V}$$

When V = 0, assume

$$i = \frac{0.252 \times 0.342}{0.0484}$$

$$= 1.78 \text{ amps}$$

Then

$$0.308 \times 10^{-11} T_1'^4 + 2 \times 10^{-3} T_1 = 1.265$$

$$- 1.78 (0.0745 + 1.78 \times 0.0242)$$

$$= 1.265 - 0.216$$

$$= 1.049 \text{ watts (th)}$$

Assume

$$T_1' = 480^\circ K$$

$$T_1 = 475^\circ K$$

$$5.3 \times 10^{10} \times 0.308 \times 10^{-11} + 2 \times 0.475 = 1.049$$

$$0.163 + 0.95 = 1.049$$

$$1.113 \neq 1.049 \text{ watts (th)}$$

Assume

$$T_1' = 475^\circ K$$

$$T_1 = 470^\circ K$$

$$5.1 \times 10^{10} \times 0.308 \times 10^{-11} + 0.940 = 1.049$$

$$1.097 \neq 1.049 \text{ watts (th)}$$

Assume

$$T_1' = 470^\circ K$$

$$T_1 = 465^\circ K$$

$$4.89 \times 10^{10} \times 0.308 \times 10^{-11} + 0.930 = 1.049$$

$$0.151 + 0.930 = 1.049$$

$$1.081 \neq 1.049 \text{ watts (th)}$$

Assume,

$$T_1' = 460^{\circ}K$$

$$T_1 = 455^{\circ}K$$

$$0.449 \times 0.308 + 0.910 = 1.049$$

$$0.138 + 0.910 = 1.048 \approx 1.049$$

for the T_1

$$i_{sc} = \frac{237 \times 342}{0.0484} \times 10^{-6} = 1.68 \text{ amps}$$

This solution is an approximation but should be close. The I-V data points are shown in Figure C-1.

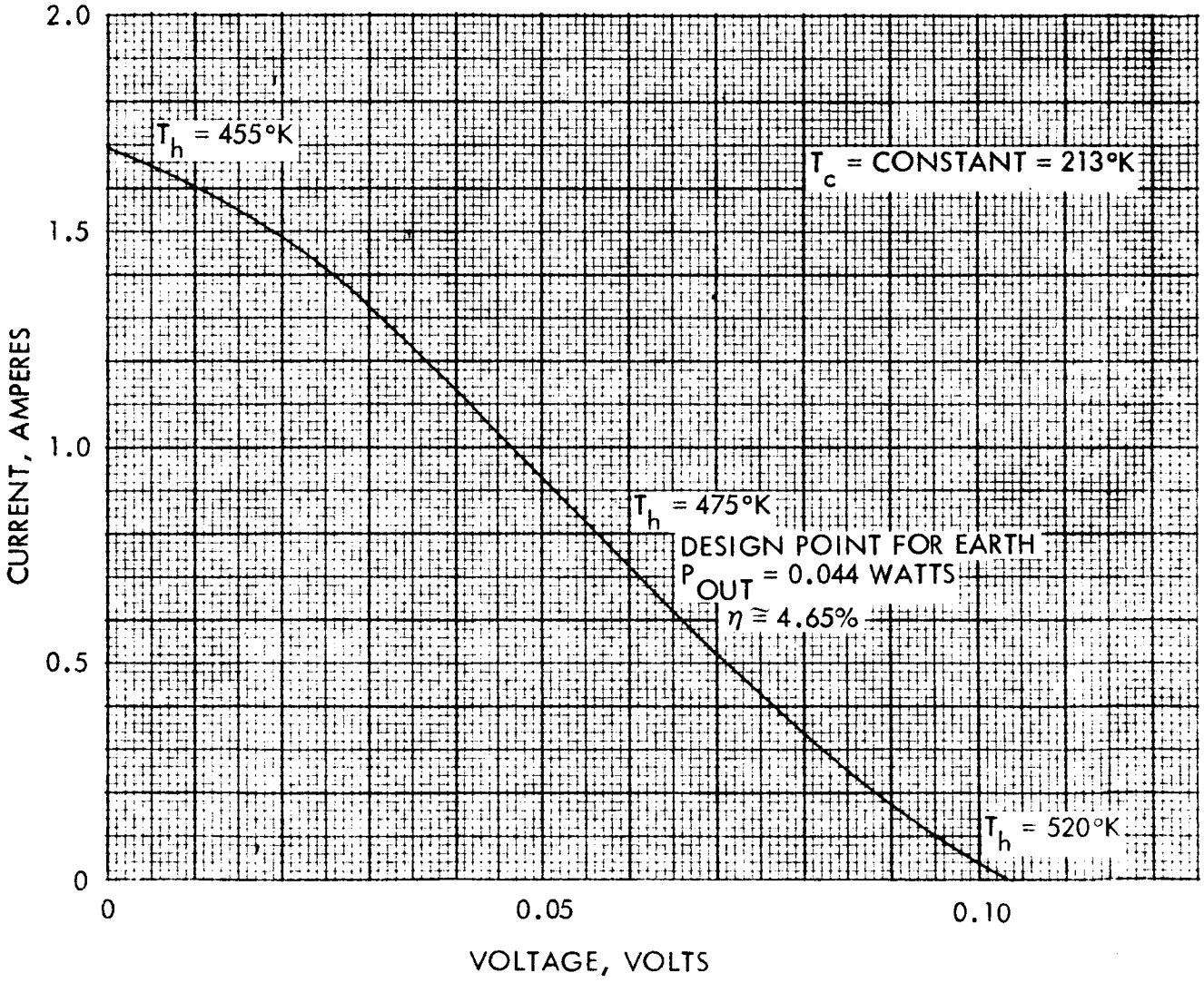

Figure C-1. I-V Curve, Flat-Plate Solar Thermoelectrics for Earth Orbit

APPENDIX D

A STUDY OF THE ELECTRO-THERMAL BEHAVIOR OF A THERMIONIC CONVERTER

The problem is to determine the effects and interrelationships of the electrical-thermal operating points for a solar-powered thermionic converter. The total thermal input to each diode emitter is:

$$Q_{in} = \overset{(1)}{i(\phi_e + V + 2kT_e)} + \overset{(2)}{\frac{\sigma A_a \epsilon_c}{n} T_e^4}$$

$$+ \overset{(3)}{\sigma \epsilon_n A_e \left(T_e^4 - T_c^4\right)} + \overset{(4)}{\sigma \epsilon_s A_s \left(T_e^4 - T_c^4\right)}$$

$$+ \overset{(5)}{(K_{cs} + K_s)(T_e - T_c)}, \quad i^2R \text{ internal to diode is neglected} \qquad (1)$$

The first term (1) is the electron cooling term where

i = the current

ϕ_e = emitter work function

k = the Boltzmann constant (8.616×10^{-5} ev/^oK)

T_e = the emitter temperature (^oK)

V = diode voltage.

The second term (2) is the heat reradiated from the aperture of the obsorber cavity per diode where

σ = the Stefan-Boltzmann constant (5.67×10^{-12} watt/cm^2 (^oK)^4)

A_a = the aperture area (cm^2)

ϵ_c = the effective emissivity of the absorber cavity

n = the number of diodes.

The third term (3) is the radiative heat transfer between emitter and collector where

ϵ_n = the effective emissivity of the elements

$$\frac{1}{\frac{1}{\epsilon_e} + \frac{1}{\epsilon_c} - 1}$$

A_c = the emitter area (cm^2)

T_c = the collector temperature (^oK).

The fourth term (4) is the radiative heat transfer between structure elements where $\epsilon_s A_s$ is the product of effective emissivity and area.

The fifth term (5) is the conductive heat transfer through the cesium gas and structure between emitter and collector where

K_{cs} = the total thermal conductivity of the cesium plasma

K_s = the total thermal conductivity of the structure.

The radiative heat transfer or "dump" from the collector to space is given by

$$\sigma A_c \epsilon_c T_c^4 \qquad (2)$$

where $\epsilon_c A_c$ is the effective product of the emissivity and collector-radiator area.

Consider the energy balance for each diode as shown in Figure D-1.

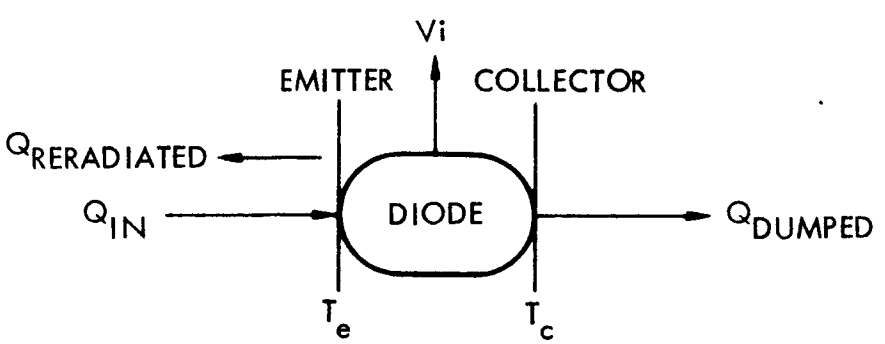

Figure D-1. Energy Flow Diagram

In equation form, this is

$$\sigma A_c \epsilon_c T_c^4 = Q_{in} - iV - \sigma \frac{A_a \epsilon_c}{n} T_c^4 \tag{3}$$

Substituting Equation (1) for Q_{in}

$$\begin{aligned} \sigma A_c \epsilon_c T_c^4 = {} & i(\phi_e + 2kT_e) \\ & + \sigma\left(T_e^4 - T_c^4\right)(\epsilon_n A_c + \epsilon_s A_s) \\ & + (K_{cs} + K_s)(T_e - T_c) \end{aligned} \tag{4}$$

Equation (4) gives the relationship between T_e and T_c for any current i.

At this point, information is required to relate V and i to T_e and T_c as well as to indicate the magnitude of the constants for a particular device. Reference is made to Tapco Group Report ER-4378 (Reference 3-36) where enough details are given to allow some analysis to proceed.

The data calculated for a specific diode are given as follows:

$T_e = 2000^oK$

$T_c = 1000^oK$

$T_{cs} = 600^oK$

Interelectrode spacing = 1.77 mils

$A_c = 1.86\ cm^2$

$\phi_e = 1.96$ volts

Term (3) of Equation (1) = $1.86 \times 7.6\ w/cm^2$

$K_{cs}\Delta T = 8.0\ w/cm^2 \times 1.86\ cm^2$

$K_s \Delta T = 10$ watts

Term (4) of Equation (1) = 7.45 watts.

The cavity aperture is given as 1.45 centimeters in diameter; therefore, $A_a = 1.65\ cm^2$. Since there are five converters, $A_a/n = 0.33\ cm^2$.

The effective emissivity is given as 0.6 and will be held constant in this study. Summarizing terms for Equation (1):

1) The total electron cooling is determined as 42.5 x 1.86 = 79 watts

2) The reradiated heat per diode is 18 watts

3) The interelectrode radiative transfer is calculated as 14.1 watts

4) The structure radiative transfer is estimated as 7.45 watts

5) The net conductive heat transfer is calculated as 19 + 10 = 29 watts

The total heat input per diode is then

$$\begin{array}{r} 79.0 \\ 18.0 \\ 14.1 \\ 7.5 \\ \underline{29.0} \\ 147.6 = 148 \text{ watts} \end{array}$$

The electrical operating point for the conditions is given as 24.2 amperes at 1.07 volts which is equal to 26 watts.

From Equation (2) the heat radiated from the collector is then

$$148 - 26 - 18 = 104 \text{ watts}$$

The coefficients of the terms in Equation (1) can now be obtained.

As given before, $\phi_e = 1.96$ volts. The others are

$$\sigma \frac{A_a \epsilon_c}{n} = 1.12 \times 10^{-12} \frac{\text{watts}}{{}^oK^4}$$

$$\sigma \epsilon_n A_e = \frac{14.1}{(16 - 1)} \times 10^{-12} = 0.94 \times 10^{-12} \frac{\text{watts}}{{}^oK^4}$$

$$\sigma \epsilon_c A_s = \frac{7.45}{15} \times 10^{-12} = 0.496 \times 10^{-12} \frac{\text{watts}}{{}^oK^4}$$

$$K_{cs} + K_s = \frac{29}{1000} = 0.029 \frac{\text{watts}}{{}^oK}$$

Equation (1) now becomes

$$Q_{in} = i\left(1.96 + 0.17 \times 10^{-3}\ T_e + V\right) + 1.12 \times 10^{-4}\ T_e^{\ 4}$$

$$+ 0.94 \times 10^{-12}\left(T_e^{\ 4} - T_c^{\ 4}\right) 0.496 \times 10^{-12}\left(T_e^{\ 4} - T_c^{\ 4}\right) + 0.029\,(T_c - T_c)$$

Combining terms, this is

$$Q_{in} = i\left(1.96 + 0.17 \times 10^{-3}\ T_e + V\right) + 2.56\ T_e^{\ 4}$$

$$- 1.44 \times 10^{-12}\ T_c^{\ 4} + 0.029\ \Delta T$$

Equation (4) now becomes

$$\sigma A_c \epsilon_c T_c^{\ 4} = i\left(1.96 + 0.17 \times 10^{-3}\ T_e\right)$$

$$+ 1.44 \times 10^{-12}\left(T_e^{\ 4} - T_c^{\ 4}\right) + 0.029\ (T_e - T_c)$$

Since this is 104 watts at $1000^{\circ}K$

$$\sigma A_c \epsilon_c = \frac{104}{10^{12}} = 104 \times 10^{-12}\ \frac{\text{watt}}{{}^{\circ}K^4}$$

Therefore

$$(104 + 1.44) \times 10^{-12}\ T_c^{\ 4} = i\left(1.96 + 0.17 \times 10^{-3}\ T_e\right)$$

$$+ 1.44 \times 10^{-12}\ T_e^{\ 4} + 0.029\ (T_e - T_c)\ .$$

In order to solve this relationship, some simplification is required to make the equation workable at $T_e = 2000^{\circ}K$ and $T_c = 1000^{\circ}K$. The terms are as follows:

$$105.44 = i(1.96 + 0.34) + 231 + 29$$

The 0.34 volt term is relatively small and will be considered constant at the $2000^{\circ}K$ value. The 29-watt conductive term will also be considered constant at its $2000 - 1000^{\circ}K$ value. These terms will change slowly with temperature compared to the 4th power terms. The approximate relationship is then

$$105.4 \times 10^{-12}\ T_c^{\ 4} = i(2.3) + 1.44 \times 10^{-12}\ T_c^{\ 4} + 29$$

Then

$$T_c^{\ 4} = \frac{i(2.3) + 1.44 \times 10^{-12}\ T_e^{\ 4} + 29}{105.4 \times 10^{-12}} \tag{5}$$

Equating Equation (3) to Equation (4) with number coefficients

$$Q_{in} - iV - 1.12 \times 10^{-12}\ T_c^{\ 4} = i(2.3) + 1.44 \times 10^{-12}\left(T_e^{\ 4} - T_c^{\ 4}\right) + 29$$

or

$$Q_{in} = i(2.3 + V) + 2.56 \times 10^{-12}\ T_e^{\ 4} - 1.44 \times 10^{-12}\ T_c^{\ 4} + 29$$

Then substituting Equation (5) for $T_c^{\ 4}$

$$Q_{in} = i(2.3 + V) + 2.56 \times 10^{-12}\ T_e^{\ 4} - \frac{1.44 \times 10^{-12}}{105.4 \times 10^{-12}}$$

$$\times\left[i(2.3) + 1.44 \times 10^{-12}\ T_e^{\ 4} + 29\right]$$

Note that the third term is negligible, being about 1 percent of the others. Therefore

$$Q_{in} \cong i(2.3 + V) + 2.56 \times 10^{-12}\ T_e^{\ 4} + 29$$

Another simplification would be to consider T_c constant at $1000^{\circ}C$.

The equation then becomes

$$Q_{in} = 2.56 \times 10^{-12}\ T_e^{\ 4} + i(2.3 + V) + 0.029\ T_e - 29 \tag{6}$$

This equation can then be used to solve for emitter temperature as a function of Q_{in}, i and V. The product $i(V + 2.3)$ is the electron cooling term (Q_e). Relationships can be plotted of Q_{in} versus T_e for constant Q_e.

For

$$T_e = 2400^\circ K$$
$$= 2200^\circ K$$
$$= 2000^\circ K$$
$$= 1800^\circ K$$
$$= 1600^\circ K$$

with no electron cooling,

$$Q_{in} = 125.6 \text{ watts}$$
$$= 94.9$$
$$= 70.0$$
$$= 50.1$$
$$= 34.2$$

For other values of electron cooling, a family of curves can be obtained by simply adding Q_e to the above values at the respective temperatures. Figure D-2 shows this set of curves.

The next requirement is to obtain the I-V curves for the diode at various temperatures. One is given for $T_e = 2000^\circ K$ in Figure D-3. Note that total input heat values vary from 180 to 70 watts over the range of operating points. The equation for this curve is approximately,

$$V = 1.11 + 0.207 \, I_n \frac{I_s - I}{I} \tag{7}$$

where $I_s = 44$ amps, the short circuit current. I_s is a function of emitter temperature.* Shown on the curve at various points are the heat inputs (Q_{in}) required.

*This is a simplification as other terms are also temperature-sensitive, but it should give a reasonable approximation. If it can be assumed that only I_s is temperature-sensitive, then the analysis can proceed by generating I-V curves for various constant emitter temperatures.

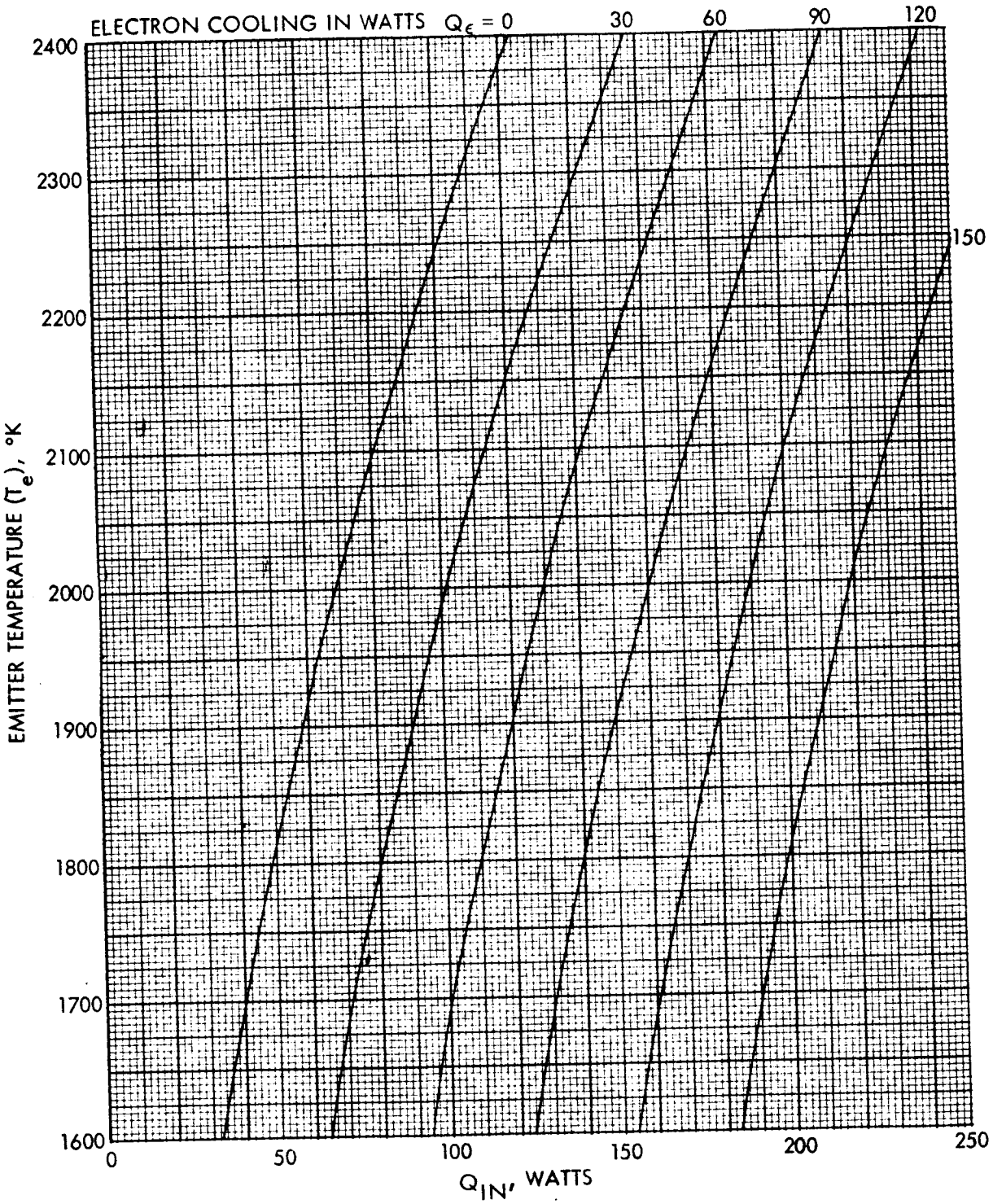

Figure D-2. Emitter Temperature Versus Thermal Input as a Function of Electron Cooling

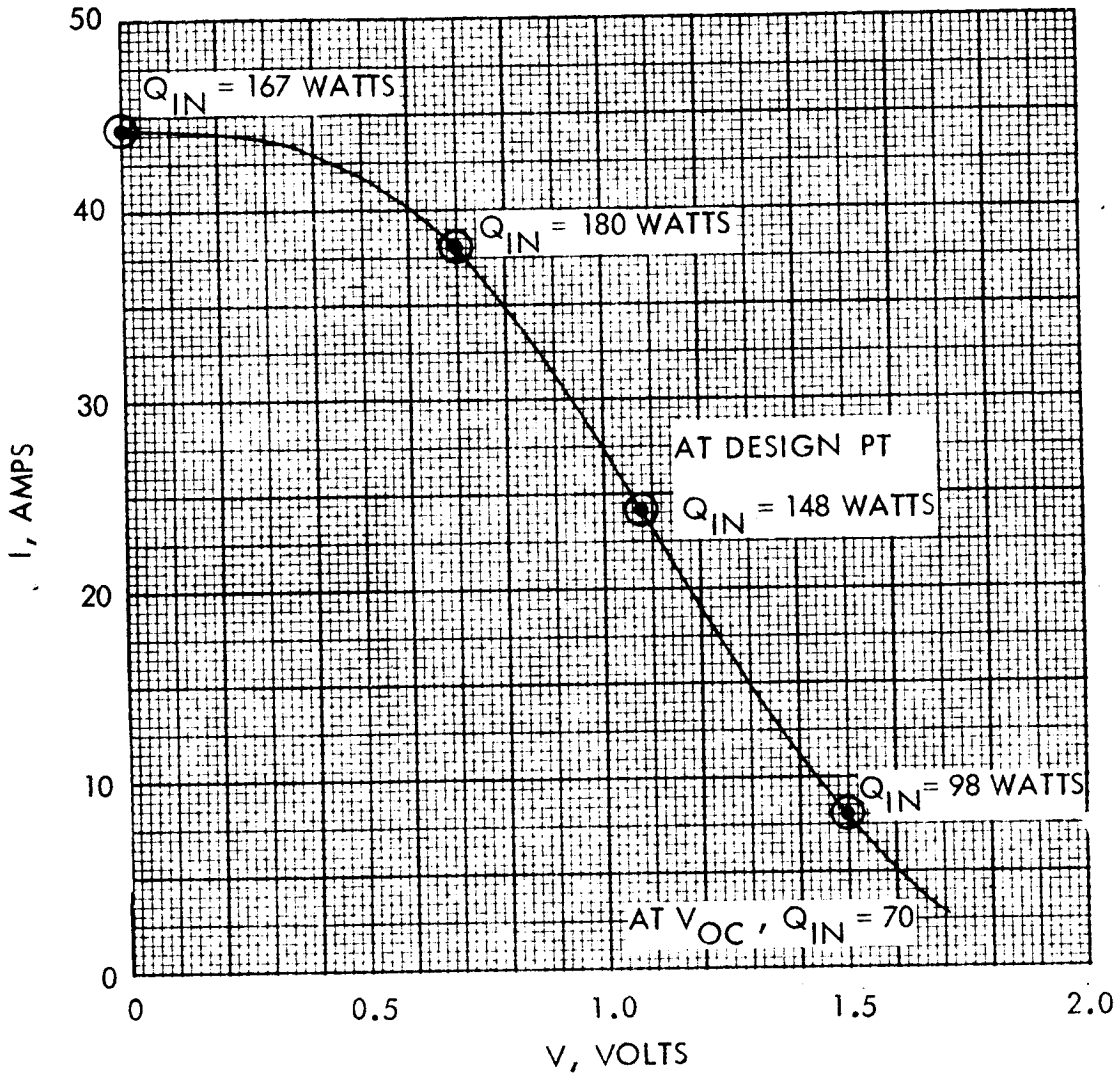

Figure D-3. I-V Curve for a Thermionic Diode at a Constant Temperature of 2000°K

So that I-V curves can be generated for other emitter temperatures, it will be assumed that the Richardson-Dushman equation can be used so that

$$I_s = KT_e^2 \epsilon^{-\frac{e\phi_c}{kT_e}} \text{ amps} \tag{8}$$

when $T_e = 2000^oK$, $I_s = 44$. Substituting in Equation (8)

$$44 = K \times 4 \times 10^6 \epsilon^{-\frac{e\phi_c}{k \times 2000}}$$

$$\phi_e = 1.96 \text{ volts}$$

Therefore

$$\frac{e\phi_c}{k} = \frac{1.96 \times 10^5}{8.616} = 22,700$$

$$\epsilon^{-\frac{22,700}{2000}} = \epsilon^{-11.3} = 10^{-4} \times 0.122$$

and

$$K = \frac{44}{4 \times 10^2 \times 0.122} = 0.901$$

then

$$I_s = 0.901\ T_e^2\ \epsilon^{-\frac{22,700}{T_e}} \text{ amps}$$

I_s may now be computed at other temperatures and the I-V relationships developed at these temperatures.

The temperatures chosen in ^oK are:

2400
2200
2100
2050
1950
1900
1800
1600

At these temperatures, the corresponding values for I_s in amperes are:

405
145
80
57.7
29.4
19.8
9.6
1.5

Using these values of I_s, I-V curves for the various constant temperatures are shown in Figure D-4. At

$V = 0$	$I = I_s$
$V = 0.5$	$I = 0.95\ I_s$
$V = 1.11$	$I = 0.5\ I_s$
$V = 1.5$	$I = 0.13\ I_s$
$V = 2.0$	$I = 0.013\ I_s$

From the I-V curves, the electron cooling can be calculated as $Q_e = I(2.2 + V)$ for each curve. In Figure D-5, Q_e is plotted versus V for the various emitter temperatures. Using the relationships in Figure D-2, with an assumed constant Q_{in}, the electron cooling required at each T_e can be found. Going to Figure D-5, this value of Q_e can be used to find the required operating voltage on the proper temperature curve. Points for equal input power are connected to give a locus of Q_e versus V for Q_{in} constant. Using the value of voltage obtained from Figure D-5, the operating point on the corresponding I-V curve of Figure D-4 can be obtained. When connected, these points give the steady-state I-V curves for constant Q_{in}.

Families of curves such as those developed in Figure D-4 are necessary if a thorough understanding is to be gained of the behavior of these devices in a system. While these curves are based on a number of approximations and can be considered as approximations only, the general shape of the constant Q curves and constant T_e curves are as shown in Reference 3-34 published by EOS.

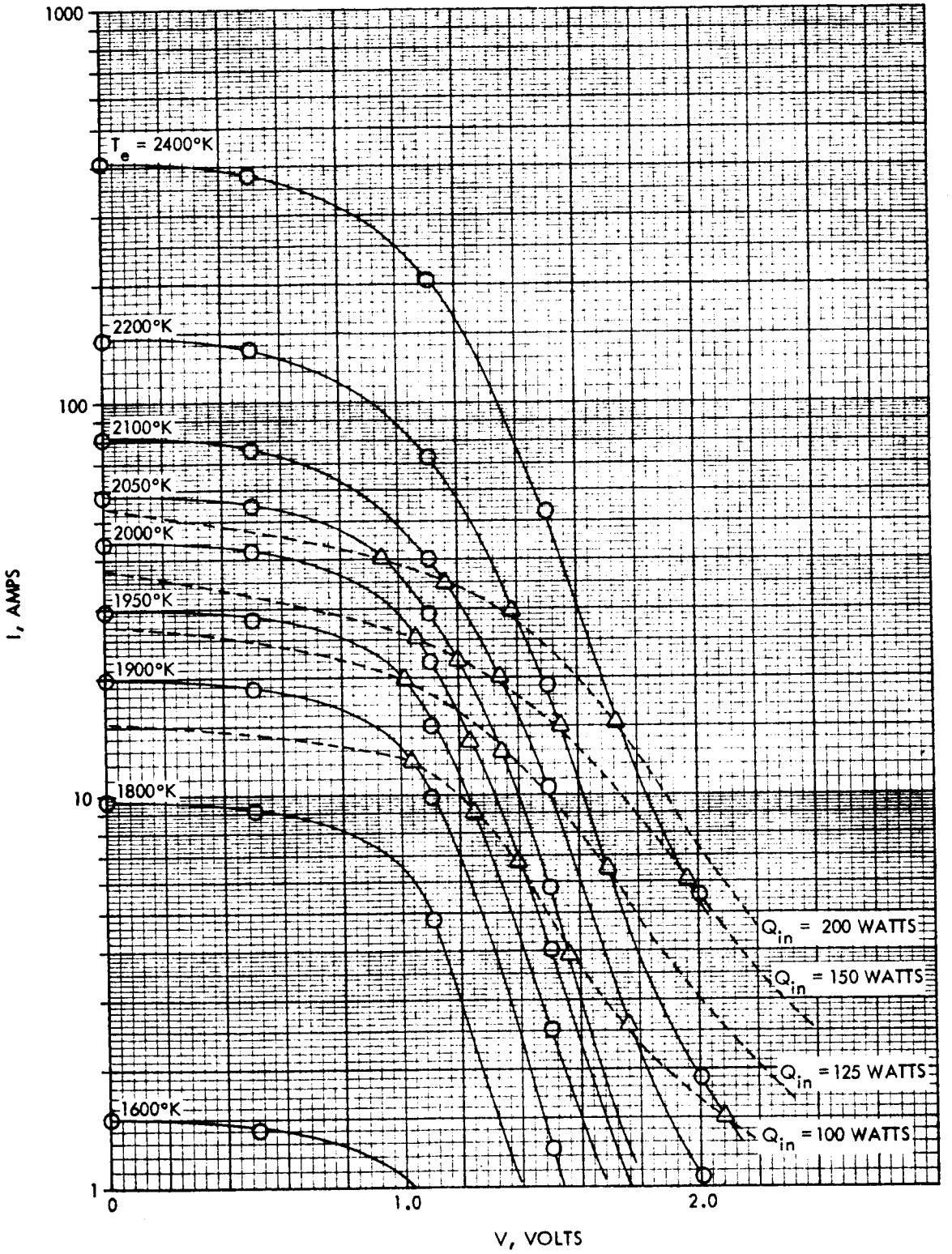

Figure D-4. Calculated I-V Curves as a Function of Emitter Temperature and Thermal Input

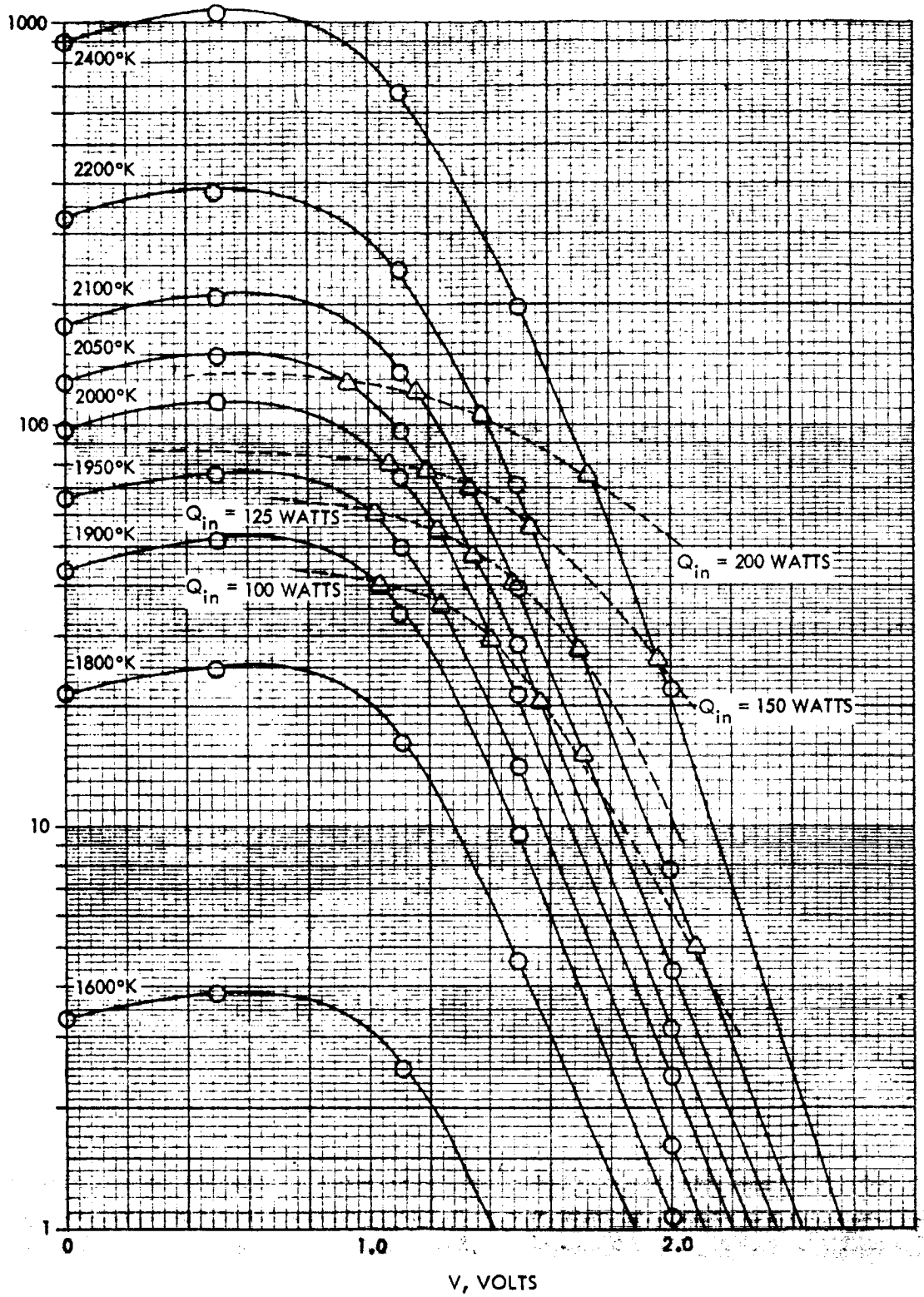

Figure D-5. Plot of Electron Cooling Versus Voltage as a Function of Emitter Temperature and Thermal Input